SAL Report No. 46

Inclusive Photoproduction of Positive Pions

Kevin G. Fissum

1993

SASKATCHEWAN ACCELERATOR LABORATORY
UNIVERSITY OF SASKATCHEWAN
SASKATOON, SASKATCHEWAN
S7N 0W0

INCLUSIVE PHOTOPRODUCTION OF POSITIVE PIONS

A Thesis Submitted to the College of

Graduate Studies and Research

in Partial Fulfillment of the Requirements

for the Degree of Doctor of Philosophy

in the Department of Physics

University of Saskatchewan

Saskatoon

By

Kevin G. Fissum

Fall, 1993

In presenting this thesis in partial fulfillment of the requirements for a Postgraduate degree from the University of Saskatchewan, I agree that the Libraries of this University may make it available for inspection. I further agree that permission for copying of this thesis in any manner, in whole or in part, for scholarly purposes may be granted by the professor or professors who supervised my thesis work or, in their absence, by the Head of the Department or the Dean of the College in which my thesis work was done. It is understood that any copying or publication or use of this thesis or parts thereof for financial gain shall not be allowed without my written permission. It is also understood that due recognition shall be given to me and to the University of Saskatchewan in any scholarly use which may be made of any material in my thesis.

Requests for permission to copy or make other use of material in this thesis in whole or in part should be addressed to:

Head of the Department of Physics

University of Saskatchewan

Saskatoon, Saskatchewan S7N 0W0

ABSTRACT

Inclusive π^+ photoproduction in the $\Delta(1232)$ region was performed using the recently commissioned photon tagging facility at the Saskatchewan Accelerator Laboratory during the Fall of 1990. This thesis reports on the measurement, which constituted the first tagged photon experiment performed in Canada.

The π^+ detectors consisted of four low-threshold, discrete ΔE-E type plastic scintillator telescopes placed at nominal laboratory angles of 50^o, 80^o, 110^o, and 140^o. Identification centered on the π^+ decay. Targets spanned the periodic table, including CH_2 for both energy calibration and H, C, Ca, Sn and Pb. Double differential cross sections, angular distributions and total cross sections were obtained for photon energies of 184, 194, 204, and 213 MeV.

Absolute measured angular distributions from the proton tended to peak at ~100^o in the Center-of-Momentum frame. They were slightly lower than previously published results obtained using bremsstrahlung photons; however, agreement existed with a tagged photon data point. Those for complex nuclei tended to be isotropic in the laboratory frame. The C angular distributions were higher than previously published results obtained using the photon difference method, but agreed well with previously published tagged photon data at all but the most forward angle.

Angular distributions were integrated to produce total cross sections. Total cross sections from the proton compared favorably with previously published tagged photon results. Total cross sections from C were slightly lower than previously published tagged photon results. For nuclei, the total cross section per proton was less than that for the free proton, and decreased as A increased.

It is hoped these new reliable tagged photon data, with the many target/angle/photon energy combinations, will stimulate further theoretical study.

ACKNOWLEDGEMENTS

I would like to thank my supervisor, Henry Caplan, for the countless hours he spent helping me see this work to its completion. His experience and support are greatly appreciated.

Thanks also go to everyone who contributed their efforts to the experiment. In particular, I would like to mention two of my collaborators from the University of Washington, Doug Rosenzweig and Derek Storm, who were instrumental to this project.

I would also like to thank the faculty, staff and graduate students of the Saskatchewan Accelerator Laboratory. From day one, no one was ever too busy to lend a helping hand. In particular, I would like to thank Emil Hallin, Johannes Vogt, Mohamed Benmerrouche, and Ru Igarashi, without whose help this work would not have been possible.

I thank Ingvar Blomqvist, Rafael Carrasco, Ralf Gothe, and Satoshi Nozawa for their interest in my work and the numerous personal communications they provided me.

I thank my family for their encouragement and support.

The financial assistance of the Saskatchewan Accelerator Laboratory is gratefully acknowledged.

TABLE OF CONTENTS

LIST OF TABLES

LIST OF FIGURES

LIST OF ABBREVIATIONS

ADC	Analog-to-Digital Converter
CAMAC	Computer Automated Measurement And Control
CFD	Constant Fraction Discriminator
CM	Center-of-Momentum
CW	Continuous Wave
DCX	Double Charge Exchange
DIF	Decay-In-Flight
ECS	Energy Compression System
FSI	Final State Interactions
FWHM	Full Width at Half Maximum
LED	Leading Edge Discriminator
LINAC	LINear ACcelerator
NIM	Nuclear Instrument Module
PSR	Pulse Stretcher Ring
QF	Quasi-Free
RF	Radio Frequency
SCX	Single Charge Exchange
TDC	Time-to-Digital Converter
TOF	Time-Of-Flight
UVT	UltraViolet Transparent
X	eXperiment

Chapter 1. MOTIVATION

A general introduction to the pion and pion photoproduction is presented. Basic theories and previous work are discussed. Units of $h/2\pi = c = 1$ are assumed.

1.1 Introduction

By 1934, it was well known that the nuclear force falls off extremely rapidly with distance from the nucleus. From this, the theorist Yukawa suggested that this "strong" force was due to virtual exchange particles of non-zero rest mass, which he called "mesotrons". In contrast, the exchange particle for the electromagnetic force, which has infinite range, is the massless virtual photon. He speculated the mesotron should have a mass of about $200m_e$, intermediate between that of the electron and the proton. Soon after, such a particle was discovered in cosmic rays by the experimentalists Anderson and Neddermeyer. However, this particle did not interact strongly, and turned out to be what we now call the μ-meson, or muon, a decay product of the pion. It was not until 1947 that the mesotron of Yukawa was first discovered in cosmic rays by the experimentalist Powell. It was renamed the π-meson, or pion.

The pion has zero spin $J^{\pi} = 0^-$ and exists in three electrical charge states: π^+,π^-, and π^0. In the modern view, the pions are composed of quark-antiquark pairs, with the particular combination defined by the resulting electrical charge state. The π^+ is the focus of this work. It has rest mass $m_{\pi} = 139.6$ MeV and a mean lifetime $\tau = 26.0$ ns. A π^+ usually (> 99.98% of the time - (Aguilar-Benitez *et al.*, 1992)) decays at rest to a μ^+ of kinetic energy 4.12 MeV, and an associated neutrino (see Appendix A)

$$\pi^+ \rightarrow \mu^+ + \nu_{\mu}. \qquad (1.1)$$

Pions were first created in laboratories using early (post-World War II) hadron accelerators. Soon after, bremsstrahlung photons produced at electron accelerators were used to photoproduce pions. It is convenient to address the history of experiments in photopion production in terms of three phases (Nagl *et al.*, 1991). During the first phase, from 1947

to 1956, the basic features of inclusive (any final state which included a π^+) photopion yields from H and other simple nuclei were investigated. Absolute cross sections were unobtainable due to normalization problems - the incident photon flux was simply not known well enough. During the second phase, from 1957 to 1976, as experimental techniques improved dramatically, exclusive (a particular final state which included a π^+) total cross sections were measured for H and more complex nuclei using bremsstrahlung photons. While normalization problems remained, it was a great advance over the unnormalized yield measurements of the 1950's. During the third phase, 1977 to approximately the mid-1980's, major advances were made into the fields of πA interactions and nuclear structure by measuring both inclusive and exclusive photopion angular distributions and total cross sections using magnetic spectrometers and the quasi-monochromatic photons from the first generation of photon taggers. These early taggers served to reduce substantially the normalization problems innate to a bremsstrahlung photon experiment. However, due to small cross sections, poor duty cycle machines, and inherently slow electronics, tagged photon experiments have not really been practical in terms of obtainable count rates until very recently.

The current era of photonuclear physics makes available for the experimentalist high duty factor, high intensity electron machines. When coupled to modern electronics, second generation photon taggers are capable of instantaneous tagging rates of tens of MHz. These facilities are powerful tools for investigating the small cross sections associated with photopion production. The Saskatchewan Accelerator Laboratory, where this work was performed, is one such facility.

1.2 The Elementary Reaction $p(\gamma,\pi^+)n$

1.2.1 Theory

Figure 1.1 represents π^+ photoproduction in a simple, diagrammatic manner.

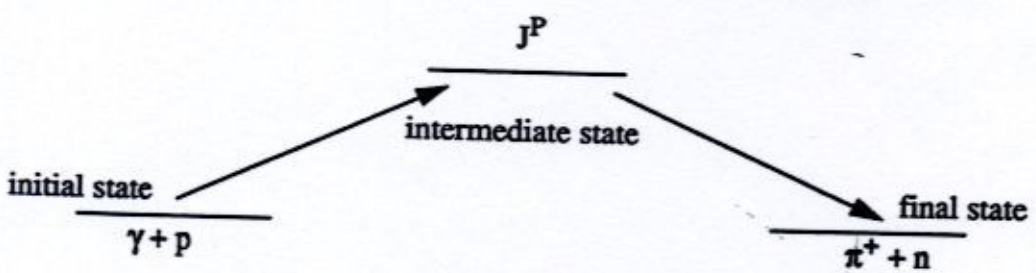

Figure 1.1: The Elementary Reaction $p(\gamma,\pi^+)n$

The initial state consists of a photon (λ^P) and a proton ($1/2^+$). The final state consists of a π^+ (0^-) and a neutron ($1/2^+$). "J" and "p" represent the total angular momentum and parity. Table 1.1 summarizes the multipole decomposition of the elementary π^+ photoproduction amplitude assuming only S (l=0) and P (l=1) π^+ waves contribute substantially to the cross section at the photon energies used for this experiment.

Table 1.1: Multipole Contributions to the Elementary Cross Section

Photon angular momentum λ	Photon Multipole	J	p	π^+angular momentum l	π^+ Multipole
1	E1	1/2	-	0 (S)	E_{0+}
	M1	1/2	+	1 (P)	M_{1-}
	M1	3/2	+	1 (P)	M_{1+}
2	E2	3/2	+	1 (P)	E_{1+}

The mechanisms which are responsible for the creation of π^+ may be represented by a series of "Feynmann diagrams" which are shown in Figure 1.2.

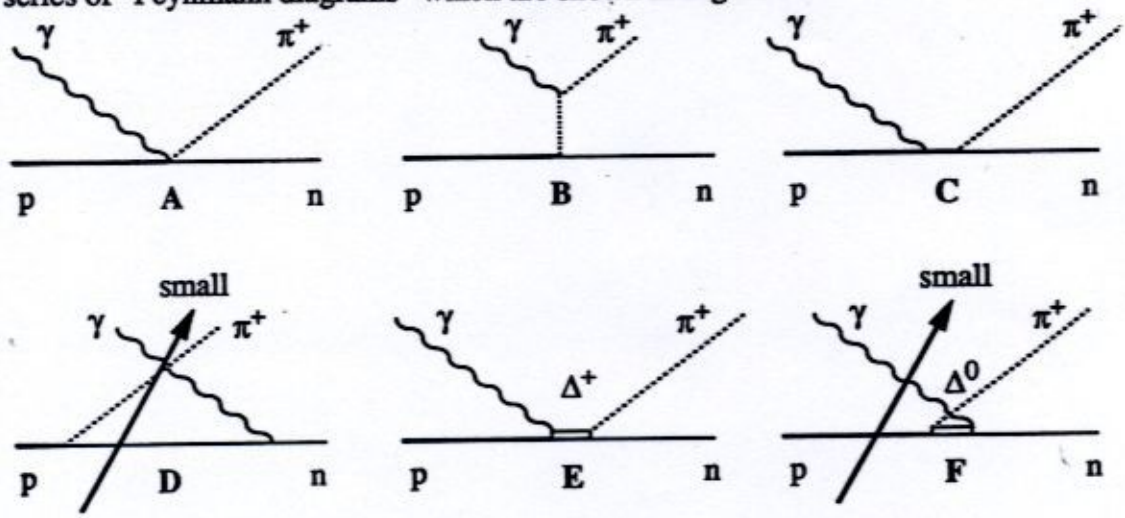

Figure 1.2: Feynmann Diagrams for the Elementary Reaction $p(\gamma,\pi^+)n$

Diagram A is known as the "Seagull" diagram. Here, a photon couples directly to the charge of the proton and a π^+ is produced at the same vertex. This term is also known as the "Kroll-Rudermann" term, and contributes solely to S-wave photoproduction (the E_{0+} multipole). It dominates the cross section at threshold and still affects it strongly at low energies. Diagram B represents the photon coupling with the charge of a virtual π^+ and putting it on the mass shell without coming into direct contact with the proton. This term

contributes to both S and P wave photoproduction (all multipoles), and is known as the "t-channel" of the reaction. Diagram C represents the photon coupling to the charge of the proton with a π^+ produced at a second vertex. This term contributes to both S-wave and P-wave photoproduction (the E_{0+} and M_{1-} amplitudes), and is known as the "s-channel" of the reaction. Diagram D has the proton emitting a π^+, and the photon coupling to the neutron. This mechanism is known as the "u-channel" of the reaction. The contribution of this diagram to the cross section is taken to be small with respect to its crossing diagram C since the reaction goes via the interaction of the photon with the magnetic moment of the neutron. Diagram E represents the photon interacting with the charge of the proton and exciting the $\Delta^+(1232)$ resonance, which subsequently decays to a π^+ and a neutron. This term contributes to P-wave photoproduction (the M_{1+} and E_{1+} amplitudes), and is known as the "delta s-channel" of the reaction. Lastly, diagram F represents the proton decaying to the $\Delta^0(1232)$ resonance and a π^+, with the photon interacting with the neutron. This is known as the "delta-u channel" of the reaction, and is also taken to be small with respect to its crossing diagram E since the reaction goes via the interaction of the photon with the magnetic moment of the neutron. In the pseudo-vector coupling scheme, diagrams A, B, C, and D constitute the "Born" term.

It has become customary (Moravcsik, 1956) to analyze the angular distribution of charged pion photoproduction in terms of a quadratic expression in $\cos(\theta^{CM})$, where θ^{CM} is the pion emission angle with respect to the photon beam in the Center-of-Momentum (CM) frame (see Appendix B). The angular distribution for this reaction in the CM frame at the photon energies of this experiment ($E_\gamma \sim 200$ MeV) may be written as

$$\left(\frac{d\sigma}{d\Omega}\right)^{CM} = \left(\frac{q}{k}\right)\left[P_1 + P_2\cos(\theta^{CM}) + P_3\cos^2(\theta^{CM})\right] \qquad (1.2)$$

where "q" is the momentum of the π^+, "k" is the momentum of the photon, and the coefficients "P_i" expressed in terms of the multipoles of Table 1.1 are given by

$$P_1 = |E_{0+}|^2 + |M_{1-}|^2 + \frac{5}{2}|M_{1+}|^2 + \frac{9}{2}|E_{1+}|^2 + \mathrm{Re}\left[M_{1-}M_{1+}^* - 3E_{1+}(M_{1+} - M_{1-})^*\right], \qquad (1.3)$$

$$P_2 = 2\mathrm{Re}\left[E_{0+}(M_{1+} - M_{1-} + 3E_{1+})^*\right], \qquad (1.4)$$

$$P_3 = 3(-\frac{1}{2}|M_{1^+}|^2 + \frac{3}{2}|E_{1^+}|^2 + \mathrm{Re}\,[M_{1^+}(3E_{1^+} - M_{1^-})^* - 3M_{1^-}E_{1^+}^*]\,). \qquad (1.5)$$

Note the amplitudes are complex valued. By fitting to the experimentally determined CM angular distributions, the coefficients P_i can be determined. However, it will not be possible to extract values for the individual multipoles from these fits, even assuming they are purely real, since they are not uniquely determined (three equations; four unknowns). Instead, knowledge of the theoretically predicted values of the multipoles will allow calculation of the theoretical coefficients P_i, thus bridging experiment and theory. In this manner, the theoretically predicted coefficients P_i will be used to determine theoretically predicted angular distributions and total cross sections.

Integrating the angular distribution given by equation 1.2 over solid angle produces the total cross section for π^+ photoproduction in terms of the coefficients P_i

$$\sigma = 4\pi(\frac{q}{k})\left[P_1 + \frac{1}{3}P_3\right], \qquad (1.6)$$

which, upon substitution for the π^+ multipoles, becomes

$$\sigma = 4\pi(\frac{q}{k})\left[|E_{0^+}|^2 + |M_{1^-}|^2 + 2|M_{1^+}|^2 + 6|E_{1^+}|^2\right]. \qquad (1.7)$$

There have been many theoretical attempts to explain the elementary cross section. The first such attempts involved dispersion relations (Berends *et al.*, 1967). The next generation of calculations involved effective Lagrangians (Blomqvist *et al.*, 1977). Modern calculations employ dynamical models (Nozawa *et al.*, 1990). Figure 1.3 illustrates the energy dependence of the P_i coefficients for a multipole analysis and a dispersion relation calculation.

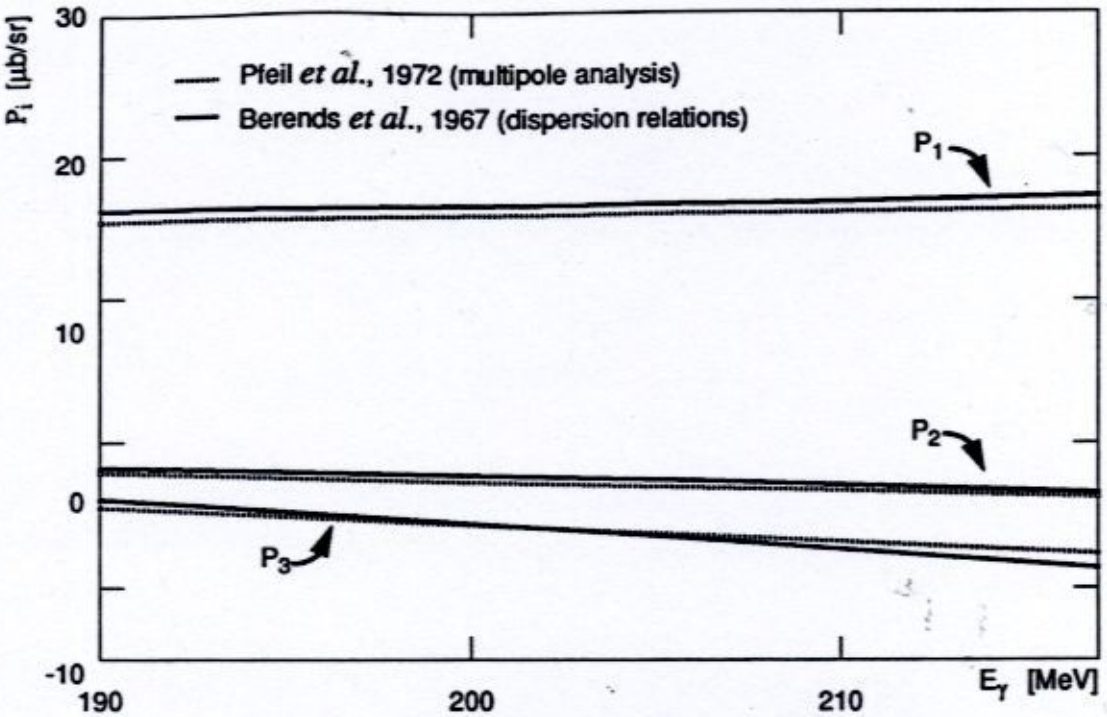

Figure 1.3: Literature Values of P_i Coefficients

It is not the goal of this thesis to investigate the details of these calculations. Rather, comparisons between the various predictions as well as previous data and this experiment will be made.

1.2.2 Comparison of Predictions With Previous Experiments

In Figures 1.4 to 1.7, calculated angular distributions at four photon energies are compared with the data set of Adamovich *et al.* and a single data point obtained by van den Brink. The Adamovich *et al.* data represents a series of measurements of the elementary cross section performed at the Lebedev Physics Institute in the late 1960's using bremsstrahlung photons and emulsion stacks as π^+ detectors. It was selected as being representative of the pre-1970 bremsstrahlung data for this reaction (Genzel *et al.*, 1973). The van den Brink data point represents an independent tagged photon measurement of the elementary reaction performed in the summer of 1992 at SAL detecting the π^+ using a combination of scintillator stacks and wire chambers.

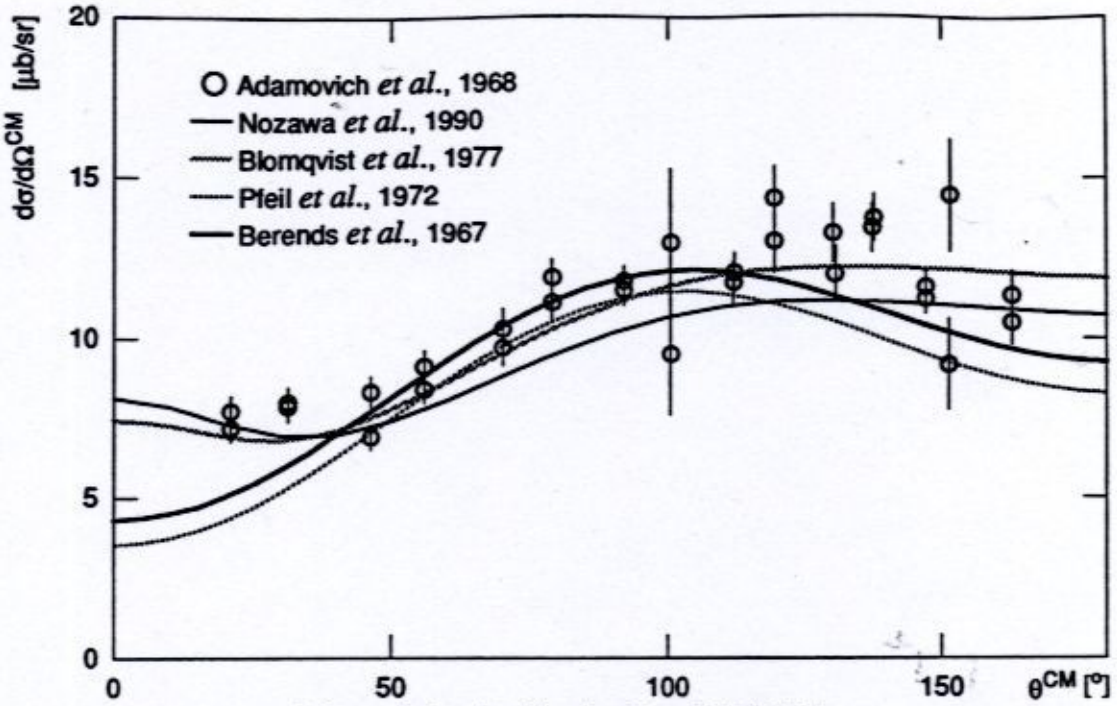

Figure 1.4: $p(\gamma,\pi^+)n$ for $E_\gamma = 213$ MeV

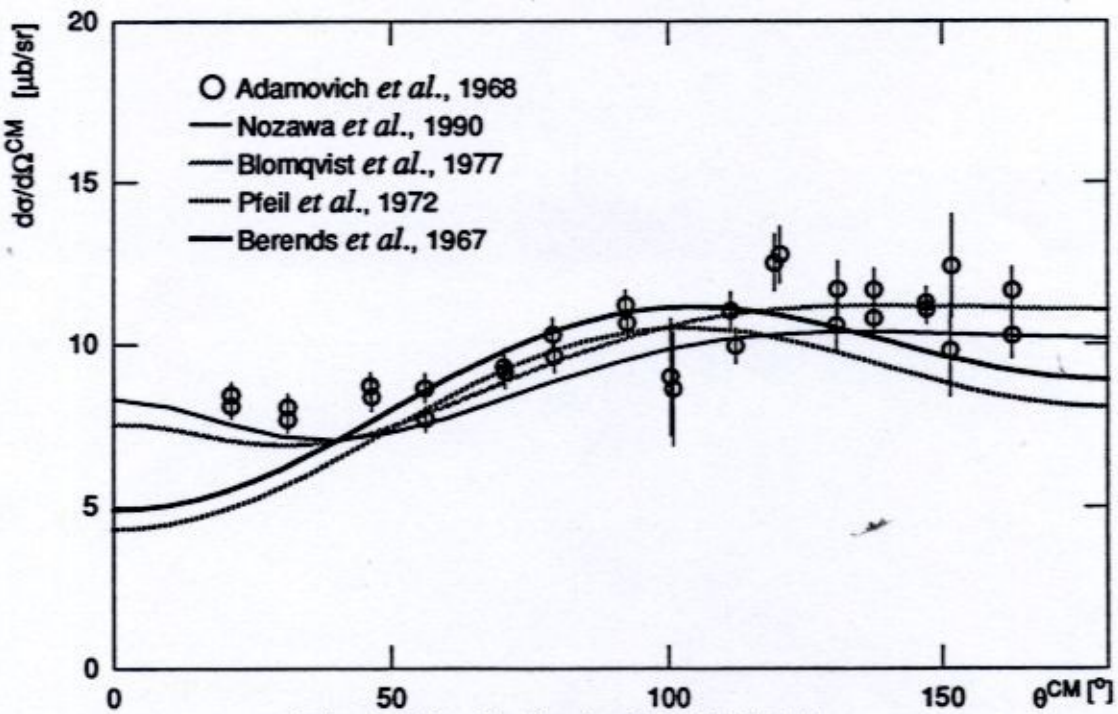

Figure 1.5: $p(\gamma,\pi^+)n$ for $E_\gamma = 204$ MeV

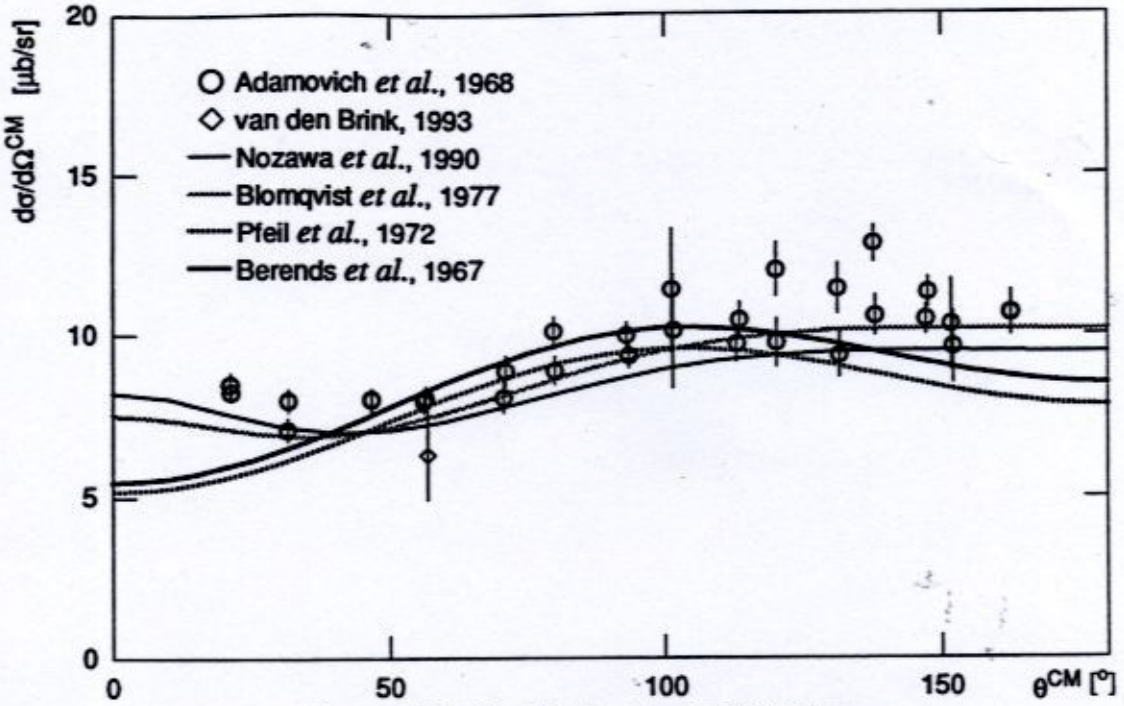

Figure 1.6: $p(\gamma,\pi^+)n$ for $E_\gamma = 194$ MeV

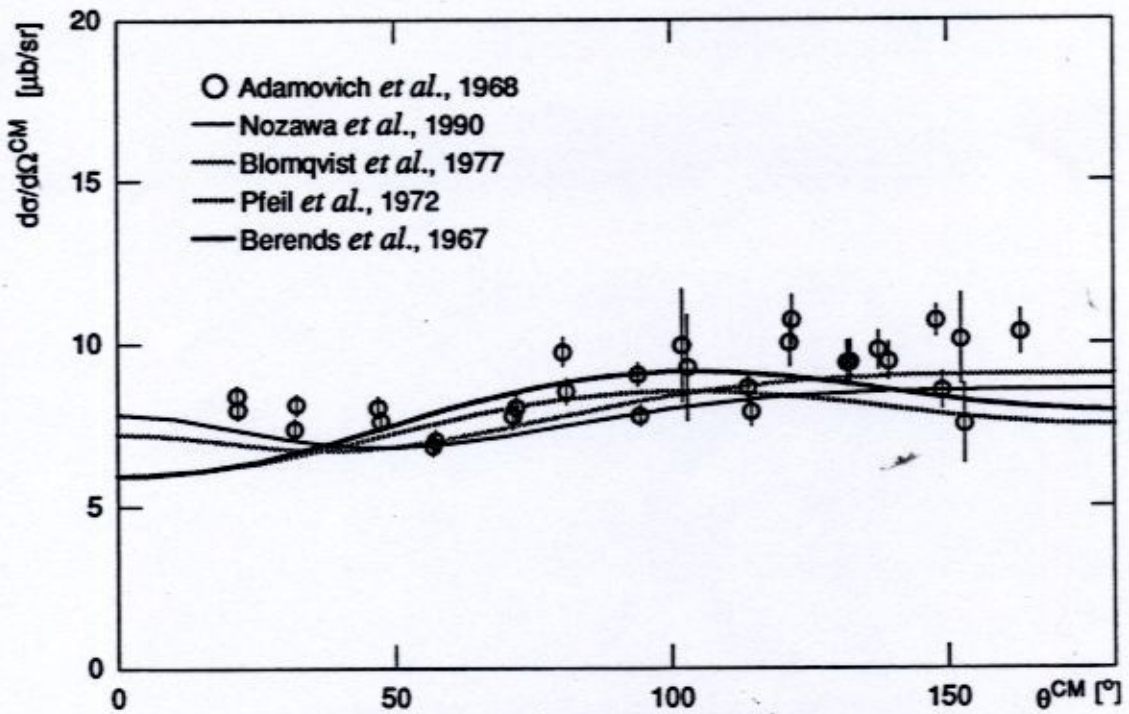

Figure 1.7: $p(\gamma,\pi^+)n$ for $E_\gamma = 184$ MeV

A common feature of the previous four figures is that the multipole analysis and dispersion relation calculations tend to peak at approximately 100° in the CM frame, while the effective Lagrangian and dynamic calculations tend to give higher cross sections in the backward direction. With respect to these data, no calculation type is obviously superior.

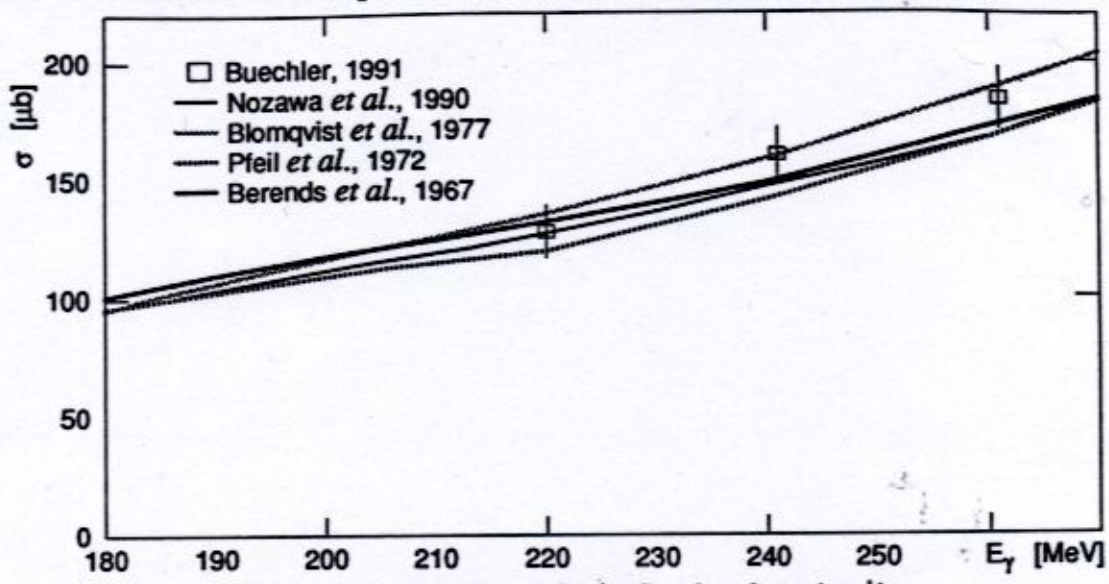

Figure 1.8: The Total Cross Section for $p(\gamma,\pi^+)n$

Figure 1.8 shows the corresponding predictions for the total cross section for the $p(\gamma,\pi^+)n$ reaction, as well as a recent tagged photon measurement by Buechler at Bonn. The Bonn measurement was an extensive investigation of the angular distributions associated with the elementary reaction from 220 to 900 MeV, and involved detecting the recoil neutron. Data from the Bonn experiment were integrated to produce total cross sections which are consistent with all the calculations.

1.2.3 This Experiment

Modern, tagged photon data simply do not exist for this important reaction from threshold (153 MeV) to the lowest energy data point shown above (220 MeV). This is due to the fact that of the modern tagged photon facilities available worldwide, none was capable of tagging the photon energies necessary to map this region. When tagged photons of this energy range became available at SAL, two experiments were undertaken to attempt to bridge the gap. The present experiment (SAL 013) measured this reaction from 175 to 215 MeV. The second experiment (SAL 027) will measure this reaction over the threshold region, from 148 to 160 MeV. These two data sets should serve to tie the

reaction both to threshold, and to the tagged photon data of Buechler from 220 to 900 MeV, thereby forming a complete tagged photon survey of the reaction from threshold to 900 MeV.

1.3 The Quasi-Free Reaction X(γ,π^+)

1.3.1 Theory

Suppose the differential or total photopion production cross section for π^+ from the proton (the "free" π^+ photoproduction discussed in the previous section) is given by

$$S(\gamma + p \rightarrow \pi^+ + n). \tag{1.8}$$

Because the reaction mechanism for nuclear π^+ photoproduction is "incoherent" (the recoil nucleus is different from the target nucleus), the first approximation to the quasi-free (QF) π^+ photopion production cross section from nuclei may be expressed as

$$S(\gamma + {}^{A}_{Z}X \rightarrow \pi^+ + Y) \approx Z \cdot S(\gamma + p \rightarrow \pi^+ + n), \tag{1.9}$$

where "Z" is just the number of protons in the target nucleus. That is, to first approximation, the QF cross sections should simply be due to "Z" elementary cross sections.

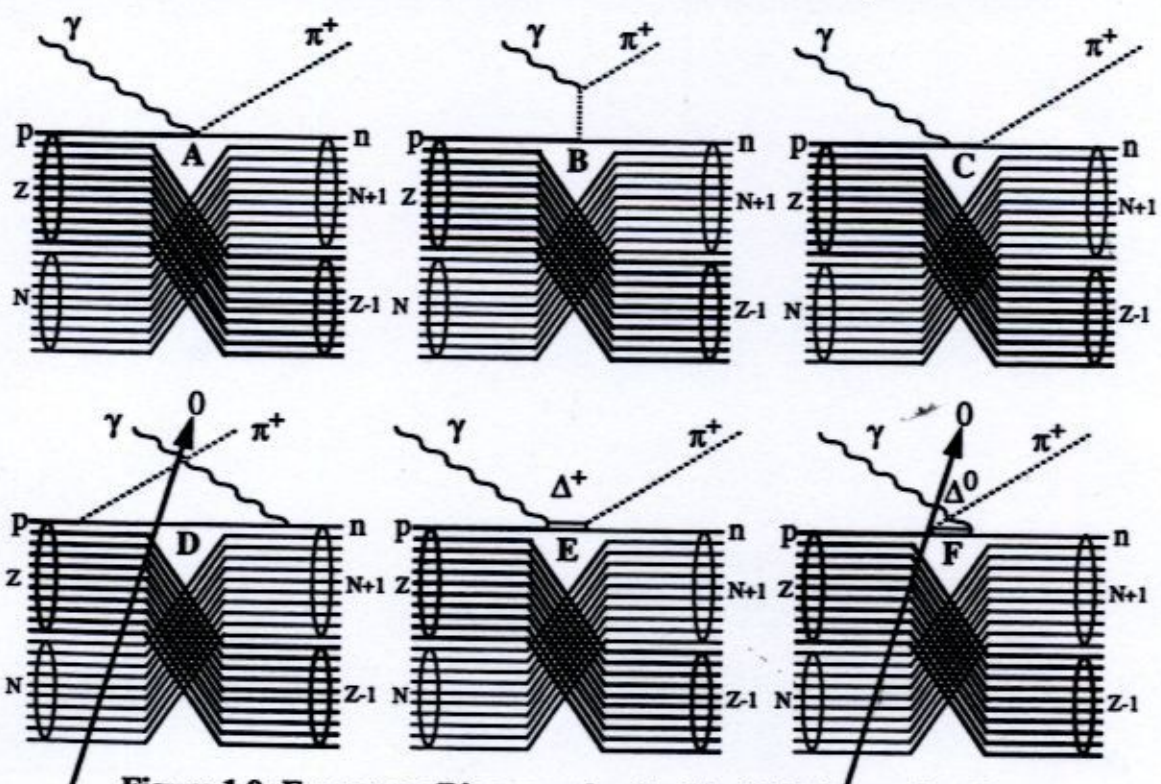

Figure 1.9: Feynmann Diagrams for the First QF Approximation

Figure 1.9 presents the Feynmann diagrams for this first approximation to QF photoproduction from nuclei. Note the similarity between each of the above diagrams and their free photoproduction counterparts (see figure 1.2).

Realistic QF calculations are far from trivial since the following effects must be considered (MacDonald *et al.*, 1979):

1. The target protons are not at rest within the nucleus. This is usually addressed using "Fermi-gas" models of nuclear matter.
2. The final state that the recoil neutron wants to occupy may already by filled. This effect is known as "Pauli-blocking".
3. The π^+ may interact with nucleons as it leaves the nucleus - "πA interactions".

In simple Fermi-gas models, the nucleus is considered to be composed of non-interacting protons and neutrons which are uniformly distributed in momenta up to k_F, the Fermi-momentum (Wong, 1990). A photon puts a π^+ on the mass shell, transferring both energy and momentum to the target nucleon. A form of the transition amplitude for the elementary reaction is then chosen. Integrating this over the Fermi-gas momentum distribution for the target nucleon will yield the first approximation to the QF amplitudes of Figure 1.9, but corrected for motion of the target nucleons.

The Pauli Exclusion Principle states that no two identical fermions may share the same set of quantum numbers. Because of this, the recoil nucleon momentum must be greater than the Fermi momentum, or the reaction will be Pauli-blocked. This effect may also be pictured using the shell model representation of the nucleus.

Consider the ground state configuration of Ca, a nucleus which is reasonably heavy, and one of the targets in the present experiment. Notice that many of the neutron quantum number configurations are taken up in the initial state.

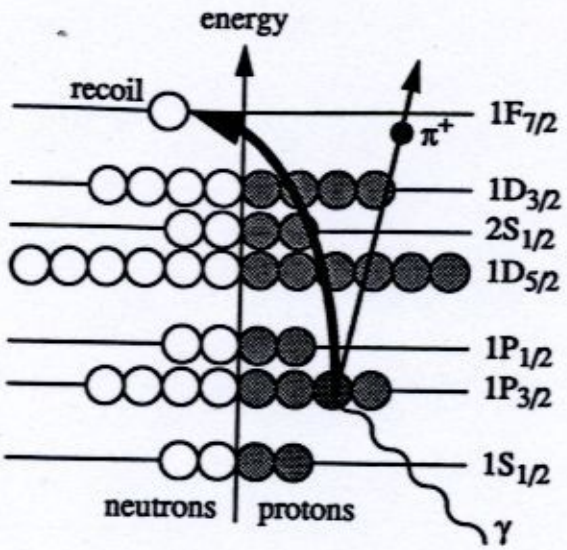

Figure 1.10: The Shell Model Representation of Ca

If a π^+ is photoproduced off the indicated proton as per the elementary reaction, the recoil neutron is blocked by the exclusion principle from any quantum number configuration currently occupied. Further, energy may be required to promote the neutron to the first unoccupied neutron state in the nucleus. If there is not enough energy available for the neutron to be promoted to this state, the photoproduction mechanism cannot proceed. The amount of energy the recoil neutron must obtain in order for the reaction not to be blocked may be substantial, as estimated in Table 1.2.

Table 1.2: A Summary of Fermi Momenta (Moniz *et al.*, 1971)

Nucleus	N/Z	$k_F^{protons}$ [+/-5 MeV]	$k_F^{neutrons} = k_F^{protons} \cdot (\frac{N}{Z})^{1/3}$ [+/-5 MeV]	$T_F^{neutrons}$ [+/-5 MeV]
C	6/6	220	220	25
Ca	20/20	250	250	33
Sn	70/50	260	290	44
Pb	126/82	265	305	49

From kinematics (see Appendix C), it is known that more energy is available to the recoil neutron if the photoproduced π^+ is ejected in the backward direction ($\theta_{LAB} > 90^o$). Thus, Pauli-blocking suppresses QF π^+ photoproduction in the forward direction, and only to a

lesser extent in the backward direction. Further, as evidenced by the trend in the Fermi-momentum in Table 1.2, the blocking becomes stronger as the size of the nucleus increases.

A photon incident upon the nucleus can only produce a π^+ in the non-Pauli-blocked region. For C the Pauli-blocked core is small, so almost all π^+ produced should be observed - a spherical source distribution. In contrast, for Pb, the Pauli-blocked region is large, such that the non-blocked region constitutes only the surface portion of the nucleus. This results in a spherical shell source distribution of π^+. Also, the four complex nuclei chosen for this experiment, C, Ca, Sn, and Pb, are 0^+ and thus approximately spherical in their ground state, having a matter radius given by $R(A) = R_0 A^{1/3}$. Combining these arguments yields approximations to the total cross section

$$\sigma_{TOTAL}(\text{low } A) = \frac{4}{3}\pi R^3 = \frac{4}{3}\pi (R_0 A^{1/3})^3 \propto A, \tag{1.10}$$

$$\sigma_{TOTAL}(\text{high } A) = 4\pi R^2 = 4\pi (R_0 A^{1/3})^2 \propto A^{2/3}. \tag{1.11}$$

Thus, the total QF π^+ photoproduction cross section for low A nuclei should vary approximately as A, while that for high A nuclei should go like $A^{2/3}$ according to this simple model. Finally, the transition region, where nuclei are not quite volume and not quite surface, should have a total QF π^+ photoproduction cross section which goes like $A^{n(A)}$, where $1 > n(A) > 2/3$, and varies smoothly.

Note that since the photoproduced π^+ may traverse nuclear matter before it emerges from the nucleus, the net yield predicted by the simple model presented above may be distorted by πA final state interactions (FSI) - particularly absorption, inelastic scattering, and charge exchange. These mechanisms are discussed in Appendix E. FSI are presumably more numerous in nuclei such as Sn and Pb where the number of nucleons in the recoil nucleus is greater, and will act to reduce the number of π^+ observed. The probability of a FSI occurring is inversely proportional to the π^+ mean-free-path in nuclear matter - the average distance it travels in the nucleus before coming into contact with a nucleon. Free πN cross sections predict that at 20 MeV, mean-free-paths are roughly 8 fm, while at 100 MeV, they have decreased to less than 2 fm (Doss *et al.*, 1988). Thus, as the energy of the π^+ increases, the probability of FSI also increases, resulting in a further loss of

yield. Recent calculations (Carrasco *et al.*, 1992) include FSI, which are built into the calculations via optical potentials (to govern absorption), and Monte Carlos (to control scattering and charge exchange).

The net result of all these considerations is that for a given non-trivial nucleus, the total QF π^+ photoproduction cross section *per proton* is expected to be less than that for the free process, and to decrease as A increases.

1.3.2 Comparison of Predictions With Previous Experiments

Figures 1.11 and1.12 illustrate a comparison between theory and existing tagged photon experimental data for the double differential cross sections with respect to both solid angle and π^+ energy at $E_\gamma \sim 215$ MeV for laboratory angles of approximately 50^o and 110^o. Total errors are shown.

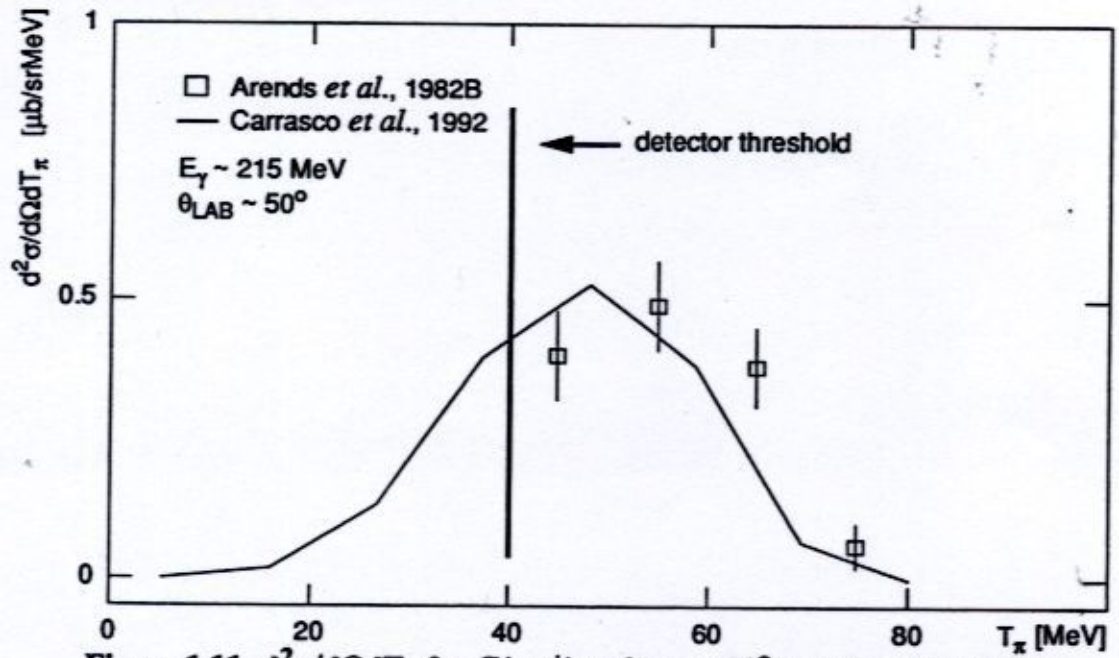

Figure 1.11: $d^2\sigma/d\Omega dT_\pi$ for $C(\gamma,\pi^+)$ at $\theta_{LAB} \sim 50^o$ and $E_\gamma \sim 215$ MeV

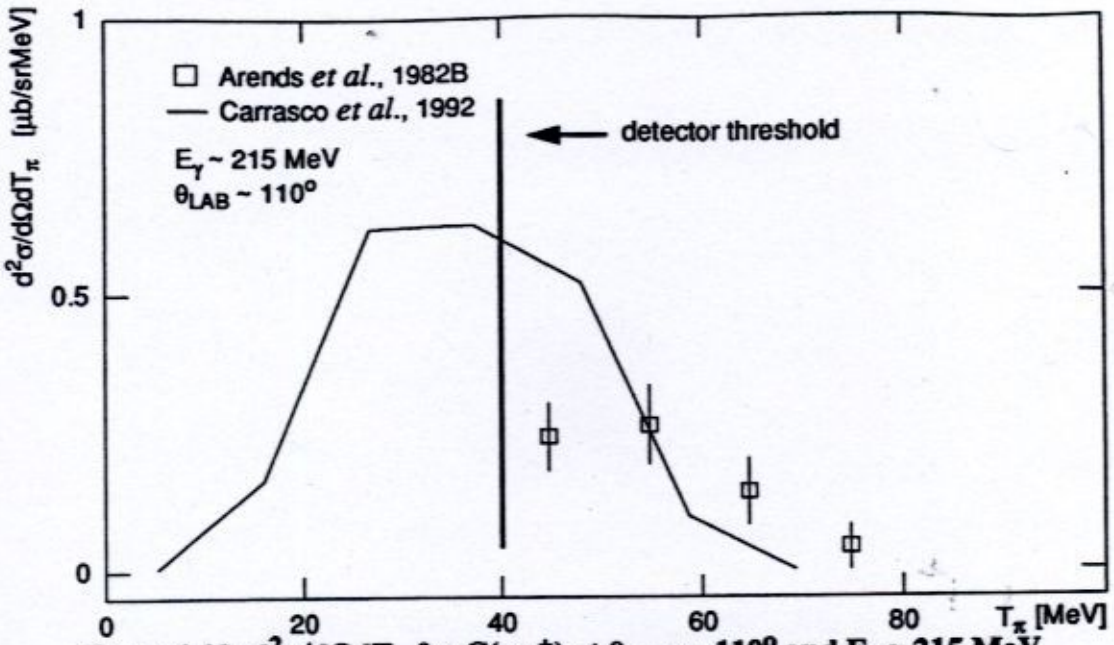

Figure 1.12: $d^2\sigma/d\Omega dT_\pi$ for $C(\gamma,\pi^+)$ at θ_{LAB} ~ 110° and E_γ ~ 215 MeV

The theoretical predictions presented on these plots were the most recent QF calculations available at the time of this work, and included all effects discussed in the previous section. Note that these calculations were only available for E_γ ~ 215 MeV, because Carrasco *et al.* felt their model was not applicable to any lower photon energies. They suggested the lower the energy of the detected π^+, the poorer their model. Thus, disagreement between the calculations and the data are expected to become more pronounced as the reaction moves backward in angle, due to the kinematically predicted reduction in the energy of the photoproduced π^+. It should also be noted that the data set which will be referred to repeatedly in this section (Arends *et al.*, 1982B) was used extensively by Carrasco *et al.* in the development of their model. These data were obtained at Bonn using tagged photons, and involved detecting the photoproduced π^+ in a magnetic spectrometer with a threshold for π^+ detection of 40 MeV.

The agreement between the theory and the data is quite good at a laboratory angle of 50°, with the data exceeding the calculation somewhat in the region above detector threshold. The agreement between the theory and the data is poor at a laboratory angle of 110°, with the calculation disagreeing with the data in the region above detector threshold. The effect of the detector threshold is readily apparent in these figures. A large portion of the π^+ yield is missed, making it impossible to compare to the theoretical predictions over

the entire range for which they were available. Thus, in general, it is desirable to have as low a threshold for detection as possible, such that the measured angular distributions and total cross sections are representative of as much of the reaction yield as possible. It is important to examine these double differential cross sections because integrating over T_π to obtain the angular distributions can wash out disagreement between theory and experiment, as in the case of the data obtained above detector threshold at 110°, where the calculation both overestimates (at ~ 50 MeV) and underestimates (at ~ 70 MeV) the data.

Integrating the double differential cross sections over T_π from detector threshold produces a series of single differential cross sections with respect to solid angle, collectively referred to as an angular distribution. Further comparison between theory and experiment may be made at the angular distribution level of the data.

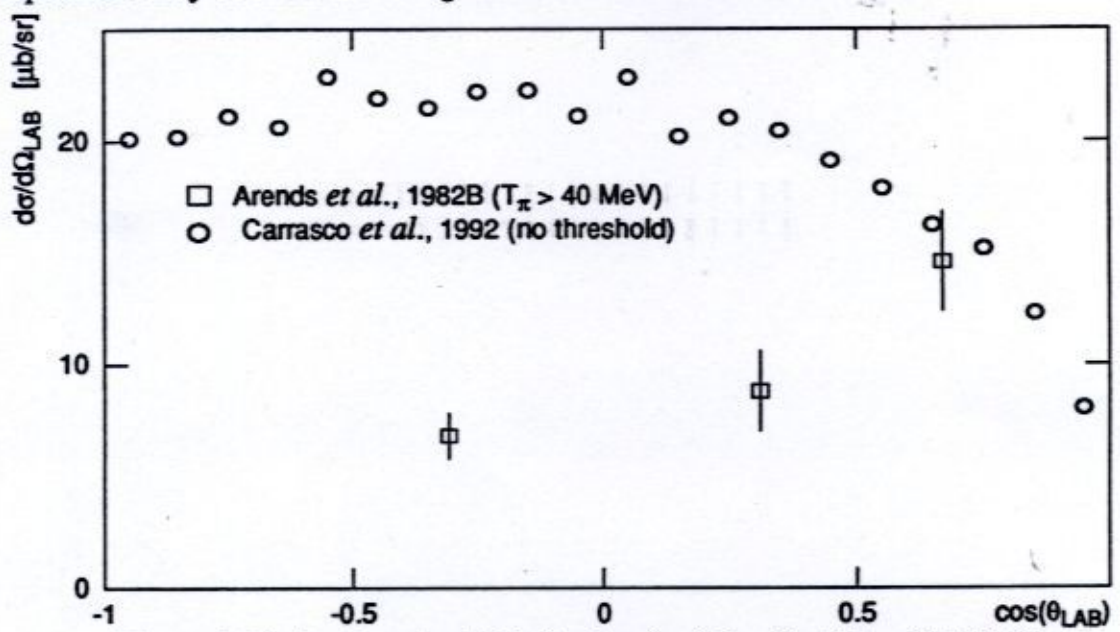

Figure 1.13: An Angular Distribution for $C(\gamma,\pi^+)$ at $E_\gamma \sim 215$ MeV

Figure 1.13 illustrates such a comparison. The circles represent the calculation of Carrasco *et al.* for the angular distribution, while the squares represent the integrated double differential cross sections of Arends *et al.* Total error bars are shown. Again, a detector threshold of 40 MeV is present in the data of Arends *et al.*, but not in the calculations of Carrasco *et al.* This is because the double differential cross sections corresponding to each differential cross section were not available, so the effect of the detector threshold on the calculation could not be estimated over the entire angular distribution. Agreement at the forward angle is good, but is due to the fact that the data of Arends *et*

al. overestimate the calculation of Carrasco *et al.* in the region above detector threshold, while the detector threshold itself excludes only roughly 25% of the yield. Agreement off the forward angle is poor, but is expected to be since the π^+ energy is decreasing.

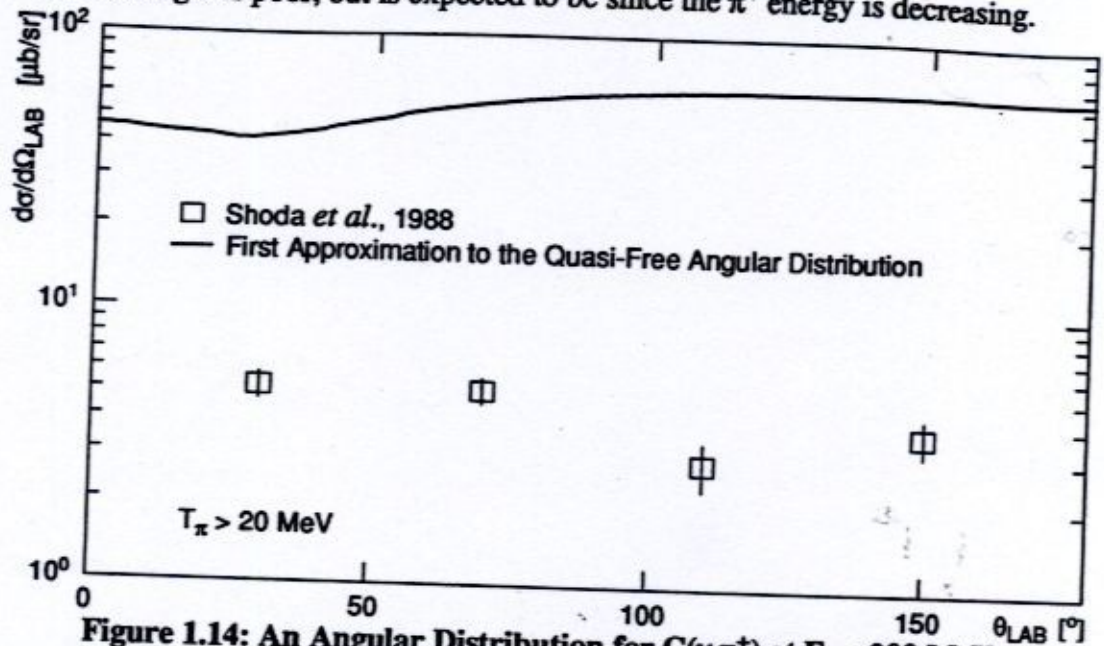

Figure 1.14: An Angular Distribution for C(γ,π⁺) at E_γ ~ 200 MeV

Figure 1.14 illustrates another recent data set for C from Tohoku obtained using virtual photons (electroproduction of π^+), and a comparison between it and the first approximation to the QF production model. No comparison is made to the calculation of Carrasco *et al.* since it is not valid for this photon energy. Instead, since the elementary cross section was basically the same for all calculation types previously discussed, the parameterization of Blomqvist *et al.* was selected to represent the elementary reaction, and scaled by $Z = 6$ to obtain the first approximation to the QF angular distribution. In the Tohoku experiment, the virtual photoproduction reaction to several discrete final states which included a π^+ was measured using a magnetic spectrometer with a detection threshold of 20 MeV, and "monoenergetic" photons obtained using the photon difference method. The "inclusive" photoproduction angular distribution was obtained by summing over these discrete final state angular distributions. The absolute values of the differential cross sections in the Tohoku experiment were determined by normalizing spectra obtained for the elementary reaction to the previously presented results of Adamovich *et al.* Statistical error bars only are shown, as no mention of the systematic error is made in the reference. Clearly, the first approximation to the QF model does not do a very good job predicting this angular distribution. Further, while the angular distributions of Arends

et al. and Shoda *et al.* cannot be compared directly because of the differences in photon energy and detector threshold, the results of Arends *et al.* at a 7% higher photon energy are surprisingly a factor of three larger, even with twice the detector threshold. Clearly a significant discrepancy exists here.

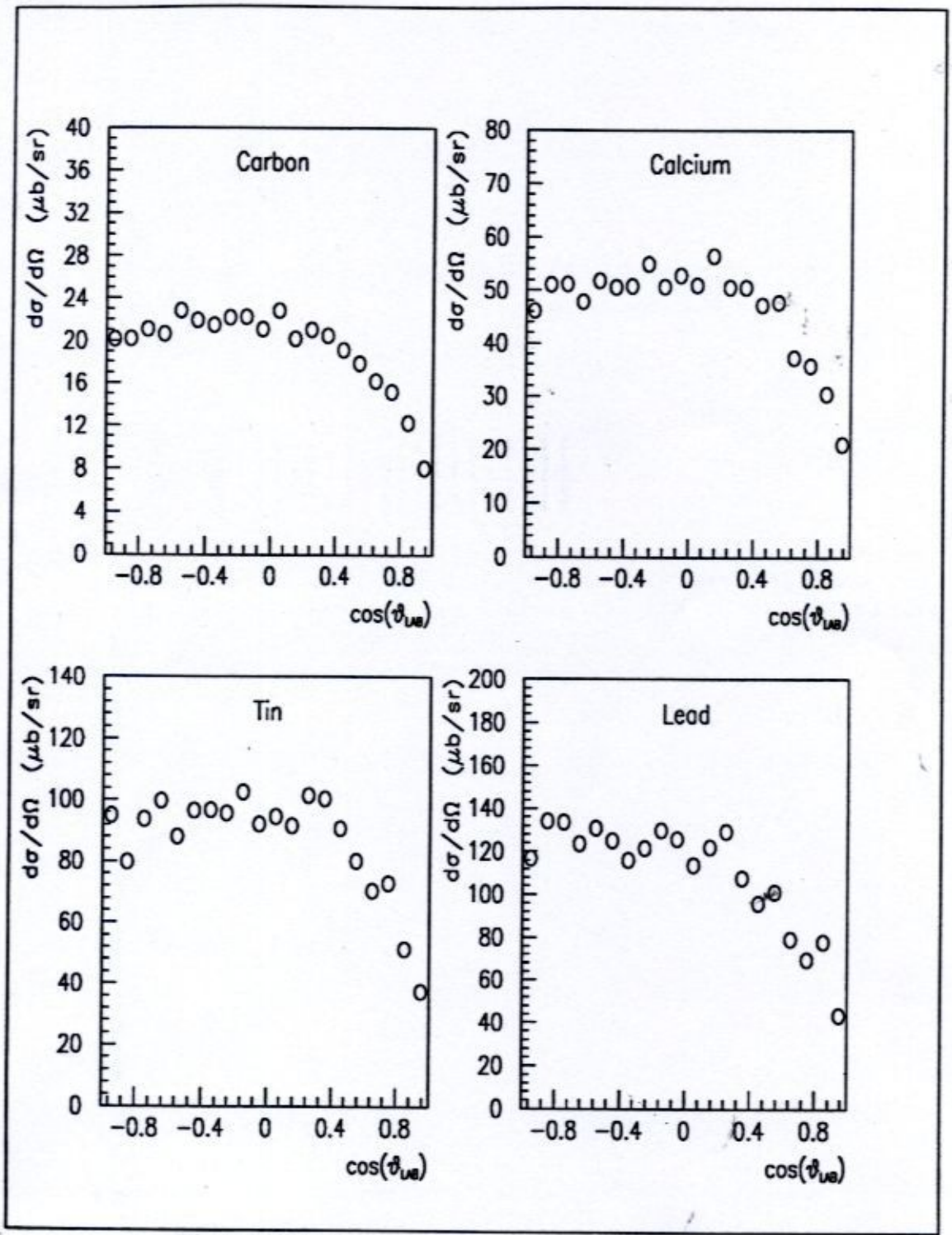

Figure 1.15: Angular Distributions at $E_\gamma = 213$ MeV

Figure 1.15 shows again the QF π^+ photoproduction angular distributions of Carrasco *et al.* for C, as well as for Ca, Sn, and Pb. There are no detector thresholds present in the calculations. Note the striking similarities in shape, consistent with the first approximation to QF π^+ photoproduction (see equation 1.9).

Integrating the angular distributions over solid angle yields the total cross sections. An illustration of the QF predictions for the total cross section for C as a function of photon energy is presented in Figure 1.16 with the data of Arends *et al.*

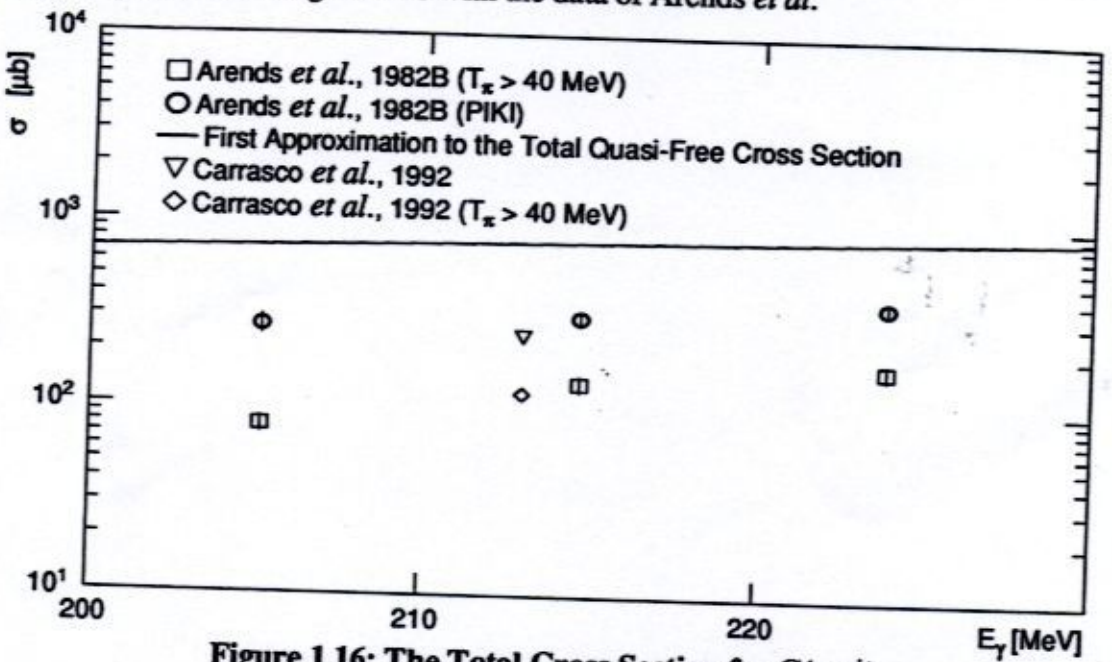

Figure 1.16: The Total Cross Section for C(γ,π⁺)

The squares represent the total inclusive cross sections measured by Arends *et al.*, and include a detector threshold of 40 MeV. The circles represent the best estimation of the total cross section down to the reaction threshold using the Arends *et al.* data and an internuclear cascade Monte-Carlo code known as PIKI. The solid line represents the first approximation to the total QF cross section, and is clearly too high. The triangle represents the total cross section determined by integrating the previously presented angular distribution for C of Carrasco *et al.* The diamond represents the same integration but with a detector threshold of 40 MeV installed. The calculations of Carrasco *et al.* seem to do a good job at predicting the measured total cross section. While the angular distributions predicted by Carrasco *et al.* seriously overestimate the data of Arends *et al.* for all but the most forward angles, the inclusion of the detector threshold of 40 MeV in the total cross section calculation improves the agreement dramatically. This is because detector

threshold results in the exclusion of 25% (at the forward angle) to as much as 75% (at the backward angles) of the strength in the angular distribution, as evidenced by double differential cross sections shown in Figures 1.11 and 1.12. The agreement between Carrasco *et al.*'s calculation and the PIKI scaled data is not bad. Note that all differences are less apparent because of the logarithmic scale of the diagram.

1.3.3 This Experiment

This portion of the current experiment was proposed to complement two recent measurements of inclusive inelastic pion scattering: one for π^+ at 67, 85, and 100 MeV performed by a University of Washington (UW)/Carnegie-Mellon University (CMU)/Los Alamos National Laboratory (LANL)/Saclay collaboration at the Los Alamos Meson Physics Facility (LAMPF) (Aniol *et al.*, 1986), and a second for π^+ and π^- at 100 MeV performed by a UW/LANL/Massachusetts Institute of Technology (MIT) collaboration at LAMPF (Rosenzweig *et al.*, 1992). The measurements are complementary in the sense that they involve two completely different nuclear source distributions of pions. In (π,π') measurements, pions are scattered from the surface of the target nucleus since the pion mean-free-path in nuclear matter at these energies is short (a surface-type source distribution). In (γ,π) measurements, since the photon probe illuminates the entire nucleus, pions are produced uniformly throughout the region of the nucleus which is not Pauli-blocked (basically a volume-type source distribution, particularly for simple nuclei). By comparing the two studies, it was hoped that values of mean-free-paths might be extracted. The comparison was the main interest of the UW collaborators, while the photoproduction measurement itself was the focus of the SAL contingent.

The present measurement constitutes the first attempt at investigating π^+ photoproduction using low threshold (~15 MeV) plastic scintillator telescopes and tagged photons on $Z \geq 20$ nuclei. As previously noted, the low detector threshold is important because it allows for a much larger sampling of the π^+ energies produced in the QF reaction. The inclusion of C in the target set allows for comparison between this tagged photon measurement and an existing one. It was hoped that this measurement would shed light on the glaring discrepancy in angular distributions between Arends *et al.* and Shoda *et al.* Finally, trends in the total π^+ photoproduction cross section as a function of A would be established, since nuclei spanning the full range of the periodic table were to be investigated.

Chapter 2. THE EXPERIMENT

An overview of the experiment is presented. The facility, the generation of the bremsstrahlung photon beam, the photon tagging procedure, the experiment arm apparatus, and the data acquisition system are discussed. A run summary is presented. Units of $h/2\pi = c = 1$ are assumed.

2.1 General Introduction

This experiment was performed as a collaboration between groups at the Saskatchewan Accelerator Laboratory, the University of Washington, the University of Melbourne, and Queen's University, and involved three graduate students. The production run spanned approximately a one month period from 3 October to 8 November, 1990.

Conceptually, it was a very simple measurement. Monoenergetic time-tagged photons in the energy range 175-215 MeV were used to irradiate solid targets to produce three charged particle types: pions (π), protons (p), and deuterons (d). These particles were detected in one of four detectors, set at nominal laboratory angles of 50^{o}, 80^{o}, 110^{o}, and 140^{o}. For the purposes of this work, it was the (γ,π^{+}) reaction which was of interest. The (γ,p) and (γ,d) results will be reported on independently.

The targets were mounted in a ladder which was both remotely monitored and controlled. The ladder was set at 30^{o} with respect to the photon beam, effectively doubling the target thickness along the beamline. The targets included CH_2 and CD_2, as well as natural C, Ca, Sn, and Pb. CH_2 served as both a π^{+} energy calibration target and a production target (H). CD_2 served as a proton energy calibration target for the independent (γ,p) experiment. An empty slot was left in the target ladder to measure the contribution to the target yields of the room air (N_2 and 0_2). The production targets were cheap, safe, and evenly spaced on the ln(A) scale.

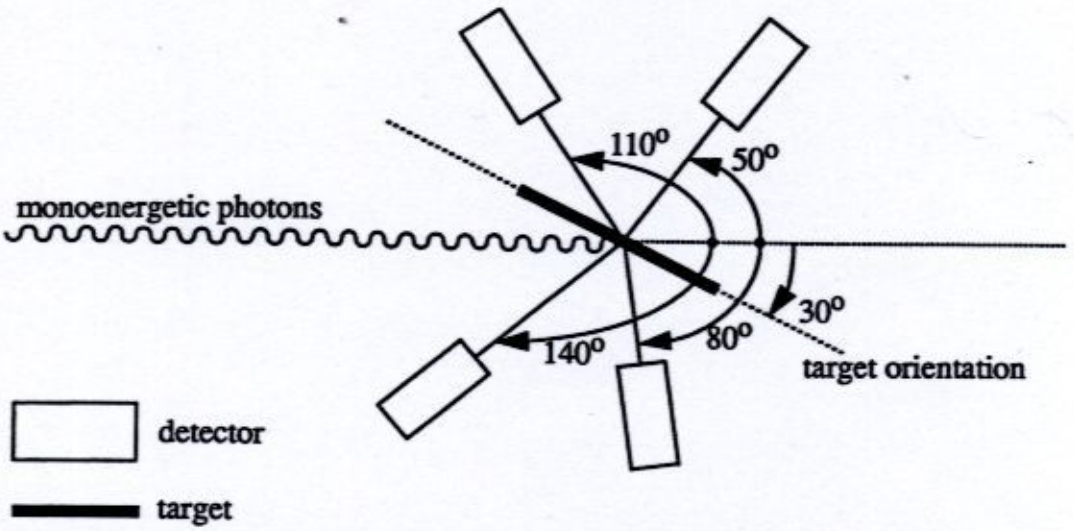

Figure 2.1:A Schematic of the Experiment

2.2 The Facility

The experiment was performed at the Saskatchewan Accelerator Laboratory. The facility boasts a 300 MeV, six section linear accelerator (LINAC) coupled to an Energy Compression System (ECS) (Laxdal, 1980) and a Pulse Stretcher Ring (PSR) (Dallin, 1990). This apparatus was capable of producing a monochromatic, continuous wave (CW) electron beam and delivering it to experimental area 3 (EA3), which was, at the time of the experiment, the tagged photon hall (see Figure 2.2). The method by which the beam was produced and delivered to an experimental area is well documented elsewhere (Amendt, 1990), and thus will only be discussed here briefly.

The production of the CW, monoenergetic electron beam used in this experiment involved three stages. In the first stage, the LINAC accelerated a 360 ns long pulse of electrons with a momentum spread of 1% to 288 MeV. In the second stage, these pulses passed through the ECS, a device which utilized dipole magnets and an accelerating section to reduce the momentum spread in the electron pulses to 0.1% without sacrificing beam current. In the third stage, the energy compressed 360 ns electron pulses were injected into the PSR. A circulating pulse was then extracted in a continuous manner until the next pulse from the linac/ECS was injected. In the process, the momentum spread of the electron bunches was further reduced to a "monoenergetic" 0.01%. After extraction

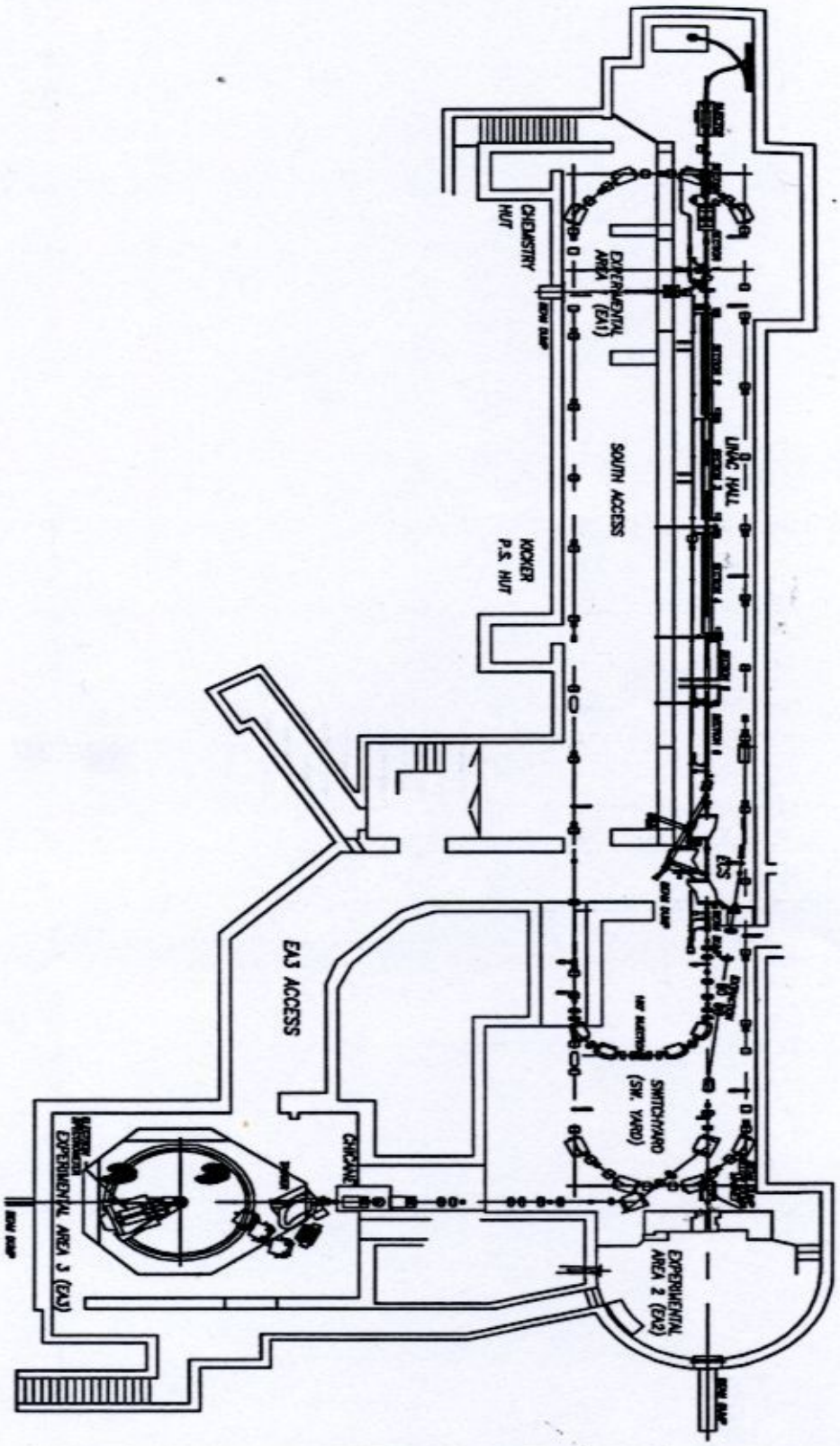

Figure 2.2:Saskatchewan Accelerator Laboratory (November, 1990)

from the PSR, the electron beam passed through the beam switchyard where it was directed towards EA3, the tagged photon hall. Beam current amounted to approximately 50 nA.

2.3 Bremsstrahlung

2.3.1 Generation of the Bremsstrahlung Photon Beam

Upon entering EA3, the beam was incident upon a vacuum chamber which contained a radiator wheel. To a good approximation, the relative power in the bremsstrahlung radiation "R" produced at the radiator was given by

$$R = 1 - \frac{P(x)}{P_0} = 1 - e^{-\frac{x}{x_0}} \approx 1 - (1 - \frac{x}{x_0}) \approx \frac{x}{x_0}; \quad x_0 \gg x, \tag{2.1}$$

where "P(x)" is the power in the electron beam at a depth x inside the radiator material, "$P_0(x)$" is the power of the incident electron beam, "x" is the thickness of the radiator, and "x_0" is one radiation length of the radiator material. Over one radiation length, the power of the incident electron beam would be reduced by a factor of 1/e.

Mounted in the wheel was a 115 μm thick Al radiator. Radiator thicknesses are usually expressed as fractions of the radiation length. In the present case, the Al radiator corresponded to 0.1% which by equation 2.1 converts 0.1% of the energy in the incident electron beam into bremsstrahlung photons.

For conventional bremsstrahlung photon experiments, it is not uncommon to use a 2% radiator. However, these thick radiators yield ionization energy loss of the incident electrons, are susceptible to multiple scattering, and produce far too much bremsstrahlung for easily produced electron currents for a tagged photon experiment. The 0.1% radiator was used since it yielded the largest possible amount of bremsstrahlung the photon tagger could handle while at the same time minimizing the other undesirable processes.

Electrons which interacted with the thin radiator yielded a forward-peaked cone of bremsstrahlung photons. The opening angle of the bremsstrahlung photon cone was given by

$$\theta_{opening} \approx \frac{1}{\gamma} \approx \frac{1}{E_e/m_e} \approx 1.8 \text{ mrad}, \tag{2.2}$$

where "E_e" was the energy of the electron beam (288 MeV), and "m_e" was the mass of the electron (0.511 MeV).

Electrons which did not interact with the radiator were directed into a beam dump using a sweep magnet. In a true bremsstrahlung experiment, the cone angle of the photon beam would be limited using a collimator. This limited angle and the radiator-to-target distance determine the size of the beam spot on the target.

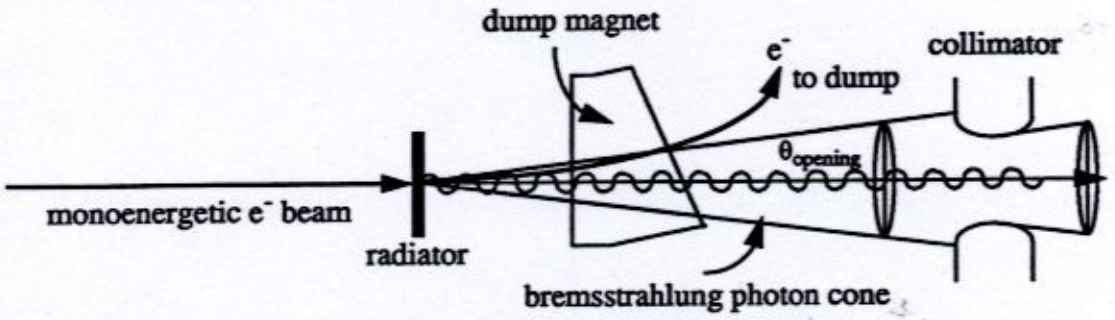

Figure 2.3:The Bremsstrahlung Photon Cone

While the energy of any given bremsstrahlung photon is simply

$$k = E^{e^-}_{\text{incident}} - E^{e^-}_{\text{post bremsstrahlung}}, \qquad (2.3)$$

the energy distribution of bremsstrahlung photons is continuous. Figure 2.4 shows the bremsstrahlung photon distribution for an incident electron energy of 288 MeV (Schiff, 1951).

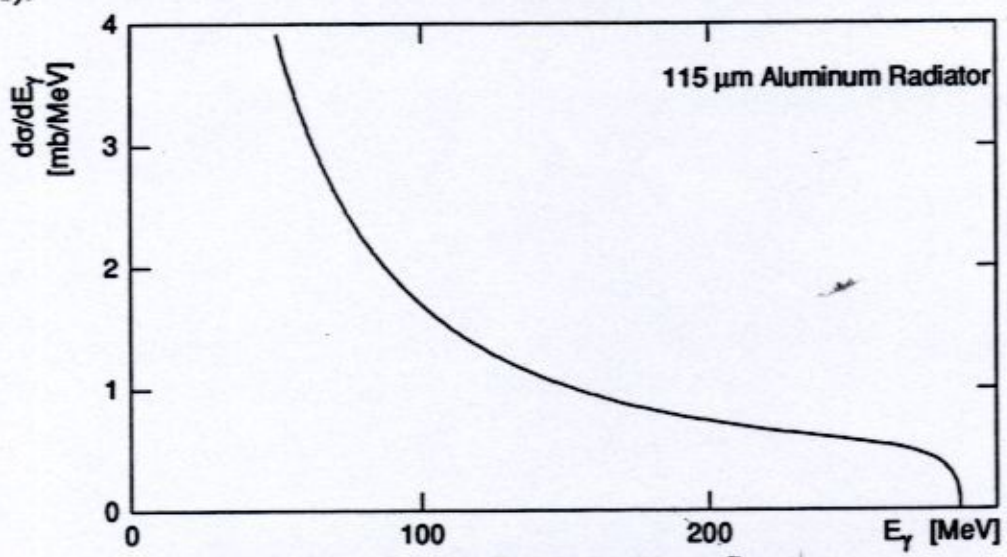

Figure 2.4:A Sample Bremsstrahlung Spectrum

2.3.2 Problems With Bremsstrahlung Photon Experiments

The large range of photon energies present in the bremsstrahlung photon cone results in incomplete kinematics for most bremsstrahlung experiments. Because the incident photon energy is simply not known on an event-by-event basis, a given low-energy particle that is detected could have been due to either a low energy photon, or a high energy photon plus final state interactions which degraded the energy of the detected particle. To extract the monoenergetic contribution from the bremsstrahlung photon flux, photon difference methods and single-difference bremsstrahlung unfolding techniques (Matthews *et al.*, 1971) were developed. However, these are susceptible to large systematic uncertainties. Further, accurate determination of the total number of photons incident upon the target is a difficult and involved process (Sarty, 1992; Igarashi, 1993). Finally, no timing reference signal corresponding to the creation of the photon is available in a bremsstrahlung experiment. A practical solution to the problems associated with bremsstrahlung photon experiments is the photon tagging technique.

2.4 Photon Tagging

The method for selecting individual photons of similar energy from the continuous bremsstrahlung photon energy distribution was first suggested independently by Camac at Cornell and Koch at Illinois. However, until recently, photon tagging was impractical because of intrinsically slow electronics and the low duty cycle pulsed-beam accelerators (Weil *et al.*, 1953; Cence *et al.*, 1961; O'Connell *et al.*, 1962). The duty cycle measures the continuousness of the electron beam. A low duty cycle machine blasts the target with high peak currents for short periods of time leading to event rates the electronics simply cannot handle, and then presents long periods of time where no beam is delivered to the target. A high duty cycle machine uniformly distributes the current, leading to low peak currents, but the same integrated charge over a given period of time. This helps keep event rates at a level which the electronics can handle. Thus, crucial to a tagged photon experiment is a high duty cycle CW accelerator. This makes the limiting factor on practical event rates the speed of the electronics.

Several modern tagging spectrometers and high duty cycle accelerators exist at facilities worldwide (Arends *et al.*, 1982A; Kellie *et al.*, 1985; Terasawa *et al.*, 1986; Blomqvist, 1993). The photon tagging facility at the Saskatchewan Accelerator Laboratory is well documented elsewhere (Vogt *et al.*, 1993), and thus, will only be discussed here briefly.

2.4.1 The Photon Tagging Spectrometer

For the bremsstrahlung photons to be tagged, a tagging spectrometer or photon tagger is required between the radiator and the collimator. The SAL tagger consists of a clam-shell magnet and a set of scintillator detectors known as the focal plane array.

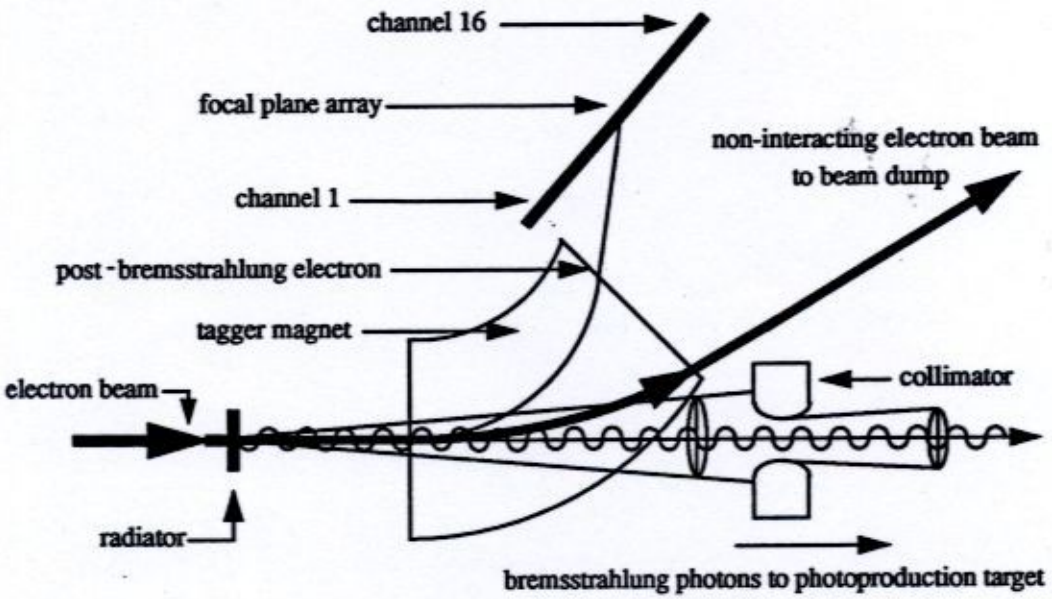

Figure 2.5:A Schematic of the Photon Tagging System (Top View)

The intermingled beams, both electrons and bremsstrahlung photons, as well as the vast majority of electrons which had not interacted with the radiator, pass through the field of the tagger magnet. Rather than dumping all post-radiator charged particles, the tagger magnet acts selectively. Electrons which did not produce bremsstrahlung were simply deposited in a well-shielded beam dump, located far from the experimental apparatus. A Faraday cup located in the beam dump served to crudely monitor beam current. Electrons which produced bremsstrahlung had significantly less energy than those which did not, and thus endured a greater bend in the field of the tagger magnet. If these electrons were

within the momentum acceptance of the tagger magnet, they were directed towards the tagger focal plane detector system for momentum analysis. If they were not, the corresponding bremsstrahlung photons remained untagged.

The radius described by a bremsstrahlung electron was proportional to its momentum, and hence the least energetic electrons struck tagger channel 1, while the most energetic electrons struck tagger channel 16 (see Figure 2.5). For a given field setting, the optics of the spectrometer provided knowledge of the electron trajectory as a function of its energy. Thus, the physical location of a given tagger channel was sufficient to determine the energy of a bremsstrahlung electron. This yielded the energy of the corresponding bremsstrahlung photon, by equation 2.3. By altering the field of the tagger magnet, the momentum acceptance of the tagging spectrometer could be changed. In this manner, the entire photon tagging system could be set up to take a user-defined "bite" out of the bremsstrahlung photon spectrum (see Figure 2.6). This focal plane bite was divided into 16 smaller bites, each of which corresponded to a single tagger "channel".

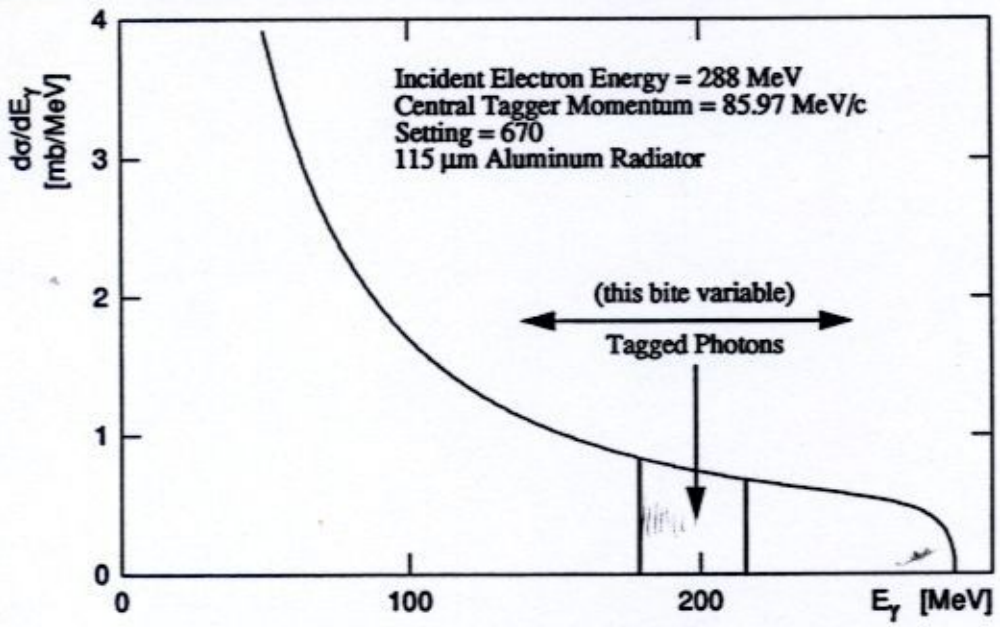

Figure 2.6:The Tagger Bite

A bremsstrahlung electron within the momentum bite $p \pm \delta p$ of a given tagger channel was associated with a bremsstrahlung photon of a given energy $k \pm \delta k$. The relationship between tagger channel and photon energy was documented (Pywell, 1987), and accessible via the SAL system program TAGENG. While the intrinsic energy resolution of the tagger magnet was 0.1%, the tagger channels corresponded to a resolution of about 1.5%

in the energy of the recoil electron. Thus, the energy resolution of a given tagger channel was determined by its physical size. Table 2.1 shows a sample TAGENG output, which corresponded to the actual operating conditions for the 288 MeV electron beam. The input parameters appear at the top, and are labeled "diagnostics".

DIAGNOSTICS:
Standard Tagger Focal Plane.
Incident electron beam momentum: 288.00 MeV/c.
Setting number: 670.
Central Tagger Momentum (P0): 85.97 MeV/c.
Tagger Field (B0): 0.537 Tesla.
Correction Factor: 1.0236.
16 Channel Configuration

Table 2.1: A Sample TAGENG Output

Tagger Channel	Position [cm]	Central Momentum [%]	Central Momentum [MeV/c]	Central Momentum Spread [MeV/c]	Photon Energy [MeV]	Photon Energy Spread [MeV]
01	-31.09	-18.77	71.74	1.08	217.38	1.08
02	-26.75	-16.29	73.65	1.10	215.21	1.10
03	-22.41	-13.77	75.87	1.12	212.99	1.12
04	-18.07	-11.20	78.13	1.14	210.73	1.14
05	-13.73	-8.59	80.43	1.16	208.43	1.16
06	-9.39	-5.92	82.78	1.18	206.08	1.18
07	-5.05	-3.21	85.16	1.20	203.70	1.20
08	-0.70	-0.45	87.59	1.22	201.27	1.22
09	+3.64	+2.35	90.06	1.25	198.80	1.25
10	+7.98	+5.21	92.57	1.27	196.29	1.27
11	+12.32	+8.11	95.12	1.29	193.73	1.29
12	+16.66	+11.06	97.72	1.31	191.14	1.31
13	+21.00	+14.05	100.36	1.33	188.50	1.33
14	+25.34	+17.10	103.03	1.35	185.83	1.35
15	+29.68	+20.19	105.75	1.37	183.11	1.37
16	+34.02	+23.33	108.51	1.39	180.34	1.39

All bremsstrahlung photons were unaffected by the magnetic field, and thus passed down the beamline 1.92 m to a 20 mm diameter collimator, and a further 2.5 m to the target ladder as candidate tagged photon events. The photon beam was collimated to ensure all tagged photons were incident upon the target. This resulted in a beam spot on the target of about 1 cm in diameter. Some photons which made it to the target initiated nuclear reactions whose products fired the detectors in the experiment arm ("X-arm"), such that an electronic experiment trigger ("X-trigger" - see section) was produced. An overlap in time (coincidence) between an X-trigger and any electron hits on the focal plane was defined to be a valid, tagged photon event, and led to the generation of an interrupt. The tagger electronics identified the coincidence and returned a signal (hereafter referred to as "X-reference") to the X-arm electronics (see Figure 2.7).

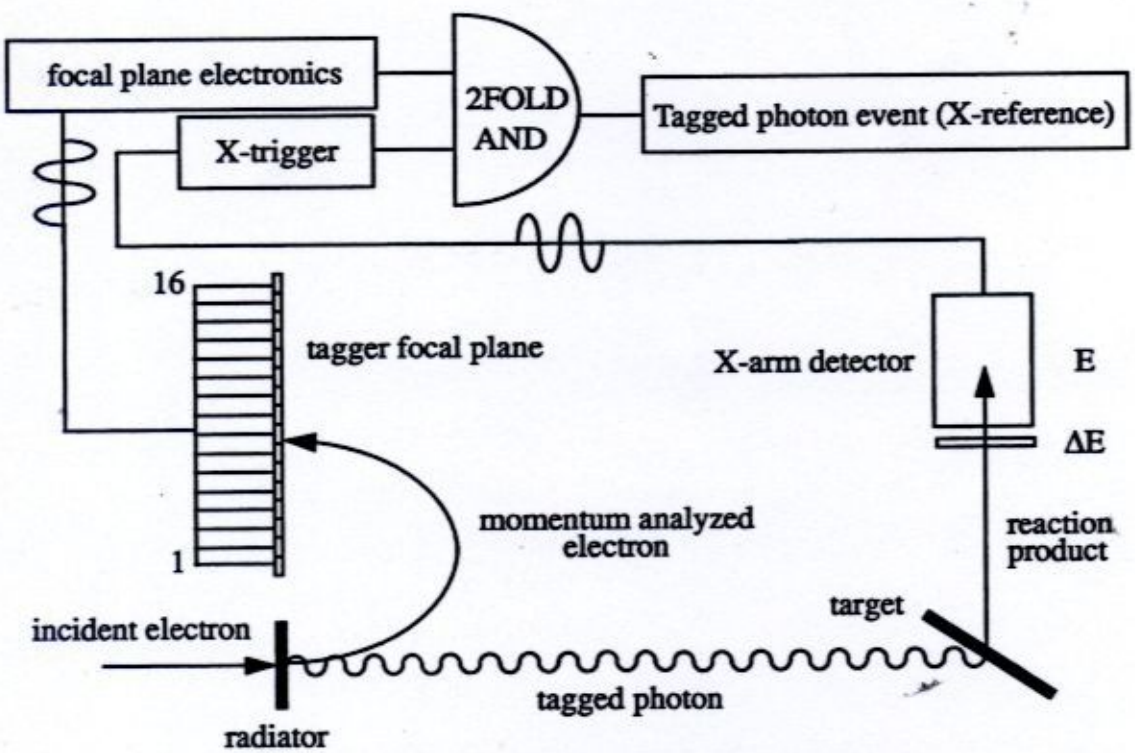

Figure 2.7:Detail of a Tagged Photon Event

Each tagger channel was connected to a time-to-digital converter (TDC) which measured the time in TDC channels (1 channel = 0.1 ns) between the bremsstrahlung electron striking a given tagger channel in the focal plane and the X-trigger (effectively the time-of-flight (TOF) of the reaction product from the target to the detector). Figure 2.8

shows a typical tagger TDC spectrum representing the sum of all 16 tagger channels. Note that because only one tagger channel corresponds to the true π^+ event, stops in the other 15 tagger channels are purely random.

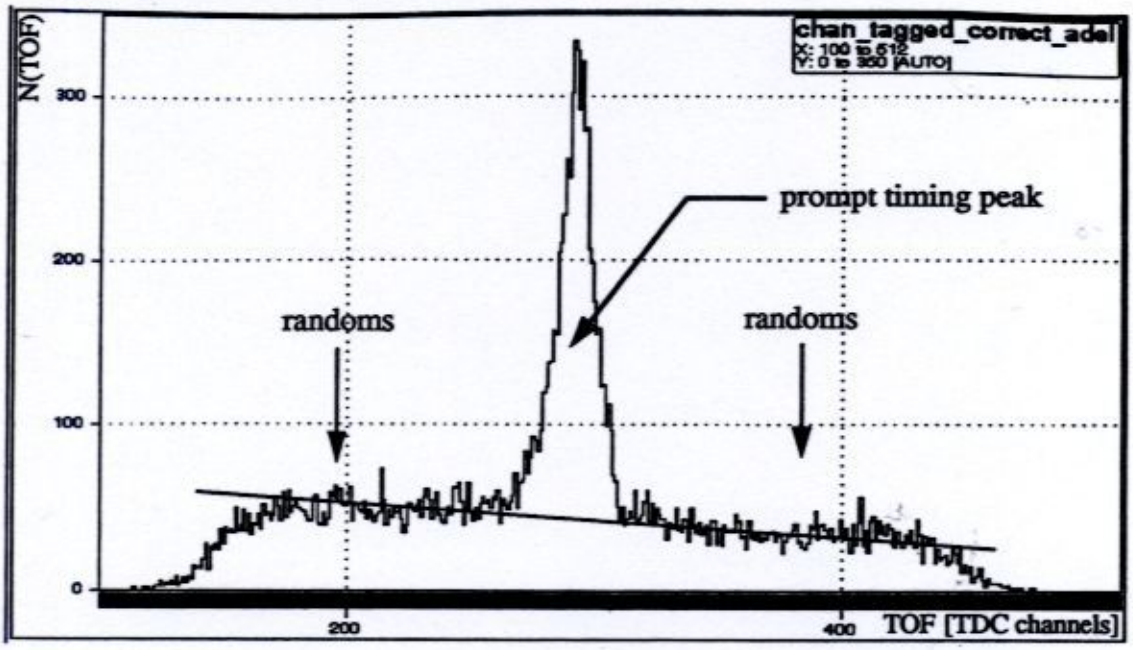

Figure 2.8:A Typical Tagger TDC Spectrum

The spike represents tagged photon events having similar TOF, and is known as the "prompt timing peak". Events which do not lie within the prompt timing peak correspond to random hits in the tagger focal plane, which were thus completely uncorrelated in time. The linearity of the random event distribution across the background region illustrates the events were truly random. A slightly negative slope was a consequence of the stolen coincidence phenomenon, which will be discussed shortly. The width of the timing distribution in the tagger TDC spectrum, ~360 channels = 36 ns, is referred to as the "hardware coincidence resolving time".

Event Multiplicity

Each channel of the photon tagger was also connected to a scaler. This scaler counted every electron which struck the channel. The incident electron flux per tagger channel, "$N_e(i)$", was known to the resolution of the tagger scalers, +/-5 counts (the tagger scalers are prescaled by a factor of 10). As shown in Figure 2.8, there are two event types displayed in a typical tagger TDC spectrum: prompt and random. The number of electron hits on the focal plane corresponding to a single X-trigger was defined to be the event

multiplicity. For example, if there were three electron hits on the tagger focal plane corresponding to a given X-trigger, the event multiplicity would be three. Because randoms were also present in the prompt timing peak, events of multiplicity greater than one were necessarily present in the data. A bit pattern register recorded the pattern of hits across the focal plane per X-trigger. Figure 2.9 shows a typical multiplicity distribution.

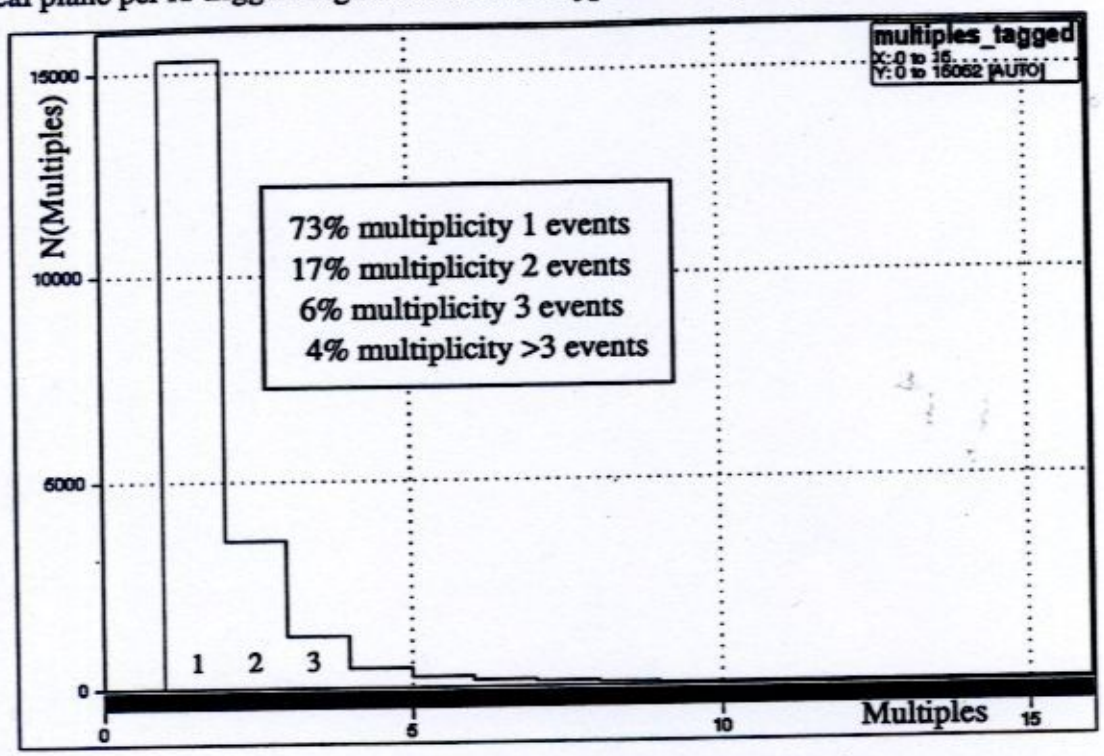

Figure 2.9:A Typical Multiplicity Distribution

The technical details of the 16 channel photon tagger are well documented elsewhere, and thus will not be dealt with here (Vogt, 1989; SAL, 1989; SAL, 1990A). The tagger electronics were designed to run at instantaneous focal plane rates of up to 50 MHz, although typical rates for this experiment were on the order of 35 MHz, for reasons that will be presented later (see page 55).

Typical tagged photon event rates were on the order of 50 Hz in this experiment. Note that this rate was inclusive over several particle types since it was not known on-line if the detected particle was a pion, a proton, or a deuteron. It was the relatively long TOF of the deuteron which made necessary the 35 ns hardware coincidence resolving time. Also, because the focal plane was mounted vertically, it was only visible to horizontal cosmic rays, which are extremely few in number.

Stolen Coincidences

The fact that the prompt peak is superimposed on a background of random events led to the stolen coincidence phenomenon. Consider a single π^+ event occurring in one of the four detectors of the X-arm. Suppose that at the time the π^+ was detected, there was more than one electron hit in the tagger focal plane. This occurs since the coincidence resolving time gate has finite width. Were it possible to reduce this gate to an infinitesimal, stolen coincidences would not occur. Of the multiple electron hits on the focal plane at the time the X-arm event was recorded, only one was the true electron, while the rest were simply randoms. Because the randoms were evenly distributed across the focal plane, it was possible that a random electron hit the same tagger channel as the true electron, and prior to it. Thus, the tagger TDC could have been stopped by the random hit instead of the true electron, and the event which should have fallen within the correlated peak was instead registered before it. The key idea is that the tagger TDCs can only be stopped once. Thus, later TDC channels have a lower efficiency for detection, since any earlier stop pulses, real or random, will prevent their registering the true stop pulse. The stolen coincidence correction per tagger channel is given by (Owens, 1990)

$$\text{stolen (i)} = e^{-\frac{(N_e(i)\cdot\tau_c)}{T\cdot df}} \approx \left[1-\left(\frac{N_e(i)\cdot\tau_c}{T\cdot df}\right)\right], \qquad (2.4)$$

where "$N_e(i)$" was the number of electrons actually detected by tagger channel i, and "τ_c" was the time difference between the leading edge and the mean of the prompt peak for the i^{th} tagger TDC spectrum. The variables "T" and "df" in equation 2.4 represent the live time and average duty factor for the electron beam. The evaluation of the duty factor is presented on page 39. Table 2.2 presents the average duty factors and live times that were used in the stolen coincidence corrections.

Table 2.2: Duty Factor and Live Time Summary

Target	Detector	df (%)	T (sec)
CH_2	Melbourne, large collimator	24.04	64203
	Melbourne, small collimator	26.61	40167
	Sydney/Adelaide/Seattle	24.92	104369

Table 2.2: Duty Factor and Live Time Summary

Target	Detector	df (%)	T (sec)
Carbon	Melbourne, large collimator	24.45	130802
	Melbourne, small collimator	19.59	17799
	Sydney/Adelaide/Seattle	23.88	148601
Calcium	All Detectors	23.88	92706
Tin	Melbourne, large collimator	26.49	74188
	Melbourne, small collimator	28.76	112296
	Sydney/Adelaide/Seattle	27.26	186484
Lead	All Detectors	16.89	288235
Out	Melbourne, large collimator	27.23	42641
	Melbourne, small collimator	22.07	27757
	All Detectors	25.14	70398

The calculated stolen coincidences did not exceed 3% of the total electron flux for any tagger channel for any combination of target and detector.

The actual number of electrons seen by a given tagger channel was thus given by

$$N_e^{true}(i) = N_e(i) \cdot \text{stolen}(i). \qquad (2.5)$$

2.4.2 Tagging Efficiency Measurements

Knowledge of the efficiency at which photons were tagged was necessary. Had the photon tagging system been 100% efficient, there would have been a one-to-one correspondence between the number of electrons incident on the i^{th} tagger channel (or combination of tagger channels which defined a photon energy bin) and the number of photons incident upon the target. However, this is not the case. The efficiency was less than unity simply because some of the bremsstrahlung electrons within the momentum acceptance of the tagging spectrometer corresponded to tagged photons which did not make it through the collimator (recall Figure 2.5). That is, the tagging efficiency measured the probability for a tagged photon to make it through the collimator and hit the target.

The tagging efficiency was measured periodically throughout the experiment using a lead glass detector, which was assumed to be 100% efficient for the purpose of detecting photons over the tagged photon energy range. The intensity of the bremsstrahlung beam was reduced several orders of magnitude, and the detector was moved into the beamline. A pair of runs was performed, one in which the radiator was in the electron beam, and thus bremsstrahlung was produced, and another in which the radiator was out of the electron beam, and thus theoretically, no bremsstrahlung was produced. Assuming the electron beam currents were the same in both runs, the overall tagging efficiency was given by

$$\text{tagging efficiency} \approx \frac{\text{total tagged lead glass events}}{\text{total electron hits on focal plane}}. \tag{2.6}$$

In order to determine the tagging efficiency as a function of photon energy bin, equation 2.6 was evaluated for each collection of tagger channels which defined a photon energy bin. Further, it was necessary to account for room background. This resulted in the expansion of equation 2.6 to

$$\text{tagging efficiency}\,(E_\gamma) = \frac{\text{electron hits}\,(E_\gamma)\big|^{\text{in}} - R \cdot \text{electron hits}\,(E_\gamma)\big|^{\text{out}}}{\text{total}\big|^{\text{in}} - R \cdot \text{total}\big|^{\text{out}}} \tag{2.7}$$

where

$$R = \frac{\text{livetime}\big|^{\text{in}}}{\text{livetime}\big|^{\text{out}}}. \tag{2.8}$$

The livetime is simply the fraction of time during which the experiment electronics were capable of accepting an interrupt. "Total" refers to the total number of electron hits across the entire focal plane, and "in" and "out" label the radiator-in and radiator-out runs respectively. It was observed that there were essentially no electron hits in the tagger focal plane when the radiator was out of the beamline. It was also observed that the tagging efficiency was constant as a function of photon energy.

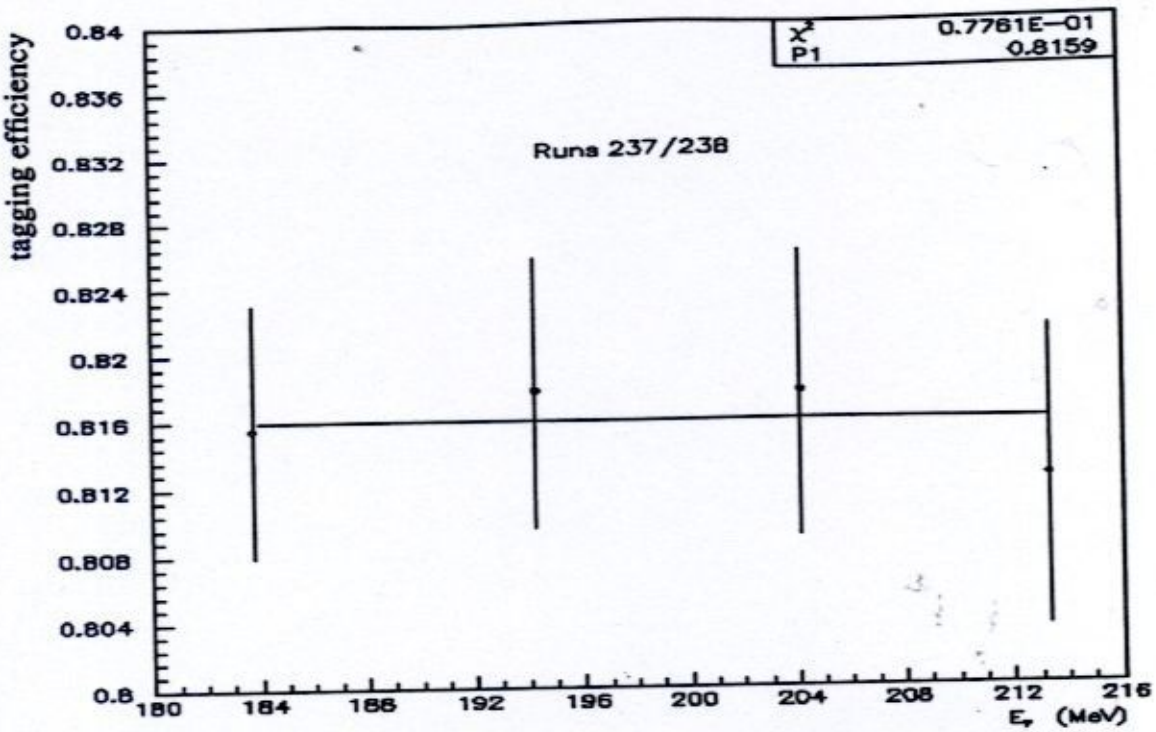

Figure 2.10:Tagging Efficiency as a Function of Photon Energy

The tagging efficiency was measured eight times over the course of the experiment. Each tagging efficiency measurement consisted of both a radiator-in and radiator-out run. Table 2.3 presents the results. These results and a fit are plotted in Figure 2.11.

Table 2.3: A Summary of Tagging Efficiency Measurements

Runs	Tagging Efficiency (+/- 0.01)	Runs	Tagging Efficiency (+/- 0.01)
237/238	0.82	337/338	0.79
260/261	0.78	369/370	0.81
307/308	0.76	394/395	0.81
331/333	0.80	410/411	0.81

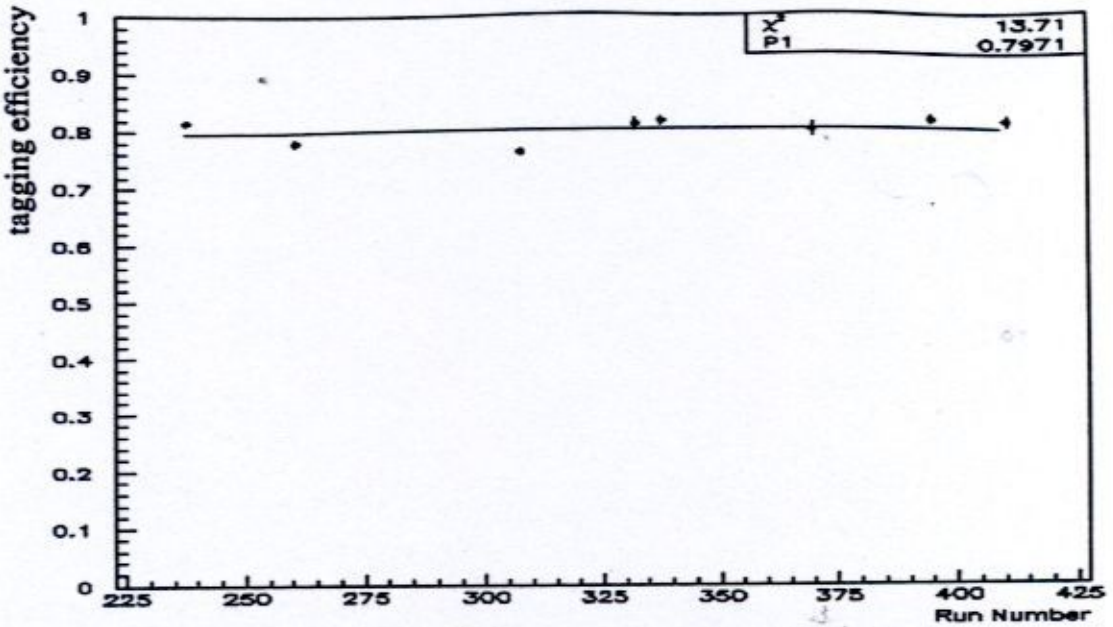

Figure 2.11:Tagging Efficiency as a Function of Run Number

Since there were no major changes in the tagging efficiency over the course of the four weeks, the eight measurements were simply averaged to yield a mean tagging efficiency for this experiment of 0.80+/-0.01.

2.4.3 Beam Monitoring Using the Tagger

Beam Quality

Since each tagger channel was connected to a scaler, the distribution of electron hits across the focal plane was known. Figure 2.12 shows a typical distribution.

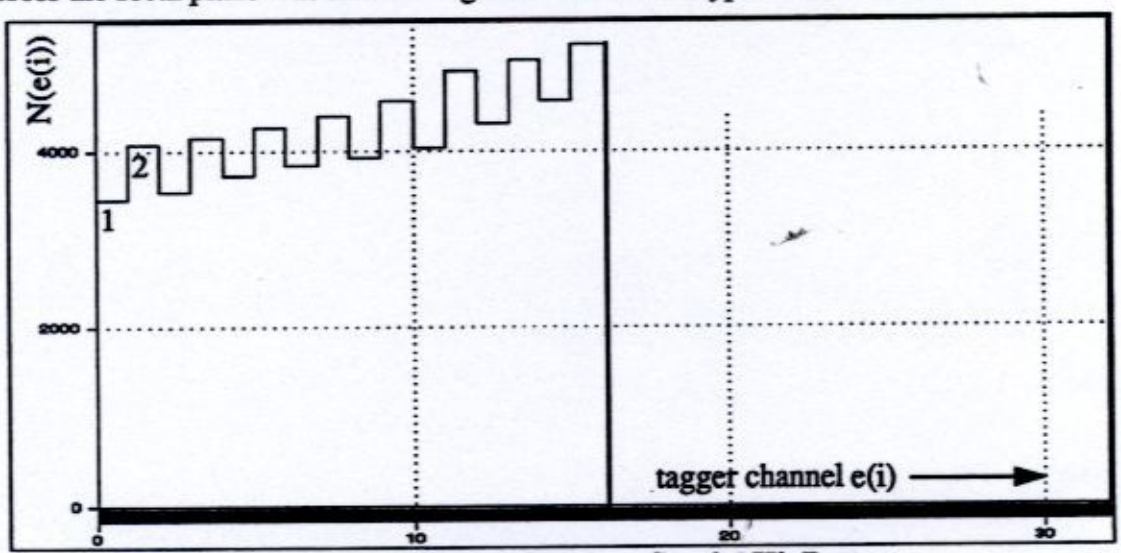

Figure 2.12:A Typical Electron Spatial Hit Pattern

A striking feature of this distribution is that the odd numbered tagger channels have consistently fewer counts than the even numbered tagger channels. This is a geometric effect due to a combination of the overlap of the individual tagger counters to define tagger channels and the fact that the electrons struck the focal plane at an oblique angle. However, because the experiment was performed on a channel-by-channel basis, the "odd-even effect" was not a problem since it divided out in the cross section calculation. That is, a channel which had extra electron hits and thus associated photon flux due to the odd-even effect also had the exact same proportion of π^+ yield in excess, so that the cross section, which depended on the ratio, was unaffected.

The distribution should correspond to the shape of a bremsstrahlung spectrum. The quality of the beam could be monitored by periodically checking a histogram of the tagger scalers for deviations from this shape. For example, if the beam was missteered, electromagnetic scrapings from the beam pipe appeared as copious amounts of hits in the lower energy tagger channels, and thus dramatically distorted the shape of the distribution. In fact, by closely monitoring the tagger scalers, the experimenter was able to recognize problems with the beam well in advance of the machine operator.

There is an apparent deviation from the bremsstrahlung distribution for a perfectly steered beam in Figure 2.12. This is caused by the fact that although each of the tagger channels has the same physical dimensions, they each have a different momentum acceptance, with the tagger channels corresponding to high photon energies (and thus low electron energies) having the least. Because of this, the tagger channels corresponding to low photon energies saw more electrons due to their acceptance, which distorted the bremsstrahlung shape of the spectrum. If the individual channels were normalized to their acceptance, the true bremsstrahlung shape was recovered.

Beam Continuity

To minimize background and reduce deadtime in the electronics, it was desirable to have as nearly CW an electron beam as possible. The duty factor is a measurement of this beam continuity. For a given period of time "T", the duty factor "df" was given by

$$df = \frac{\frac{1}{T}\left(\int_0^T dt\ I(t)\right)^2}{\int_0^T dt\ I^2(t)} \qquad (2.9)$$

where "I(t)" was the instantaneous current at time t. A duty factor of 1 corresponded to a perfectly steady beam, while a duty factor of 0 corresponded to a delta function pulse. This expression may be equivalently written (Florizone *et al.*, 1990) in terms of the counts seen in time T by two well-separated tagger channels A and B

$$df = \frac{N_A N_B}{N_{AB}} \left(\frac{\tau}{T}\right) \qquad (2.10)$$

where "τ" was the hardware coincidence resolving time. The channels were well-separated to ensure that the coincidences between them, "N_{AB}", were random events. Purpose-built electronics were combined with the tagger focal plane to carefully monitor the duty factor of the electron beam over the course of the experiment, since poor duty factor meant poor beam and often indicated machine problems. Duty factors ranging from 5% to 40% were recorded over the course of the run, with a time-averaged value of ~25%.

2.5 The Experiment Arm Apparatus

The detector telescopes, the electronics, hardware π^+ identification and the determination of acceptable events rates are discussed.

2.5.1 The Detector Telescopes

The X-arm consisted of four ΔE-E type plastic scintillator telescopes of medium energy resolution (~15% - see Appendix D) placed at a nominal distance of 30 cm from the target at nominal angles of 50°, 80°, 110°, and 140° with respect to the photon beamline. Use of the ΔE-E technique allowed particle identification via the determination of the charge-to-mass ratio (see Figure 2.21). Over the course of the experiment, these telescopes came to be known as Melbourne, Sydney, Adelaide, and Seattle respectively (see Figure 2.13).

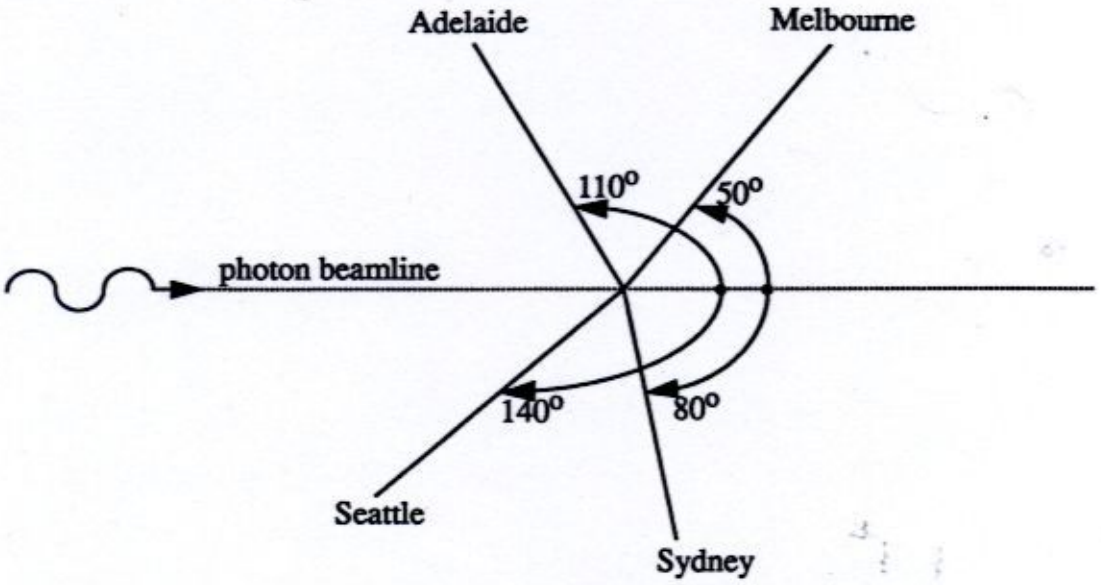

Figure 2.13:The Geometry of the X-arm

Table 2.4: X-arm Detector Summary

Detector angle	Detector Name	Funded By:
51° 12'	Melbourne	University of Melbourne/Trent University
80° 57'	Sydney	University of Melbourne/Trent University
109° 14'	Adelaide	University of Melbourne/Trent University
140° 38'	Seattle	University of Washington

Each telescope consisted of a relatively thin ΔE-type detector followed by a very thick E-type detector (see Figure 2.14). The ΔE served as a transmission detector for all but the lowest energy π^+. A π^+ passing through it would lose some, but rarely all, of its energy. Note that the effective π^+ detection threshold of the telescopes reflected the fact that some low energy π^+ were actually stopped by the ΔE. The integral of the analog output pulse from the anode of the ΔE-detector was proportional to the energy deposited by the π^+ as it passed through.

The ΔE counters consisted of 100 mm X 100 mm X 6 mm thick BC400 scintillators optically coupled via a tapered, adiabatic lucite light guide and optical grease to 51 mm Philips XP2262 photomultipliers mounted on CERN 4244 bases. The small scintillator volume of the ΔE detectors made them invisible to almost all cosmic rays.

The thick E-detector served to stop π^+ of all energies created in this experiment. The integral of the analog output pulse from the anode of the E-detector was proportional to the total energy of the π^+. There were two types of E-detectors employed in the experiment. Three of them, identified as Melbourne, Sydney, and Adelaide, were supplied by the University of Melbourne. These rectangular blocks of NE 102A measured 165 mm X 165 mm X 360 mm in length and were optically coupled to 127 mm Philips XP2040/ XP2041 photomultipliers and SAL-designed bases via UVT (ultra-violet transparent) acrylic adaptor plates and Dow-Corning Q2-3067 optical grease (O'Rielly, 1993). The fourth E-block, Seattle, was furnished by the University of Washington. This cylindrical block of BC 408 measured 150 mm X 305 mm in length, and was optically coupled to a 127 mm Hammamatsu R-1250-03 photomultiplier and base using UVT acrylic lightguide and optical grease (Rosenzweig, 1993). Similar E-detectors have been reported on previously (Saltmarsh *et al.*, 1972; Axen *et al.*, 1974).

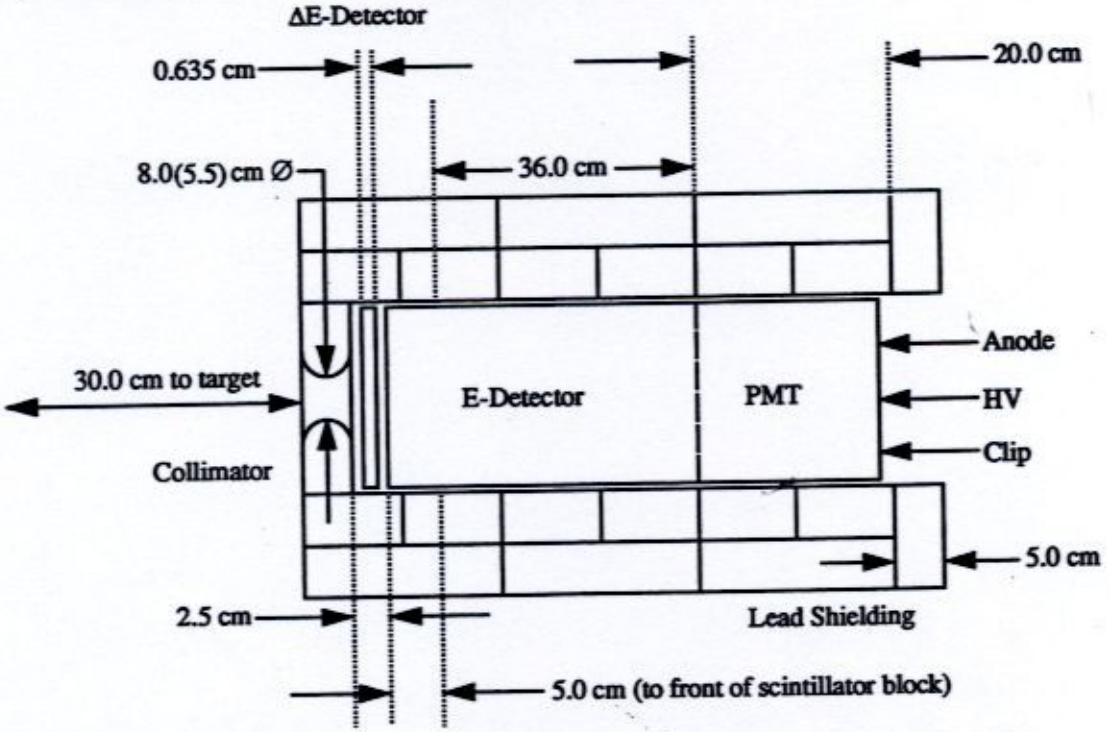

Figure 2.14:A Typical ΔE-E Telescope and Housing (Not to Scale)

The telescopes were surrounded with up to 10 cm of lead in the form of a hut, to shield them from room background such as the radiation from the beam dump. Three of the four were collimated to an 8 cm diameter circular aperture for all targets. The fourth, Melbourne, located at the most forward angle, was collimated to an 8 cm diameter circular aperture for the targets having $A \leq 40$, and a 5.5 cm circular aperture for the targets having $A \geq 120$. However, some runs for lower A targets were taken with this smaller collimator as well. The collimator was changed to keep the singles rates (see page 55) to an acceptable level, since as the number of protons Z in the target nucleus increased, so did the number of pair produced electrons (the pair production cross section goes roughly like Z^2 at these energies). The collimator bore was not cylindrical, but instead the apertures were rounded to minimize inscattering to the detectors. If a collimator was perfectly cylindrical, energetic charged particles could scatter off the bore and be cylindrically focussed into the active volume of the detector. Not only does this increase the number of unwanted events reaching the detector, but it also makes solid angle calculations difficult. By rounding off these edges, a uniform, thick lip was achieved, which greatly reduced the probability of charged particles scattering from the collimator into the detector.

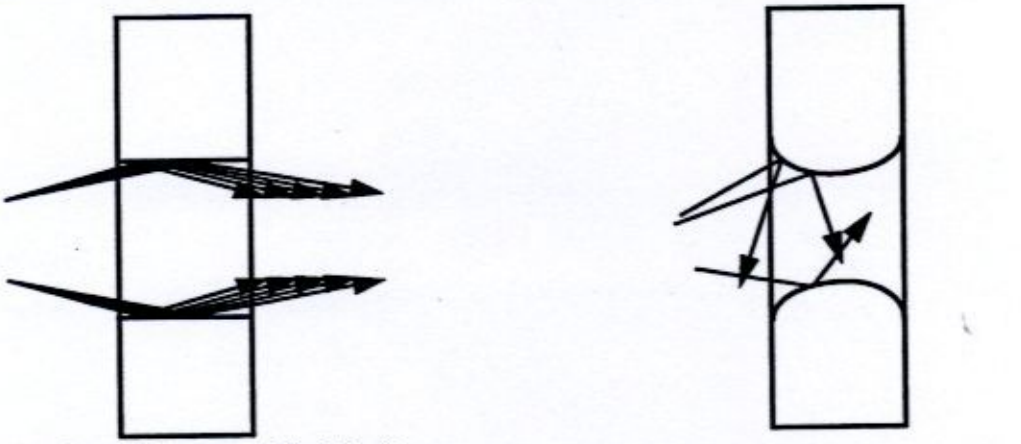

charged particles are cylindrically focussed into the detector

"no" inscattering into the detector

Figure 2.15:Collimators

The gains of the ΔE detectors were set such that a minimum ionizing electron produced a -75 mV pulse. Typical ΔE pulse shapes had a risetime of about 8 ns and a duration of 25 ns. The gains of the E-detectors were set such that a 100 MeV proton produced

a -1 V signal. Typical E pulse shapes had a risetime of about 5 ns, and a duration of 30 ns. Because of propagation delays within the photomultiplier itself, a given E-detector took about 30 ns longer than its ΔE counterpart to process a given event.

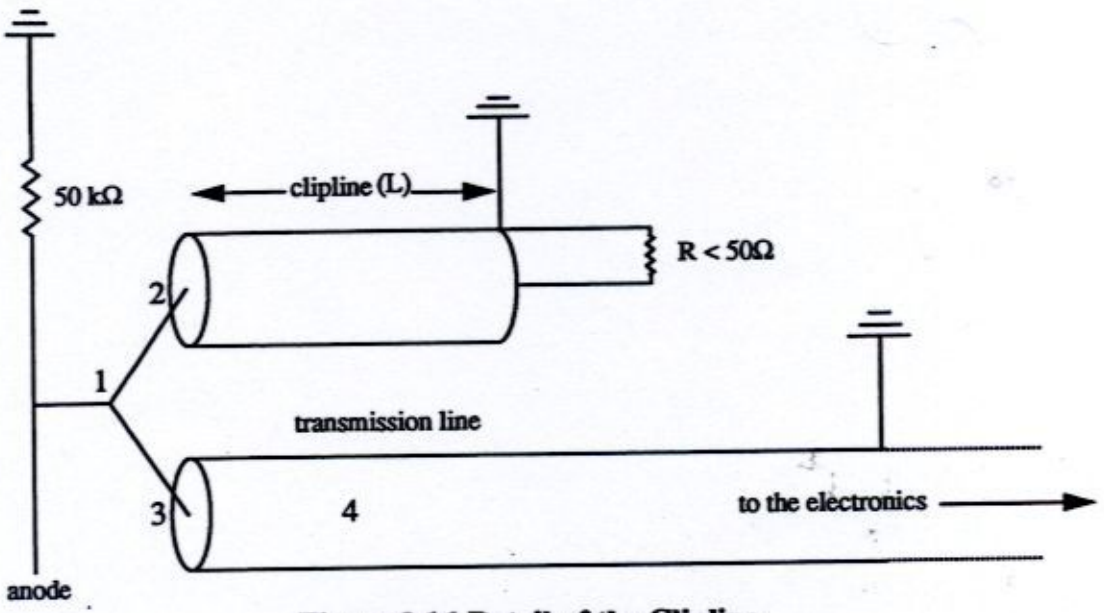

Figure 2.16:Detail of the Clipline

It was desired to have the best decay pulse integrity possible, so the falltime of the E pulse was crucial to the experiment. Thus, the E-signal was modified to make its duration in time as short as possible, using a procedure known as "clipping". The analog signal produced by the photomultiplier was split at point 1, the anode. A portion of the signal proceeded down the clip line (point 2 onward), while the remainder was passed down the transmission line (point 3 onward). The clipline signal cable was connected to ground through a resistor, R. If R was not equal to the characteristic impedance of the transmission line (50 Ω), then the signal would be reflected at the impedance mismatch. If R was greater than 50 Ω, the reflected signal had the same polarity as the original signal. If R was less than 50 Ω, the reflected signal had the opposite polarity to the original, which was the desired situation. The length in time of the clipline, 2L/v, where "v" was the signal propagation speed (about 2/3 the speed of light), was set to be slightly less than the rise-time of the pulse originating at the anode. In this manner, the reflected signal added in a destructive fashion to the tail of the transmitted signal at 3, and this decreased the falltime

of the analog sum (point 4 onward). Note that for pulse minimization without a net loss in overall signal amplitude, 2L/v should have been set equal to the risetime of the analog signal. By setting 2L/v to a value slightly less than the risetime, amplitude was lost in the sum signal. However, the reduction of the pulse width was the goal. A potentiometer was used to determine the resistance value necessary for the desired minimization. Subsequently, resistors (of typical value 20 Ω) with very short leads were substituted for the potentiometers. This was done to decrease noise pickup and signal ringing, and also because potentiometers have undesirable associated inductance. The resulting clipped anode signals from the E-counters had risetimes of approximatelly 5 ns and falltimes of 15 ns.

2.5.2 The Electronics

The electronics consisted of standard NIM and CAMAC modules. The most important modules were the Phillips NIM 715 Octal Timing Constant Fraction Discriminators (CFDs), the LeCroy CAMAC 2228A Octal Time-to-Digital Converters (TDCs), the LeCroy CAMAC 2249A Twelve Channel Charge Sensing Analog-to-Digital Converters (ADCs), and the Kinetic Systems KS3615 Hex Scalers.

A CFD is a discriminator which triggers at a constant fraction of the input analog pulse height to minimize timing jitter in the output logic signal. It was the best type of discriminator to use for this experiment because of the large amplitude range of analog input signals. The more typical Leading Edge Discriminators (LEDs) which trigger at a fixed level of the input analog pulse height shift in time as the amplitude of the input analog signal changes. A TDC is a module to which two logic pulses are passed, a start and a stop. The former starts an internal clock while the latter stops it. The time difference between the two pulses in the form of an integer is returned. All TDCs used in this exper-

iment had 2048 channels, and were set to the 100 ps per TDC channel scale. Figure 2.17 illustrates typical TDC stop spikes for the ΔE and E detectors. These TDCs were started by the X-reference signal, and stopped by the appropriate discriminator event signal.

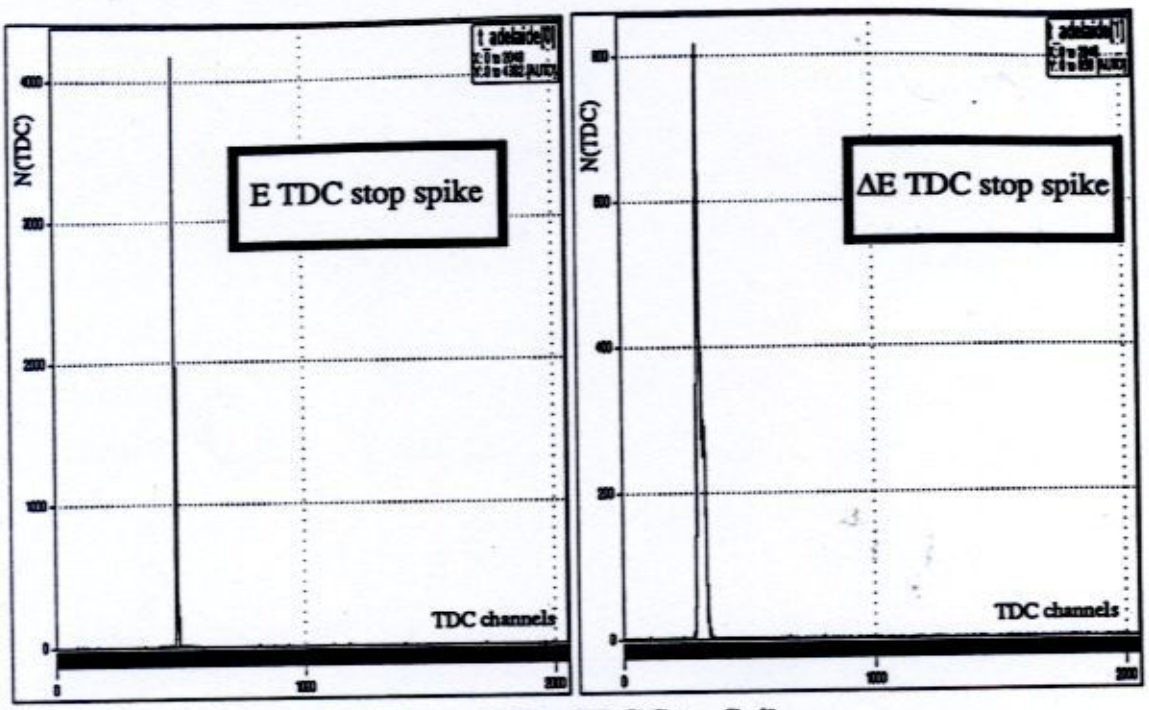

Figure 2.17:The TDC Stop Spikes

A charge sensing ADC is a module to which an analog input pulse and a gating pulse are passed. While the ADC is enabled, the analog pulse current is integrated, and an integer proportional to the integrated current (total charge) is returned. Finally, a scaler is a module to which logic pulses and an inhibit are passed. If the inhibit is not in effect, the logic pulses are counted.

Figure 2.18 presents a block diagram of the electronics, including all pertinent delay values, gate widths, and thresholds. The most important aspects of the electronics are dealt with in the following four subsections.

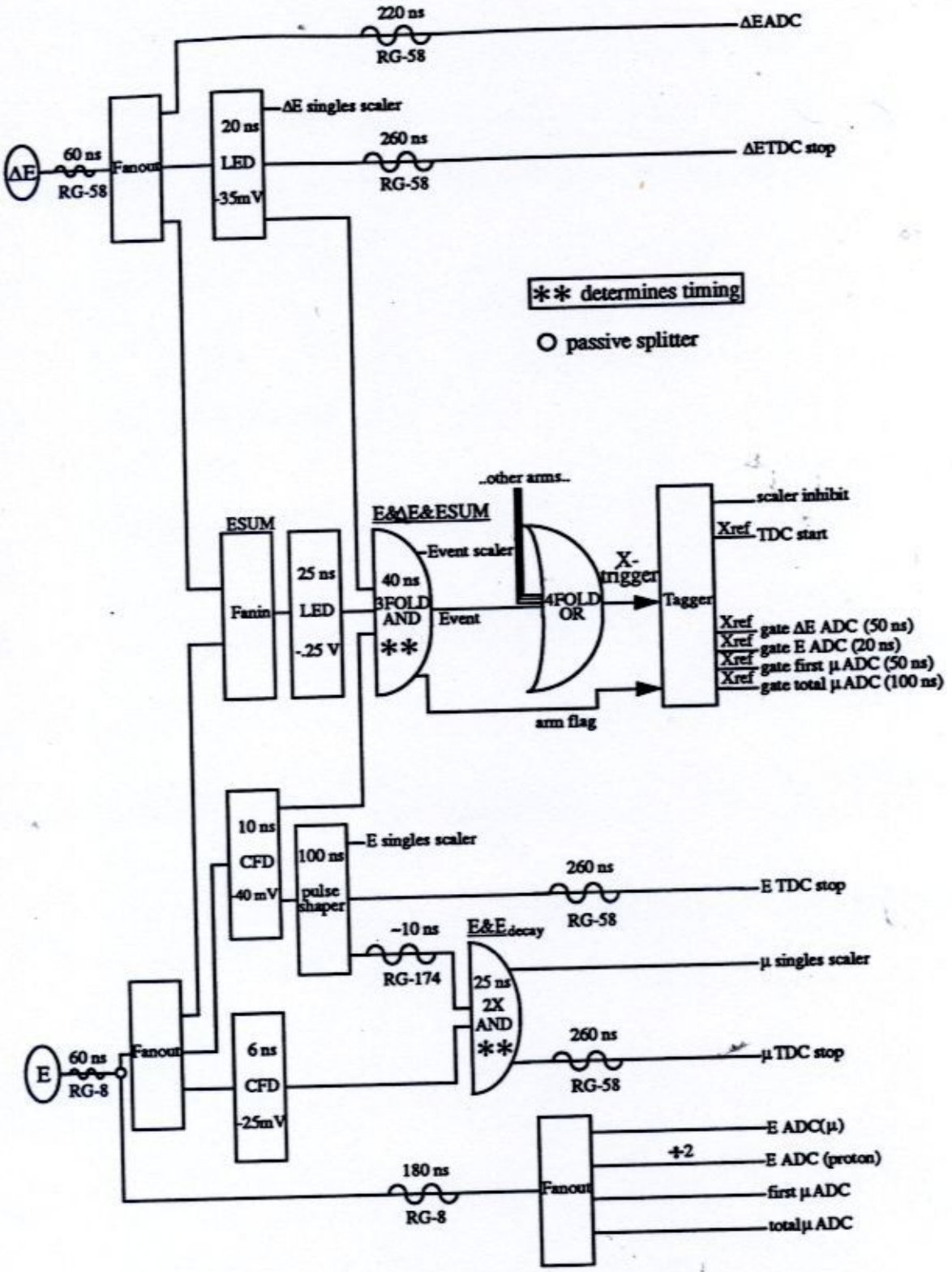

Figure 2.18:A Block Diagram of the Electronics

The X-Trigger

An X-trigger was defined to be the logical OR of an event in any one of the four detector telescopes. Typical X-trigger rates were on the order of 100 Hz.

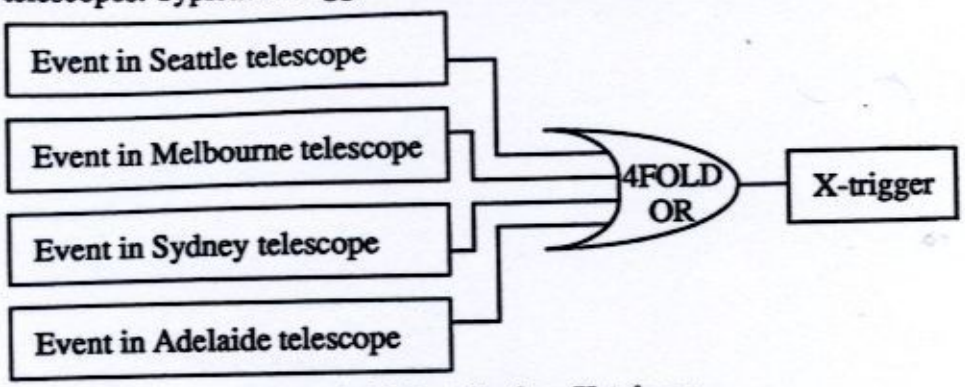

Figure 2.19:Detail of an X-trigger

The ESUM Threshold

As mentioned in section 2.5.1, pair production was the dominant mechanism which lead to the creation of unwanted background. This resulted in thousands of uninteresting electron or electron-positron pair events being detected by a given telescope for every π^+ event. Because these background events were of low energy, the easiest way to eliminate them was to substantially raise the discriminator thresholds on both the ΔE and E counters. However, this would have reduced the detection efficiency, since as the energy of the π^+ decreased, the ΔE signal increased in size, while the E signal decreased. Thus, an alternate method was adopted to keep the number of electron events which were processed to a minimum. Using a linear fan-in (adder), the analog pulses from the ΔE and E counters were summed into a single analog pulse (hereafter referred to as the "ESUM" pulse). This signal was then discriminated and included in the event trigger.

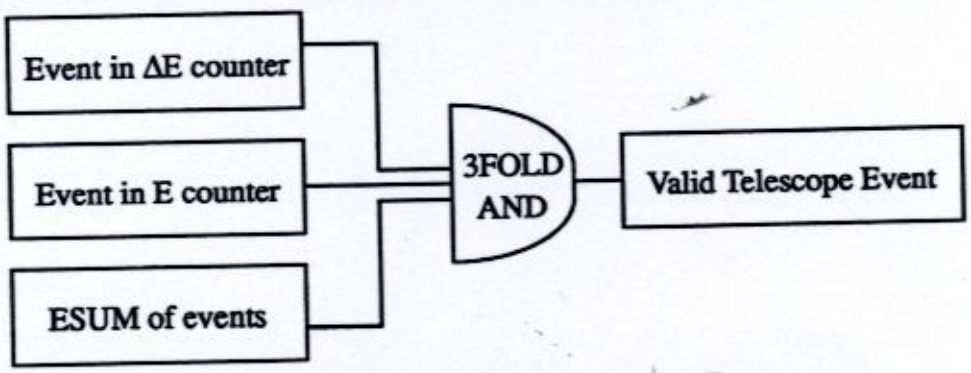

Figure 2.20:Detail of a Valid Telescope Event

A valid telescope event was thus defined to be the logical AND of three conditions: the energy deposited by the particle in the ΔE-detector had to exceed the ΔE-detector threshold, the energy deposited by the particle in the E-detector had to exceed the E-detector threshold, and the sum of these two energies had to exceed the ESUM threshold (see Figure 2.20).

By strongly discriminating on the ESUM signal rather than either the ΔE or E signals, the electron event rate was kept to tolerable levels. In fact, the ESUM method of electron rejection proved to be so effective that the ΔE and E thresholds were set to just above the noise level (-35 mV and -40 mV respectively). Figure 2.21 illustrates the manner in which these three discriminator thresholds actually affected the data which was collected.

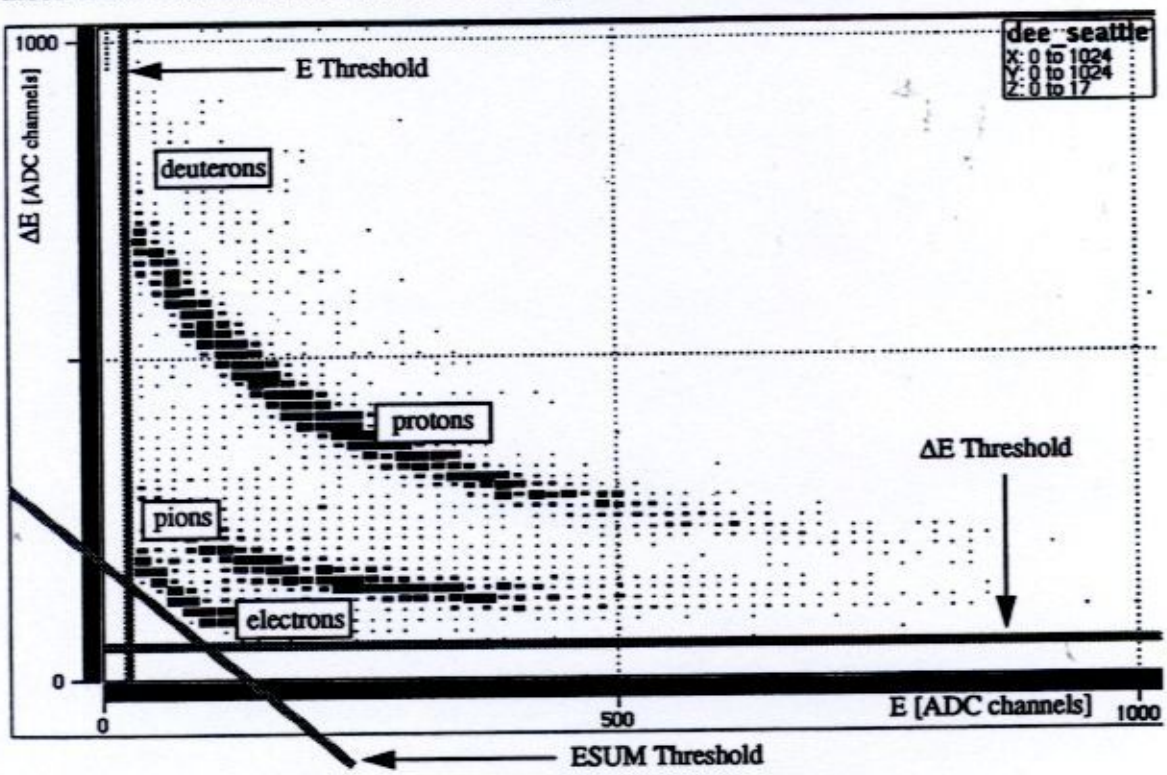

Figure 2.21:An On-line ΔE-E Scatterplot

Hardware π^+ Identification

The ΔE-E combination allowed the determination of the charge-to-mass ratio of the detected particles as shown in Figure 2.21. A charged particle which had enough energy to pass through the ΔE scintillator and into the E scintillator and produced pulses in each large enough to exceed all the thresholds previously discussed produced a valid telescope event (see Figure 2.20). Thus, electrons, protons, deuterons and pions, both positive and

negative, were all detected. However, this method of detection did not help to distinguish π^+ from π^-. Further hardware measures were thus taken to allow for the separation of the π^+ events from the others in the data analysis. This identification hardware made use of the fact that a π^+, after stopping in a given E-detector, decayed to a (μ^+,ν_μ) pair, with a mean lifetime τ of 26 ns. π^-'s do not produce such a decay pulse. The reaction kinematics for this decay (see Appendix A) yield

$$T_\mu = \frac{1}{2}\left[M_\pi + M_\mu\left(\frac{M_\mu}{M_\pi}\right)\right] - M_\mu = 4.12 \text{ MeV}, \qquad (2.11)$$

where "T_μ" was the μ^+ kinetic energy, "M_π" was the mass of the π^+ (139.6 MeV), and "M_μ" was the mass of the μ^+ (105.7 MeV). The kinetic energy of the decay μ^+ was thus constant. Two independent methods were devised to provide hardware validation of a π^+ event. The first method involved a delay gate ADC (hereafter referred to as "μADC") which looked for energy deposited subsequent to the primary event pulse consistent with the μ^+ afterpulse. The second method involved a TDC (hereafter referred to as "μTDC") which served to check the decay constant of events labeled as π^+.

The μADC

As shown at the bottom of Figure 2.18, the analog pulse from a given E-detector was passed to the μADC along a low dispersion, low loss RG-8 cable in order to preserve the risetime, falltime, and shape of the pulse over delays of up to 0.25 μs. The X-reference signal was used both to gate the prompt ADC on the primary π^+ event pulse, and to reference in time the subsequent delay gates of the μADC. These gates looked for the decay μ^+ over the first 100 ns subsequent to the primary event (see Figure 2.22).

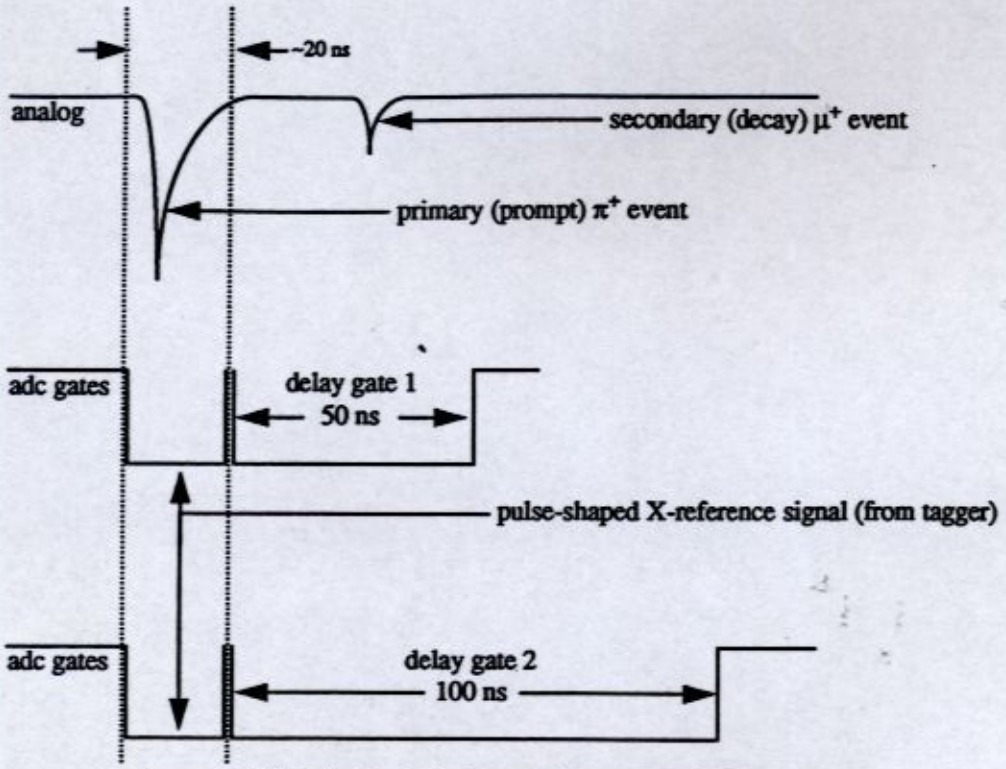

Figure 2.22:Relative Timings of the μADC Gates

The major drawback of this method of π^+ identification was that it was extremely difficult to determine the detection efficiency. It was possible for the pulse from the decay μ^+ to appear on the shoulder of the pulse from the primary π^+, lying either completely within the prompt ADC gate, or somewhere across the junction between the prompt and delay gate. This resulted in misidentification of π^+ events, since the decay energy was missing, either in whole or in part. Thus, it was decided to use this method of identification as a check of that provided by the μTDC, whose absolute detection efficiency was more readily obtainable.

The μTDC

The primary hardware method used to identify π^+ in this experiment was the μTDC. This was simply a TDC started by the primary (π^+) event and stopped by the secondary (μ^+) event. The spectrum of the μTDC should show the time constant of the π^+ decay. The beauty of this method of identification was that the detection efficiency was completely quantifiable - see page 96 for a complete discussion.

The analog pulse from a given E-detector was split and sent in parallel to two CFDs: one with a threshold of -40 mV (hereafter referred to as "hi-thresh"), and one with a threshold of -25 mV (hereafter referred to as "lo-thresh" - see Figure 2.23). Note that both of these thresholds are in fact very low, such that no π^+ escaped detection because of discriminators. Again, it was the effectiveness of the ESUM threshold which allowed this.

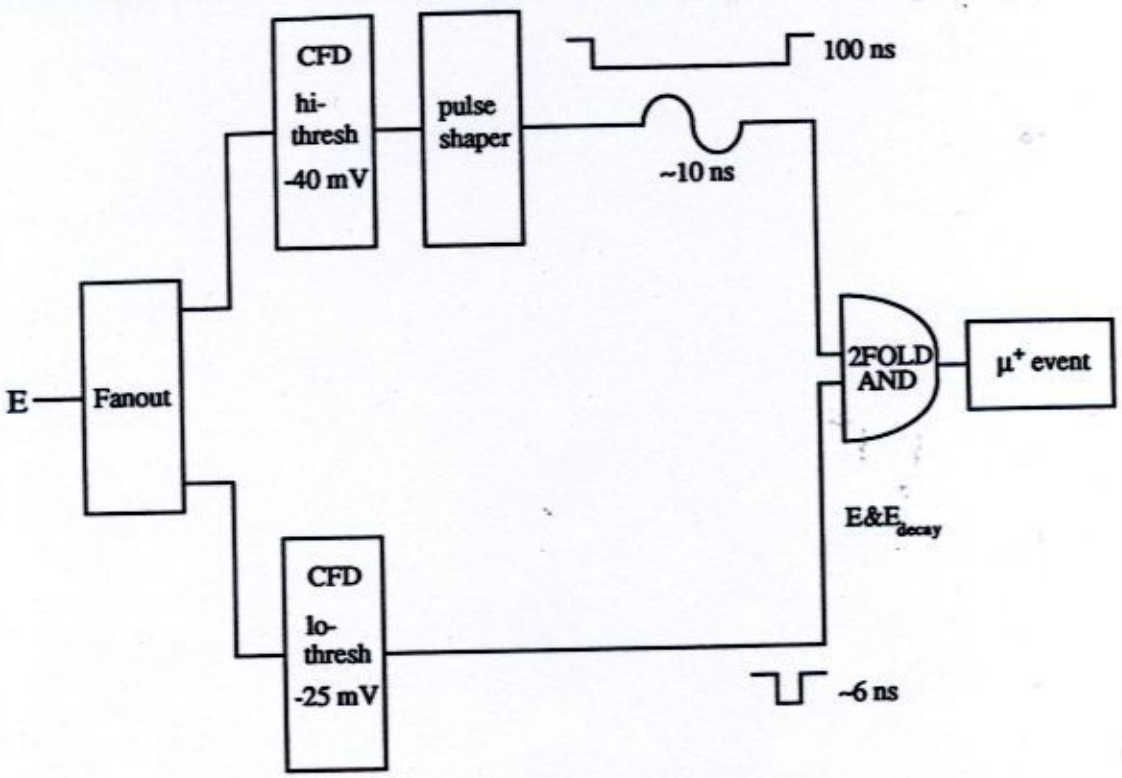

Figure 2.23:Detail of the μTDC Hardware

The hi-thresh CFD fired on the primary π^+ event portion of the E-pulse. The lo-thresh CFD fired on both the primary event and the much smaller μ^+ event produced by the π^+ decay. The width of the lo-thresh CFD output pulse was set to a nominal value (~6 ns), and the output pulse of the hi-thresh CFD was delayed by ~10 ns and pulse-shaped to 100 ns in length. Figure 2.24 details the resulting situation.

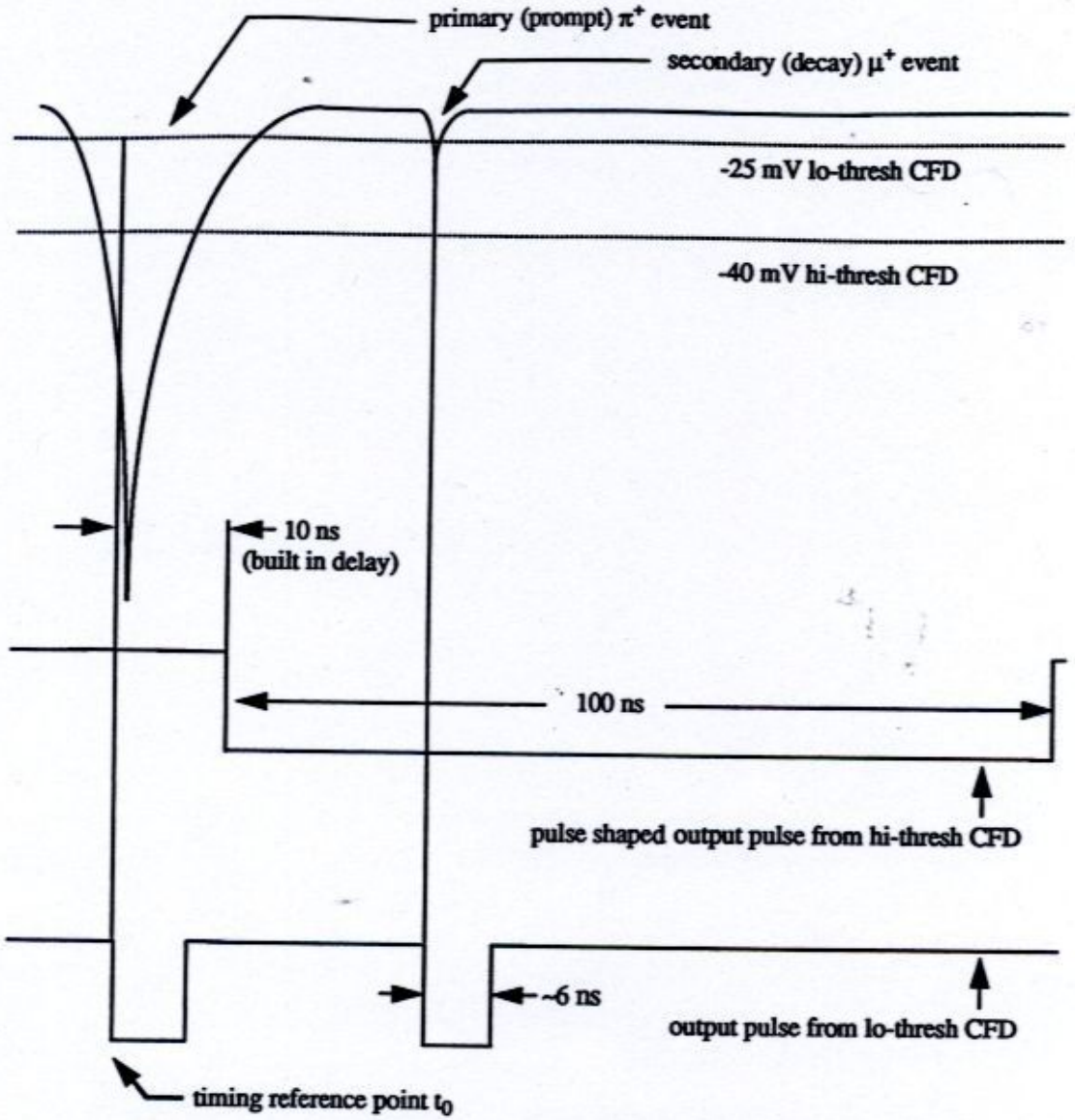

Figure 2.24:Detail of the CFD Timing

The logical AND of the short decay event signal and the long primary event signal resulted in hardware validation of a π^+ event. This AND was then used to stop the μTDC which had been started by the X-reference signal. Figure 2.25 illustrates the correlation between the μTDC spectrum and the CFD gates for π^+ of energy T_π incident on a given detector.

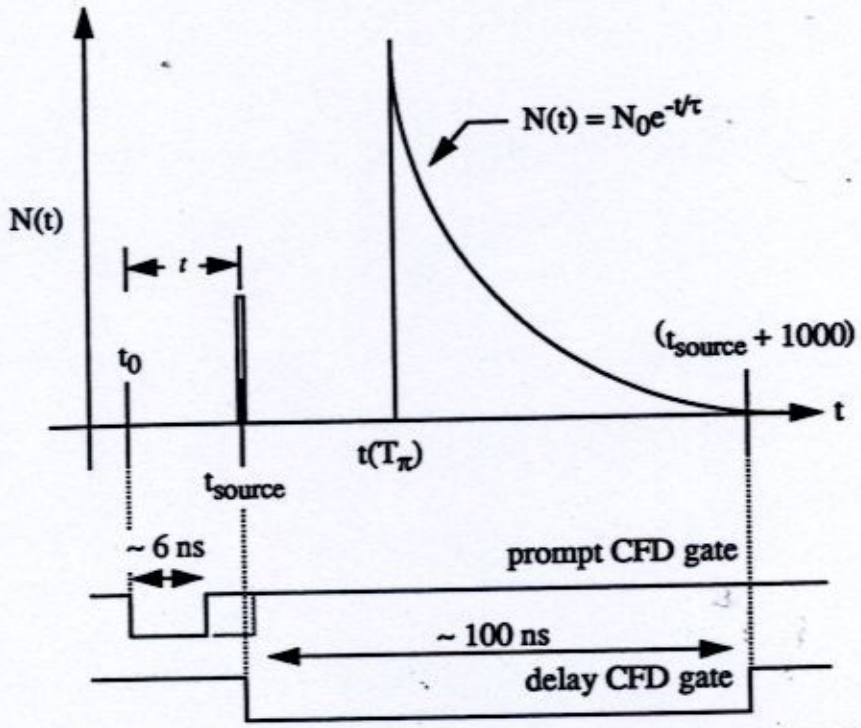

Figure 2.25:The Correlation Between the μTDC and the CFD Gates

In order to write down the detection efficiency due to this setup, it was essential to first fix a single point in time denoted "t_0" on the above diagram. This represents the point in time where the π^+comes to rest in the E-detector - the effective timing zero of the μTDC. In order to achieve this, the width of the prompt CFD gate was increased such that it overlapped the leading edge of the delay CFD gate. In this manner, events generated by a ^{106}Ru (beta) source produced a stop in the μTDC spectrum. The position of this stop spike, labeled "t_{source}" in Figure 2.25, located the leading edge of the delay CFD gate in the μTDC spectrum. Since the relative timings of the prompt and delay CFD gates were known (see Table 2.5), a simple subtraction yielded t_0. For the actual data taking, the width of the prompt CFD gate was returned to its original value of ~6 ns indicated in Figure 2.25.

$$t_0 = t_{source} - t \qquad (2.12)$$

Table 2.5: Important Timing Points

Telescope	t_{source}	t	t_0
Melbourne	213	108	105
Sydney	204	100	104
Adelaide	203	110	93
Seattle	214	100	114

Photomultiplier/discriminator deadtime due to finite pulse width caused a further difference between the earliest possible point in time a decay event could be detected (t_{source}) and the earliest possible point in time a π^+ decay actually was detected ($t(T_\pi)$). Recall from section 2.5.1, the baseline width of a typical E pulse was 20 ns. Further, since there was actually an energy range of π^+ incident upon the E-detector rather than a monoenergetic beam, it was necessary to determine whether the position of this earliest possible π^+ stop $t(T_\pi)$ was energy dependent.

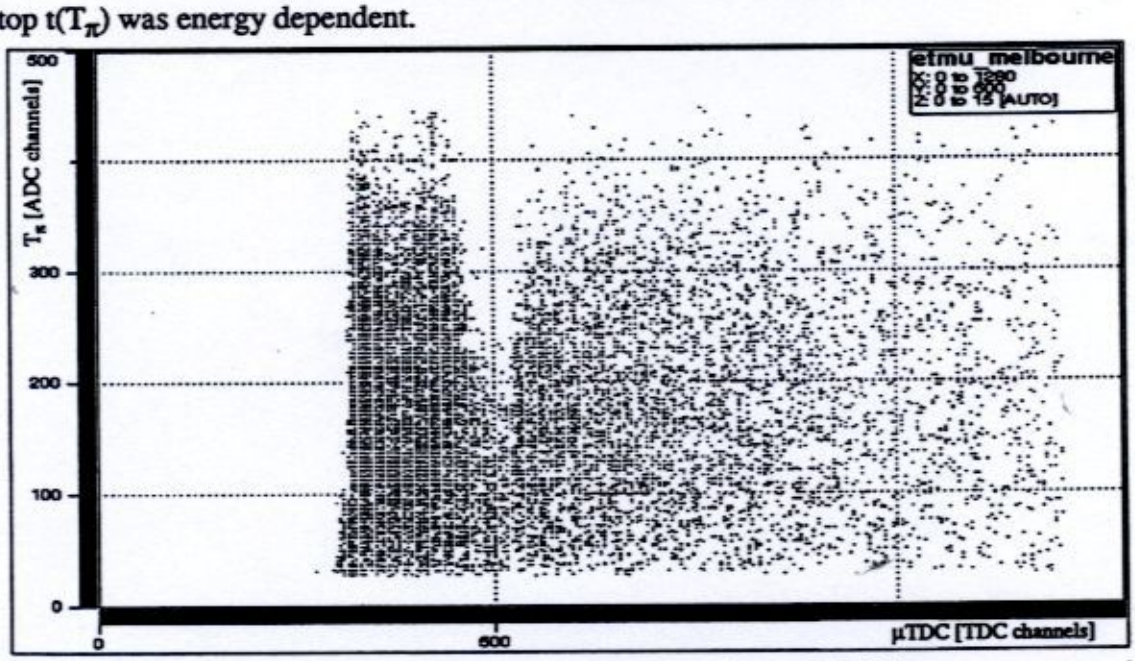

Figure 2.26:The Energy Dependence of the μTDC Stop

Figure 2.26 demonstrates the stop in the μTDC was definitely energy dependent, and that high energy π^+ tended to "ring", as evidenced by the structure in the scatterplot at high T_π. This ringing further complicated matters, since it produced false stops in the μTDC, and thus affected the π^+ detection efficiency.

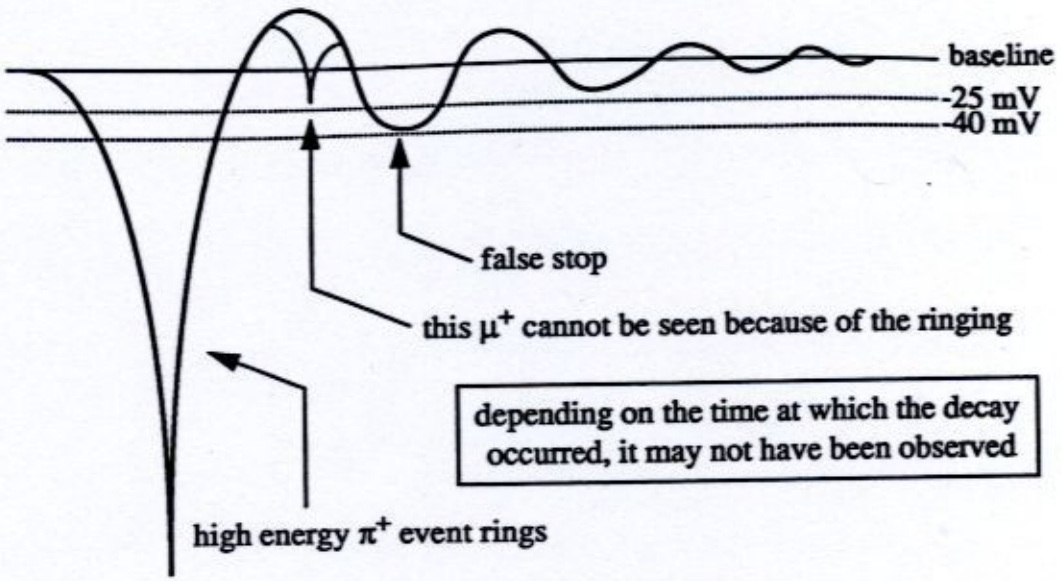

Figure 2.27:Detail of a Ringing Event

Determination of Acceptable Event Rates

The first ~100 ns subsequent to the primary π^+ event was crucial to the overall detection efficiency. It was decided that a 0.5% probability of a second event of any type striking the detector during this time span and producing a false μ^+ stop was acceptable. Since the instantaneous tagger focal plane rate was proportional to the instantaneous count rates in the detectors, and since Melbourne was the most forward detector and thus had the highest instantaneous count rate (pair production is very forward peaked), it was the singles rate in the Melbourne detector which was used to set the maximum rate at which the focal plane was run, according to

$$\Phi_{\text{focal plane}} \propto \text{rate}_{(\text{Melbourne E})} = \frac{0.005}{100 \times 10^{-9}\text{ns}} = 50 \text{ kHz}. \qquad (2.13)$$

The maximum possible rate acceptable for the Melbourne detector was 50 kHz. This corresponded to an instantaneous rate across the focal plane of approximately 35 MHz. At these rates, "pileup" (high event rates causing two or more events to look like a single event of much higher energy) was not a problem. Every effort was made to restrict the instantaneous focal plane rate to this value.

2.6 Data Acquisition

A block diagram of the data acquisition hardware used for this experiment is shown in Figure 2.28. The front end CAMAC modules resided in a single CAMAC crate which was controlled by a CES Starburst J-11 microprocessor (PDP-11). The Starburst passed the data along a serial highway to a DEC MicroVAX II, which acted as the control computer for the experiment. A SUN workstation connected to the MicroVAX via ETHERNET allowed both user control over the experiment, and on-line monitoring of the data. An Exabyte EXB-8200 tape drive was also connected to the MicroVAX, so that the data could be written to 8 mm Sony P6-120MP magnetic tapes.

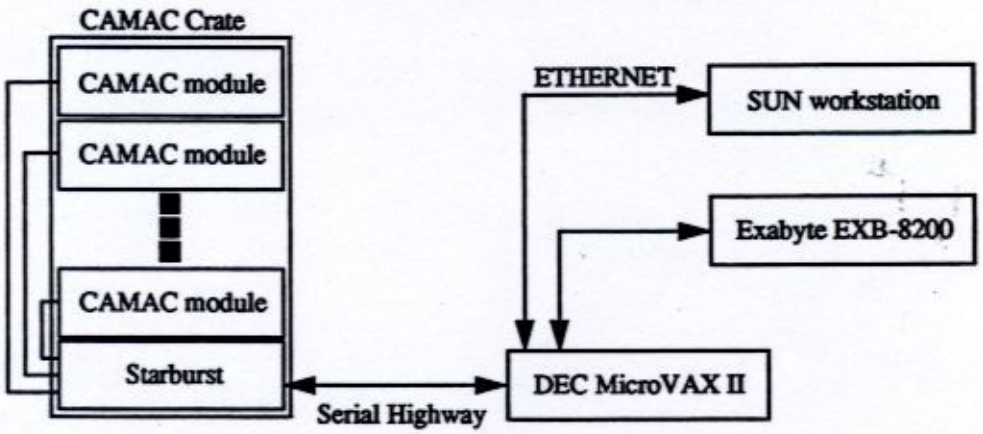

Figure 2.28:The Data Acquisition System

The entire system was tied together by the SAL in-house data acquisition/analysis software package LUCID (SAL, 1990B). This system allowed the user to interface with the electronics by writing three pieces of software: a READER, a WRITER, and a LOOKER. All software ran on the MicroVAX, and controlled communications between it and another element of the system: that is, the READER connected it to the Starburst, the LOOKER connected it to the SUN workstation, and the WRITER connected it to the Exabyte. Note that standard LUCID format READER, WRITER, and LOOKER templates existed for use with all tagged photon experiments. To this, the necessary components to describe the unique X-arm were added.

Within the READER, software events were constructed, each of which depended on a certain hardware trigger, and resulted in the execution of a different set of CAMAC commands. There were four different event types defined for this experiment: "startup", "tagdata", "scalerread", and "goodbye". The startup event (28 bytes) was a header signal-

ling that a run had begun. A tagdata event was written for every tagged photon event, and had length 172 bytes. A scalerread event (664 bytes) was performed every thirty seconds, and involved a complete readout of the entire scaler bank. The goodbye event, which was identical in structure to the scalerread event, signalled the end of the run. This software allowed complete readout of all desired modules whenever an interrupt was generated. The procedure, including interrupt response, took about 1 msec. There was no computer deadtime in this experiment due to a combination of tagged event rates and low background.

The LOOKER software allowed sampling of some of the data on-line in the form of user-defined histograms and scatterplots. In general, it was impossible to sample all the data on-line. The resulting deadtime would have crippled the data taking procedure. The LOOKER processed events only when there was ample time to do so. If another event passed through the data stream while a previous event was being processed, the READER was not held up.

The WRITER software wrote the data to tape in a format permitting off-line replay analysis. Software existed to transform LUCID format data to other formats, such as Q. Over the course of the experiment, approximately 16 Gigabytes of data were obtained.

2.7 Run Summary

Table 2.6 presents a chronological summary of the experiment. The goal was to obtain ~2000 π^+ interrupts per telescope per production target. The first 16 days of beamtime were spent on CH_2, CD_2, C, and Ca. Subsequently, the experiment was stopped for six days to perform preliminary analysis. The last 14 days of beam time were spent primarily on Sn and Pb, as well as improving statistics on the CH_2 and C targets. Each of the beam days consisted of about ten hours of beam delivered to the target, and about two hours of beam used to perform routine experimental and tagger system checks. These checks were generally performed whenever the machine was tuned, and included tagging efficiency measurements and target in/out runs. The balance of the day was spent on routine machine maintenance and tuning.

Table 2.6: Run Summary

Run Number	Target	$E^{e^-}_{incident}$ [MeV]	Number of Tagged Events
223	CD_2	289	109612
224	CD_2	150	63050
225	out (radiator)	150	4596
226	out (radiator)	150	1
230	tagging efficiency (radiator)	150	134790
231	tagging efficiency (no radiator)	150	0
232	C	150	64254
233	C	150	66767
234	C	289	86861
237	tagging efficiency (radiator)	289	219641
238	tagging efficiency (no radiator)	289	0
239	out (radiator)	289	30370
240	out (no radiator)	289	4
241	C	289	23599
242	CH_2	289	88613
243	CH_2	289	237474
244	C	289	229388
245	C	289	243390
246	out (radiator)	289	91023
247	out (no radiator)	289	0
248	out (no radiator)	289	1
249	C	289	153322
250	C	289	238380
251	CD_2	289	264446
252	CD_2	289	45831

Table 2.6: Run Summary

Run Number	Target	$E^{e^-}_{incident}$ [MeV]	Number of Tagged Events
253	CD_2	289	41765
254	CD_2	289	55871
255	CD_2	289	39062
256	CD_2	289	48759
257	C	289	274015
258	C	289	614457
259	out (radiator)	289	7350
260	tagging efficiency (radiator)	289	78193
261	tagging efficiency (no radiator)	289	0
263	out (radiator)	289	37199
264	out (no radiator)	289	5
265	C	289	68317
266	Ca	289	93638
267	Ca	289	443697
273	out (radiator)	289	26172
274	out (no radiator)	289	1
275	Ca	289	167185
276	Ca	289	1072437
277	CH_2	289	118876
278	C	289	359714
279	Ca	289	653593
280	Ca	289	599259
281	Ca	289	115893
282	Ca	289	103762
283	out (radiator)	289	66691
284	out (no radiator)	289	0

Table 2.6: Run Summary

Run Number	Target	$E^{e^-}_{incident}$ [MeV]	Number of Tagged Events
285	CH_2	289	239556
286	C	289	742287
287	C	289	285187
288	Ca	289	29546
289	Ca	289	594546
290	Ca	289	673961
291	Ca	289	115932
292	Ca	289	38075
293	Ca	289	224995
294	C	289	677
295	C	289	250049
296	out (radiator)	289	40104
297	out (no radiator)	289	0
298	CH_2	289	131239
299	Ca	289	281706
301	Ca	289	1088751
302	Ca	289	1292980
303	C	289	208872
304	C	289	79968
305	out (radiator)	289	80605
306	out (no radiator)	289	2
307	tagging efficiency (radiator)	289	131449
308	tagging efficiency (no radiator)	289	0
311	Pb	289	484102
312	Pb	289	268010
314	Sn	289	38964

Table 2.6: Run Summary

Run Number	Target	$E^{e^-}_{incident}$ [MeV]	Number of Tagged Events
325	CH_2	289	29056
326	CH_2	289	73293
327	Pb	289	389107
328	Pb	289	96868
329	Sn	289	477697
331	tagging efficiency (radiator)	289	43504
333	tagging efficiency (no radiator)	289	0
334	out (radiator)	289	24777
335	C	289	353992
336	Ca	289	1006551
337	tagging efficiency (radiator)	289	90200
338	tagging efficiency (no radiator)	289	0
339	out (no radiator)	289	0
340	out (radiator)	289	30995
341	CH_2	289	99578
342	C	289	163284
343	Sn	289	47025
344	Sn	289	71790
345	Sn	289	308837
346	Sn	289	784198
347	Sn	289	831631
348	Sn	289	525620
349	out (no radiator)	289	0
350	out (radiator)	289	11800
351	CH_2	289	129859
352	C	289	184572

Table 2.6: Run Summary

Run Number	Target	$E^{e^-}_{incident}$ [MeV]	Number of Tagged Events
353	Sn	289	1084819
356	Sn	289	1088146
362	out (radiator)	289	17668
363	out (no radiator)	289	3
364	CH_2	289	116533
365	CH_2	289	46269
366	C	289	56791
367	C	289	34818
368	C	289	5249
369	tagging efficiency (radiator)	289	29993
370	tagging efficiency (no radiator)	287	1
371	C	287	163529
372	Pb	287	341660
377	Pb	287	682811
378	Pb	287	1526865
379	Pb	287	2154080
380	Pb	287	796486
381	Pb	287	95427
382	Pb	287	118423
383	out (radiator)	287	48785
384	out (no radiator)	287	25
386	CH_2	287	51986
387	out (radiator)	287	16017
388	C	287	103732
389	Pb	287	1505758
390	Pb	287	180208

Table 2.6: Run Summary

Run Number	Target	$E^{e^-}_{incident}$ [MeV]	Number of Tagged Events
391	Pb	287	1693226
392	Pb	287	517258
393	Pb	287	1461137
394	tagging efficiency (radiator)	287	71957
395	tagging efficiency (no radiator)	287	0
396	out (no radiator)	287	0
397	out (radiator)	287	24984
398	CH_2	287	94586
399	C	287	107018
400	Pb	287	649396
401	Pb	287	334078
402	Pb	287	245127
403	Pb	287	496870
404	Pb	287	707028
405	Pb	287	1498421
406	Pb	287	226988
407	Pb	287	609426
410	tagging efficiency (radiator)	287	41383
411	tagging efficiency (no radiator)	287	1
412	out (no radiator)	287	0
413	out (radiator)	287	11733
414	CH_2	287	91634
415	Pb	287	1031488
416	Pb	287	1782567
417	Pb	287	477555
418	Pb	287	842779

Table 2.6: Run Summary

Run Number	Target	$E^{e^-}_{incident}$ [MeV]	Number of Tagged Events
419	Pb	287	1172245
420	Sn	287	878707
421	out (radiator)	287	10389
422	out (no radiator)	287	16
423	Sn	287	676254
424	Pb	287	1413044
425	CH_2	287	70352
426	Pb	287	2440812
427	out (no radiator)	287	6
428	out (radiator)	287	18796
429	Sn	287	1149426
430	Sn	287	30694
431	Sn	287	566371
432	Pb	287	1062592
433	Pb	287	386374
434	Sn	287	769919
435	CH_2	287	229992
436	out (radiator)	287	20056
437	Sn	287	2797219
438	out (no radiator)	287	1
439	Sn	287	495446
440	Sn	287	1672493
441	Sn	287	107914
442	CH_2	287	48893
444	CD_2	150	55992

Chapter 3. THE ANALYSIS

In this chapter, an overview of the data analysis is presented. Subjects include data reduction, particle identification, yield determination, energy calibration, detector efficiency, and normalization. Double differential, differential, and total cross sections are presented.

3.1 General Introduction

The goal of the data analysis was to extract double differential, differential and total cross sections for π^+ photoproduction from the data taken. Over the course of the experiment, approximately 16 Gigabytes of data were collected, encompassing the inclusive (γ,π), (γ,p), and (γ,d) reactions from the various targets. Subsequent to the production run, the data were organized by target onto separate data tapes, such that only a single target type appeared on any given tape. However, because of the large volume of data, it was too time consuming to analyze from data tape (approximately 8 hours was required for each). Thus, steps were taken to filter the (γ,π^+) data from the rest, reducing the overall data set and required replay time. Data filtering involved applying a series of cuts to the data to select the π^+ events. These cuts were made extremely loose in order to prevent the undesired removal of π^+ events. The data reduction succeeded in reducing the entire data set to a basically (γ,π^+) subset of approximately 160 Megabytes, a quantity which fit comfortably on hard disk. Filtering the data to this level dramatically reduced replay time, both because the number of uninteresting events which were analyzed was kept to a minimum, and because the hard disks were mechanically faster at replay by at least an order of magnitude.

Once the data were reduced, an algorithm consisting of a series of tight cuts was developed to extract the π^+ events which were within the prompt tagger timing peak - the "foreground" yield, and also to estimate the number of random events present within the prompt peak yield. Whenever possible, the cuts were determined using data from the C target because of the "clean" nature of the spectra (no correlated pair contamination - see

section 3.12), and then applied to the other targets. The absolute foreground and random yields were obtained from a replay of the *original* data tapes to ensure no π^+ events had been accidentally filtered out during the data reduction.

This absolute foreground yield was then corrected for the presence of randoms to determine the true or "correlated" yield. Because the air (N_2 and 0_2) in the room acted as a target, its contribution to the correlated yield was also removed. This corrected yield was calibrated and expressed as a function of π^+ energy at creation. The yields were divided by the detection efficiency, incident photon flux, target density, and detector solid angle. A π^+ energy bin width of 10 MeV was selected, and laboratory double differential cross sections were determined where possible. The double differential cross sections were integrated over π^+ energy to yield laboratory cross sections differential in solid angle. Certain of the target/angle combinations were corrected for correlated pair contamination; that is, e^+e^- pairs whose energy signature resembled that of a single π^+, and were recorded because of a random stop in the tagger focal plane within the prompt peak. In the case of H, the differential cross sections were also converted to the CM frame. Finally, the corrected differential cross sections were integrated over solid angle to determine the total photoproduction cross sections. This complicated procedure is presented pictorially in Figure 3.1.

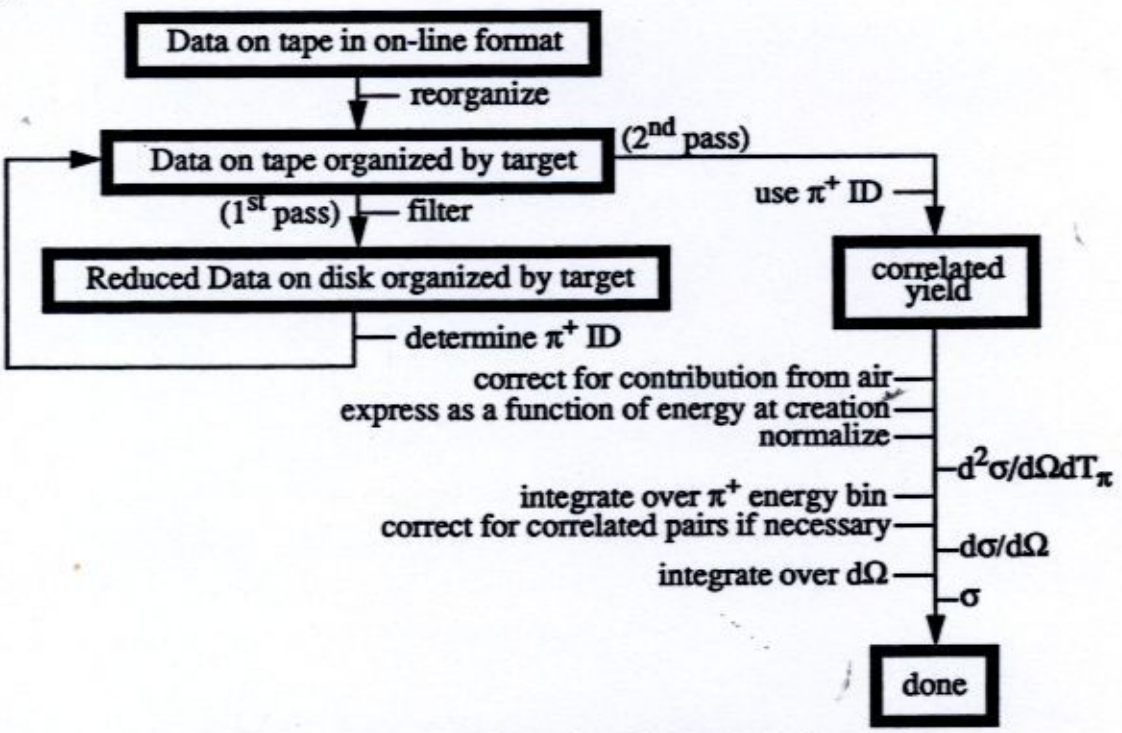

Figure 3.1: An Overview of the Analysis

3.2 Data Reduction

Because the hardware event trigger was designed to accept all charged particle events, it was necessary to take some steps to bring the π^+ events to the foreground before attempting to rigorously analyze the data. Figure 3.2 presents a schematic overview of the data reduction algorithm. Each box will subsequently be discussed in detail.

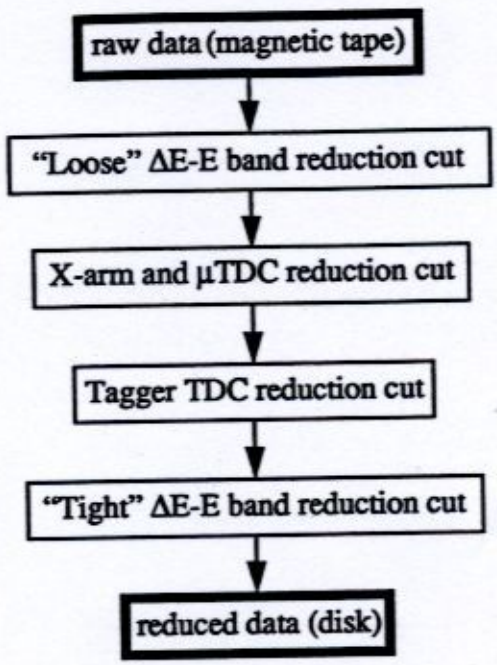

Figure 3.2: An Overview of the Data Reduction

The reduction procedure involved four steps. If a given event passed all four reduction conditions, it was labeled a *candidate* π^+ event, and written to hard disk for further analysis. If the event failed any one of the four reduction steps, it was simply discarded. Because of the much shorter replay time, the reduced data set was used to determine the π^+ identification algorithm. However, once this algorithm was finalized, the actual yields were extracted from the data tapes.

3.2.1 Loose ΔE-E Band Reduction Cut

The first cut involved the π^+ event band in the ΔE-E scatterplot. The cut was made close to the bottom of the proton band. Also, a cut was made on the maximum π^+ kinetic energy at 85 MeV. This energy was selected as it was 10 MeV above the most energetic π^+ which could be produced. The value of 85 MeV in ADC channels was crudely known at the time of data reduction due to preliminary calibration work performed on-line (see

section 3.8). Since reaction kinematics (see Appendix C) stipulated that no π^+ produced by a tagged photon had more than 85 MeV at its creation, this was safe. Note that all π^+'s, whether their decays were detected or not, passed this cut since the scatterplot looked solely at the prompt energy signal, and ignored completely all decay information. Figure 3.3 illustrates the first reduction cut.

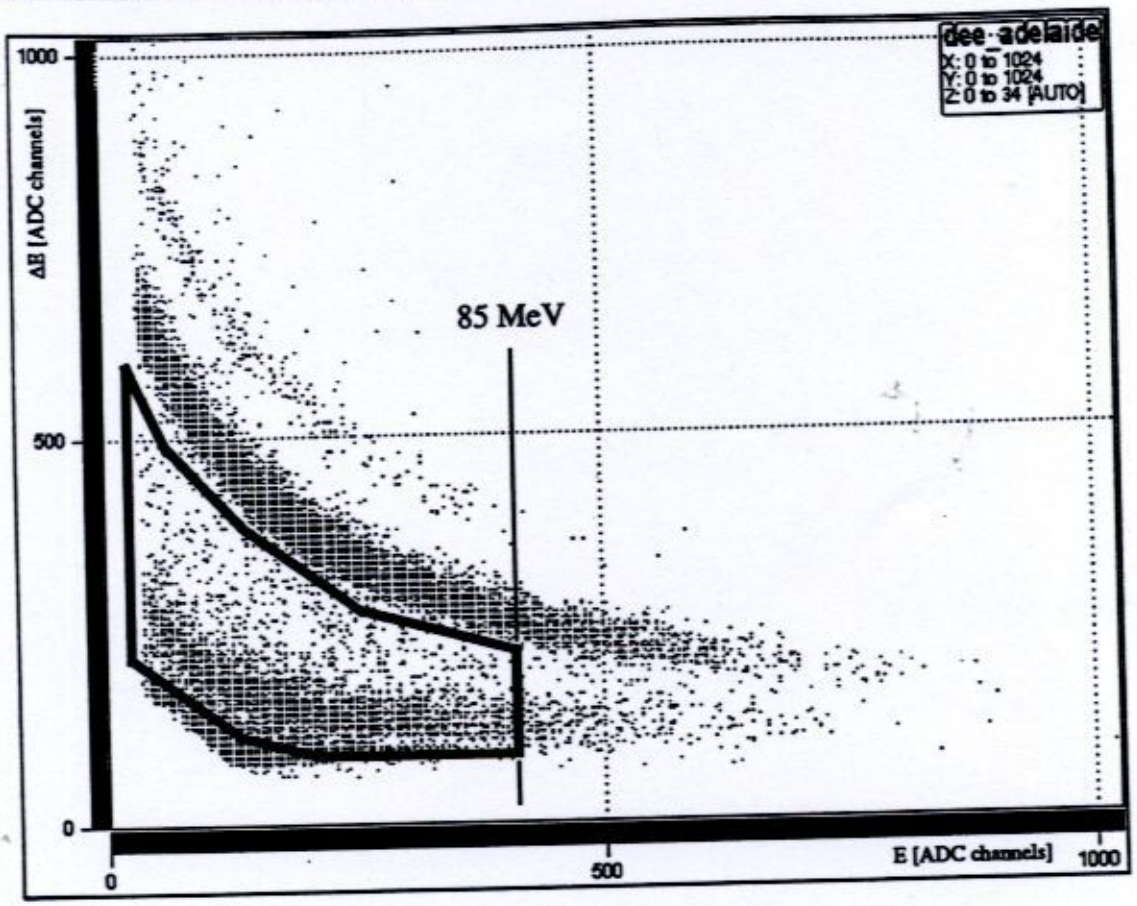

Figure 3.3: The First Reduction Cut

3.2.2 ΔE TDC, E TDC, and μTDC Reduction Cuts

The second cut was made on the X-arm TDCs. The X-arm TDC cut involved passing only the events which were within reasonable proximity of both the ΔE and E TDC stop spikes (recall Figure 2.17).

Examination of a sample of the data had demonstrated that all π^+ events which decayed to produce a stop in the μTDC also showed excess charge in the μADC, but all events which showed excess charge in the μADC did not necessarily stop the μTDC. The following Venn diagram illustrates this situation.

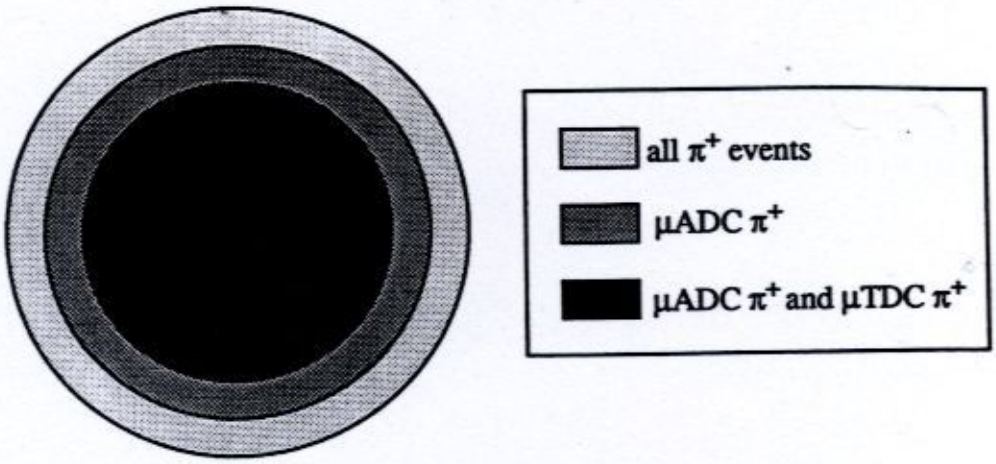

Figure 3.4: The π^+ Sample Space (Not to Scale)

Since the efficiency for the μTDC method of π^+ detection was known, while that for the μADC method of detection was not, it was decided to retain only those events which stopped the μTDC. Thus, if there was a stop in the μTDC for a given event, it was passed to the tagger TDC reduction cut. All other events were rejected.

3.2.3 Tagger TDC Reduction Cut

The reduction cuts already applied were associated with the detector telescopes. The third and perhaps most powerful cut involved the 16 tagger TDCs to determine if the event was associated with a tagged photon. Each of these TDCs demonstrated an event stop spike, but in slightly different positions in time. This was caused by channel-to-channel timing variations due to small differences in the lengths of the delay cables connecting the tagger channels to the TDCs. These differences were software corrected such that the stop spike occurred in exactly the same position for each tagger channel, and thus, all channels could be summed to produce a statistically well-defined stop spike. The energy deposited by the event in the E-detector was plotted against this corrected sum of the 16 tagger TDCs to yield an energy (T_π) vs. time-of-flight (TOF) plot. Note that because the tagger TDCs are started by the X-arm signal and stopped by the delayed tagger channel signal, the slower, less energetic particles with relatively long TOF actually stopped the TDCs sooner. This resulted in an almost vertical π^+ band, about which cuts were made.

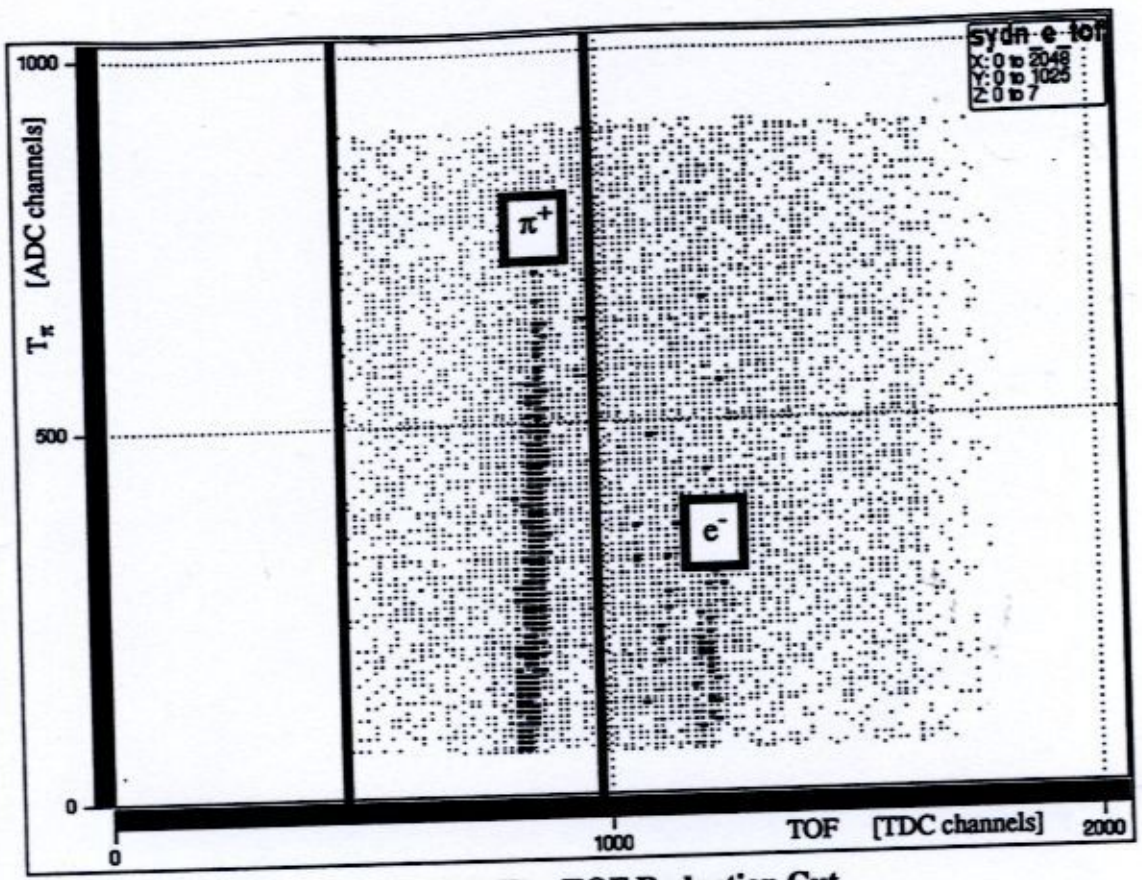

Figure 3.5: The TOF Reduction Cut

As expected, the π^+ band was in fact an arc, tailing toward the long TOF side of the tagger TDC axis as the energy of the π^+ decreased. Thus, relatively loose cuts were employed.

3.2.4 Tight ΔE-E Band Reduction Cut

The fourth reduction cut involved the reapplication of the criterion of the first cut. The second and third reduction cuts cleaned up the ΔE-E plots so much that the scatterplot reduction cuts could be tightened.

3.3 π^+ Identification

The reduced data set was used to determine the π^+ identification algorithm. The idea behind the π^+ identification software was to develop a single algorithm which would enable identification of π^+'s produced from any given target with only simple modifications to the kinematics cuts. Figure 3.6 outlines the algorithm adopted. Each of the reduction cuts are subsequently discussed in detail.

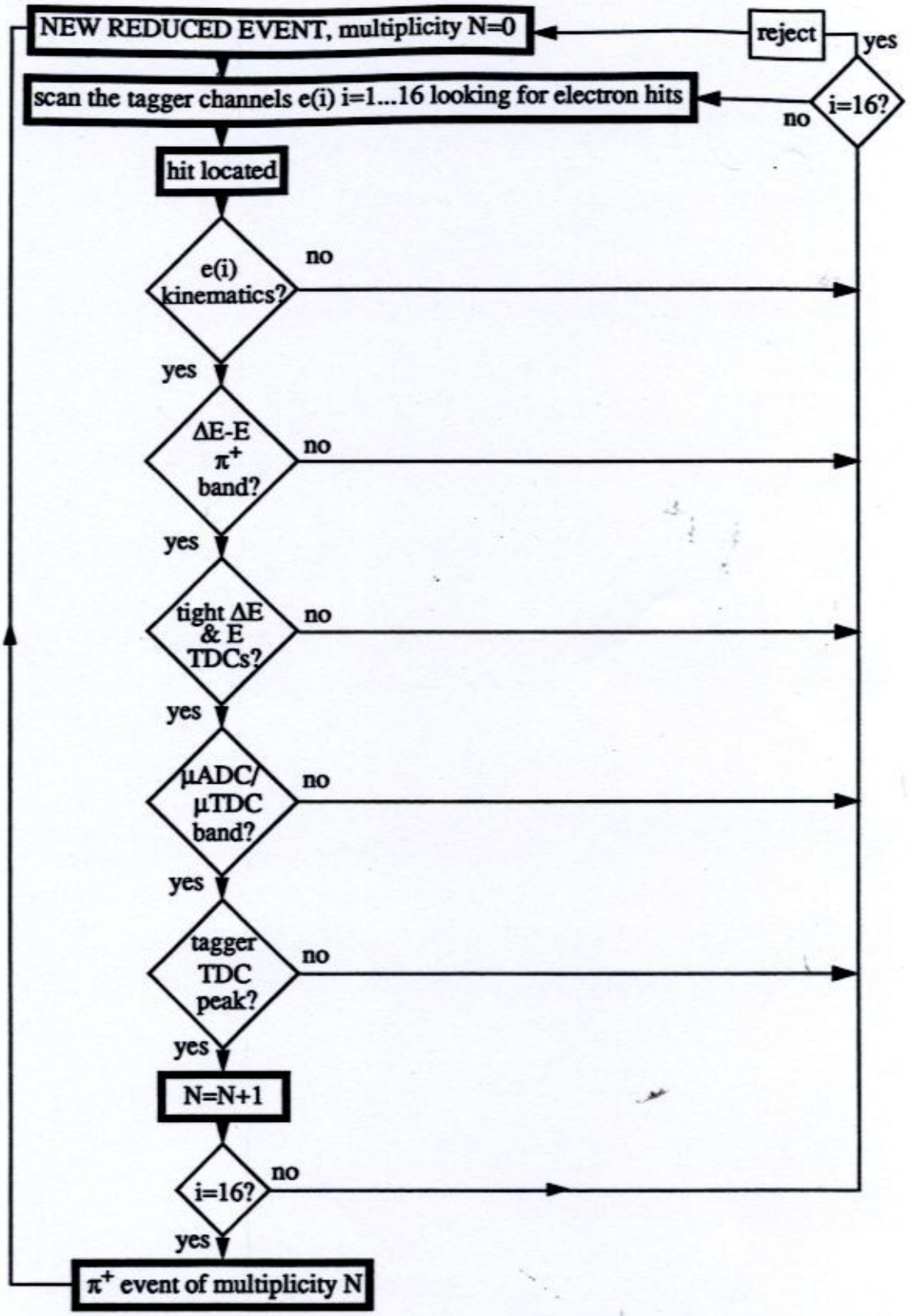

Figure 3.6: The π^+ Identification Algorithm

3.3.1 Kinematics

Kinematics constraints determine the maximum possible energy π^+ a given photon can produce. These constraints were used to cut on the data. The procedure for determining the kinematically allowed π^+ energies for each of the 16 tagger channels is presented in detail in Appendix C. A short outline of the procedure is presented here. The kinematics cuts used in this analysis corresponded to the elastic photoproduction of a π^+. For the purposes of these calculations, a two body final state was assumed, and further, no energy brought into the reaction by the photon was allowed to be carried off in the form of an excited recoil. Note that in an inclusive experiment, multi-body final states and excited recoils are perfectly valid, but correspond to much lower photoproduced π^+ energies. Further, while the calculations yield the energy of the π^+ at its point of creation in the target, it had to traverse several layers of matter between creation and detection. In traversing these layers, the π^+ lost energy. The cut values were thus expressed in terms of energy actually deposited in a given E-detector.

Additional correction was required to arrive at the cuts actually applied because of the finite energy resolution of the detector telescopes. A monoenergetic π^+ beam incident on a given detector appeared in the ADC spectrum not as a delta function located at the incident energy, but rather as a Gaussian distribution of π^+ energies centered about the monoenergetic (mean) value. Thus, the deposited π^+ energy value T_π determined by the kinematics and energy loss work was actually the mean value of this distribution. Further, the energy resolution $R(T_\pi)$ of the detector and thus the standard deviation σ of the distribution was known for all deposited π^+ energies (see Appendix D). Since 99% of all events in a Gaussian distribution fall within $\pm 3\sigma$ of the mean, each T_π cut value was incremented by 3σ in order to determine the maximum possible deposited π^+ energy cut that was actually applied, given by

$$T_\pi^{cut} = T_\pi + 3\sigma = T_\pi + 3 \cdot \frac{R(T_\pi)}{2.35} = T_\pi (1 + 1.28 \cdot R(T_\pi)) . \qquad (3.1)$$

Thus, any π^+ which deposited less energy in a given detector than the value so defined passed the kinematics cut.

For the photon energies of this experiment, the production of π^+ from the proton offered a two body final state with no possibility of exciting the recoil neutron. This allowed a second kinematics cut to be employed on the lowest energy π^+ corresponding to a given tagger channel. The procedure for determining this cut was identical to the one just outlined, save for the fact that the cut value T_π determined by the kinematics and energy loss work was also decremented by 3σ (change the "+" sign to a "-" sign in equation 3.1) in order to obtain the lower energy kinematics cut.

3.3.2 ΔE-E π^+ Band

A π^+ region in the ΔE-E scatterplot smaller than that employed for the purposes of data reduction was defined. Distinct separation existed between the π^+'s and the protons which were deliberately allowed through the loose reduction scatterplot cut.

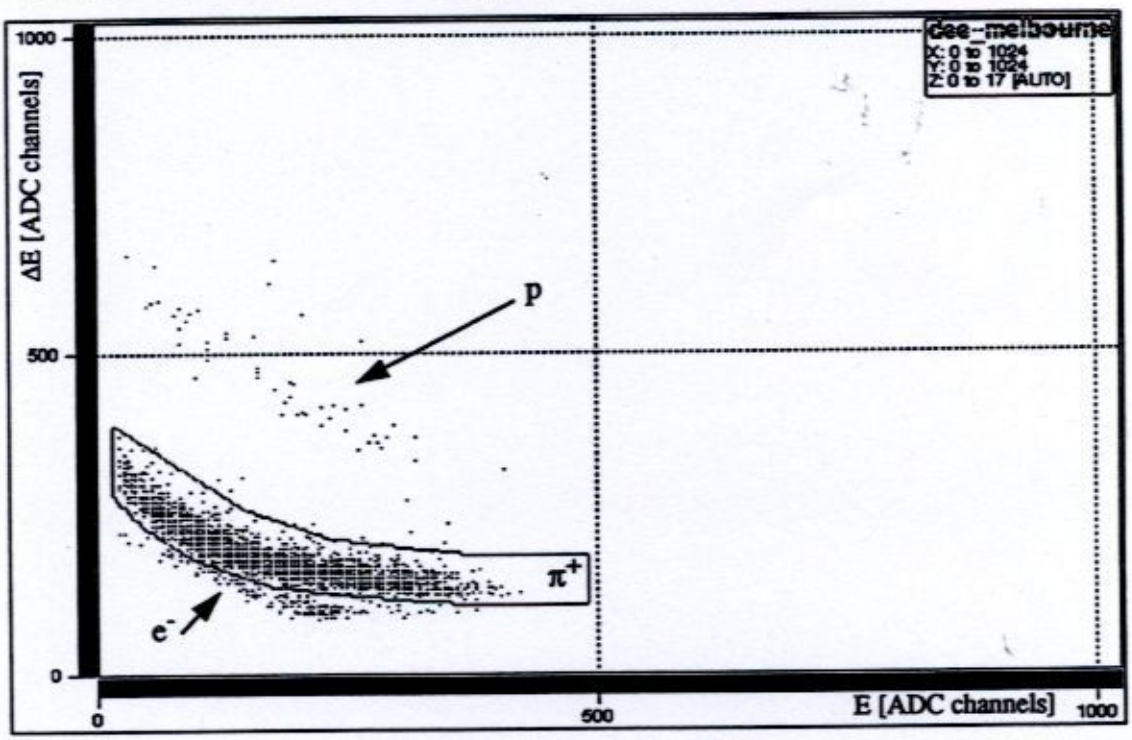

Figure 3.7: The ΔE-E π^+ Band

This signaled an absence of pileup in the ΔE detectors, which was a realistic on-line fear. Further, since the E-detectors were subjected to significantly lower singles rates, it was concluded that E-detector pileup was also not a problem.

3.3.3 Tight ΔE TDCs & E TDCs

The cuts on the ΔE and E TDCs were also tightened.

3.3.4 μADC/μTDC Band

Having passed the above cuts, all of which dealt exclusively with the prompt π^+ pulses, the behaviour of the decay μ^+ pulse was checked by plotting the excess charge in the μADC against the stop in the μTDC. While stops in the μTDC proved relatively simple to obtain, extraction of useful information from the delay gate ADC was a somewhat involved procedure. The problem was due to ringing of the E-pulses which the electronics interpreted as π^+ decay. This effect is illustrated in Figure 3.8, where the stop in the μTDC is definitely energy dependent. This effect becomes even clearer in the μTDC plot shown in Figure 3.9.

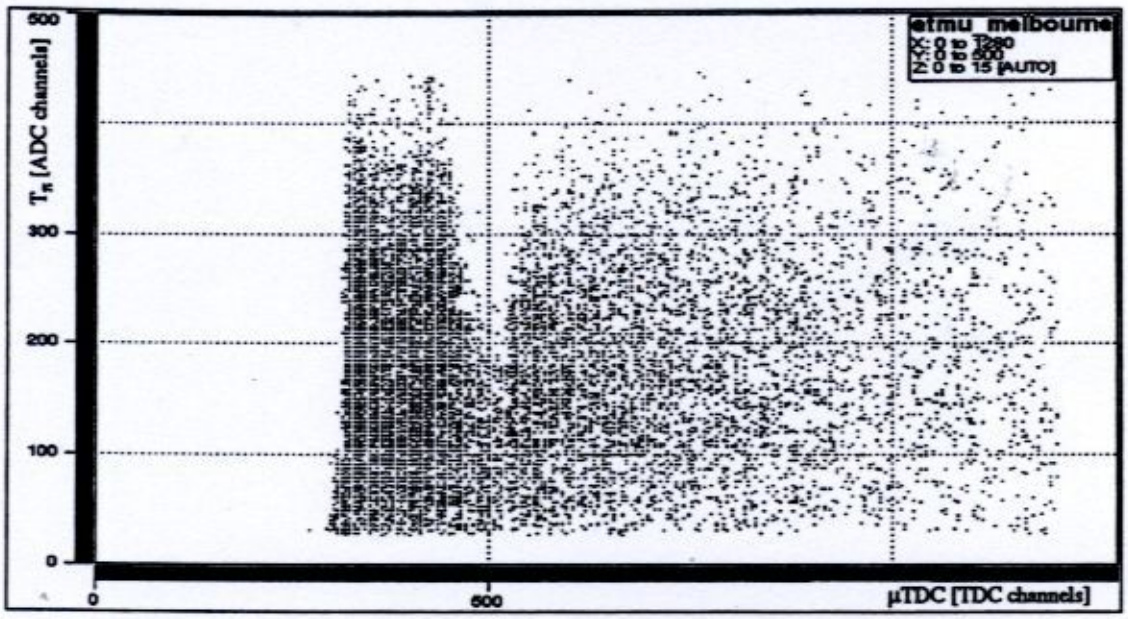

Figure 3.8: The Energy Dependence of the Ringing in the μTDC Stop

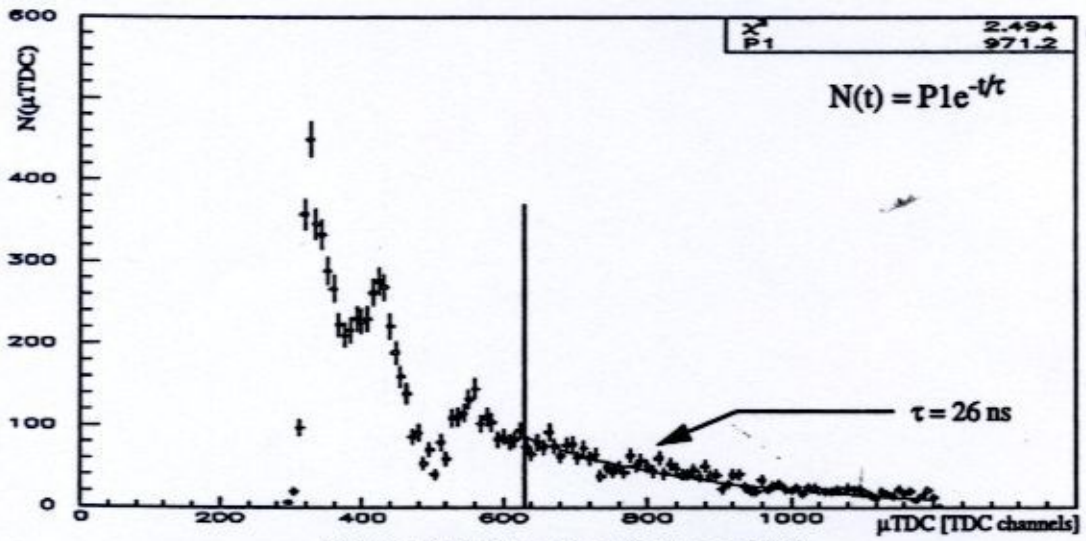

Figure 3.9: Structure in the μTDC

Thus, it was necessary to determine the range of channels in the μTDC over which the electronics were behaving as expected. Figure 3.9 shows a typical μTDC spectrum. It was determined that the time constant of the decay did not differ appreciably from the expected value of 26 ns over the region from channel 630 to channel 1200. Thus, a cut was placed at channel 630 in the μTDC spectrum. While this affected the statistical accuracy of the experiment, the trade-off between statistics and absolute cross sections was deemed worthwhile.

The first step in the extraction of useful information from the delay gate ADC was to plot the signal in the delay ADC gate against that in the prompt ADC gate. It was expected that a μ^+ band would be present separated from the ordinary by 4.12 MeV, the decay energy. That is, an event for which no decay was present would be characterized by a constant value in the delay gate corresponding to the ADC integration of the baseline offset from zero, while an event for which a decay was present would be characterized by a constant value in the delay gate corresponding to the ADC integration of the baseline offset from zero plus the constant decay energy. Thus, the two event types were expected to differ in the delay gate by the constant 4.12 MeV.

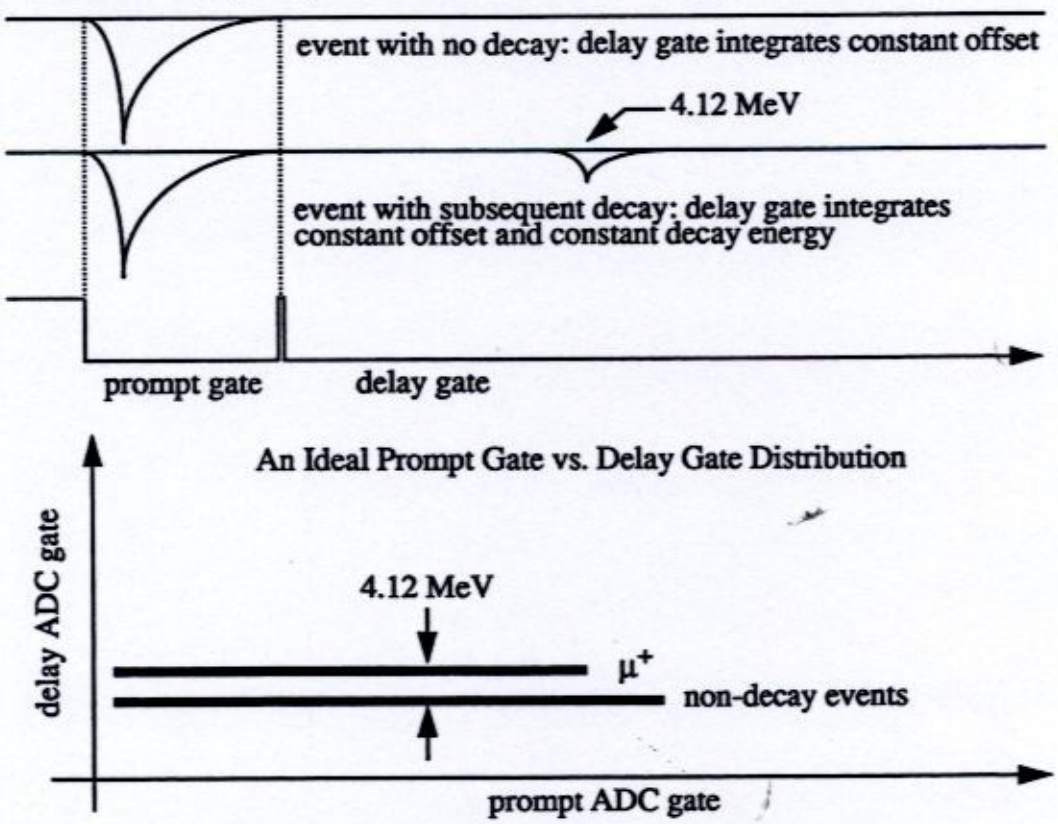

Figure 3.9: The Delay Gates

It seemed that a cut on the μ^+ band would be a straight forward way to use the constant decay energy to identify π^+ events. However, as it turned out, this was not the case.

Figure 3.10 shows an actual distribution of signal in the prompt gate plotted against signal in the delay gate. It is readily apparent that the expected separation between the μ^+ and non-decay events was not as dramatic as expected. Further, this figure shows only a very small portion of the data. When the sum total of all the data was viewed, the separation between the two bands vanished. It was also apparent that a definite slope existed, as evidenced by the non-zero value of the a1 coefficient.

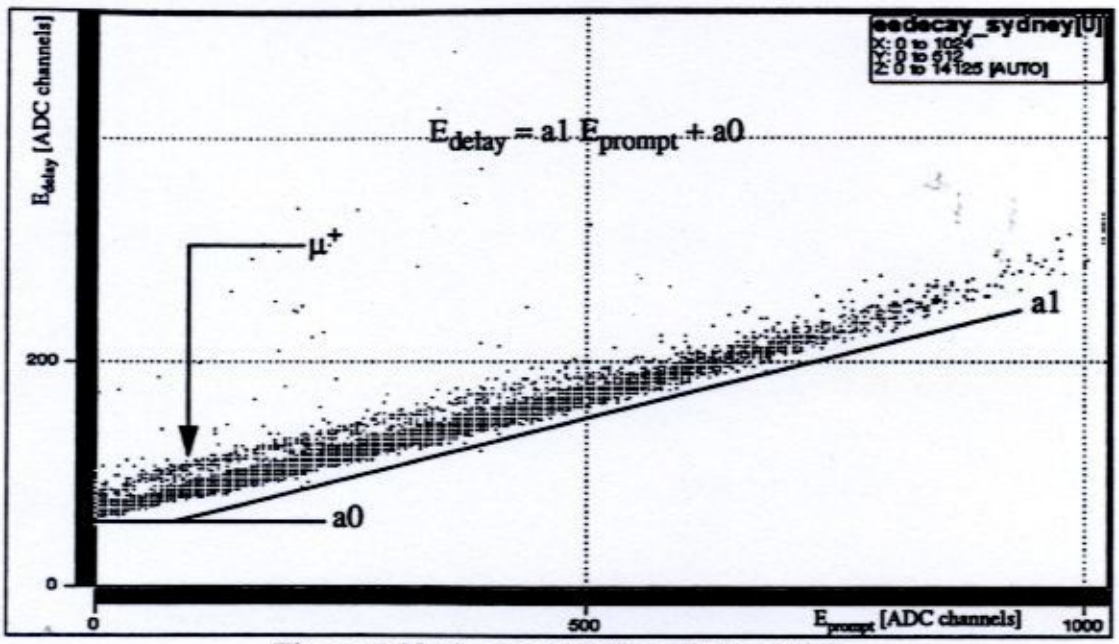

Figure 3.10: Prompt ADC vs. Delay ADC

The high density sloped region lying below the μ^+ band in Figure 3.10 represented energetic events whose baseline width was greater than that of the prompt gate. In fact, the baseline width was proportional to the energy of the event. Thus, charge spilled into the delay gate in a linear fashion producing the non-zero slope where a flat band was expected. The behaviour of the above plot was investigated on a run-by-run basis to optimize the separation between the μ^+ and ordinary bands. This involved locating the peak of the high density region as a function of delay ADC signal and prompt ADC signal and fitting these coordinates with a line to look for variations in the slope "a1" and offset "a0" coefficients, given by

$$\text{delay adc} = \text{a1} \cdot (\text{prompt adc}) + \text{a0}. \qquad (3.2)$$

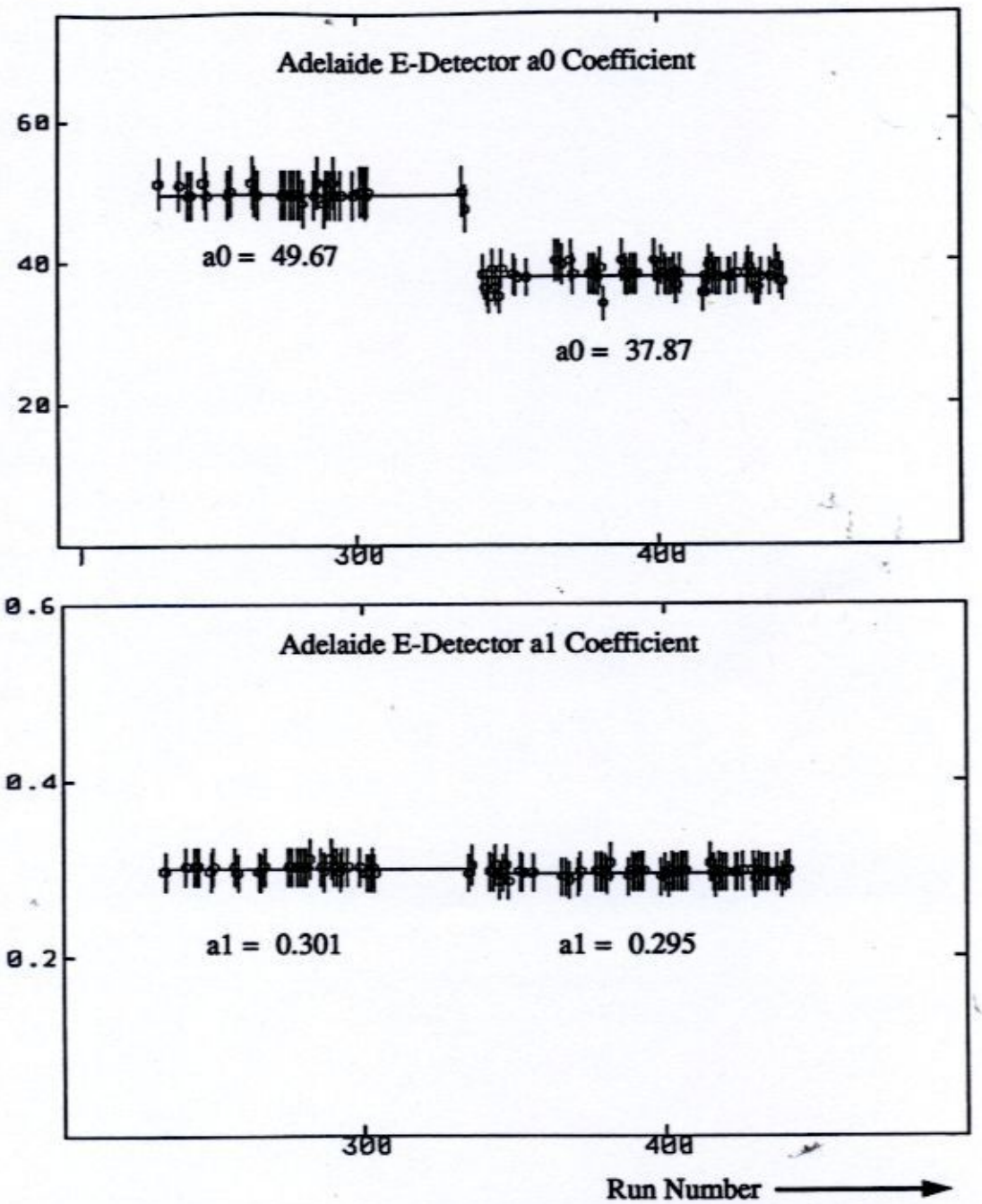

Figure 3.11: Trends in the Delay ADC Spectrum a0 and a1 Coefficients

The gap in the above plots spanning runs 300 to 325 represents the 6 day preliminary analysis shutdown and the test runs associated with restarting the experiment. Trends in the coefficients were apparent. While the slope of the line defined by the peaks in the high density region remained basically the same over the entire experiment, the offset did not.

The large step in the a0 coefficients represented a baseline shift in the electronics. A 10 ADC channel shift corresponded to roughly 2 MeV (see section 3.8), basically half of the 4.12 MeV decay energy. Knowledge of the trend in a0 and a1 allowed for software compensation for the shift.

The shift-corrected high density region was then rotated such that it was parallel to the E_{prompt} axis and projected onto a new axis called the μADC axis using the a0 and a1 coefficients and equation 3.3

$$\mu ADC = (\text{delay adc} - a1 \cdot \text{prompt adc}) + \Delta. \tag{3.3}$$

"Δ" was simply the difference between any given offset a0, and a standardized offset for all runs. The μADC axis represented μ^+ decay energy. Thus, the projected histogram was expected and determined to be Gaussian in nature, centered about the 4.12 MeV μ^+ afterpulse.

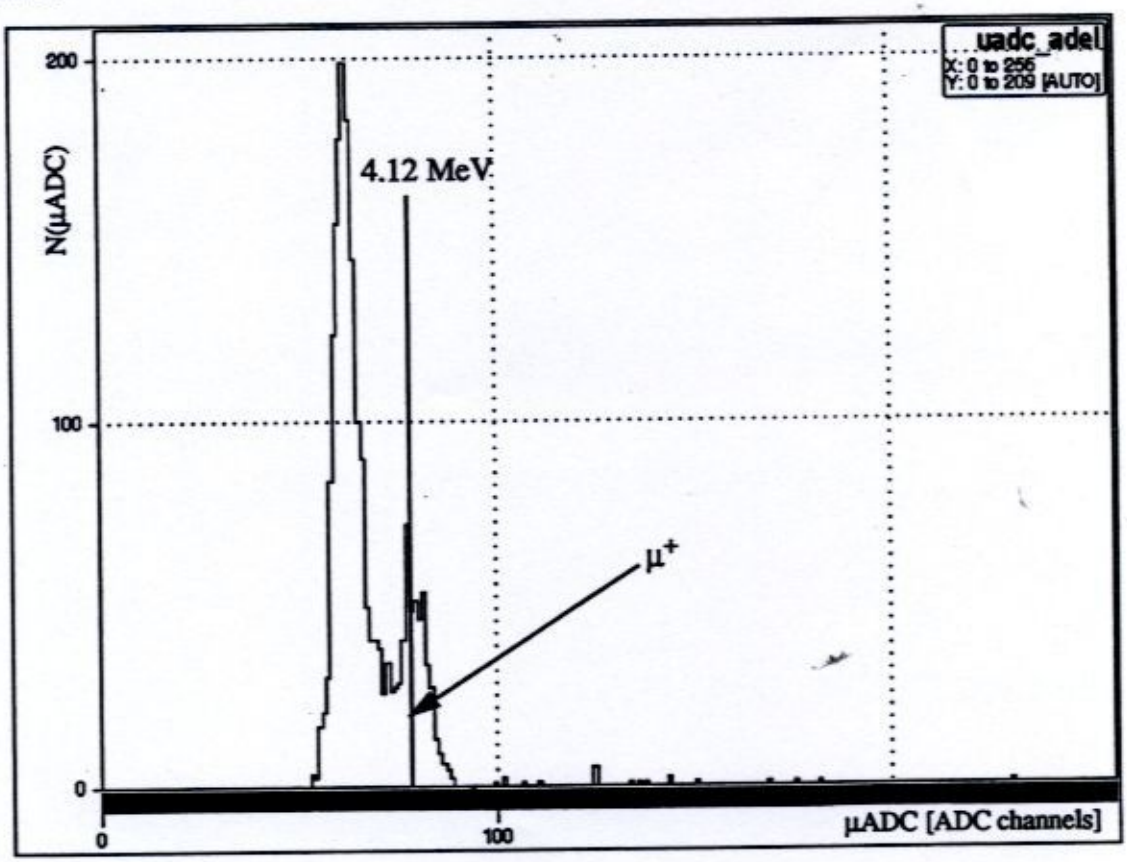

Figure 3.12: A Typical μADC Spectrum

However, a cut placed on the μ^+ peak was not desirable, since either some of the events would be rejected, or too much background would be passed through. Instead, this variable was plotted against the stop in the μTDC in order to define a single scatterplot which encompassed all the decay pulse information.

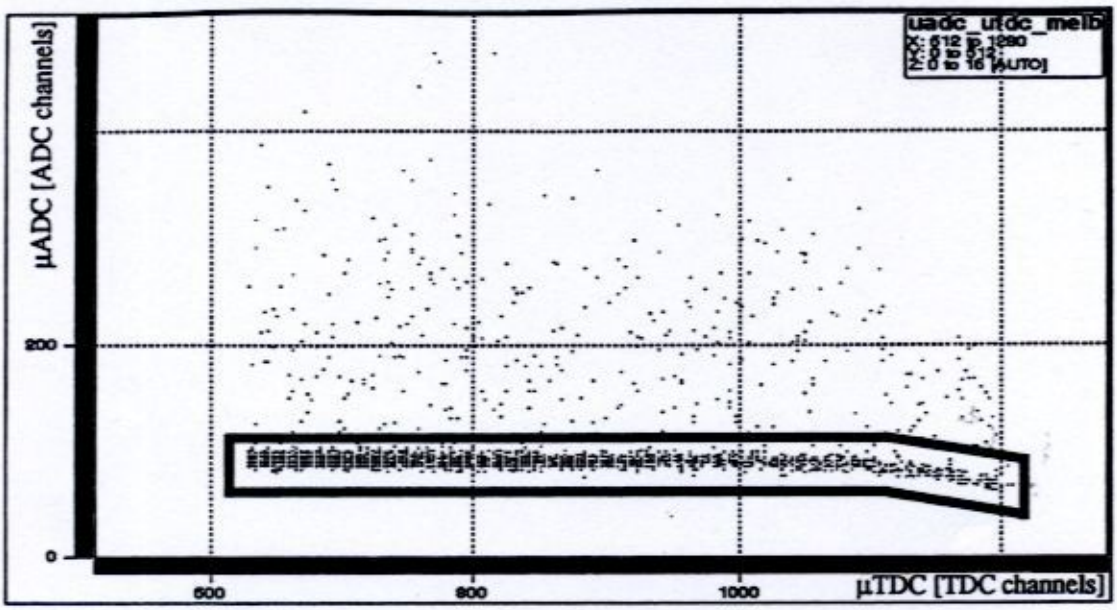

Figure 3.13: μADC versus μTDC

Figure 3.13 is such a plot. Note that for clarity, a large portion of the uninteresting events present in Figure 3.12 have been removed using the other cuts. The dark band represents events which had a decay pulse consistent with that expected for the μ^+. The other events, which corresponded to either accidentals or π^+ which decayed to μ^+ while still in flight, were discarded by defining the region indicated. The number of π^+ so discarded was compensated for in the detector efficiency calculation. The dogleg in the high density distribution was due to the fact that as the time the π^+ took to decay increased, the μ^+ pulse came dangerously close to the end of the delay gate. In fact, some of the μ^+ pulses were so close to the end of this gate, that portions of them "leaked" out, and thus, the entire pulse was not integrated.

3.3.5 Tagger TDC Peak

The final cut imposed on a given event was to check whether or not it fell within the prompt timing peak of the tagger TDCs. Recall from the tagger TDC reduction cut that an arc was observed in the π^+ E-ADC versus tagger TDC stop scatterplot. Before a cut was

placed on the tagger TDC spectrum, the twist was straightened using software by fitting a polynomial to the peak of the distribution. Thus, tighter cuts were employed in the projected histogram to rigorously extract the π^+ events.

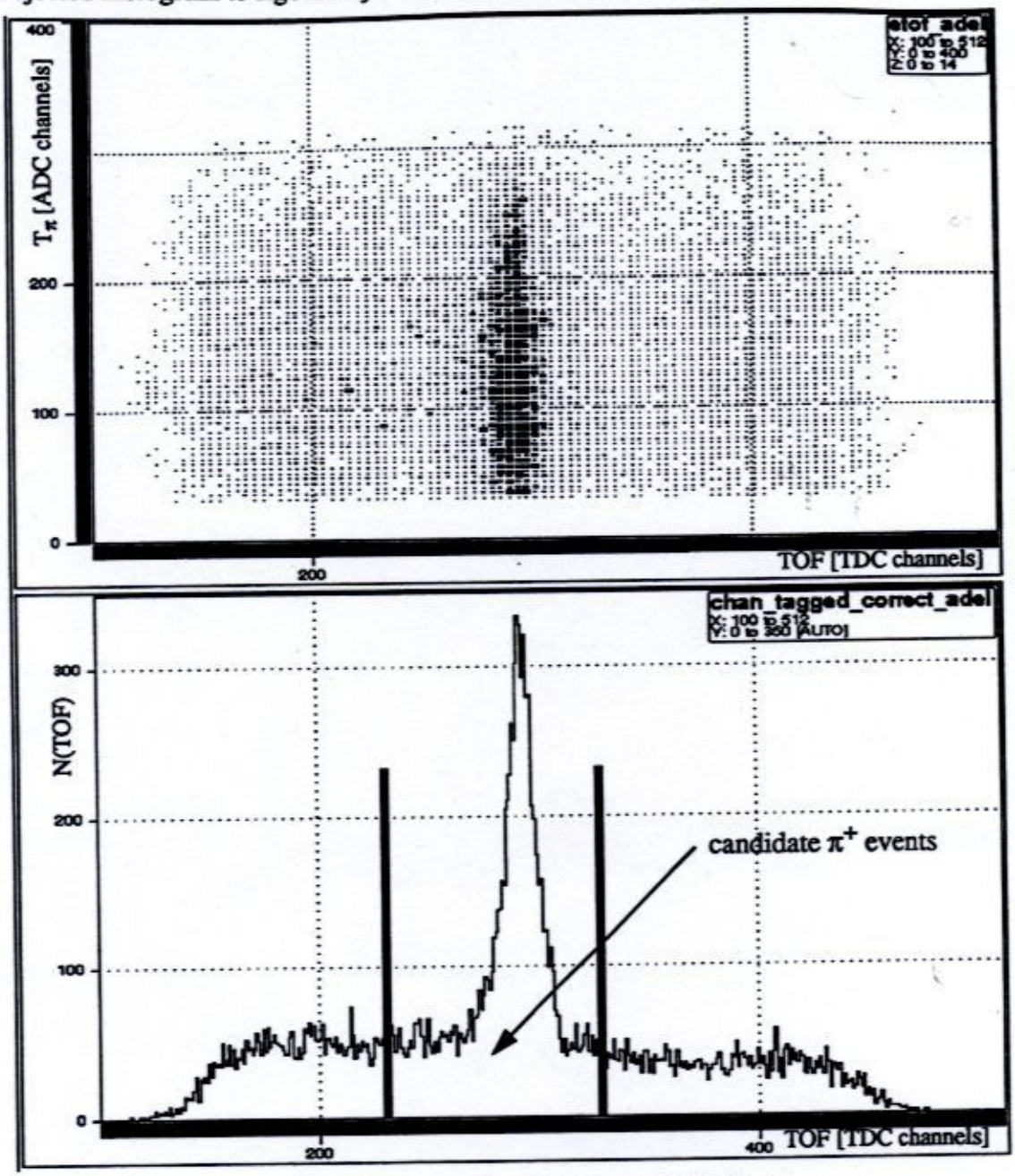

Figure 3.14: The Corrected Tagger TOF Peak

The cuts employed are shown above. They were chosen by assuming the TOF distribution to be Gaussian and determining the +/-3σ values, and then loosening somewhat. Note that the cuts are slightly skewed (not symmetrical about the peak) to compensate for any π^+ in the TOF arc which were not correctly straightened. While it was desirable to

make this window relatively tight, it was not critical since any random events which were allowed through this cut were compensated for by the uncorrelated correction to the foreground data (see section 3.6.1).

3.4 π^+ Identification Validation

Having completed the π^+ identification, it was prudent to check on the effectiveness of the algorithm.

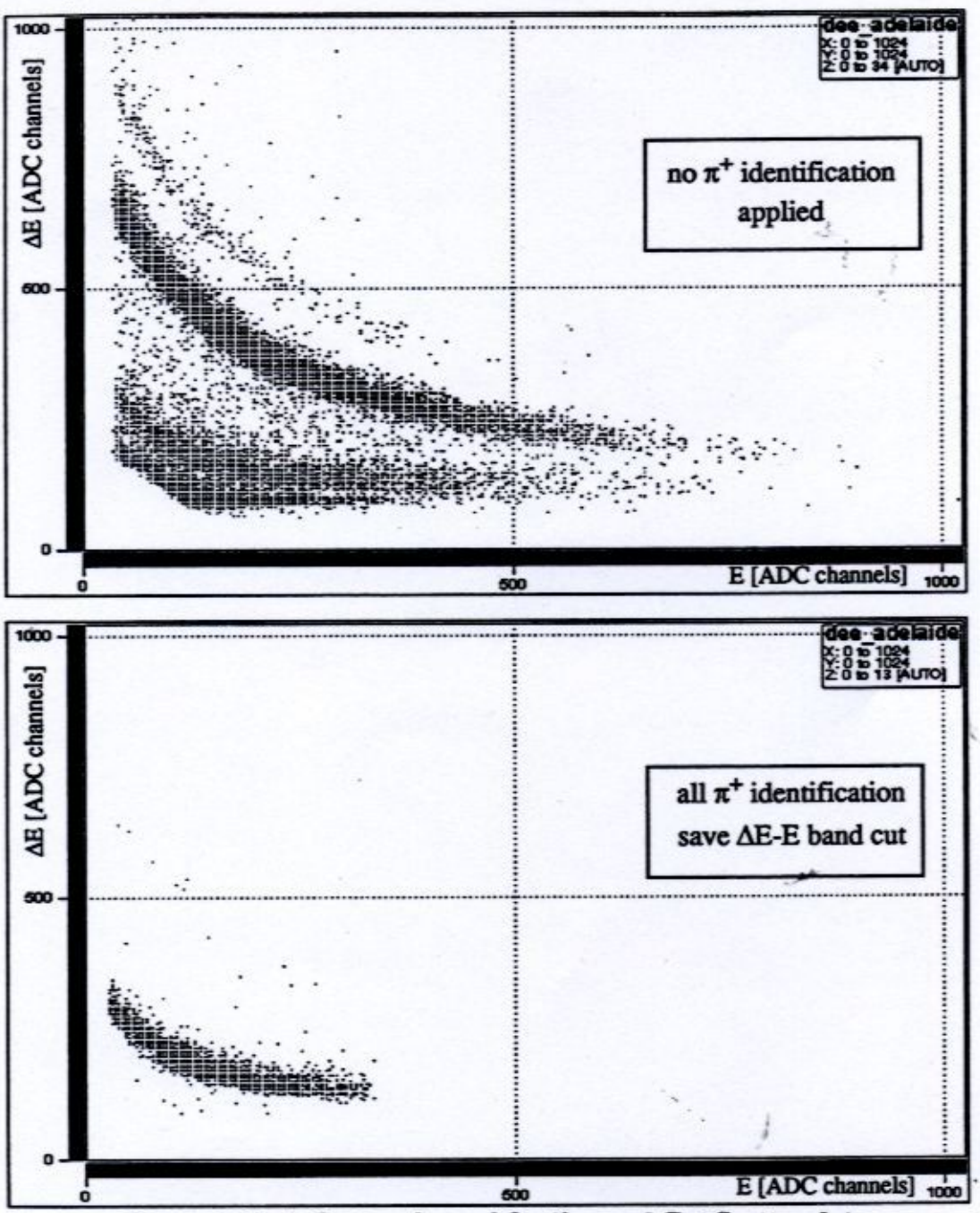

Figure 3.15: A Comparison of On-line and Cut Scatterplots

Figure 3.15 shows two scatterplots obtained from the Ca target. The top scatterplot is of the on-line variety, while the bottom scatterplot demonstrates the effectiveness of the previously discussed cuts. Note that no ΔE-E π^+ band cut is in place on the lower scatterplot, so that a few electron and proton events are present. The overall π^+ identification was obviously excellent; however, as the targets got heavier ($Z \geq 20$), pair contamination of the π^+ band for the forward angle detectors became a problem, as seen below.

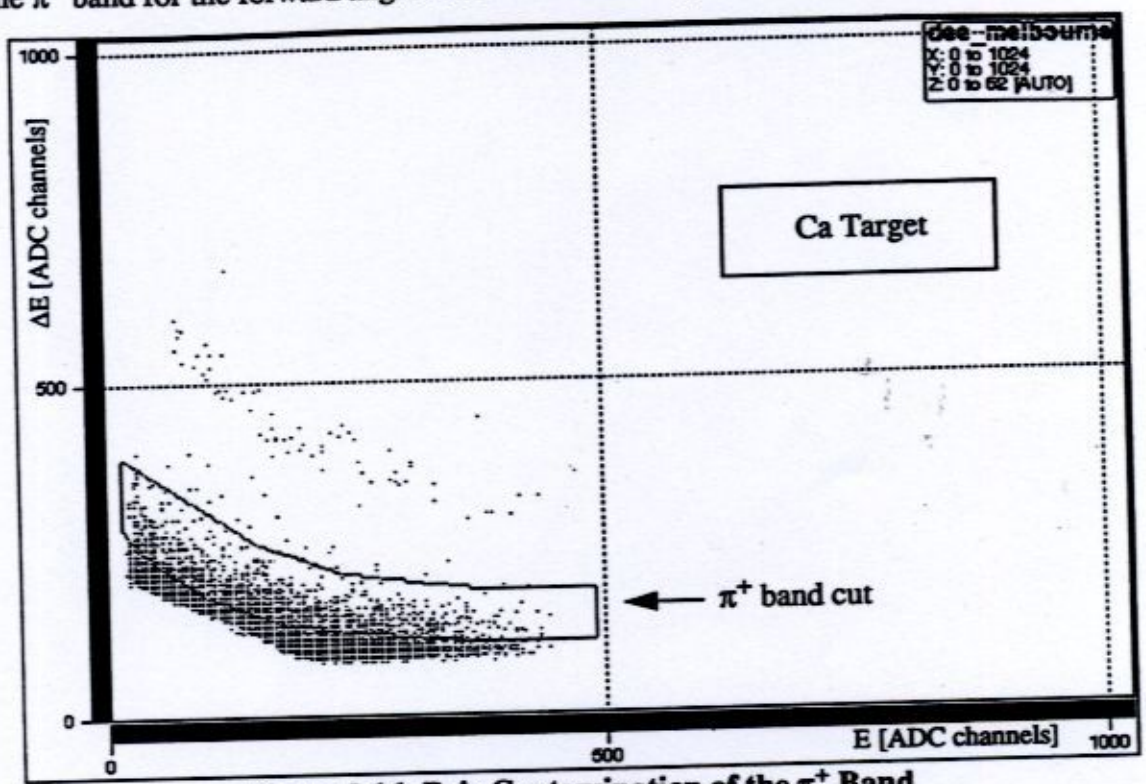

Figure 3.16: Pair Contamination of the π^+ Band

A correction was applied to the data to account for this phenomenon (see section 3.12).

3.5 Event Multiplicity

A given X-arm event was either identified as a candidate π^+ or rejected completely. This procedure was repeated for each electron hit in the tagger focal plane. The number of hits in the focal plane corresponding to a single X-arm event which was identified as a π^+ was the event multiplicity, "N". Thus, in principle, a single X-arm event could correspond to 16 different tagged photons, although in practice, there were an insignificant number of events of multiplicity greater than 3. The remaining multiples were accounted for in the random subtraction (see section 3.6.1). Figure 3.17 illustrates the multiplicity spectrum both before and after π^+ identification was applied.

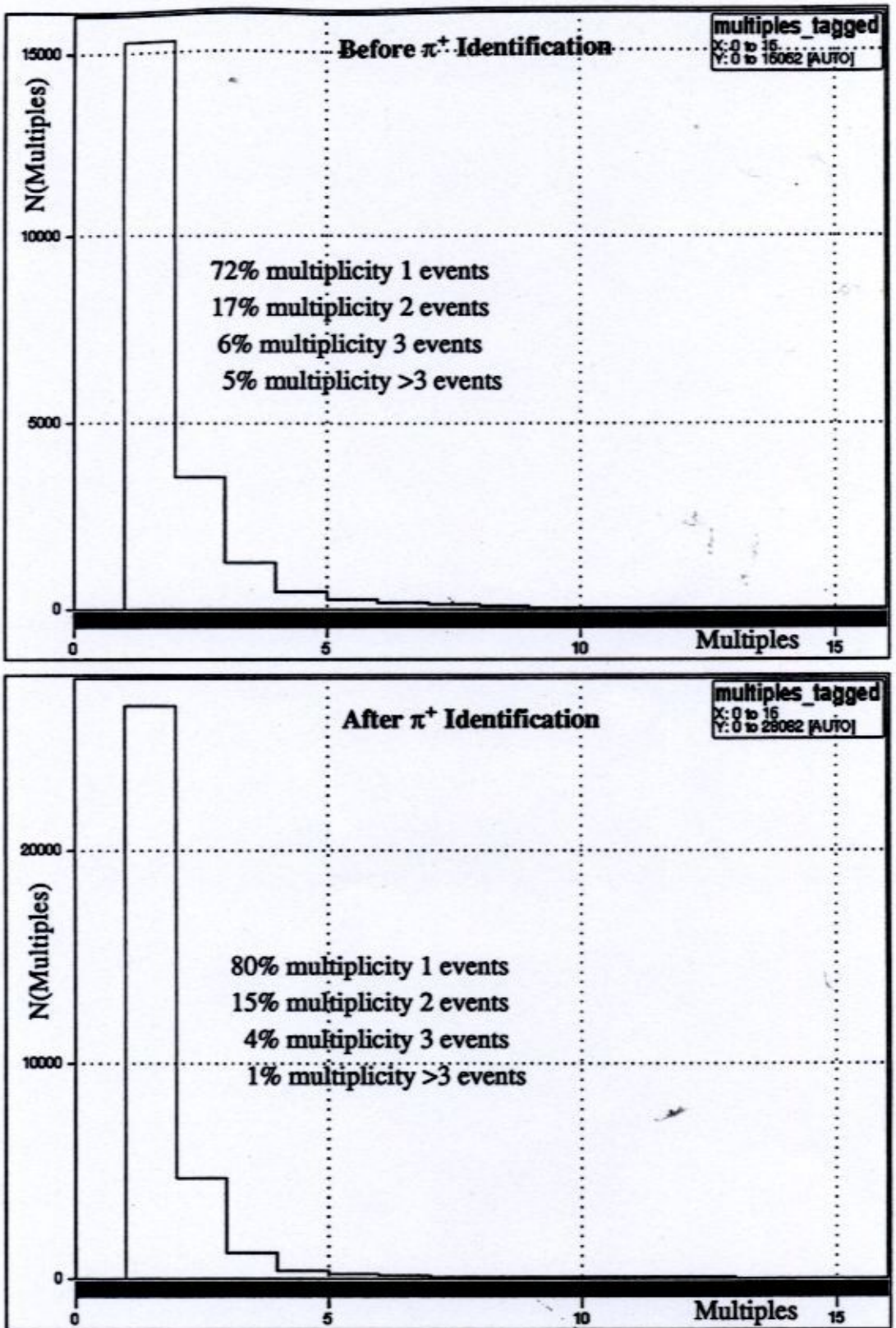

Figure 3.17: Multiplicity Distributions Before and After π^+ Identification

3.6 Determination of the True Correlated Yield

To obtain the true correlated yield used to calculate the cross sections for a given target, it was necessary to correct the foreground π^+ yield extracted from the prompt peak for both random (uncorrelated) events and correlated events due to the air in the room. Figure 3.18 illustrates the method by which the true correlated yield was determined.

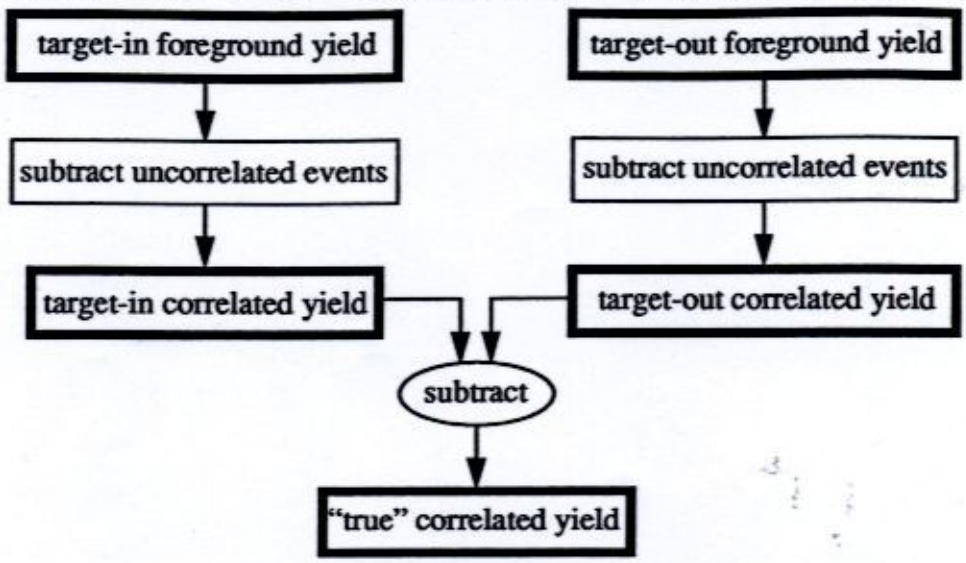

Figure 3.18: Extraction of the True Yield

3.6.1 Subtraction of Uncorrelated (Random) Events

For convenience, Figure 2.8 is reproduced below as Figure 3.19.

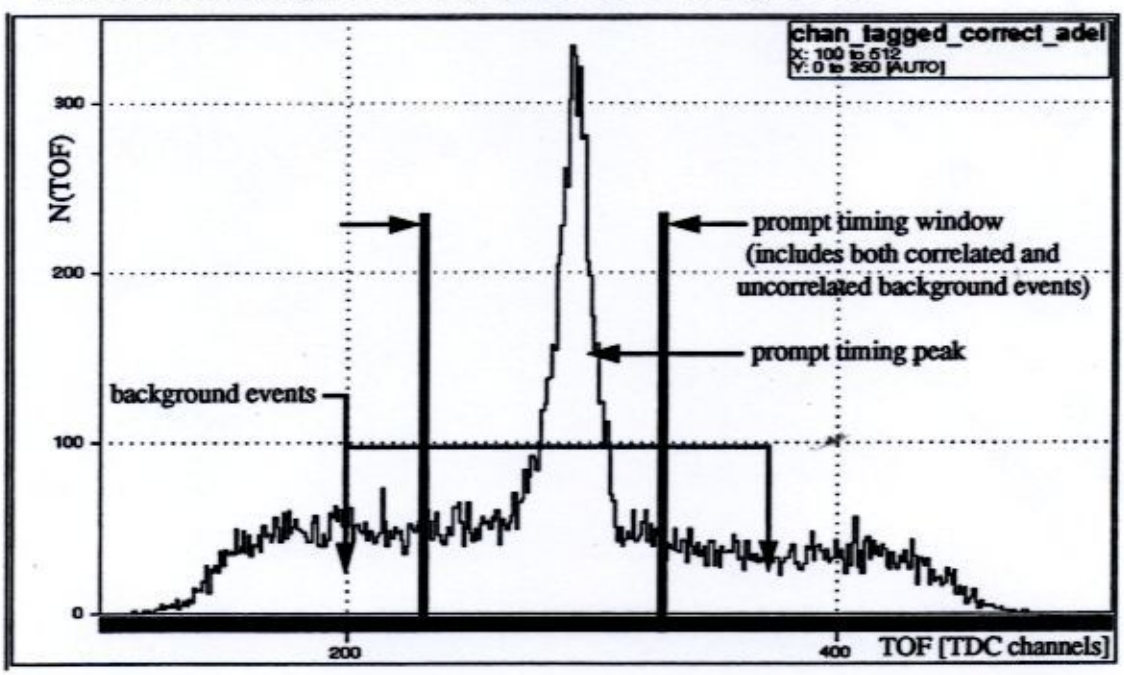

Figure 3.19: The Corrected Tagger TOF Peak

Events within the prompt timing window (which served to define the prompt timing peak) corresponded to π^+ events in the X-arm, and included both correlated (true tagged) and uncorrelated (random) events. Those which lay outside the prompt timing peak corresponded entirely to random hits in the tagger focal plane, and were completely uncorrelated events. Because uncorrelated events were also present within the prompt timing window, events of multiplicity greater than one were necessarily present in the data set subsequent to the application of the prompt timing window cut. It was important to account for uncorrelated events which passed through the prompt timing window cut in order to obtain true correlated events only. This procedure is known as "random event subtraction".

Figure 3.20 shows the same data as Figure 3.19, but now demonstrates the linearity of the random event distribution across the background region. To determine the parameters of the background, equal regions on either side away from the prompt peak were considered. A linear distribution was important since it illustrated the events were truly random. The background region of the TDC spectrum was then gated on, with two caveats: the background gates were symmetric about the prompt timing window (even if the prompt timing window was not symmetric about the prompt timing peak), and were made as wide as possible.

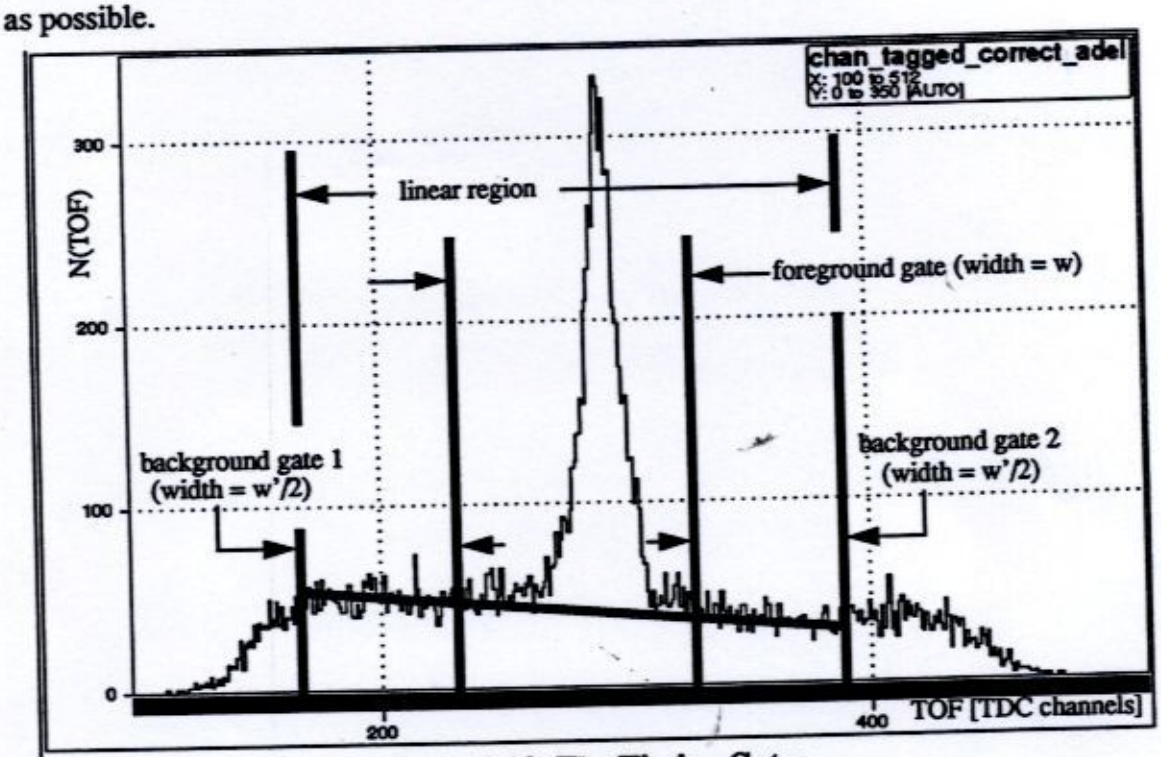

Figure 3.20: The Timing Gates

In order to obtain an estimate of the true, correlated number of π^+ events per ADC channel, the yield due to the random background was separated from that due to the foreground. Two independent sets of spectra were thus accumulated, both of which were subjected to all the cuts defined in section 3.3. The difference between these two sets of spectra was the tagger timing gate: one was incremented only for uncorrelated background events - that is, events which fell within either of the background timing gates; while the other was incremented for both correlated and uncorrelated foreground events - those which fell within the prompt timing window. Because the background distribution was linear over the region of the background and foreground gates, and because the background gate was symmetric about the foreground gate, the two yields were related by

$$N(ADC)^{\text{correlated}} = N(ADC)^{\text{foreground}} - R_w \cdot N(ADC)^{\text{background}}, \qquad (3.4)$$

where "R_w" was the ratio of the width in time of the foreground gate to the sum of the widths of the two background gates ($R_w = w/w'$). $N(ADC)^{\text{correlated}}$ defined above represented the correlated yield in a given ADC channel due to both the target and its environment (the air in the room).

3.6.2 Background Subtraction

Two distinctly different types of background subtraction were performed. For the four production targets, room background was removed. For the calibration target CH_2, the background which was removed included both room background and background due to the C content of the target. The following two sections describe the procedure.

Production Targets

The correlated yield as determined in section 3.6.1 was corrected for the contribution of the experiment environment; that is, any additional correlated π^+ yield due to the 0_2 and N_2 in the air of the experimental hall or the Al of the target ladder was accounted for. This was done by accumulating correlated target-out yields per ADC channel treating these data as if they had been taken from one of the production targets in order to match the kinematics cuts. These yields were then subtracted from the correlated target-in yields, using

$$N(ADC) = N(ADC)^{\text{correlated}}_{\text{target-in}} - R_\gamma \cdot N(ADC)^{\text{correlated}}_{\text{target-out}}. \qquad (3.5)$$

"R_γ" was the ratio of target-in photon flux to target-out photon flux. The determination of these fluxes and the choice of R_γ is outlined in section 3.13.1. N(ADC) defined above represented the true correlated π^+ yield per ADC channel for most of the target/angle combinations. However, some further corrections were applied in certain cases to compensate for correlated pairs which were indistinguishable from π^+ (see section 3.12).

CH_2

H spectra from CH_2 were interesting both for the purposes of calibrating the detector telescopes for energy, and for determining the elementary π^+ photoproduction cross section. This type of target allowed two possible π^+ production reactions: $C(\gamma,\pi^+)$ where the final state may have involved three or more particles as well as an excited recoil, and $p(\gamma,\pi^+)n$ where the final state was two body definite, and no energy was lost to exciting the recoil neutron. In the latter reaction in the CM frame, all the energy of the incident photon above the π^+ production threshold must have appeared as π^+ kinetic energy. This transformed to a unique energy in the lab. Thus, π^+ energy spectra from the CH_2 target displayed a peak due to photoproduction off the proton, and a smear due to QF photoproduction off C. The peaks were used to calibrate the E-detectors for energy.

Since it was just π^+ produced from the H component of the CH_2 target which was of interest, any π^+ produced from the C nucleus were also considered background for the purposes of the CH_2 target. The C production target was used to determine the correlated background C contribution to the CH_2 π^+ yield, with careful attention being paid to matching the relative C densities of the two targets, as well as the relative photon flux. This yield was then subtracted from the correlated CH_2 yield using

$$N(ADC)_{H_2} = N(ADC)_{CH_2}^{correlated} - R \cdot N(ADC)_{C}^{correlated}, \qquad (3.6)$$

where

$$R = \frac{N_\gamma^{CH_2}}{N_\gamma^{C}} \cdot \frac{\rho_{C\ in\ CH_2}}{\rho_C}. \qquad (3.7)$$

"R" was just the product of the ratio of the photon fluxes and the ratio of the number of C nuclei in the two targets. Any yield contributed by the experiment environment was automatically removed using this method, since air and target ladder contributions were present in both the C and CH_2 yields. Figure 3.21 shows a typical CH_2 spectrum with the C content removed. The kinematically expected peak is clearly seen.

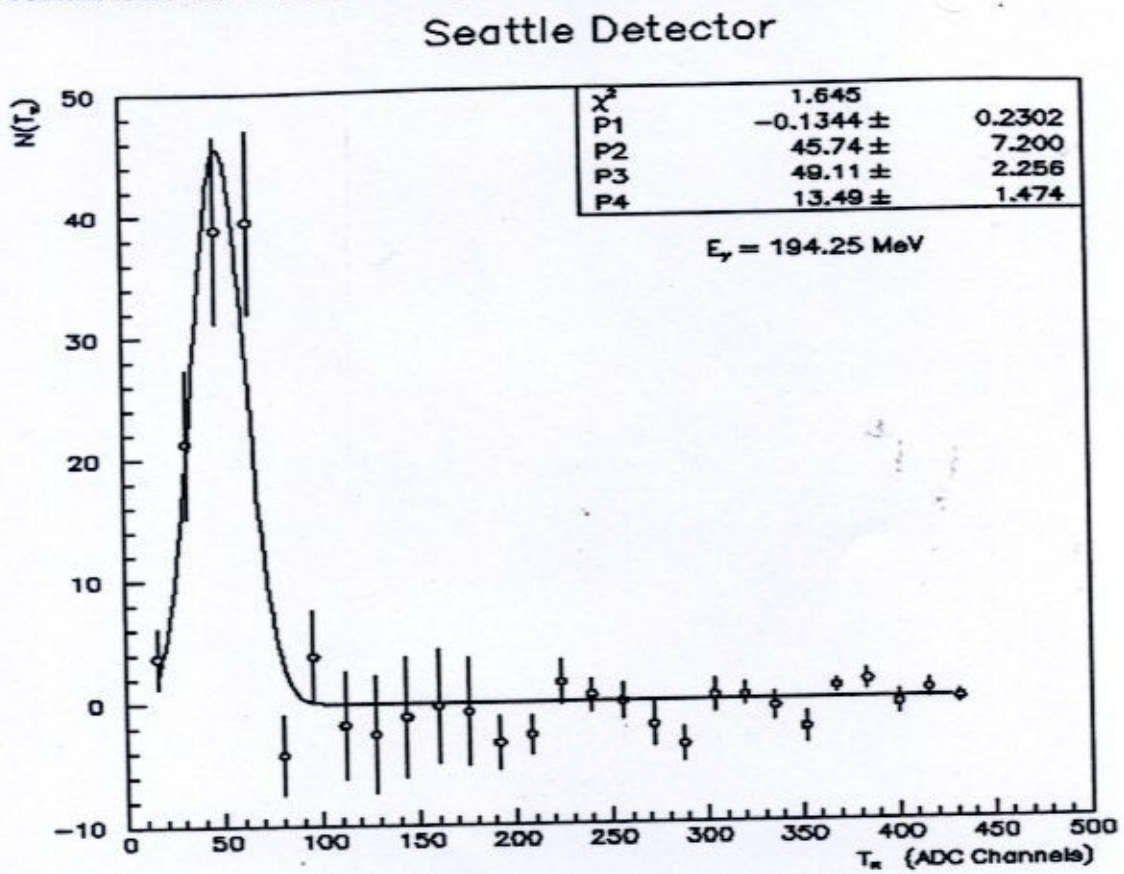

Figure 3.21: A CH_2 π^+ Energy Spectrum with the C Removed

3.7 Further π^+ Identification Validation

Further π^+ identification validation was accomplished by looking at the μTDC and μADC spectra. Theoretically, the μTDC spectra were expected to be exponential in nature, exhibiting the 26 ns mean lifetime of the π^+, while the μADC spectra were expected to be Gaussian in nature, consistent with the 4.12 MeV decay μ^+. As can be seen in Figure 3.22, the π^+ identification proved to be excellent. The events being identified as true correlated π^+ exhibited the expected characteristics.

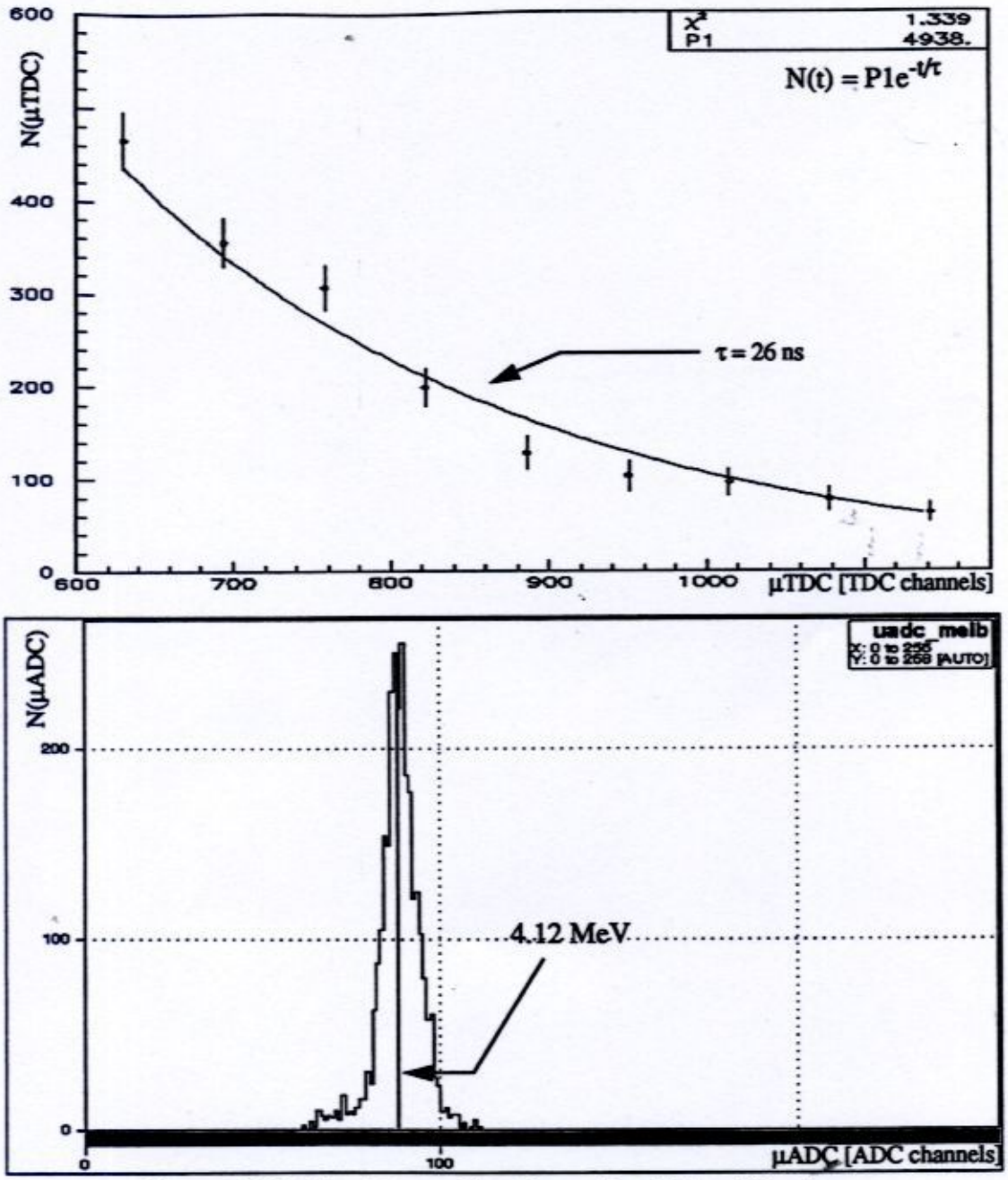

Figure 3.22: Consistency Checks on the π^+ Identification

3.8 Energy Calibration

The next step was to convert the π^+ yield from a function of ADC channel to a function of MeV. To perform this relatively simple task, the energy calibration of the X-arm detector telescopes had to be determined.

3.8.1 Determination of the Calibration Constants

The CH_2 target spectra before the removal of the C contribution were used to calibrate the detector telescopes for π^+ energy. Each tagger channel e(i) corresponded to a known photon energy range. Kinematics and energy loss programs (see Appendix C) were used to determine the corresponding range of energies deposited by the resulting π^+ in a given E-detector, supposing free photoproduction had occurred. However, since the peak in the E-ADC spectrum occurred at a different deposited π^+ energy for each e(i), and because no single E-ADC plot per e(i) had sufficient statistics to define the peak properly, the ratios of the energies at which the peaks occurred were used to "move" them to the position which corresponded to the e(9) peak, using

$$\text{peak}\,[\,e\,(9)\,] \;=\; \frac{T_\pi\,(9)}{T_\pi\,(i)}\,[\,\text{ADC}\,(i) - \text{offset}\,]\,. \qquad (3.8)$$

Tagger channel 9 was selected because it was located roughly in the middle of the tagger focal plane. In the above equation, the peak in the E-ADC spectrum for e(i) occurred at channel ADC(i) and T_π(i) MeV, while the peak in the E-ADC spectrum for e(9) was at T_π(9) MeV.

Further, CH_2 data were taken for two different focal plane configurations corresponding to two slightly different beam energies: one where the e(9) photon energy was 198.80 MeV, and one where it was 197.35 MeV. The different beam energies were also taken into consideration. Arbitrarily, the E-ADC spectra corresponding to the 198.80 MeV e(9) energy were chosen to be fixed, and the E-ADC spectra corresponding to the 197.35 MeV e(9) energy were "moved" so as to further enhance the overall spectra, according to

$$\text{peak}\,(\,[\,e\,(9)\,]^{198.80}) \;=\; \frac{T_\pi\,(9)^{198.80}}{T_\pi\,(i)^{197.35}}\,[\,\text{peak}\,[\,e\,(9)\,]^{197.35}]\,. \qquad (3.9)$$

In this manner, the "monochromatic" CH_2 peaks per telescope were optimized.

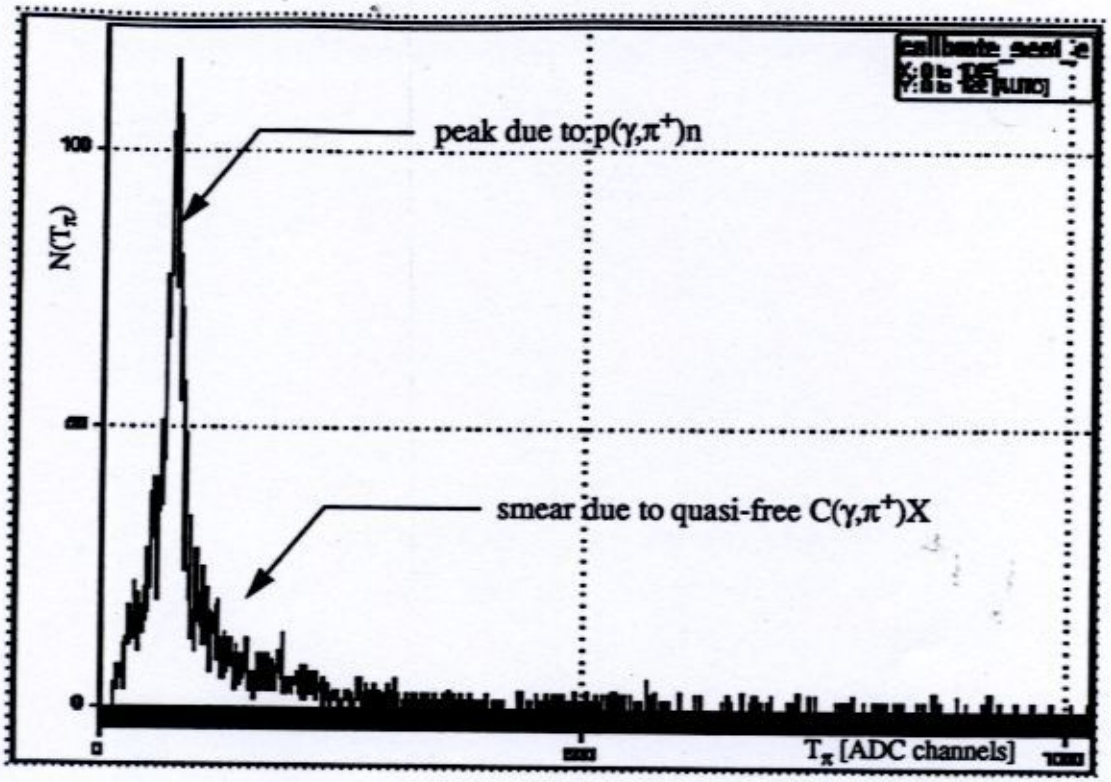

Figure 3.23: A Typical Calibration Spike

A Gaussian superimposed on a second-order polynomial was fit to the offset-corrected distribution in order to find the mean location of the peak "μ" in ADC channels. The π^+ energy this corresponded to was known from the kinematics and energy loss work. However, because the collimators for the telescopes subtended a +/-7° angular bite about the normal trajectory, a range of deposited π^+ energies were accepted.

Table 3.1: A Summary of the Deposited π^+ Energies and Peak Means

Telescope	Trajectory [°]	$T_\pi^{Deposited}$ [MeV]	μ [ADC channels]
Melbourne	43	44.74+/-0.27	256+/-1
	50	42.32+/-0.25	
	57	39.74+/-0.24	
Sydney	73	33.39+/-0.20	170+/-1
	80	30.90+/-0.19	
	87	28.48+/-0.17	

Table 3.1: A Summary of the Deposited π^+ Energies and Peak Means

Telescope	Trajectory [°]	$T_\pi^{Deposited}$ [MeV]	μ [ADC channels]
Adelaide	103	23.14+/-0.14	88+/-1
	110	20.96+/-0.13	
	117	18.78+/-0.11	
Seattle	133	16.11+/-0.16	71+/-1
	140	14.77+/-0.15	
	147	13.69+/-0.14	

These values yielded three gains for each telescope, according to

$$\text{Gain} \quad [\text{MeV/channel}] = \frac{T_\pi^{deposited}}{\text{Mean}}. \tag{3.10}$$

Extremes in the gain were used to determine the error in the mean gain.

Table 3.2: A Summary of the Gains

Telescope	Minimum Gain [MeV/channel]	Mean Gain [MeV/channel]	Maximum Gain [MeV/channel]	$\overline{\text{Gain}}$ [MeV/channel]
Melbourne	0.155+/-0.001	0.165+/-0.001	0.174+/-0.001	0.17+/-0.02
Sydney	0.168+/-0.001	0.182+/-0.001	0.197+/-0.001	0.18+/-0.02
Adelaide	0.214+/-0.001	0.238+/-0.002	0.264+/-0.002	0.24+/-0.03
Seattle	0.192+/-0.001	0.208+/-0.001	0.226+/-0.001	0.21+/-0.02

This method of obtaining the calibration constants was cross-checked with a second independent method. The C subtracted CH_2 spectra for each photon energy bin were fit to a Gaussian superimposed on a flat background, as shown in Figure 3.24.

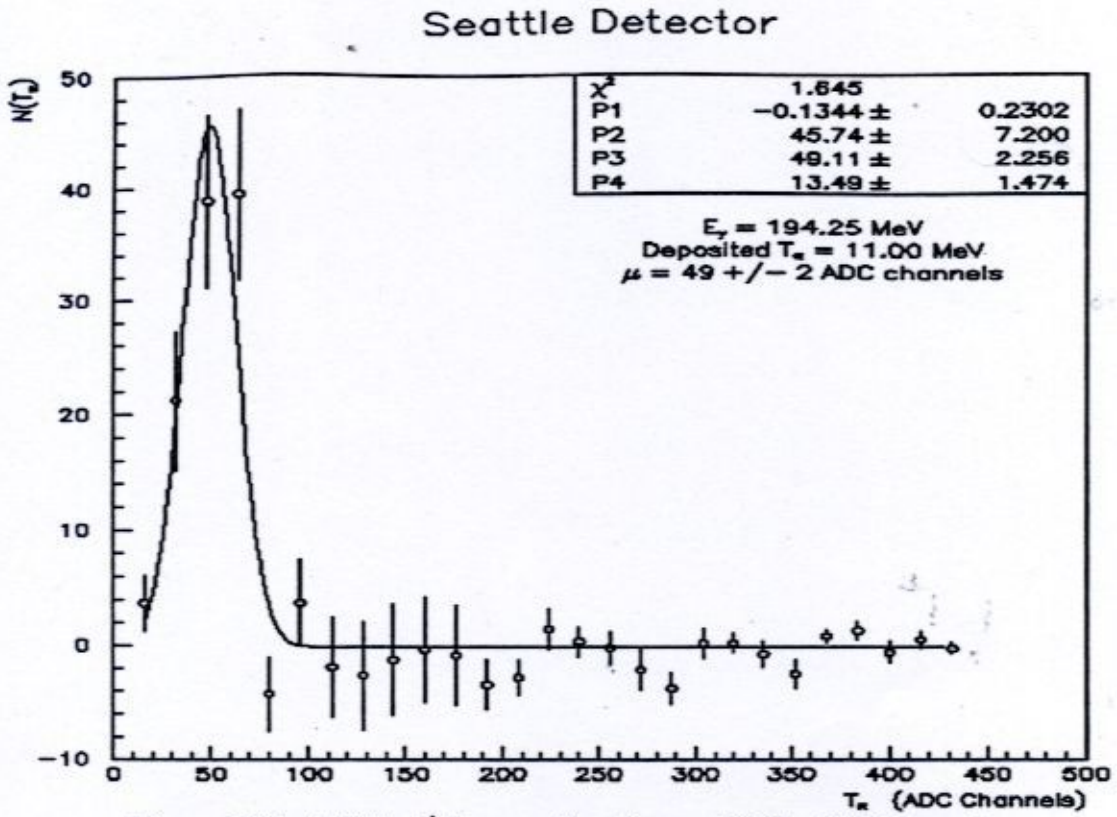

Figure 3.24: A CH_2 π^+ Energy Spectrum with the C Removed

Knowledge of the mean value of the deposited π^+ energy in both ADC channels and MeV allowed the calculation of the gain, as per equation 3.10. Table 3.3 summarizes the gains thus determined, as well as the mean gain.

Table 3.3: A Summary of the Deposited π^+ Energies and Peak Means

Telescope	$T_\pi^{Deposited}$ [+/-0.01 MeV]	μ [ADC channels]	Gain [+/- 0.01 MeV/channel]	$\overline{Gain}$ [+/- 0.01 MeV/channel]
Melbourne	54.49	336+/-3	0.16	0.17
	46.26	277+/-4	0.17	
	37.19	213+/-3	0.17	
	27.02	149+/-3	0.18	

Table 3.3: A Summary of the Deposited π^+ Energies and Peak Means

Telescope	$T_\pi^{Deposited}$ [+/-0.01 MeV]	μ [ADC channels]	Gain [+/- 0.01 MeV/channel]	$\overline{Gain}$ [+/- 0.01 MeV/channel]
Sydney	41.06	234+/-2	0.18	0.18
	34.17	188+/-2	0.18	
	25.71	139+/-2	0.18	
	16.55	85+/-3	0.19	
Adelaide	30.36	128+/-2	0.24	0.25
	24.40	97+/-2	0.25	
	16.74	63+/-2	0.27	
Seattle	22.80	118+/-1	0.19	0.21
	17.51	84+/-2	0.21	
	11.00	49+/-2	0.22	

Note that the gains determined by the independent methods were the same.

3.8.2 Application of the Energy Calibration to the Yields

The energy deposited by a π^+ in a given E-detector was converted from offset-corrected ADC channels to MeV using

$$T_\pi[\text{MeV}] = \text{Gain} \cdot T_\pi[\text{ADC channels}] \tag{3.11}$$

where "T_π [ADC channels]" was the offset-corrected E-ADC value for the event in question. Note that in the process of applying the energy calibration, the ADC channel contents were distributed evenly across the π^+ energy bins.

3.9 Conversion of Deposited T_π to T_π at Creation

Because of the energy loss work (Appendix C), it was a simple matter to determine the correlation between the deposited energy and the average energy at creation of the detected π^+'s. The conversion was performed via a lookup table since there was a non-linear one-to-one correspondence, particularly near detector threshold.

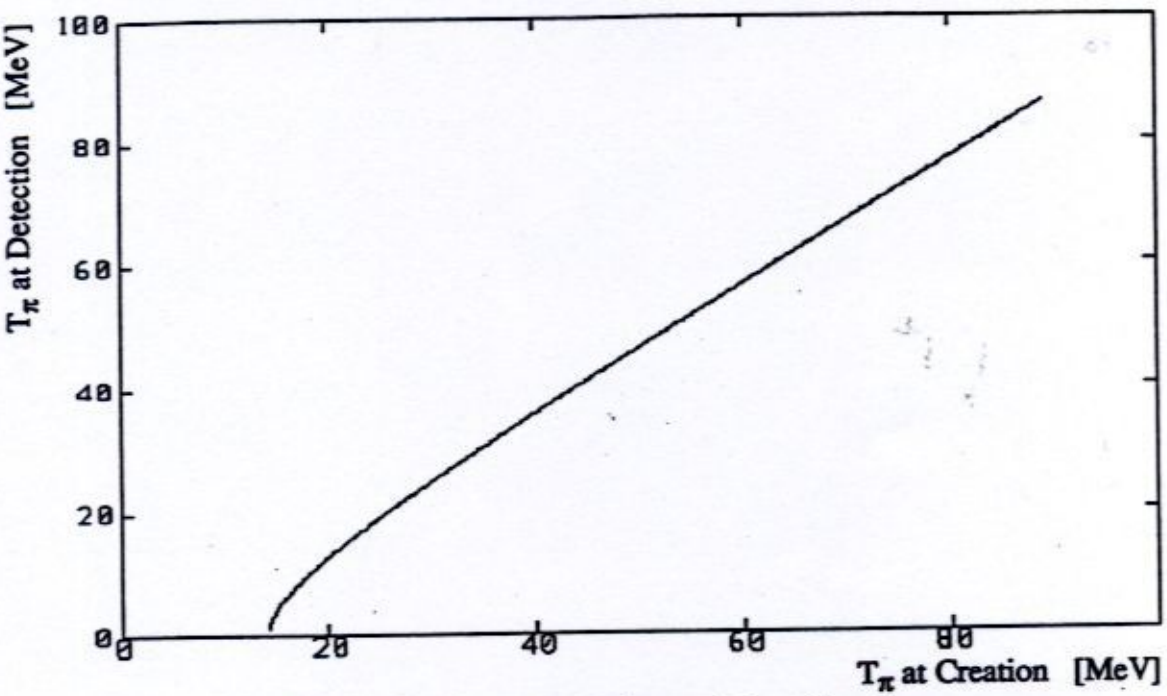

Figure 3.25: T_π at Detection vs. T_π at Creation

3.10 Scaling the Yields for X-arm Detector Efficiency

Once the yields as a function of T_π at creation were known, it was necessary to divide them by the π^+ detection efficiency in order to obtain the efficiency-scaled yields.

3.10.1 Determination of the π^+ Detection Efficiency

The detection efficiency as a function of T_π for those π^+ which produced a stop in the μTDC was given by

$$\text{eff}(T_\pi) = \text{elec}(T_\pi)\,\text{DIF}(T_\pi)\,\text{threshold}(T_\pi)\,\pi\text{A}(T_\pi)\,. \qquad (3.12)$$

The various terms in the above expression were defined as follows: "elec(T_π)" was the efficiency due to the relative timing of the CFDs which produced the μTDC stop, "DIF(T_π)" was the loss in efficiency due to π^+ decay-in-flight between the target and the detector, "threshold(T_π)" was the loss in detection efficiency due to discriminator

threshold effects, and "$\pi A(T_\pi)$" encompassed both π^+ decay before stopping in the E-detector itself and π^+ interactions with the nuclei of the scintillator plastic. Figure 3.26 shows a sample π^+ detection efficiency curve as a function of T_π at detection.

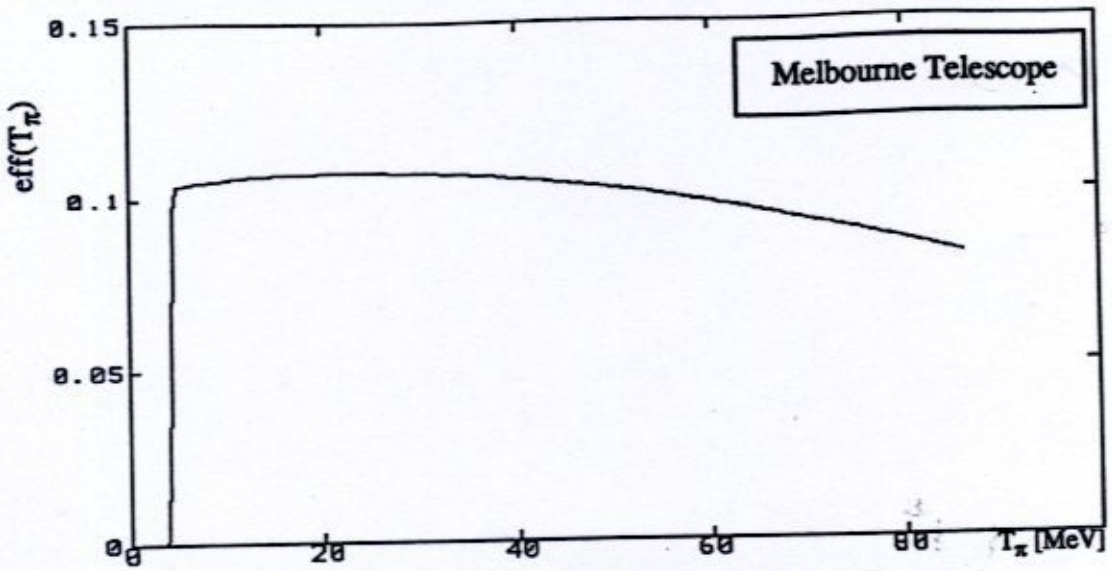

Figure 3.26: A Sample π^+ Detection Efficiency Curve

The following sections deal with equation 3.12 on a term-by-term basis.

Elec(T_π)

The μTDC was discussed in detail on page 50. Figure 3.27 illustrates once again the correlation between the μTDC spectrum and the CFD gates:

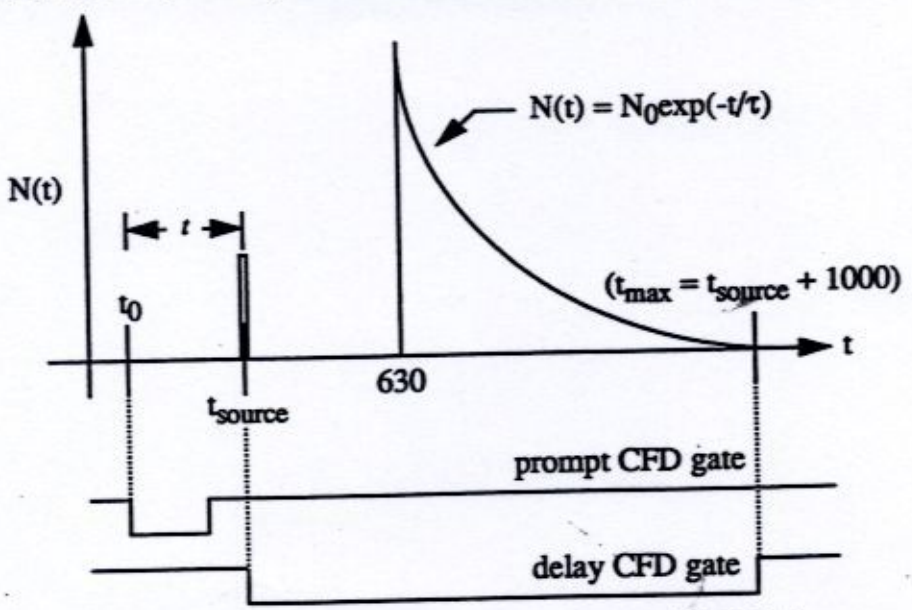

Figure 3.27: The μTDC Spectrum and the CFD Gates

The normalized π^+ detection efficiency as a function of T_π was thus

$$\text{elec}\,(T_\pi) = \frac{\int_{630}^{[t_{source}+1000]} e^{-\left[\frac{(t-t_0)}{\tau}\right]} dt}{\int_{t_0}^{\infty} e^{-\left[\frac{(t-t_0)}{\tau}\right]} dt}. \qquad (3.13)$$

It should be noted that this was a constant independent of π^+ energy. However, it did vary slightly from telescope to telescope, as summarized in Table 3.4.

Table 3.4: The Detection Efficiency due to the Electronics Term

Detector Telescope	Electronics Efficiency [+/-0.001]
Melbourne	0.118
Sydney	0.117
Adelaide	0.113
Seattle	0.123

The systematic error in this term was <1%.

DIF(T_π)

The π^+ detection efficiency was further complicated by the fact that the π^+ may have decayed-in-flight traversing the distance between the target and the detector telescope, or within the detector telescope itself before it came to rest. While the latter process is dealt with in a Monte Carlo (see Appendix E), the former is dealt with here.

Between its creation and subsequent detection, a π^+ had to traverse several layers of matter, depositing some of its energy in each layer. Because the layers were thin, the average π^+ energy in a given layer of matter Δz was defined to be the average of the maximum (upstream) energy and the minimum (downstream) energy for the layer

$$\bar{T}_\pi = \frac{1}{2}\left(T_\pi^{max} + T_\pi^{min}\right). \qquad (3.14)$$

The time Δt_i spent by the π^+ in the i^{th} layer of matter Δz_i was given by

$$\Delta t_i = \frac{1}{\gamma}\left(\frac{\Delta z_i}{v}\right), \tag{3.15}$$

where "γ" is the Lorentz factor, and "v" is the velocity of the π^+. Note that for the purpose of calculating the time spent in the target, the π^+ was assumed to be produced on the midplane.

The velocity of the π^+ was given by

$$v = c\sqrt{1-\frac{1}{\gamma^2}}, \tag{3.16}$$

while the Lorentz factor was

$$\gamma = \frac{\bar{T}_\pi}{m_\pi c^2} + 1. \tag{3.17}$$

The total time TOF spent by the π^+ travelling from the target to the upstream edge of a given E-detector was thus

$$TOF = \sum_i \Delta t_i, \tag{3.18}$$

so that the probability a π^+ did not decay in flight was simply

$$DIF(T_\pi) = e^{-\frac{TOF}{\tau}}. \tag{3.19}$$

Figure 3.28 demonstrates a sample contribution of the decay-in-flight term to the overall π^+ detection efficiency.

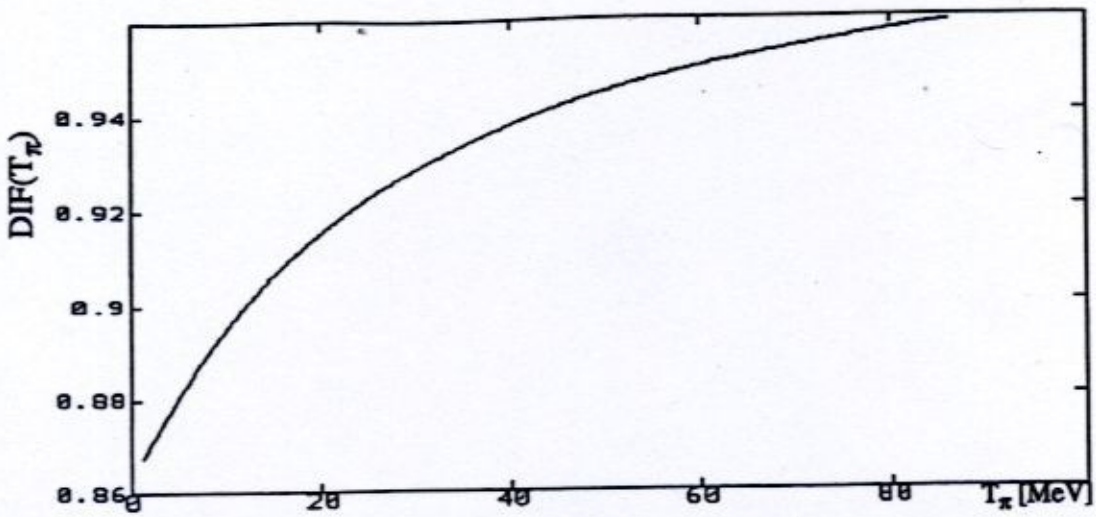

Figure 3.28: DIF Contribution to the π^+ Detection Efficiency

The systematic error in this term was <1%.

Threshold(T_π)

Since a given E-detector had a non-zero energy resolution which was a function of the deposited π^+ energy (see Appendix D), some π^+'s with energy less than the hardware detection threshold were actually detected, while some π^+'s with energy above detector threshold were missed. Normalized Gaussians representing the energy resolution were generated for a wide range of π^+ energies near the hardware detector threshold. While the threshold region was not a step function, it was presumably much sharper than the energy resolution, and thus the probability of detection was simply the area of the distribution above detector threshold.

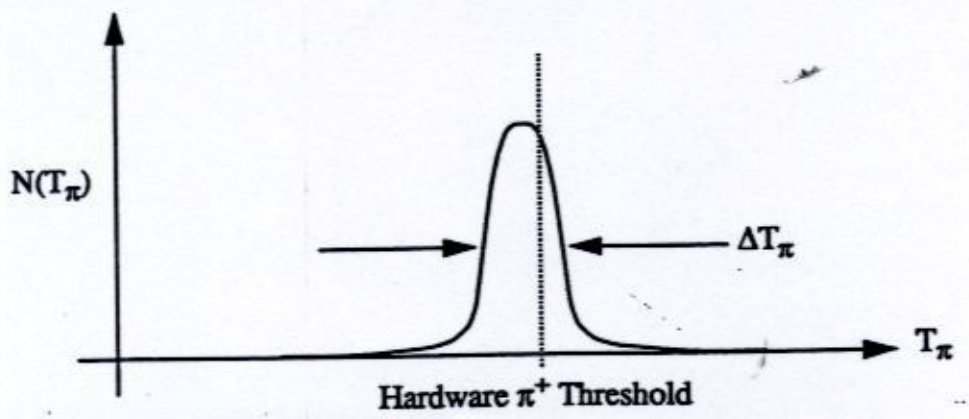

Figure 3.29: The Probability of Detection Near Threshold

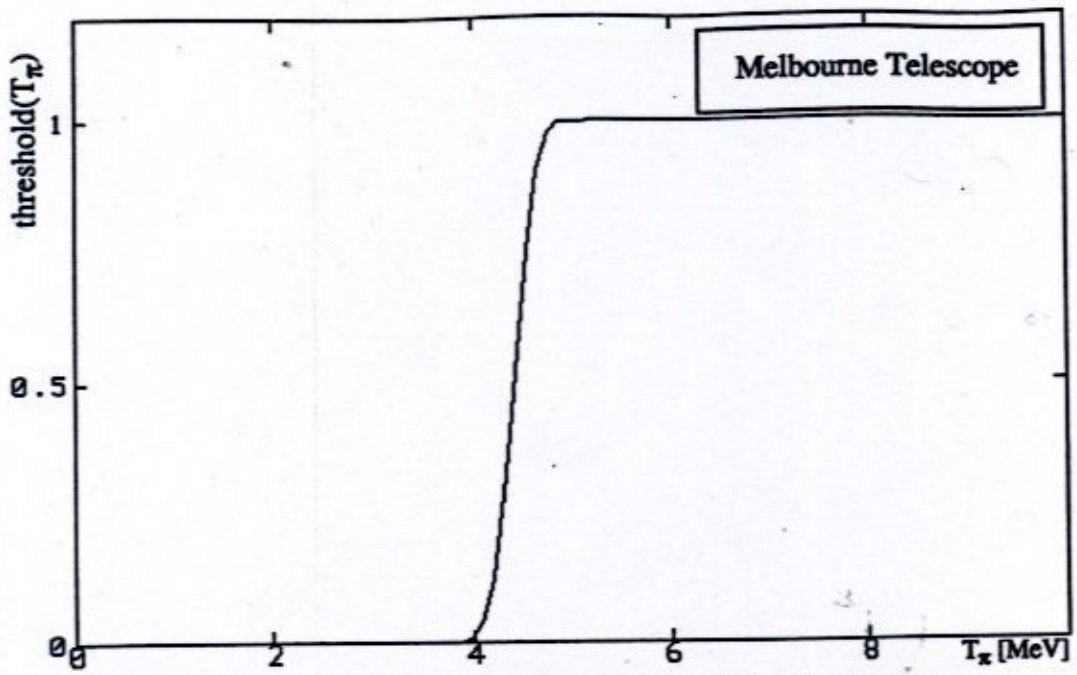

Figure 3.30: Threshold Contribution to the π^+ Detection Efficiency

Figure 3.30 demonstrates the results. The systematic error in this term was <1%.

$\pi A(T_\pi)$

This contribution to the detection efficiency was due to π^+ interactions in the scintillator plastic, as well as in-flight π^+ decay in the E-detector itself. Such processes lead to some π^+'s going undetected. The detectors gave pulses corresponding to the arrival of the π^+, but the nuclear interactions threw the pulse height out of the identification cuts imposed. These effects were difficult to calculate outright, so a statistical approach was adopted. In order to investigate the magnitude of the effect on the detection efficiency, a Monte Carlo simulation program was written. The simulation is fully documented in Appendix E. The net result is a series of detection efficiency curves which represent the contribution to the π^+ detection efficiency of πA interactions. A curve for one detector is presented in Figure 3.31.

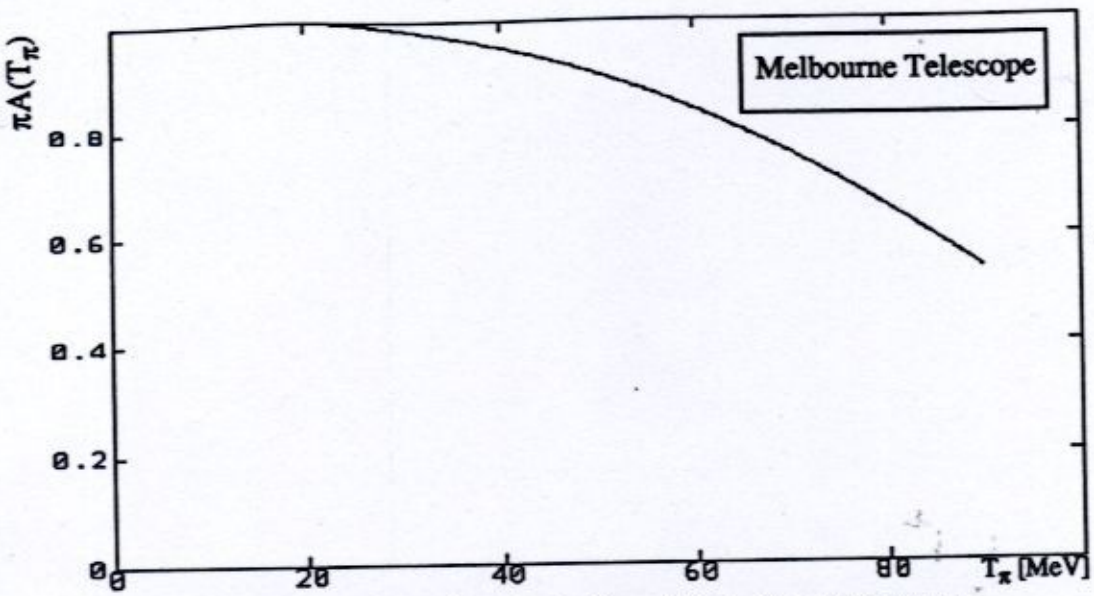

Figure 3.31: πA Contribution to the π^+ Detection Efficiency

The systematic error in this term was taken to be 10% in the *in*efficiency for detection.

3.10.2 Correction of the Yields for Detector Efficiency

The detector efficiencies as a function of deposited π^+ energy determined in section 3.10.1 were then converted to a function of π^+ energy at creation using the lookup tables detailed in section 3.9. The yield as a function of π^+ energy at creation was then

$$\text{Yield}\,(T_\pi, \theta) = \frac{N\,(T_\pi, \theta)}{\text{Efficiency}\,(T_\pi, \theta)}, \tag{3.20}$$

where "θ" labels the X-arm detector.

3.11 Integration of the Yields

3.11.1 Over π^+ Energy Bins

Once the yield as a function of π^+ energy at creation had been determined for each detector, the data were integrated to determine the total yield $N\,(E_\gamma, \theta, T_\pi)$ in a given π^+ energy bin ΔT_π for a given photon energy

$$N\,(E_\gamma, \theta, T_\pi) = \int_{\Delta T_\pi} \text{Yield}\,(T_\pi, \theta)\, dT_\pi \ . \tag{3.21}$$

By normalizing this yield and dividing the result by the width of the π^+ energy bin ΔT_π, double differential cross sections were obtained for certain combinations of E_γ and θ (see section 3.15).

3.11.2 Over Photon Energy Bins

The total yield $N'(E_\gamma, \theta)$ for a given photon energy bin was then obtained by summing over the yields due to the individual π^+ energy bins

$$N'(E_\gamma, \theta) = \sum_{\Delta T_\pi} N(E_\gamma, \theta, T_\pi) \quad . \tag{3.22}$$

By normalizing this yield, differential cross sections were obtained (see section 3.16).

The photon energy bins centered at E_γ corresponded to four tagger channels; that is, the 16 channel focal plane was broken up into four bins of four channels each, whose width was approximately 10 MeV. Note that E_γ is the bremsstrahlung weighted mean of the photon energy bin.

Table 3.5: Mean Photon Energies for the Four Photon Energy Bins

Tagger Channels	Photon Energy Bin	E_γ [MeV]
1-4	1	213
5-8	2	204
9-12	3	194
13-16	4	184

The integration was performed from a consistent detector threshold of 17 MeV for all targets (save CH_2) such that a normalized target-to-target comparison of the cross sections could later be made. Different thresholds existed for different targets due to varying amounts of energy left by the π^+ in the various targets. Note that the statistical errors were accumulated in quadrature, while the systematic errors were accumulated linearly. Note also that $N'(E_\gamma, \theta)$ does not, in general, represent the absolute π^+ yield per photon energy bin per detector telescope. The correction for correlated pairs, if appropriate, was still necessary.

3.12 Estimating the Correlated Pair Contribution

For the energy range of this experiment, pair production was the dominant mechanism for background. The cross section for pair production is forward peaked and goes roughly like Z^2. Pair contamination of the π^+ energy spectra became a problem for the heavier ($Z \geq 20$) targets, but only at the forward angles. Recall the pair contaminated ΔE-E scatterplot first presented in Figure 3.16.

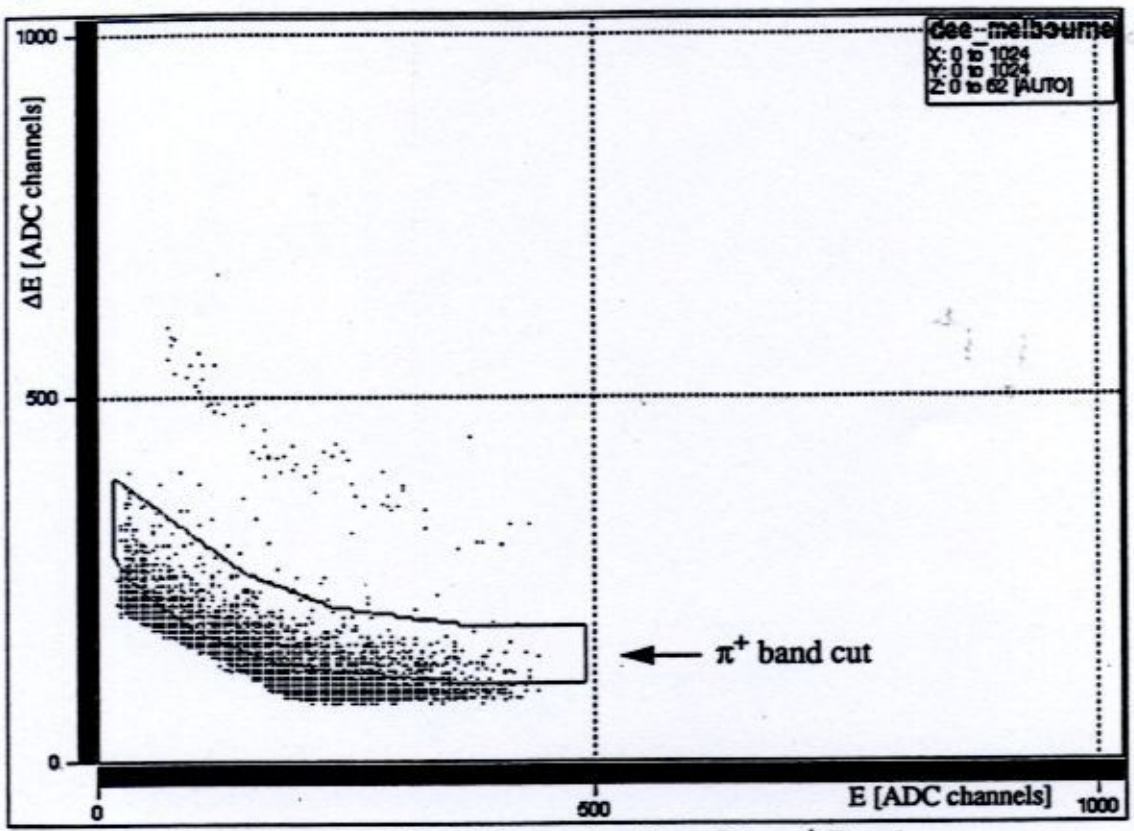

Figure 3.32: Pair Contamination of the π^+ Band

A "pair event" represented both an electron and a positron depositing their energy simultaneously in a telescope, effectively doubling the pulse heights in both the ΔE and E detectors. Thus, the energy signature of a pair event was almost identical to that of a single π^+ event, so that rejection on the basis of deposited energy was impossible. Also the timing resolution of the TDCs used in the experiment could not differentiate the small change in time-of-flight between a pair and a π^+ event, so timing criterion could not be used to reject pair events. Of course, pair events did not have the delayed pulses used for π^+ identification. However, they did contribute to the μTDC spectrum when they were followed by a random pulse within the μTDC time range. Fortunately, these random pulses were

distributed uniformly in time, unlike the decay pulses which had a well-defined exponential distribution density. Thus, while it was not possible to remove the pair events from the data, it was possible to estimate their contribution.

Further, while it was not possible to estimate the level of correlated pair contamination in an individual π^+ energy bin due to statistical limitations, it was possible to estimate the level of contamination for a given photon energy bin. It was first necessary to determine exactly which combinations of target, angle, and photon energy bin corresponded to contaminated yields. In order to do this, μTDC spectra were accumulated for each of the four photon energy bins. It was assumed that a random event stopped the μTDC while a pair event was in the prompt gate, so that the resulting spectrum consisted of an exponential of 26 ns time constant "τ" superimposed on a flat (random) background

$$N(\mu TDC) = A_0 + A_1 e^{-\frac{\mu TDC}{\tau}} . \qquad (3.23)$$

The $\mu TDC(E_\gamma)$ spectra were rebinned by a factor of 64 and then fit to this shape. A further constraint was imposed - the integral of the fit coefficients was normalized to the total number of counts in the spectrum. In some cases, it was necessary to rebin by a factor of 128 to get the fit to converge (indicated by "#" in Table 3.6); in other cases, it was necessary to extend the fit over one further μTDC bin (from channel 566 onward instead of channel 630) to obtain convergence (indicated by "*" in Table 3.6). If this was necessary, an extra 10% systematic error was assigned to the yield. However, in this manner, the coefficients A_0 and A_1 were determined for every target, angle, and photon energy bin. A non-zero value for the background coefficient A_0 indicated the yield was contaminated. Figure 3.33 shows a typical $\mu TDC(E_\gamma)$ spectrum.

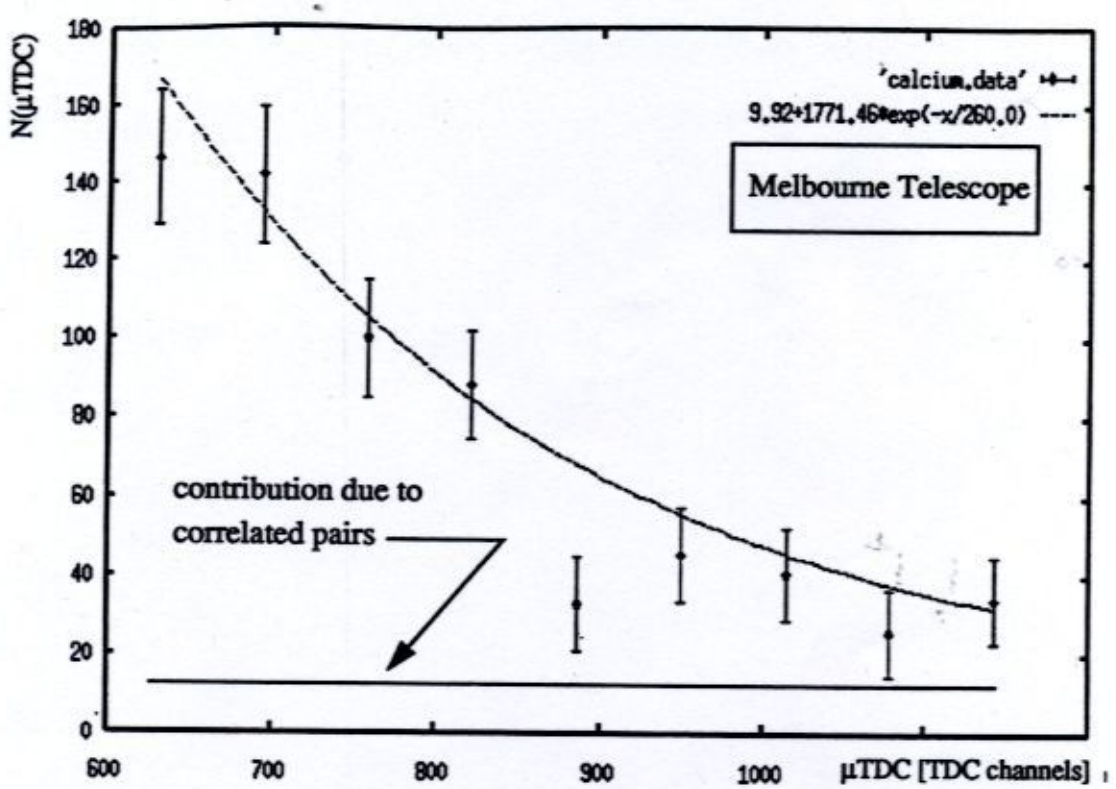

Figure 3.33: A Contaminated μTDC Spectrum

Once the magnitude of the flat background (A_0) was known, the pair contribution to the π^+ yield was determined by integrating over the appropriate region of the μTDC spectrum

$$\text{Pair Yield}\,(E_\gamma\,\theta) = \int_{630}^{t_{max}} A_0 dt = A_0 \cdot (t_{max} - 630)\,, \qquad (3.24)$$

where "t_{max}" was the last μTDC channel to have a count in it. The absolute π^+ yield for a given photon energy was then the difference between the contaminated yield and the pair yield

$$N_\pi\,(E_\gamma\,\theta) = N'\,(E_\gamma\,\theta) - \text{Pair Yield}\,(E_\gamma\,\theta)\,. \qquad (3.25)$$

Table 3.6 summarizes the degree of contamination present in the various yields. Any combination of target/telescope/photon energy bin not present in this table corresponded to an uncontaminated π^+ yield.

Table 3.6: A Contamination Summary

Target	Telescope	E_γ bin	% Contamination
Ca	Melbourne	1	13.4+/-1.6
		2	16.1+/-2.0
		3	52.1+/-8.5
		4	12.2+/-2.2
Sn	Melbourne, large collimator	1	26.4+/-4.8
		2	10.1+/-3.5 #
		3	67.6+/-29.6
		4	38.3+/-23.3 *
	Melbourne, small collimator	1	14.0+/-3.4
		2	17.4+/-4.4
		3	12.7+/-4.9
		4	48.1+/-40.2
	Sydney	1	0.5+/-0.1
		2	20.4+/-3.6
		3	28.5+/-6.6 *
		4	41.2+/-14.1
Pb	Melbourne	1	70.2+/-38.5 *
		2	99.9+/-66.7 *
		3	95.7+/-58.9
		4	18.7+/-22.8
	Sydney	1	11.8+/-2.3
		2	17.8+/-4.4 *
		3	47.1+/-21.7
		4	41.7+/-17.8

3.13 Normalization of the Yields

The absolute π^+ yields of sections 3.11.1 and 3.11.2 were normalized to incident photon beam flux "N_γ", number of photoproduction centers "N", and detector solid angle "$\Delta\Omega$" to express them as double differential and differential cross sections respectively.

3.13.1 Incident Photon Beam Flux

The incident photon beam flux per photon energy bin was directly related to the electron flux detected by the tagger focal plane corrected for stolen coincidences and tagging efficiency

$$N_\gamma(E_\gamma) = N_e^{true}(E_\gamma) \cdot \text{tagging efficiency}(E_\gamma), \tag{3.26}$$

where the true electron flux per photon energy bin was given by

$$N_e^{true}(E_\gamma) = \sum_{E_\gamma \text{ bin}} N_e^{true}(i), \tag{3.27}$$

and "$N_e^{true}(i)$" was the number of electrons actually detected by tagger channel i, corrected for stolen coincidences as detailed on page 33. The systematic error in the incident photon beam flux per photon energy bin was < 1%. It is in this systematic error that the presence of the photon tagger is most strongly felt.

3.13.2 Target Densities

The effective thicknesses of the various targets t′ in g/cm^2 was given by

$$t' = \frac{\rho t}{\sin(\theta)} = \frac{\text{density} \cdot \text{thickness}}{\sin(\theta)} = \frac{\text{mass}}{\text{volume}} \cdot \frac{\text{thickness}}{\sin(\theta)}, \tag{3.28}$$

where "θ" was the angle the target made with respect to the photon beam axis (30°). This effective thickness was converted from g/cm^2 to number of photoproduction centers per cm^2 using

$$N = \frac{1}{A} \cdot t' \cdot N_A, \tag{3.29}$$

where "A" was the molar weight of the target, and "N_A" was Avogadro's number. Table 3.7 summarizes the targets selected for the run. Note that it was the H content of the CH_2 target that was interesting for the purpose of extracting the elementary cross section. The systematic error in the target density was < 1%.

Table 3.7: A Summary of Target Densities

Target	$t'=\rho t/\sin(\theta)$ [+/-0.001 g/cm^2]	N [+/- 0.001 X10^{22}cm^{-2}]
CH_2	0.596	5.136 (H); 2.568 (C)
C	1.028	5.155
Ca	2.240	3.366
Sn	1.570	0.797
Pb	1.086	0.316

3.13.3 Solid Angles

The point source solid angle subtended by a telescope located at angle θ was given by

$$\Delta\Omega(\theta) \approx \pi \left(\frac{r}{d}\right)^2, \tag{3.30}$$

where "r" was the collimator radius and "d" was the distance from the target to the center of the collimator. This approximation was valid only for d >> r. The actual solid angles subtended by the various telescopes were corrected for the finite extended target (Garrow, 1991), and are presented in Table 3.8. The systematic error associated with the solid angle was < 1%.

Table 3.8: A Summary of Solid Angles

Telescope	Collimator [+/-0.1 cm]	θ [+/- 1']	ΔΩ [+/-0.2 msr]
Melbourne	5.5	51° 12'	23.4
Melbourne	8.0	51° 12'	49.2
Sydney	8.0	80° 57'	47.9
Adelaide	8.0	109° 14'	48.4
Seattle	8.0	140° 14'	47.7

3.14 Systematic Error

Since the systematic errors associated with $N_\gamma(E_\gamma)$, N, and $\Delta\Omega(\theta)$ were all < 1%, the systematic error associated with the cross sections was basically determined by the systematic error in the yield. Two factors contributed to this: the detection efficiency (< 13%) and the degree of pair contamination (10% as appropriate). Due to the excellent particle identification, a nominal value of <1% was assigned to the systematic error in this quantity. The resulting maximum possible systematic error associated with any given cross section value was < 27%. The average systematic error was ~15%.

Table 3.9: A Summary of Systematic Errors

Quantity	$\delta^{systematic}$
$N_\pi(E_\gamma,\theta)$	< 14% (< 24%)
$N_\gamma(E_\gamma)$	< 1%
N	< 1%
$\Delta\Omega(\theta)$	< 1%

3.15 Laboratory Double Differential Cross Section

3.15.1 Calculation

The laboratory double differential cross section as a function of photon energy was given by

$$\frac{d^2\sigma}{d\Omega_{LAB}dT_\pi}(E_\gamma,\theta,T_\pi) = \frac{N_\pi(E_\gamma,\theta,T_\pi)}{N_\gamma(E_\gamma)\cdot N\cdot\Delta\Omega(\theta)\cdot\Delta T_\pi}. \qquad (3.31)$$

3.15.2 Results

The following eleven plots (Figures 3.34 to 3.44) illustrate the double differential cross sections obtained for the $Z \geq 6$ targets in this experiment as a function of T_π. The width of the π^+ energy bins is 10 MeV. The numerical values for the laboratory double differential cross sections which are not statistically consistent with zero are presented in Appendix F. The arrow indicates the approximate maximum energy π^+ kinematically expected, weighted by the width of the photon energy bin, detector resolution, and the width of the π^+ energy bin. As previously mentioned, because the number of pairs in the yields was not known to the level of $N_\pi(E_\gamma,\theta,T_\pi)$, double differential cross sections for contaminated combinations of target and angle could not be determined.

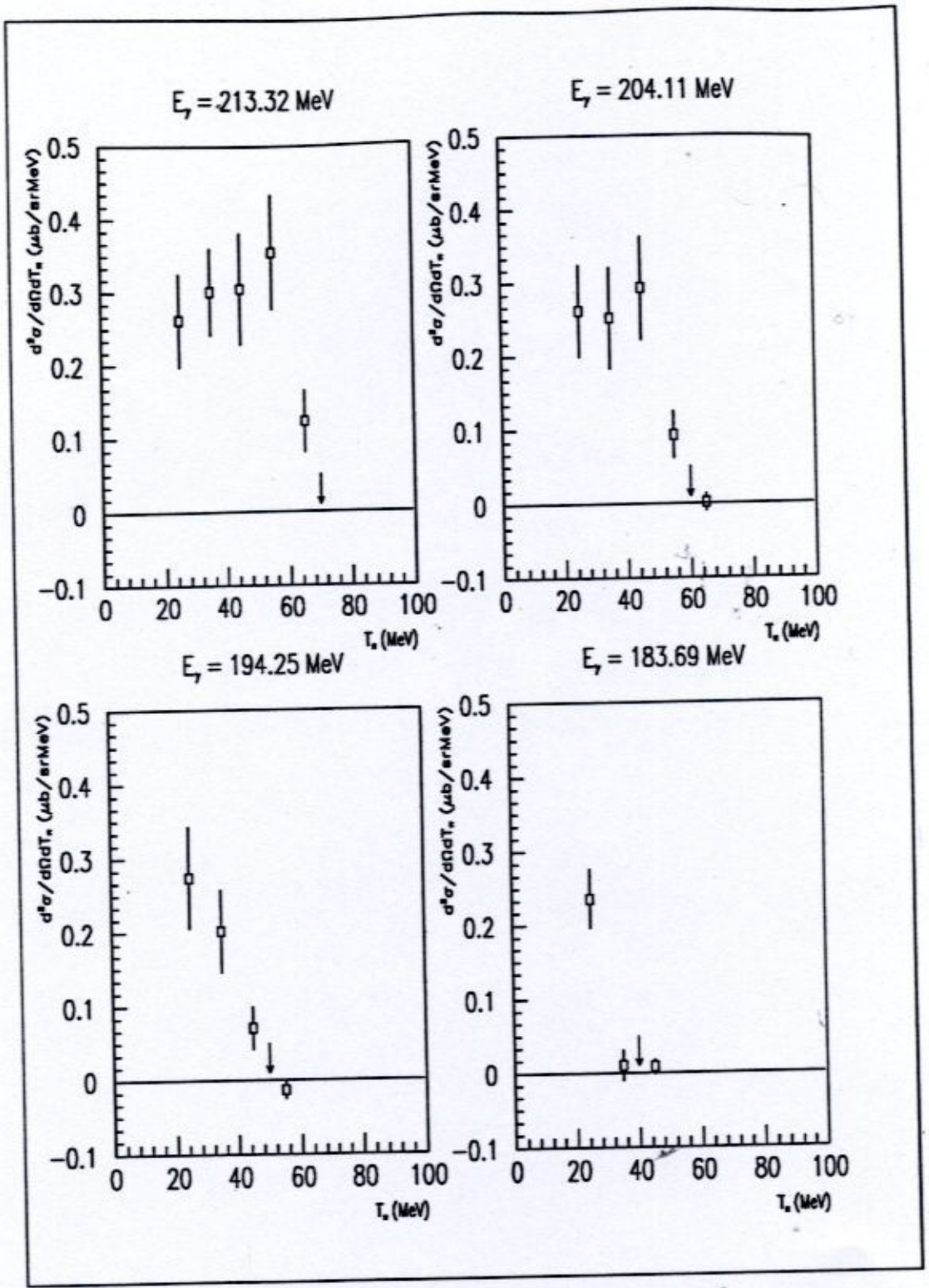

Figure 3.34: $d^2\sigma/d\Omega dT_\pi$ for C at $\theta_{LAB} = 51^o$

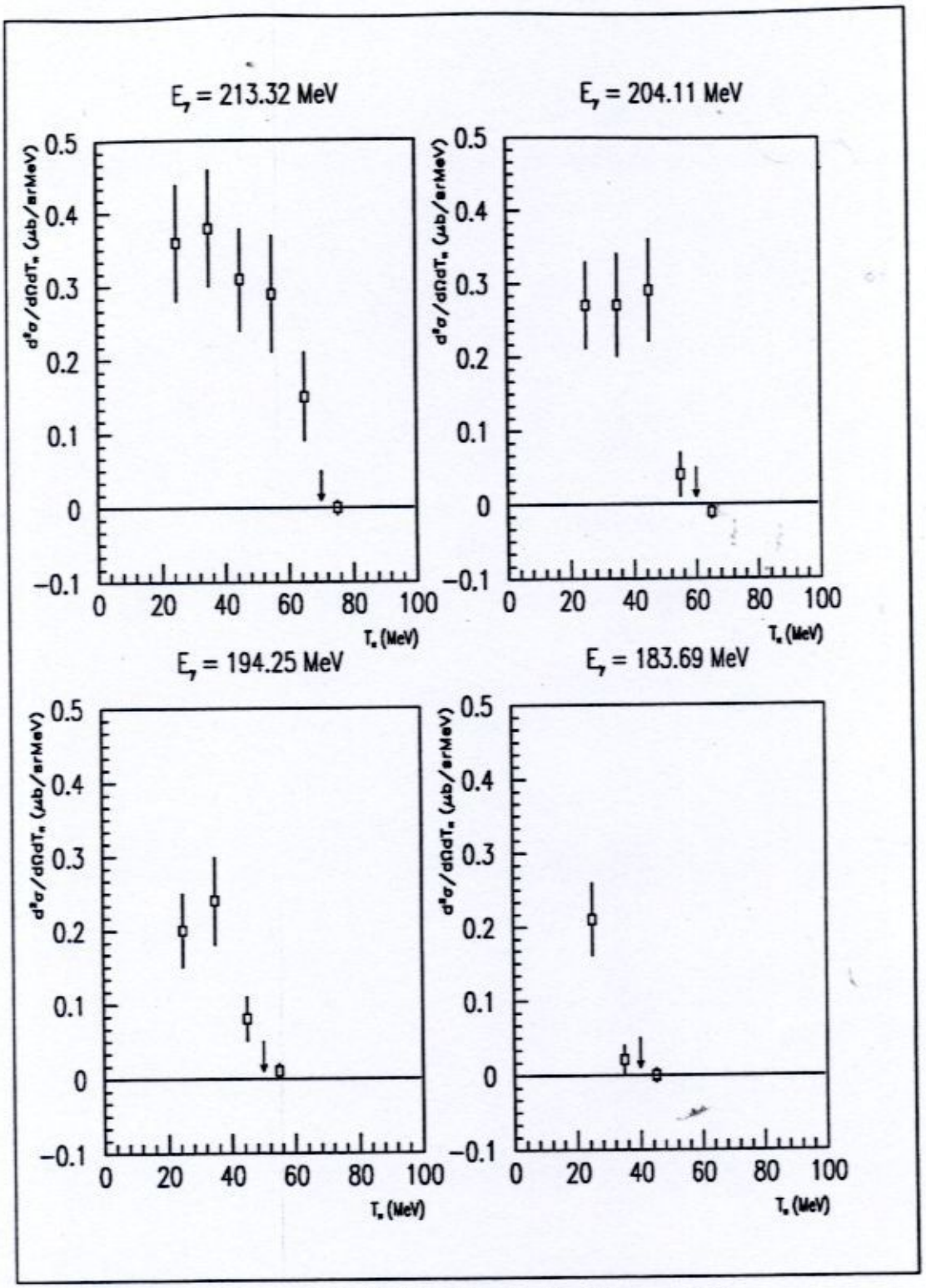

Figure 3.35: $d^2\sigma/d\Omega dT_\pi$ for C at $\theta_{LAB} = 81^o$

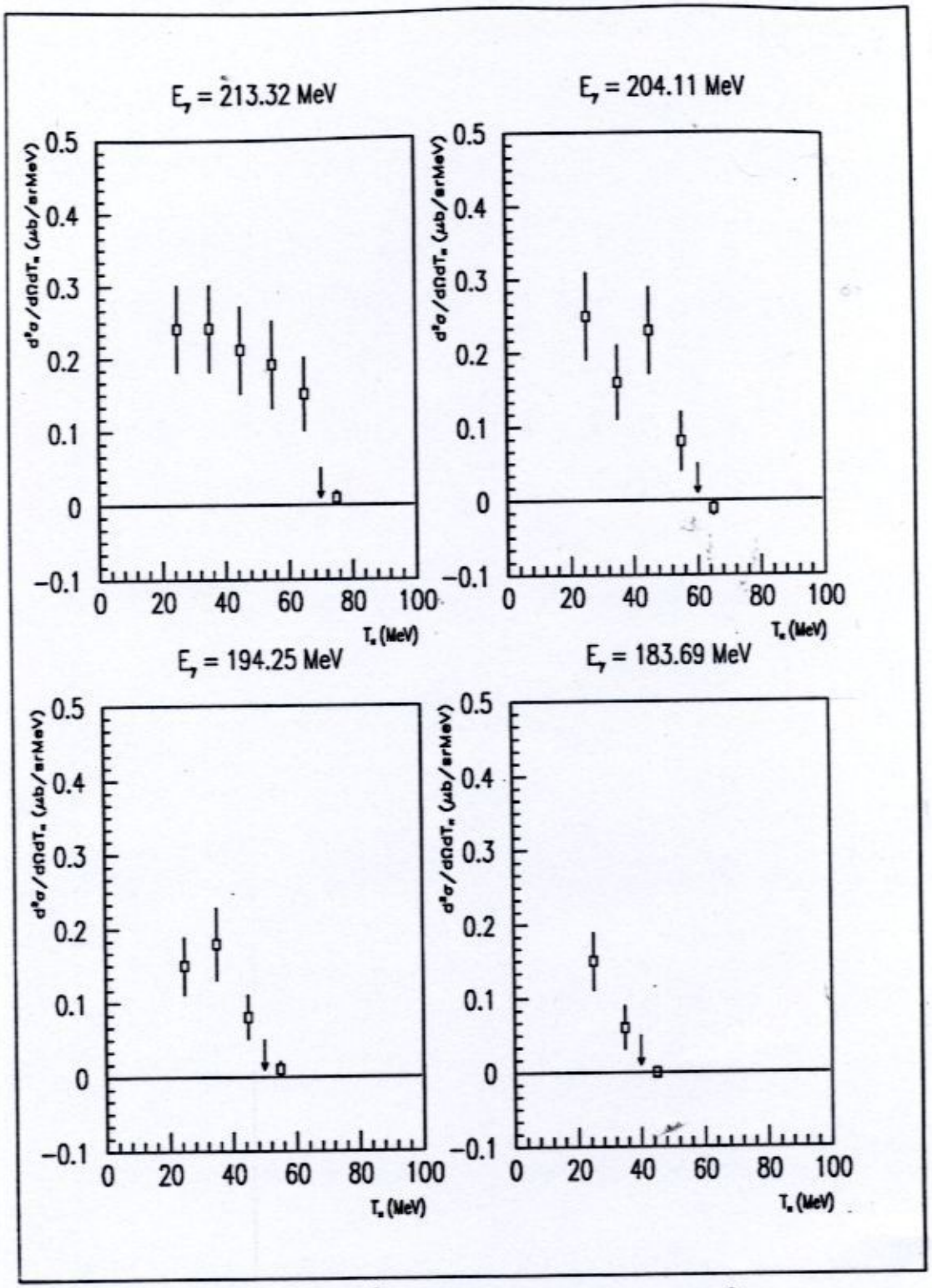

Figure 3.36: $d^2\sigma/d\Omega dT_\pi$ for C at $\theta_{LAB} = 109^o$

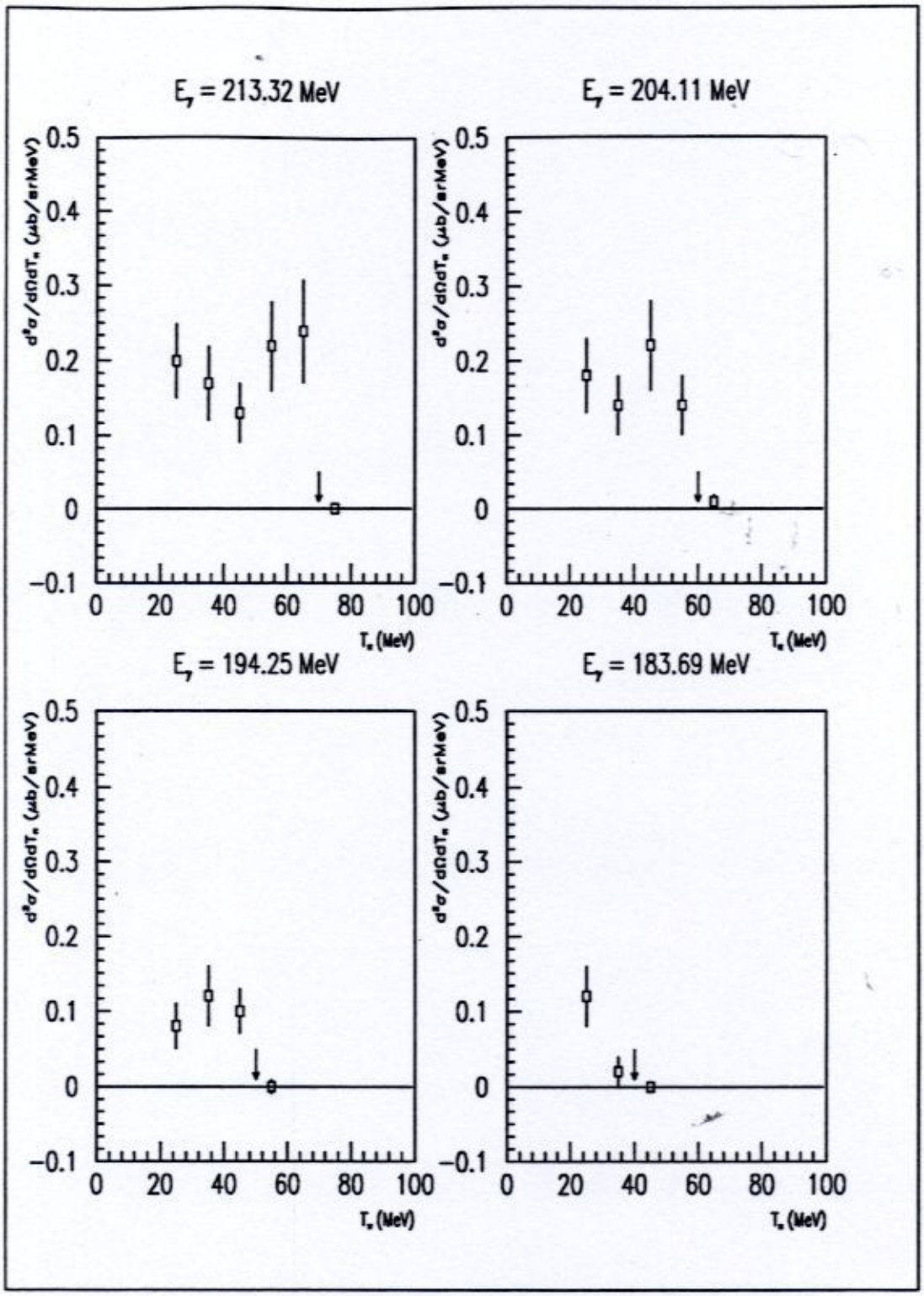

Figure 3.37: $d^2\sigma/d\Omega dT_\pi$ for C at $\theta_{LAB} = 141^o$

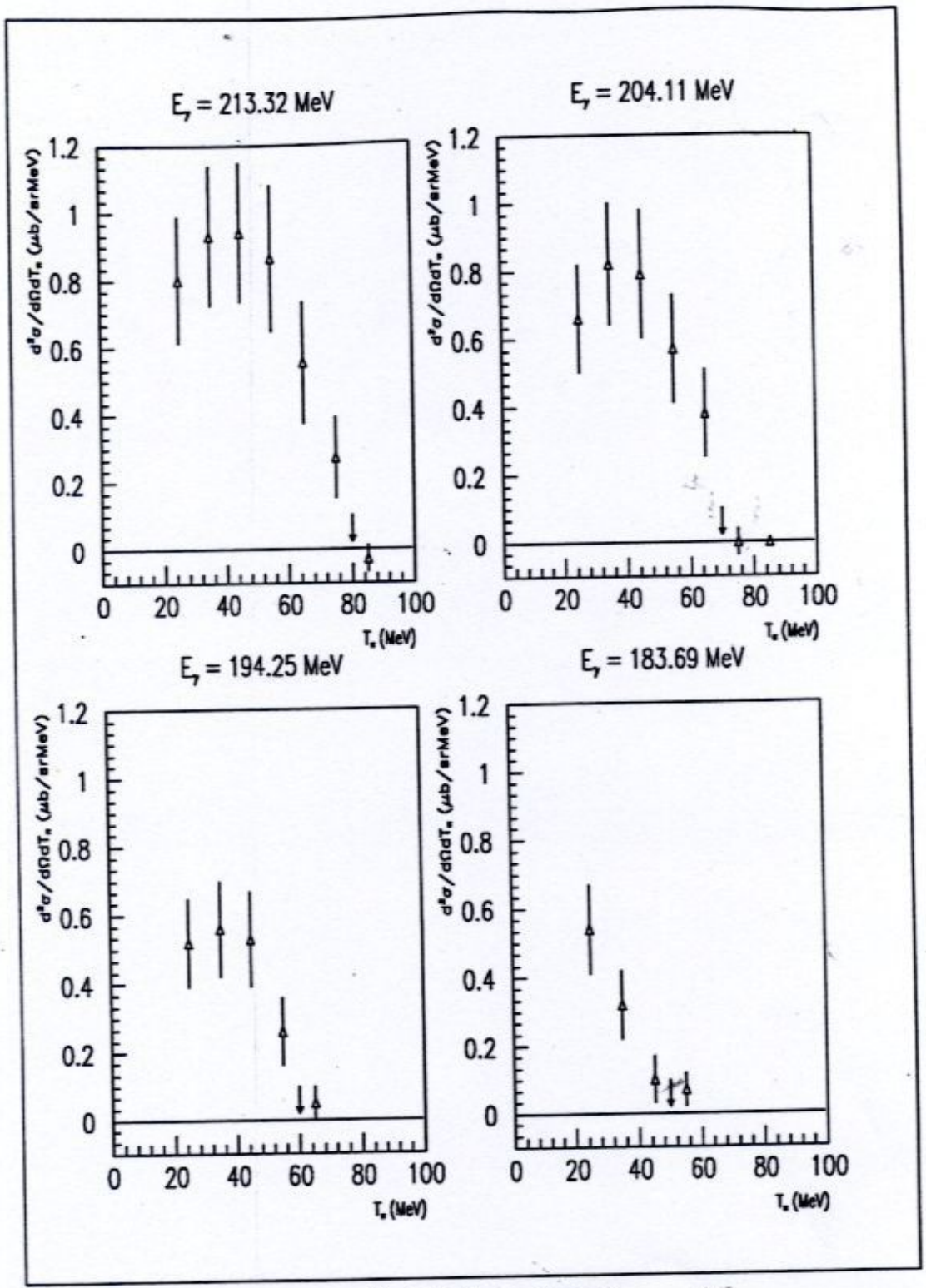

Figure 3.38: $d^2\sigma/d\Omega dT_\pi$ for Ca at $\theta_{LAB} = 81^o$

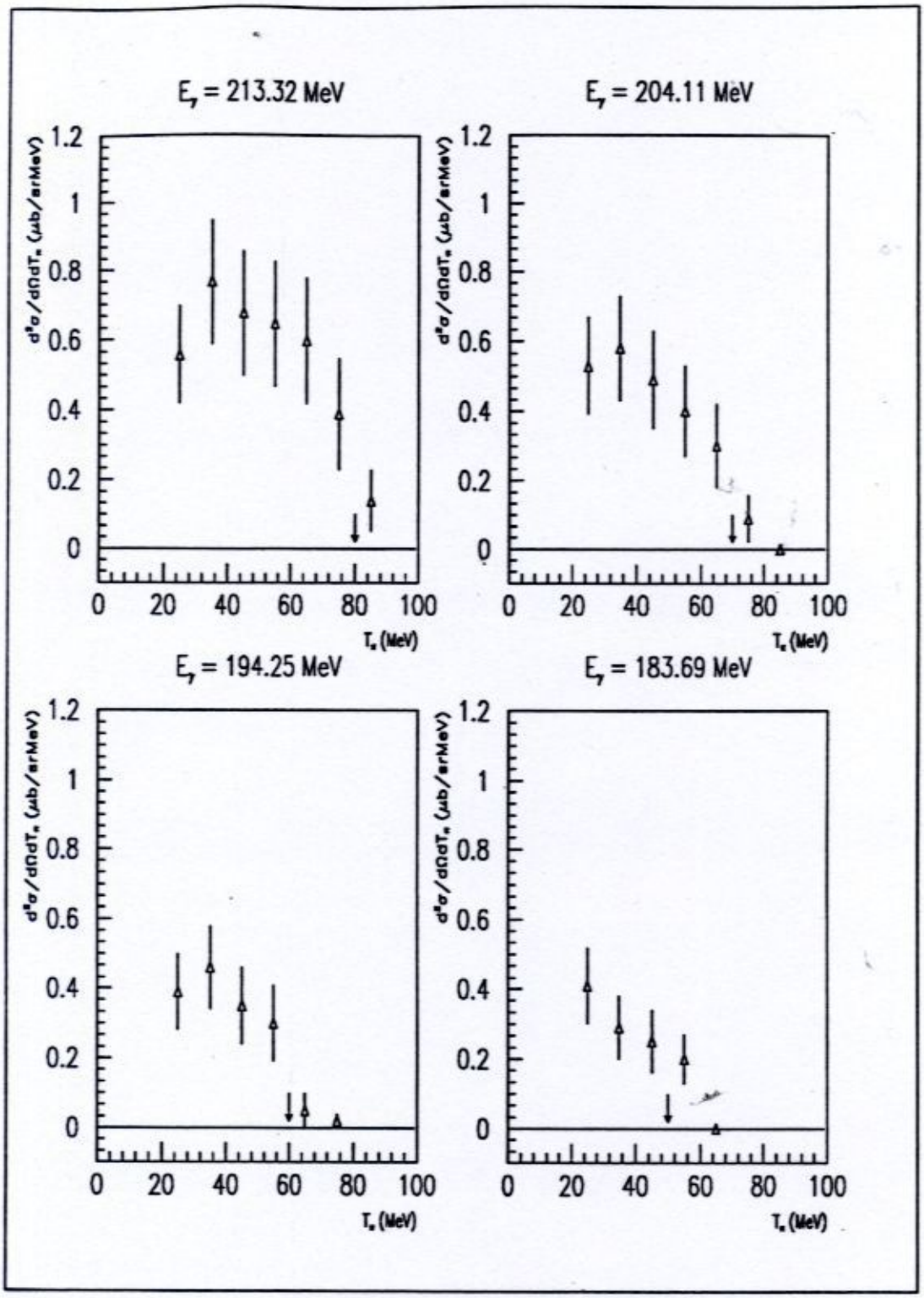

Figure 3.39: $d^2\sigma/d\Omega dT_\pi$ for Ca at $\theta_{LAB} = 109^o$

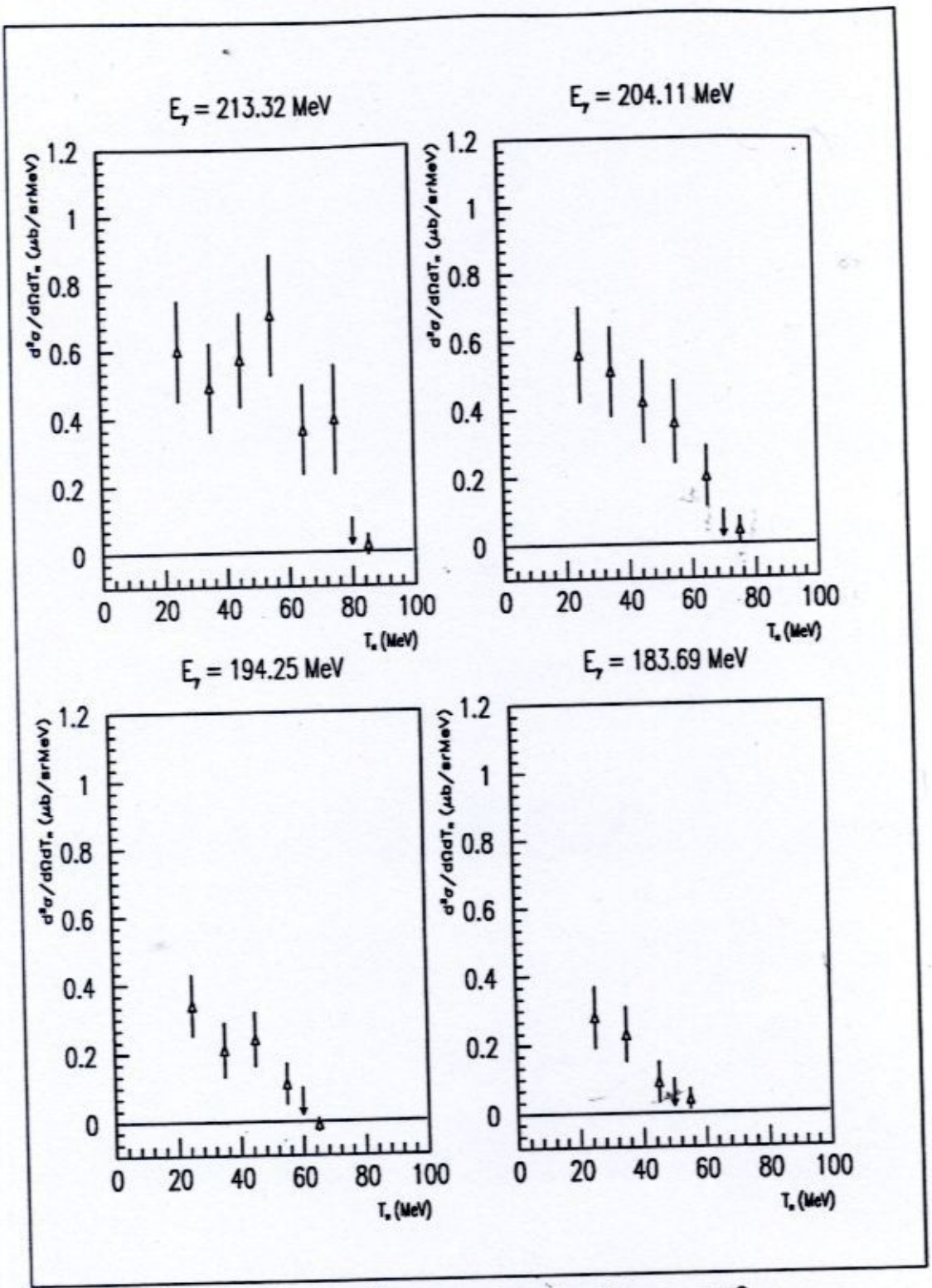

Figure 3.40: $d^2\sigma/d\Omega dT_\pi$ for Ca at $\theta_{LAB} = 141^o$

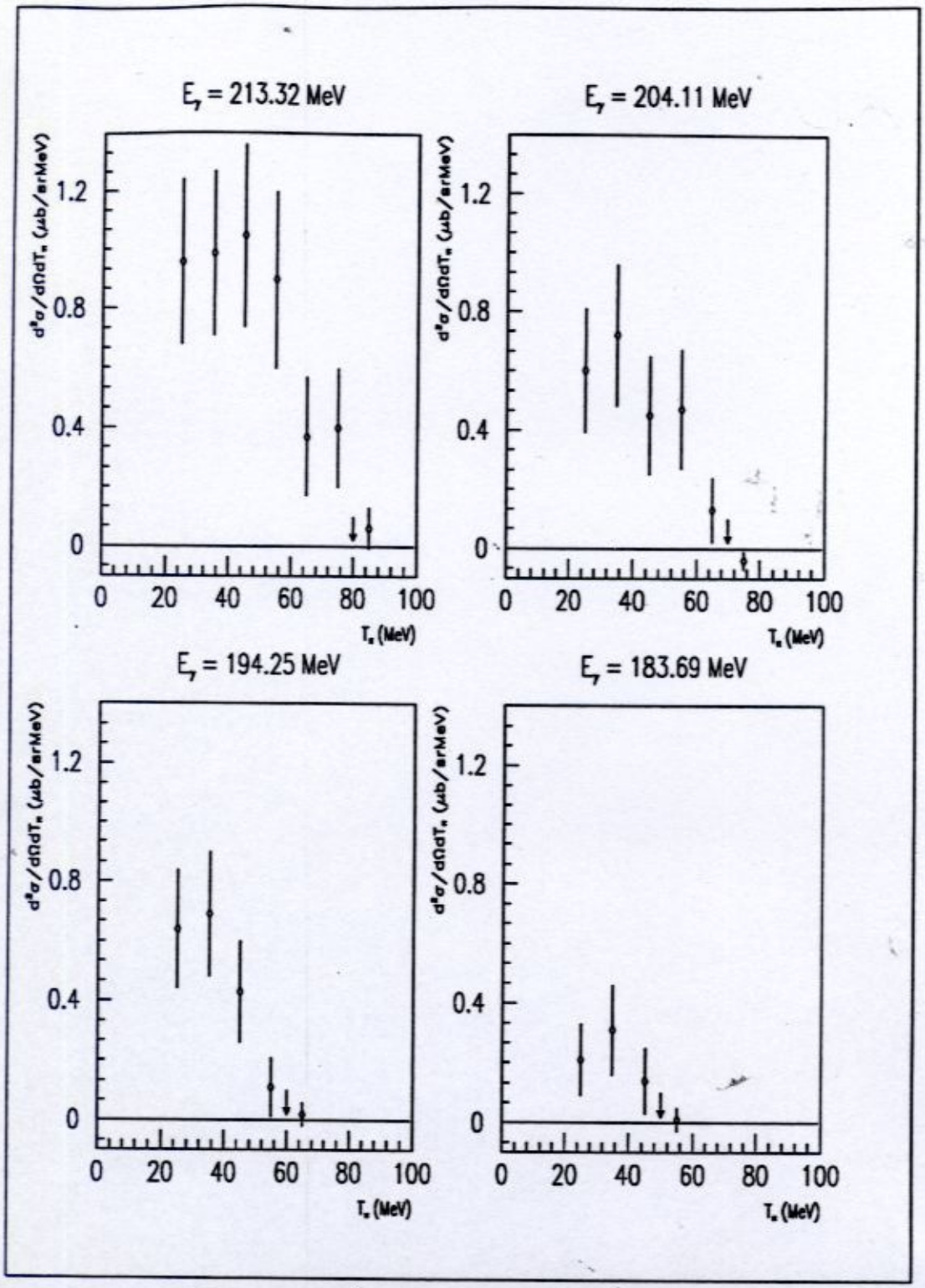

Figure 3.41: $d^2\sigma/d\Omega dT_\pi$ for Sn at $\theta_{LAB} = 109^o$

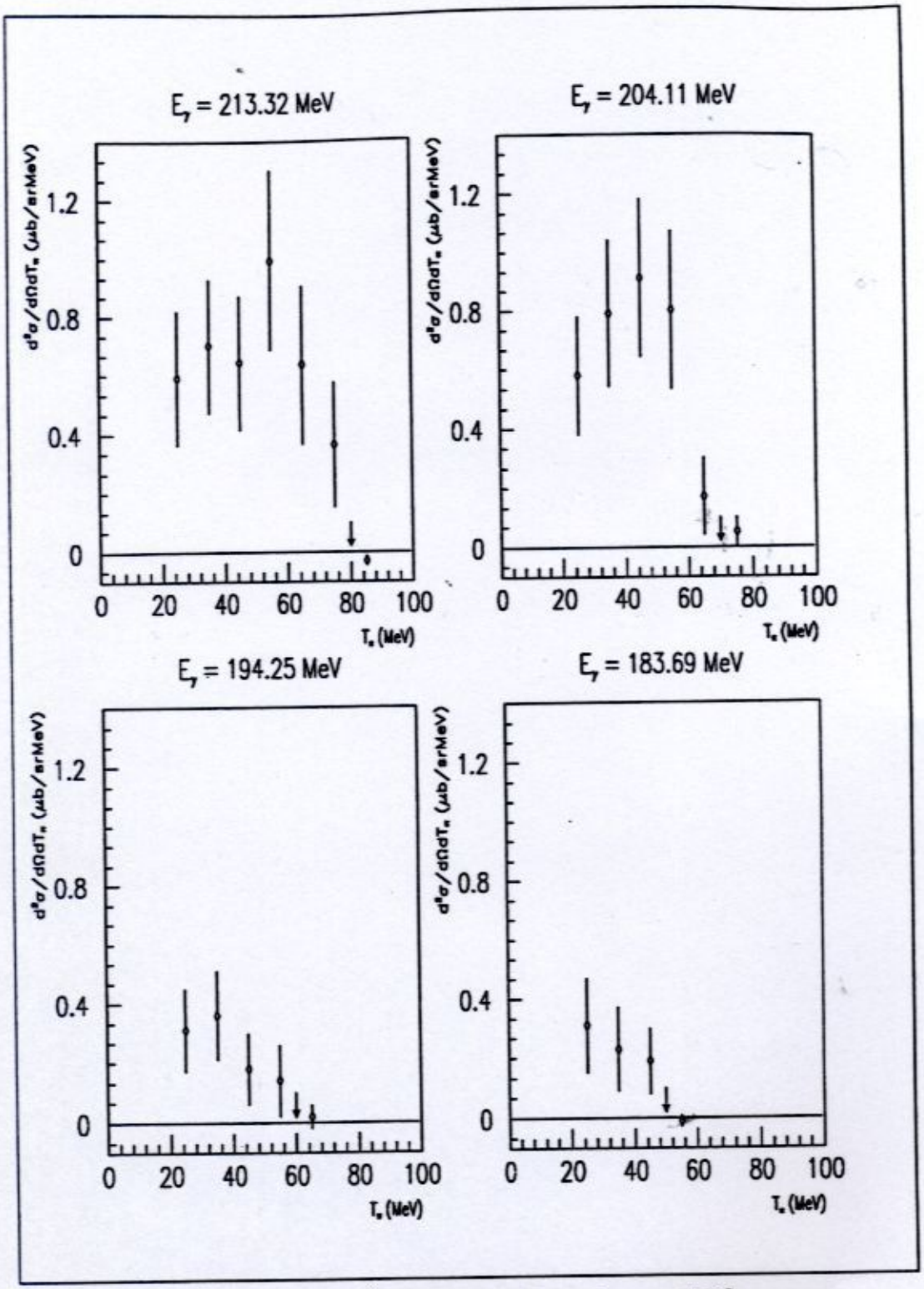

Figure 3.42: $d^2\sigma/d\Omega dT_\pi$ for Sn at $\theta_{LAB} = 141^o$

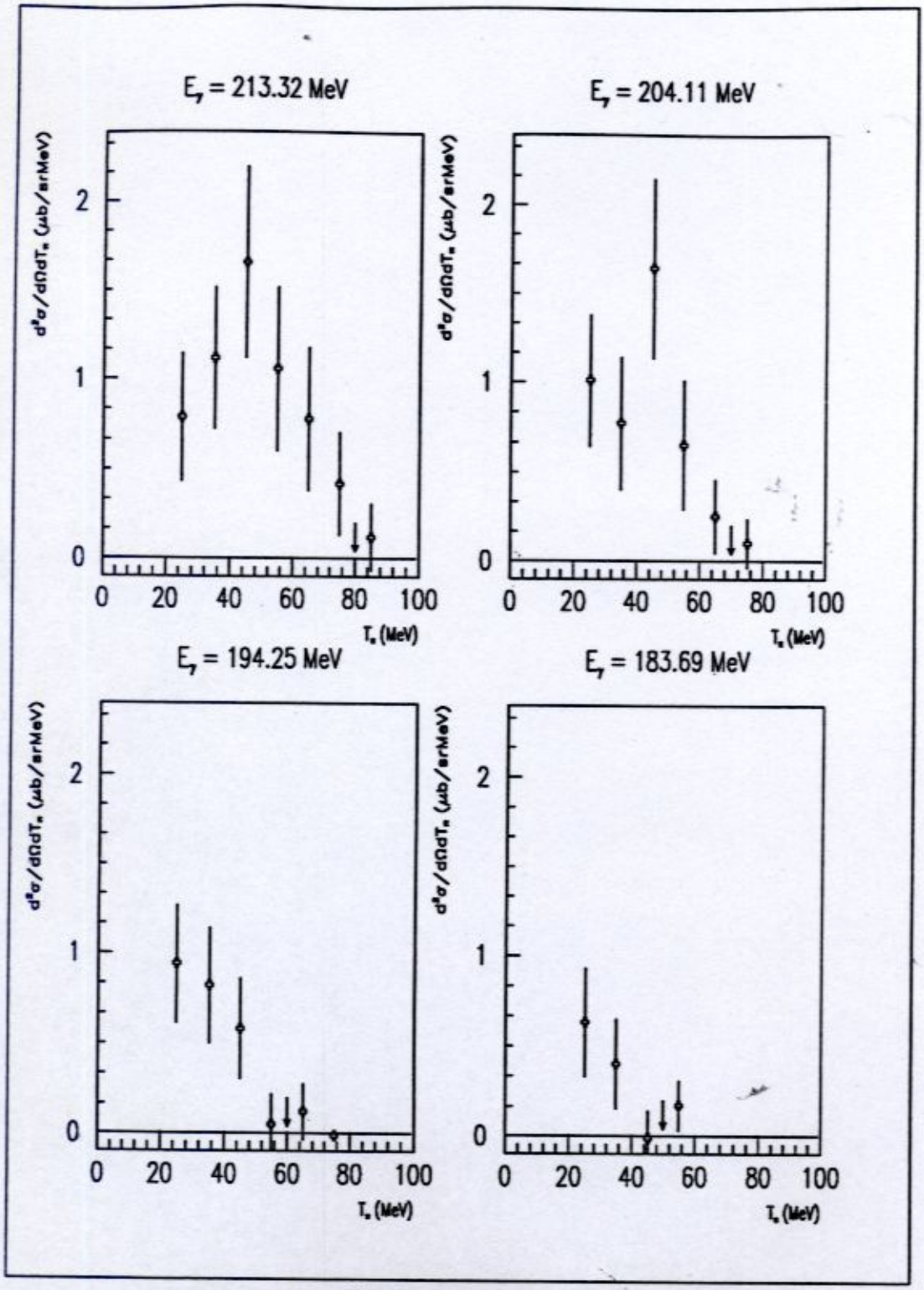

Figure 3.43: $d^2\sigma/d\Omega dT_\pi$ for Pb at $\theta_{LAB} = 109^o$

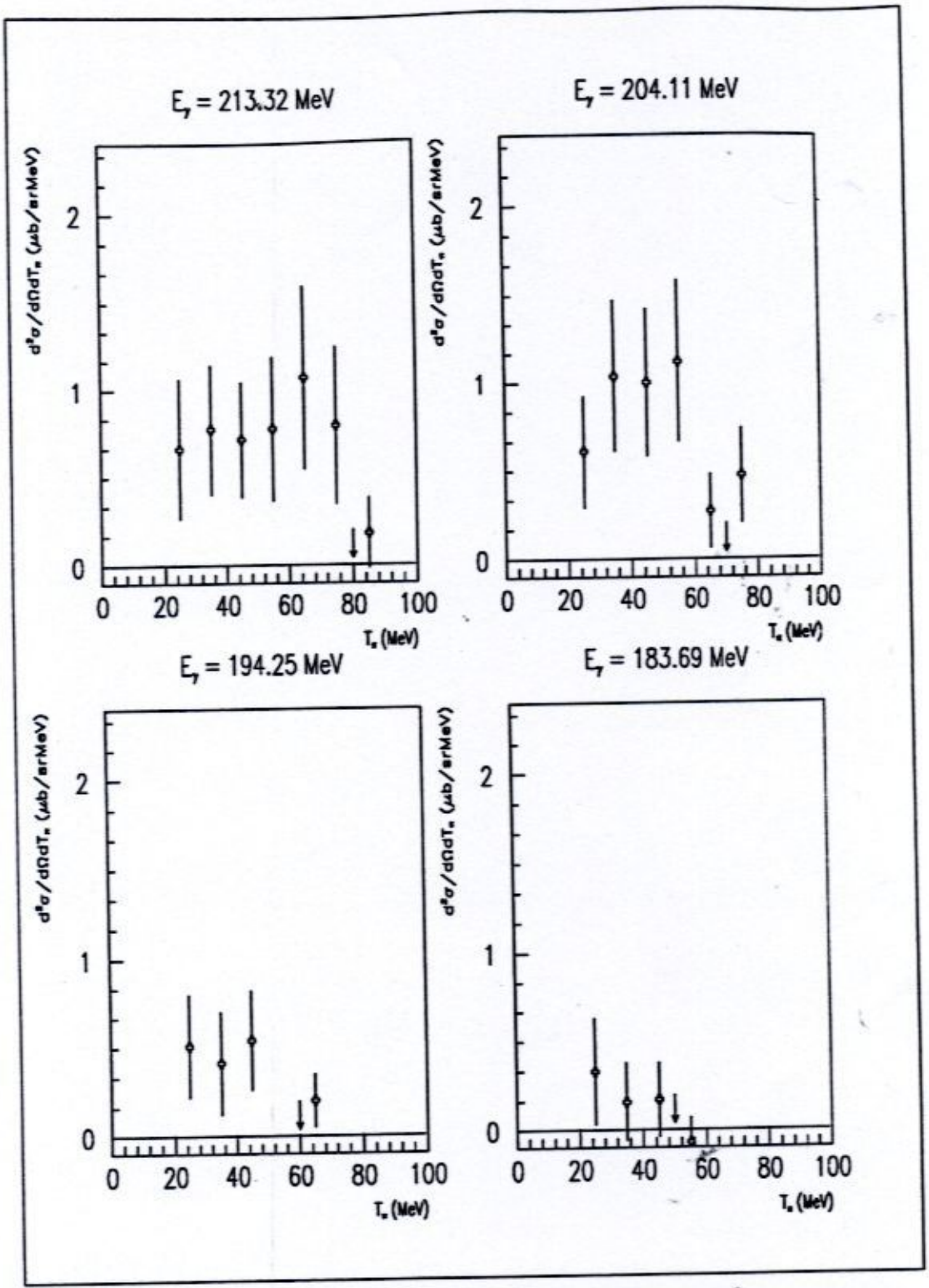

Figure 3.44: $d^2\sigma/d\Omega dT_\pi$ for Pb at $\theta_{LAB} = 141^o$

3.16 Laboratory Differential Cross Section

3.16.1 Calculation

The laboratory differential cross section as a function of photon energy was given by

$$\frac{d\sigma}{d\Omega_{LAB}}(E_\gamma, \theta) = \frac{N_\pi(E_\gamma, \theta)}{N_\gamma(E_\gamma) \cdot N \cdot \Delta\Omega(\theta)}. \qquad (3.32)$$

Due to pair contamination in the yield for θ_{LAB}=51° for the Pb target, no differential cross section values are available. Only two points are available for H at E_γ=184 MeV.

3.16.2 Results

Figures 3.45 to 3.49 illustrate the angular distributions as a function of cos(θ_{LAB}). The numerical values for these angular distributions are presented in Appendix F.

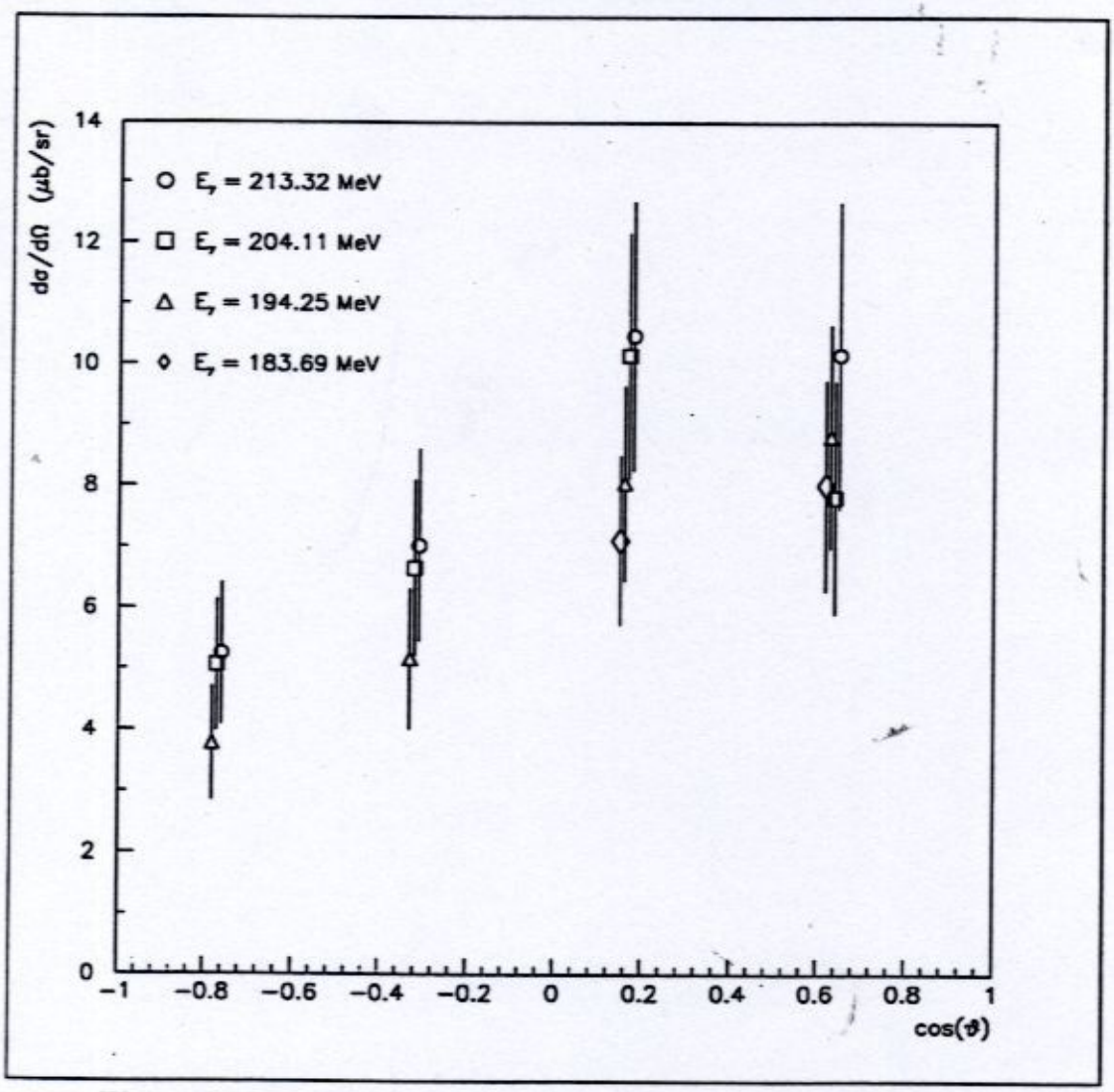

Figure 3.45: Laboratory Angular Distributions for the H Target

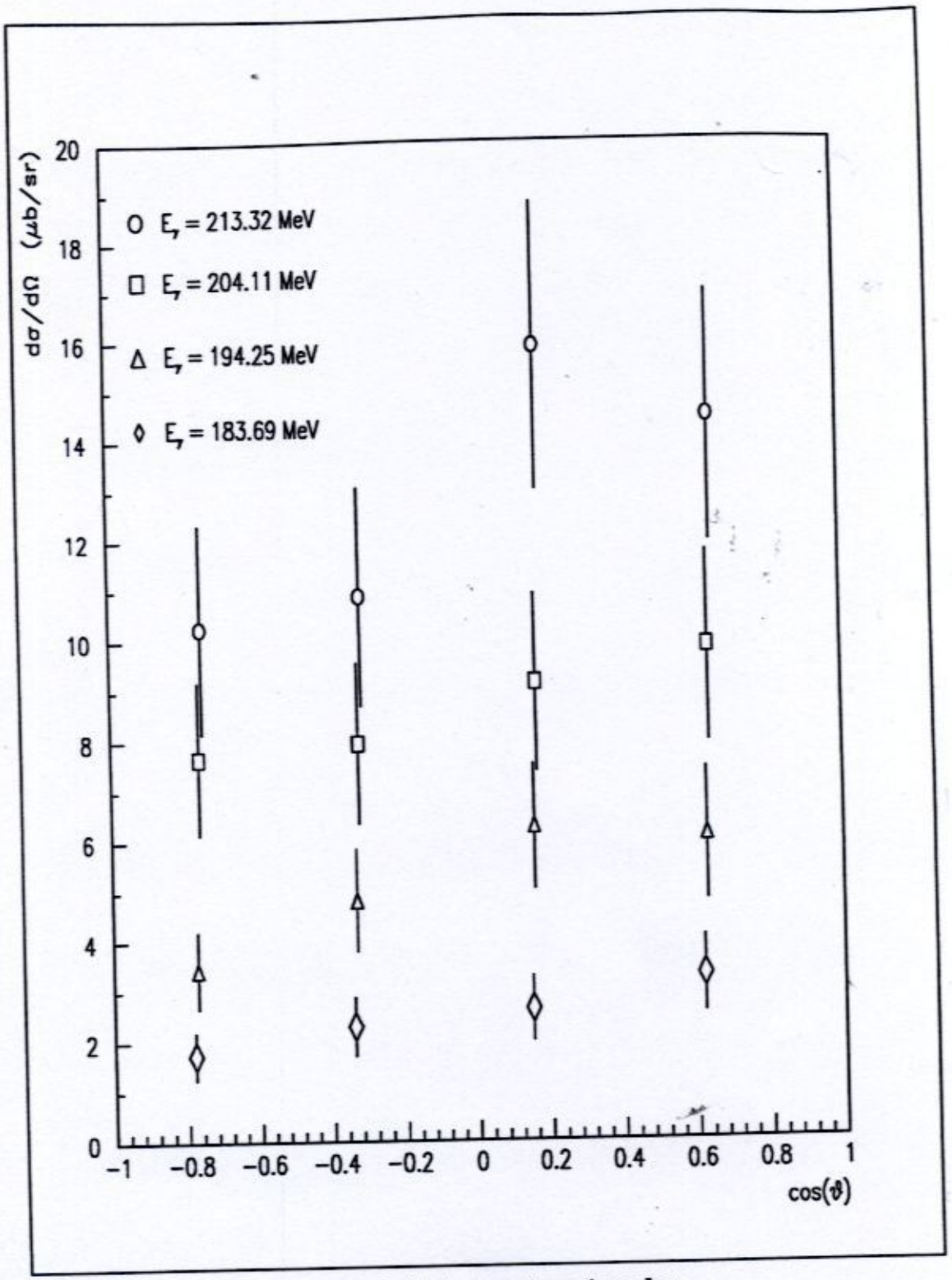

Figure 3.46: Laboratory Angular Distributions for the C Target

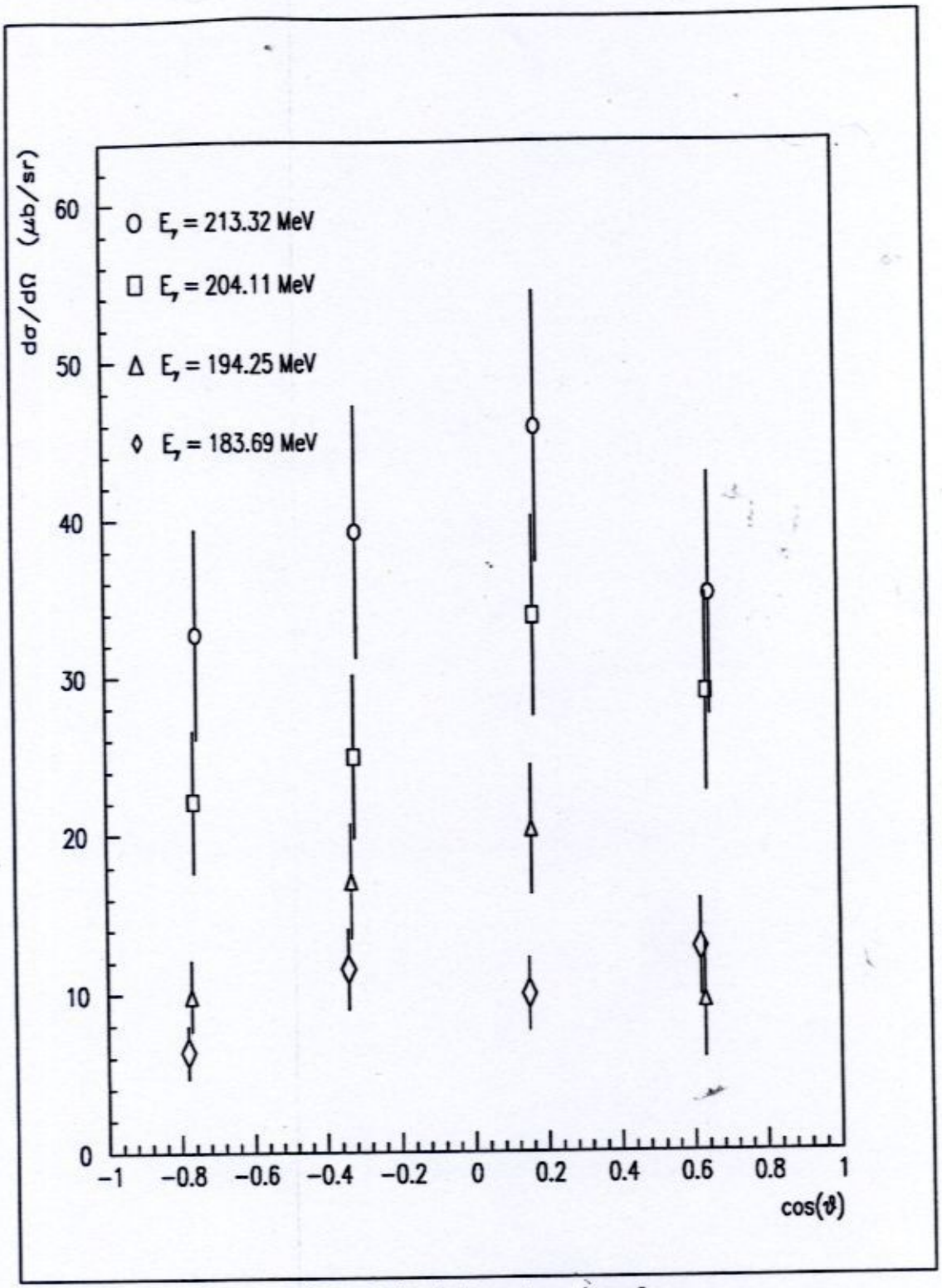

Figure 3.47: Laboratory Angular Distributions for the Ca Target

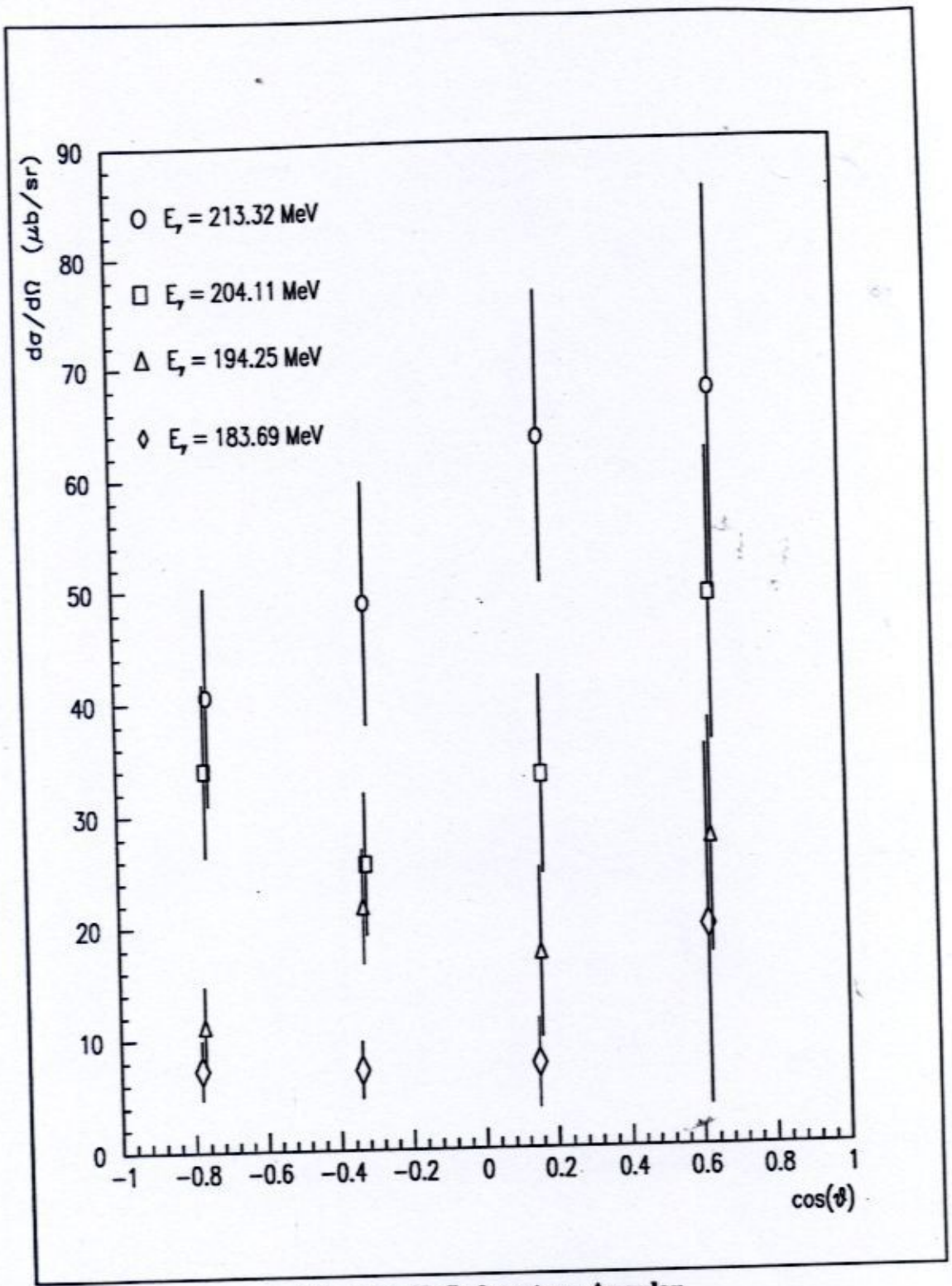

Figure 3.48: Laboratory Angular Distributions for the Sn Target

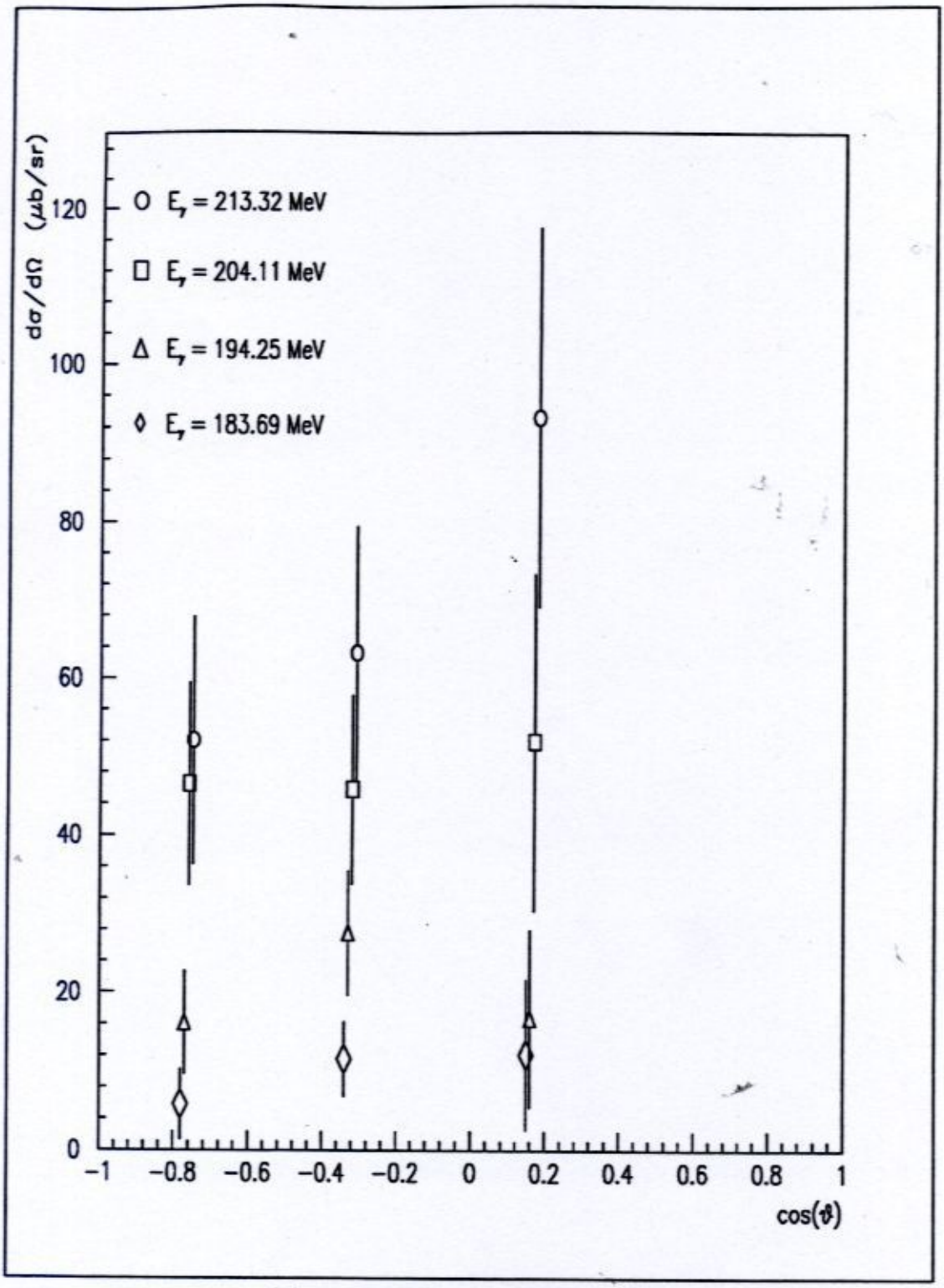

Figure 3.49: Laboratory Angular Distributions for the Pb Target

3.17 Center-of-Momentum Differential Cross Section

3.17.1 Calculation

The CM differential cross section is related to the lab cross section by a Jacobian

$$\frac{d\sigma}{d\Omega^{CM}} = \frac{d\Omega^{LAB}}{d\Omega^{CM}} \cdot \frac{d\sigma}{d\Omega^{LAB}}(E_\gamma, \theta) . \tag{3.33}$$

A discussion of the Jacobians is presented in Appendix B. The differential cross sections for π^+ from H were converted to the CM frame.

3.17.2 Results

Figure 3.50 illustrates the angular distribution obtained for H in the CM frame. The numerical values for the CM angular distributions are presented in Appendix F.

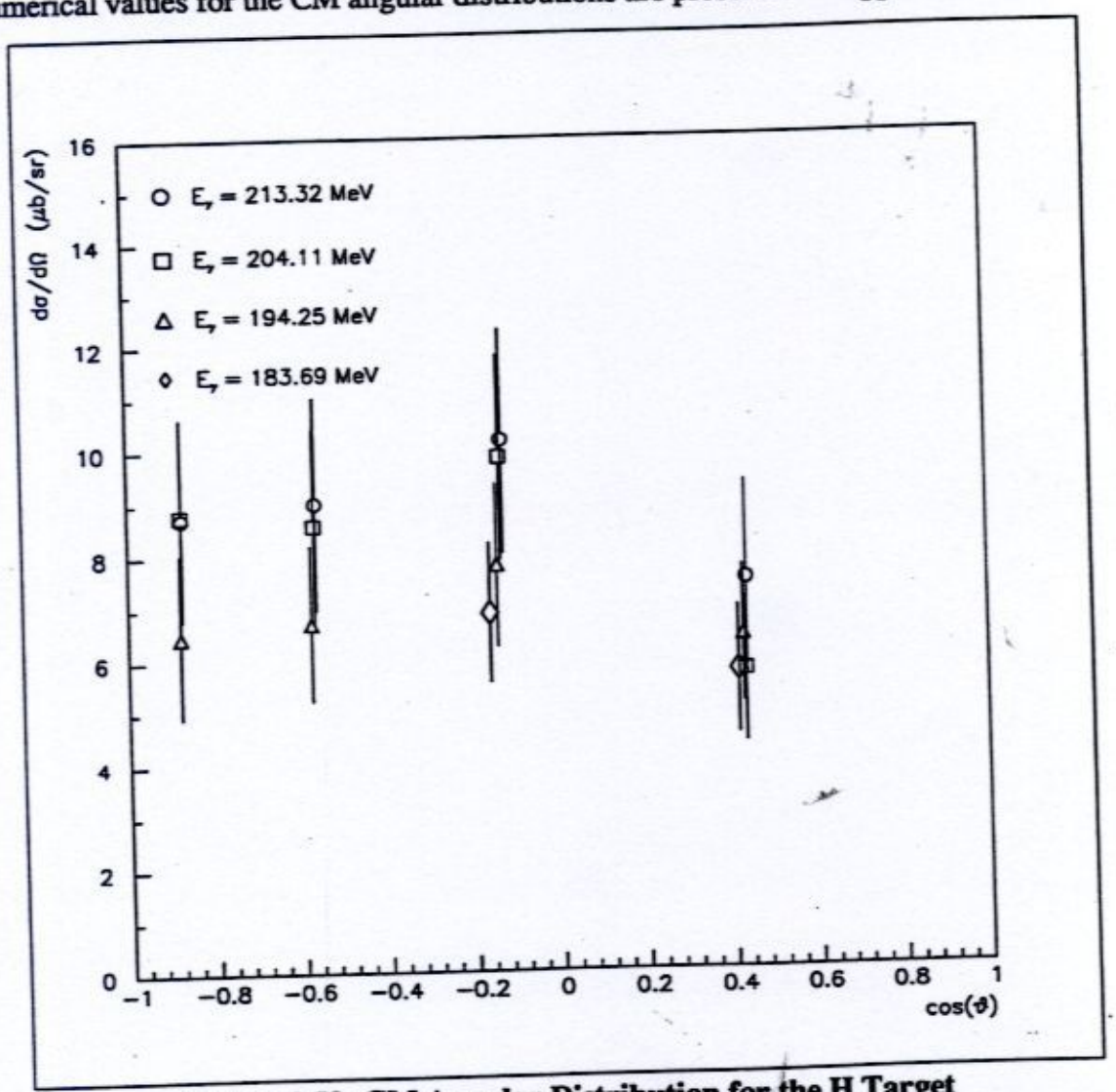

Figure 3.50: CM Angular Distribution for the H Target

3.18 Total Cross Sections

3.18.1 Calculation

The total cross section was obtained by integrating the angular distribution over $d\Omega$

$$\sigma_{Total}(E_\gamma) = \int_\Omega d\Omega \frac{d\sigma}{d\Omega}(E_\gamma, \theta) = \int_\phi d\phi \int_\theta d\theta \sin\theta \frac{d\sigma}{d\Omega}(E_\gamma, \theta). \quad (3.34)$$

The integration over φ was trivial, and the integration over θ became a sum due to the discrete nature of the π^+ detectors

$$\sigma_{TOTAL}(E_\gamma) = 2\pi \cdot \sum_{\theta=\theta_{min}}^{\theta_{max}} \frac{d\sigma}{d\Omega}(E_\gamma, \theta) \cdot \Delta(\cos(\theta)). \quad (3.35)$$

Figure 3.51 illustrates the definition of $\Delta(\cos(\theta))$. Integration of the angular distributions involved adding up the areas of the rectangles so defined.

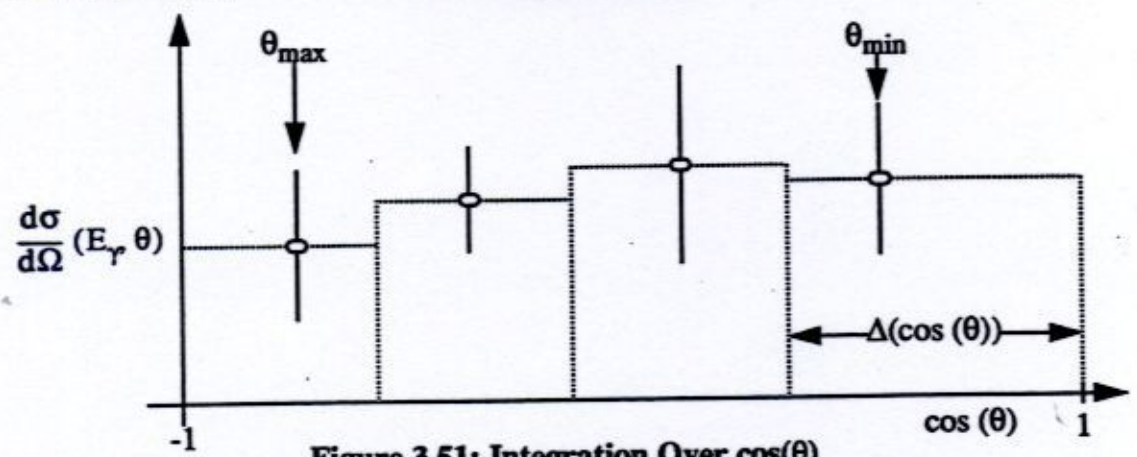

Figure 3.51: Integration Over cos(θ)

Although different values for $\Delta(\cos(\theta))$ gave different weighting to the data points, this was justified since for any given value of $\cos(\theta)$, the nearest data point was the best to use.

3.18.2 Results

Note that the angular distributions for Pb had only three points. This resulted in a variation in the width of the boxes $\Delta(\cos(\theta))$ for the purposes of the integration. No finite acceptance correction was made to the total cross section values, since the angular distributions were reasonably flat over the angular bite of the detectors. The following plot (Figure 3.52) illustrates the total cross sections as a function of photon energy. The numerical values for the total cross sections are presented in Appendix F.

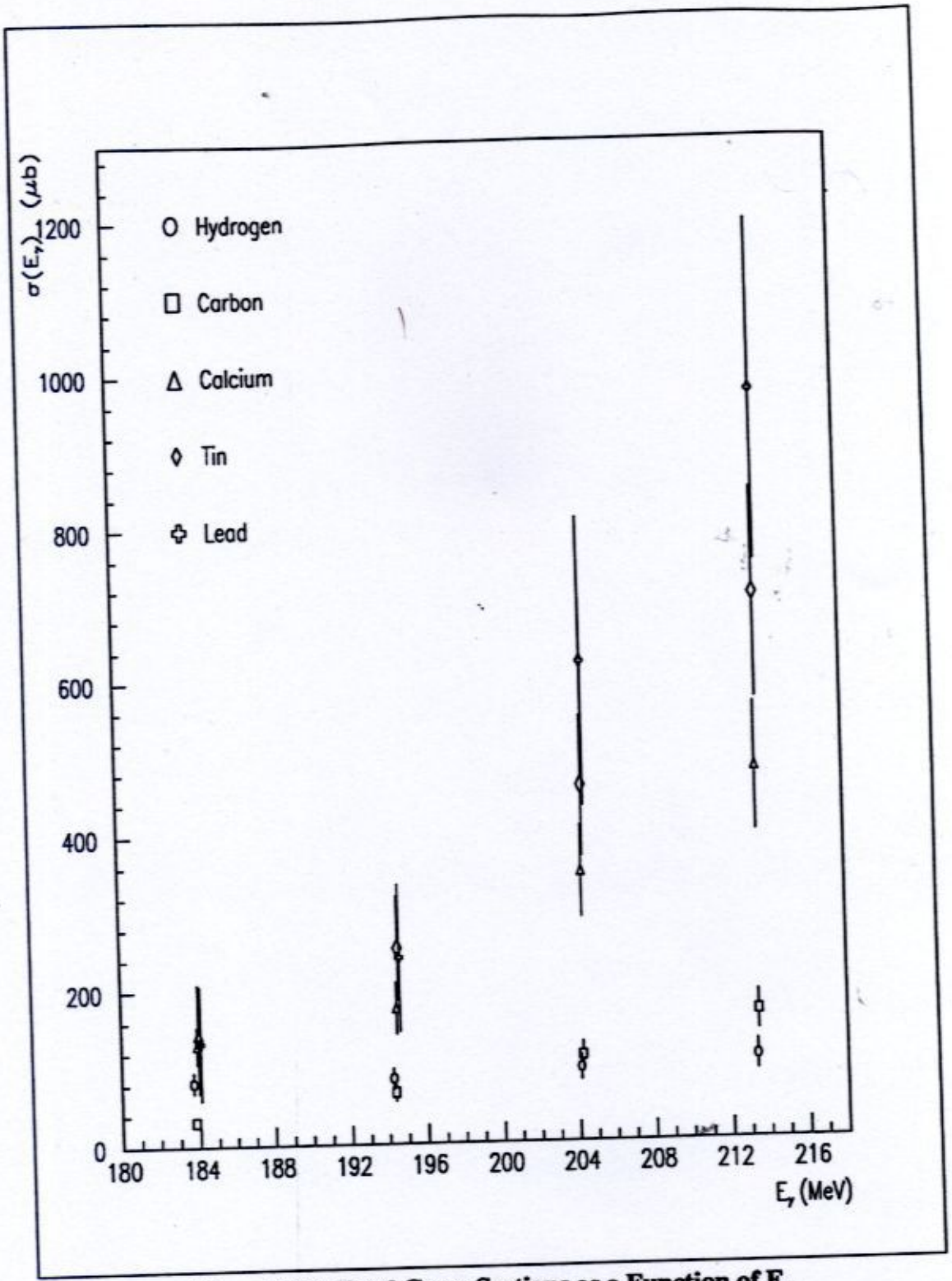

Figure 3.52: Total Cross Sections as a Function of E_γ

Chapter 4. COMPARISONS AND CONCLUSIONS

Comparisons between results and existing data sets and calculations are made. Conclusions are drawn, and further work is suggested.

4.1 Comparisons of Selected Results

4.1.1 The Elementary Reaction $p(\gamma,\pi^+)n$

The angular distribution coefficients P_i presented in equations 1.3 through 1.5 were calculated for the literature values of the amplitudes, and compared with the experimental values extracted from the CM angular distributions.

Figures 4.1 to 4.3 illustrate the fit of a second order polynomial in $\cos(\theta^{CM})$ to the CM angular distributions from the proton for three of the four photon energy bins. No fit was attempted for the fourth photon energy bin, 184 MeV, because only two points were present in the angular distribution. Total errors are shown. A summary of the results of these fits is presented in Table 4.1.

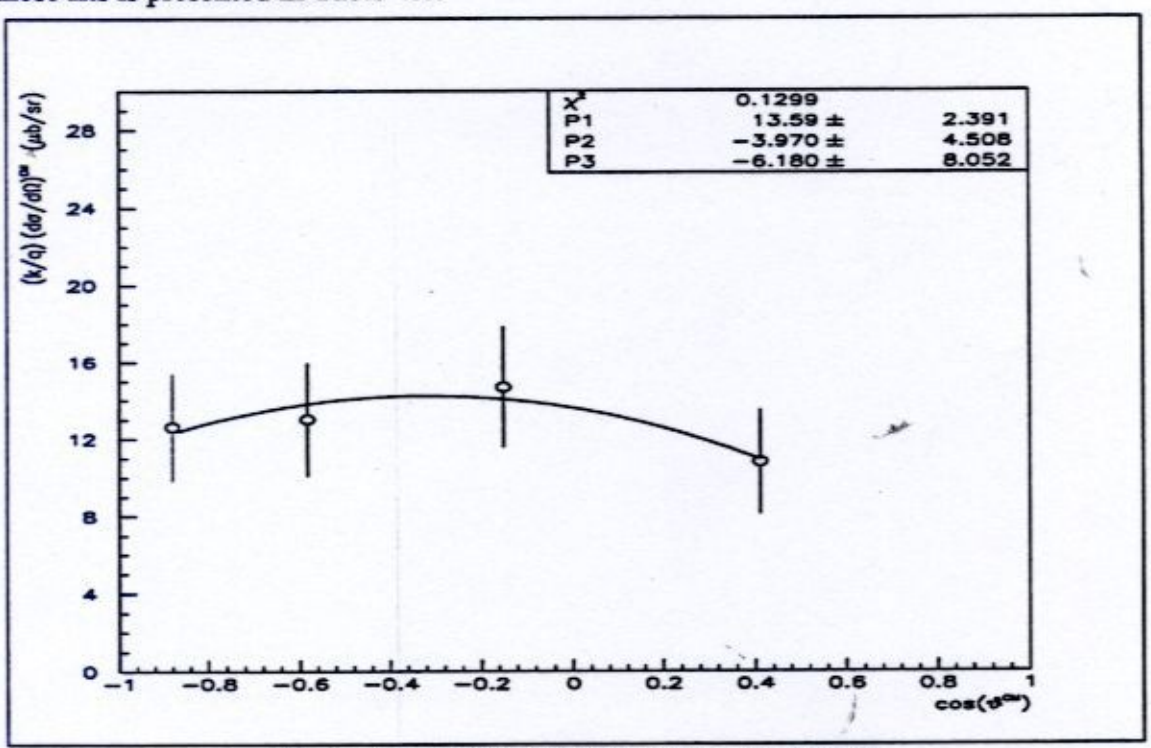

Figure 4.1: P_i Coefficients at E_γ = 213 MeV

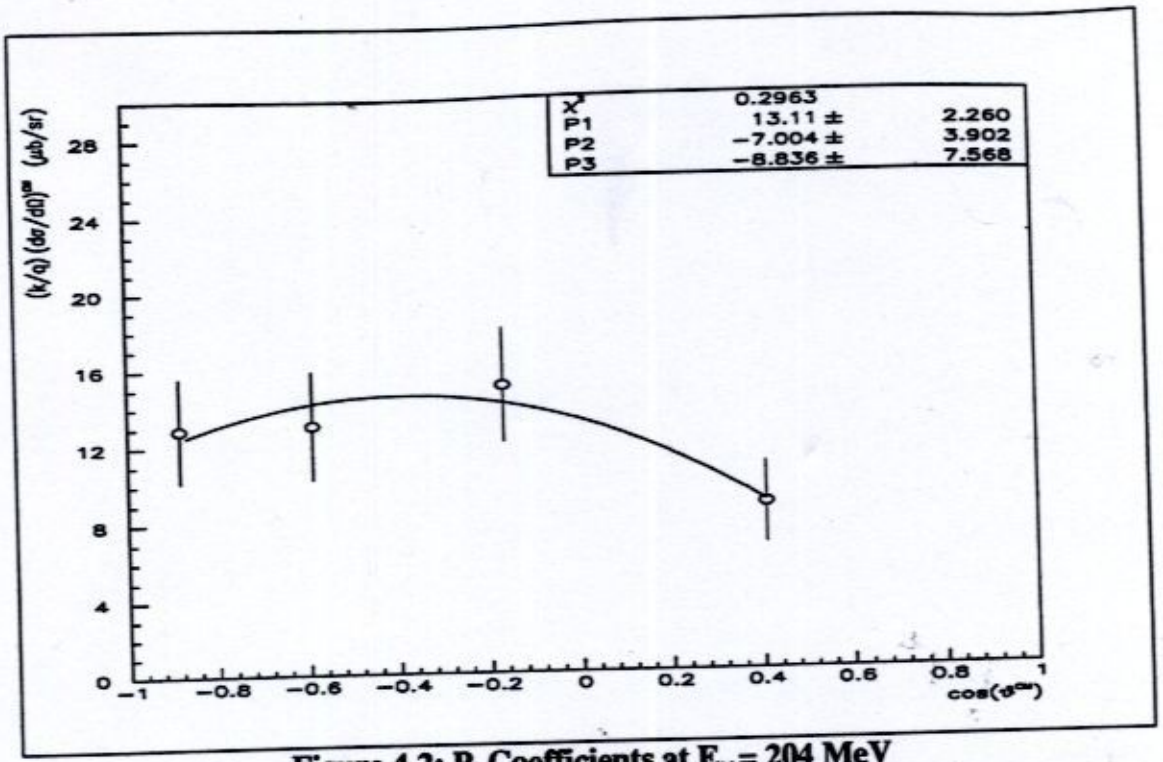

Figure 4.2: P_i Coefficients at E_γ = 204 MeV

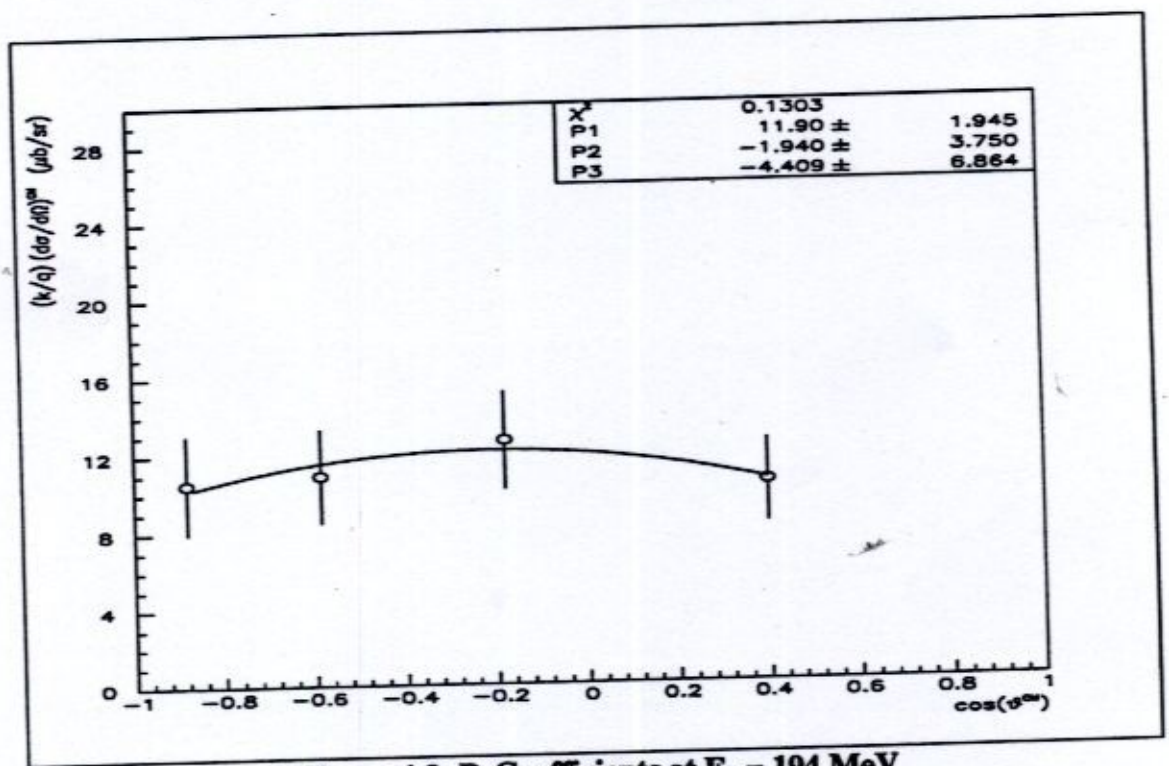

Figure 4.3: P_i Coefficients at E_γ = 194 MeV

Table 4.1: Experimentally Determined P_i Coefficients

E_γ [MeV]	P_1 [μb/sr]	P_2 [μb/sr]	P_3 [μb/sr]
213	13.59+/-2.39	-3.97+/-4.51	-6.18+/-8.05
204	13.11+/-2.26	-7.00+/-3.90	-8.84+/-7.57
194	11.90+/-1.95	-1.94+/-3.75	-4.41+/-6.86

The experimentally determined P_i coefficients are plotted against the theoretically predicted values of Berends *et al.*, and the results of the multipole analysis of Pfeil *et al.* in Figure 4.4. The P_1 coefficients determined in this experiment are lower than the predictions. The P_2 and P_3 values seem to reproduce the expected values somewhat better, although the error bars on the points obtained from the fits are quite large. The overall agreement is good.

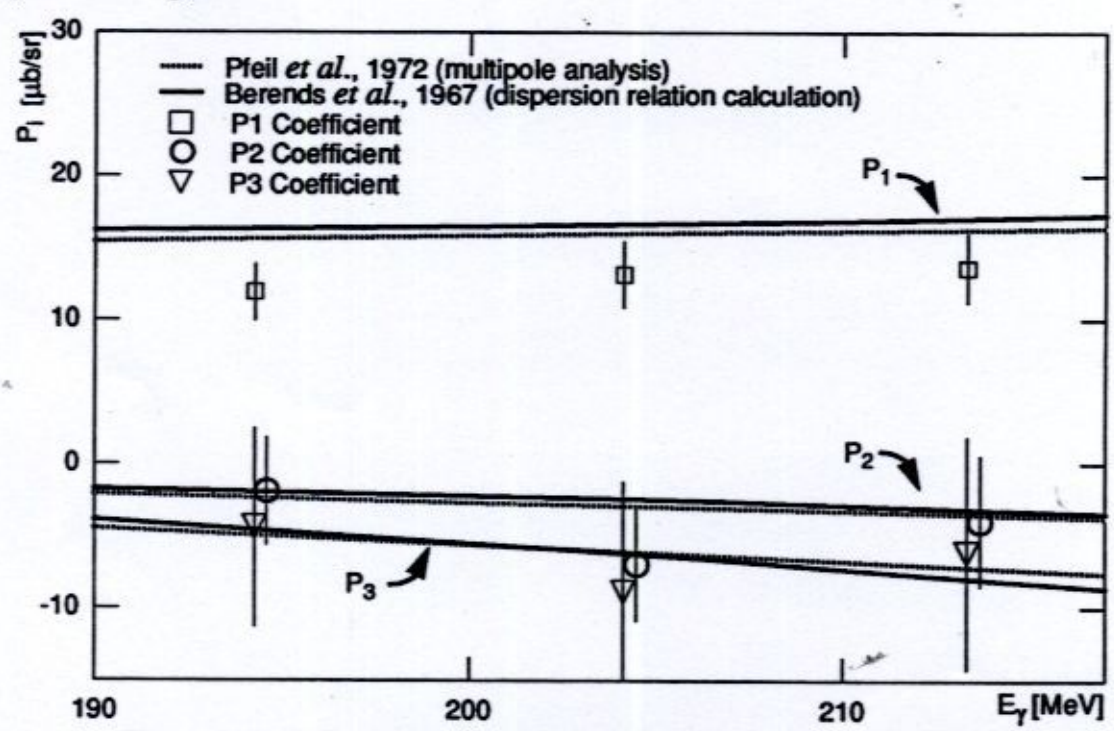

Figure 4.4: A Comparison of P_i Coefficients to Literature Values

In order to facilitate a direct comparison, the experimental data points with their total errors are plotted in Figures 4.5 through 4.8, together with the previously introduced theoretical predictions and data sets.

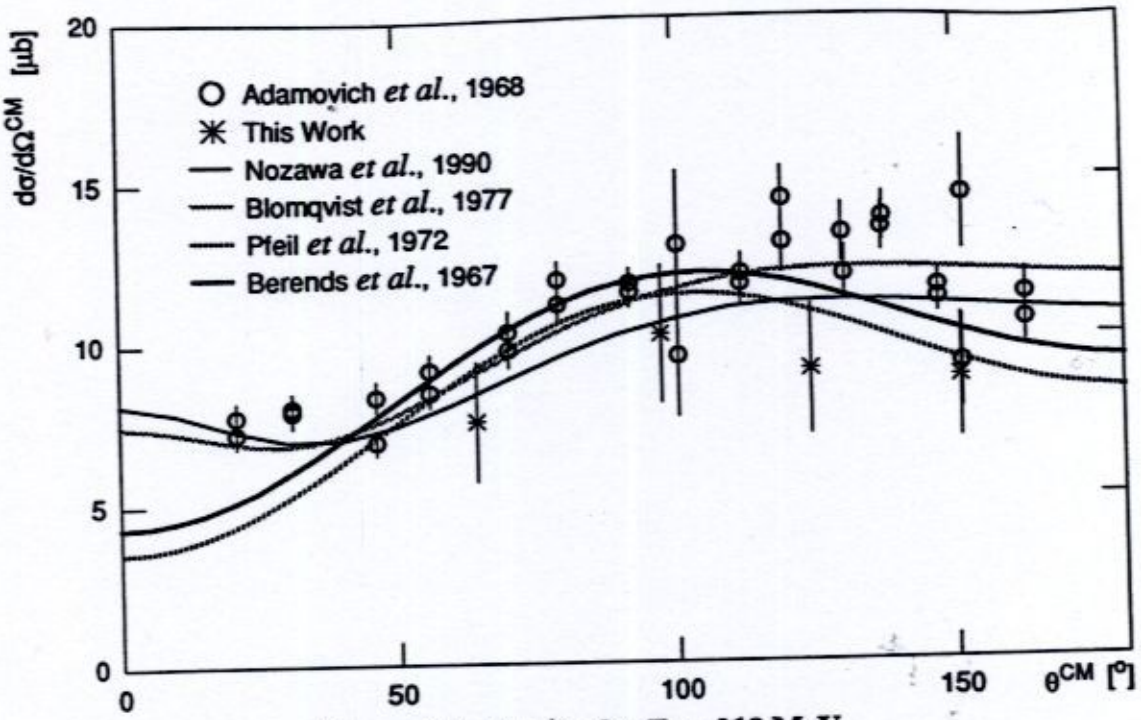

Figure 4.5: $p(\gamma,\pi^+)n$ for $E_\gamma = 213$ MeV

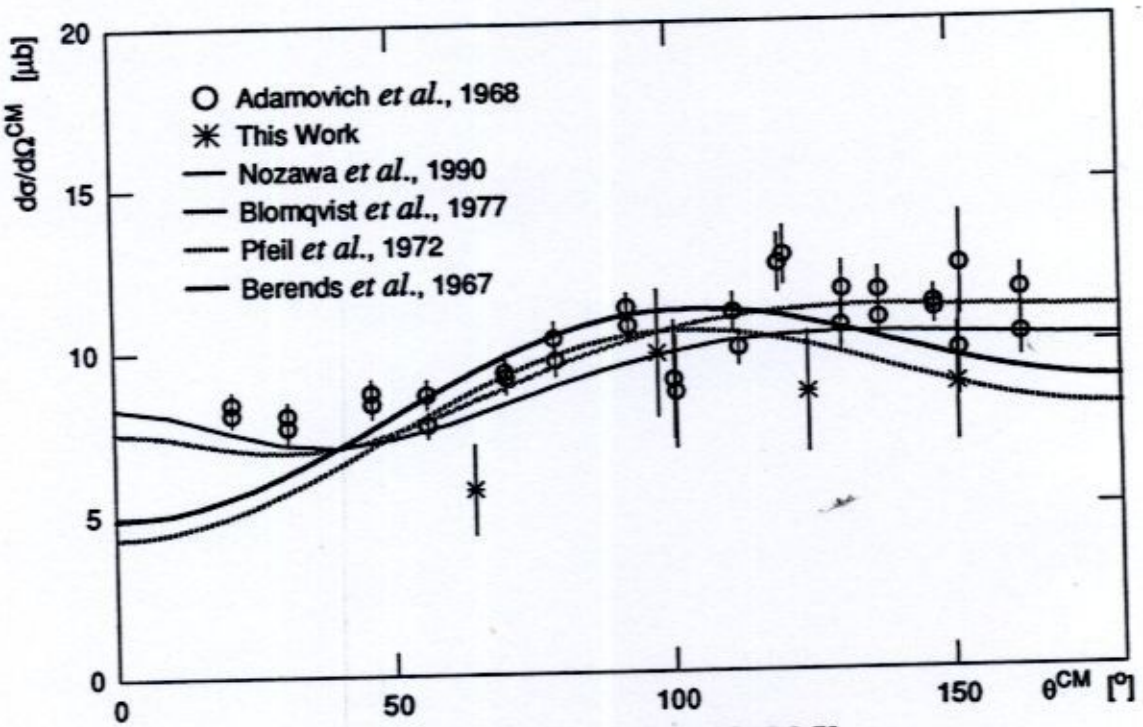

Figure 4.6: $p(\gamma,\pi^+)n$ for $E_\gamma = 204$ MeV

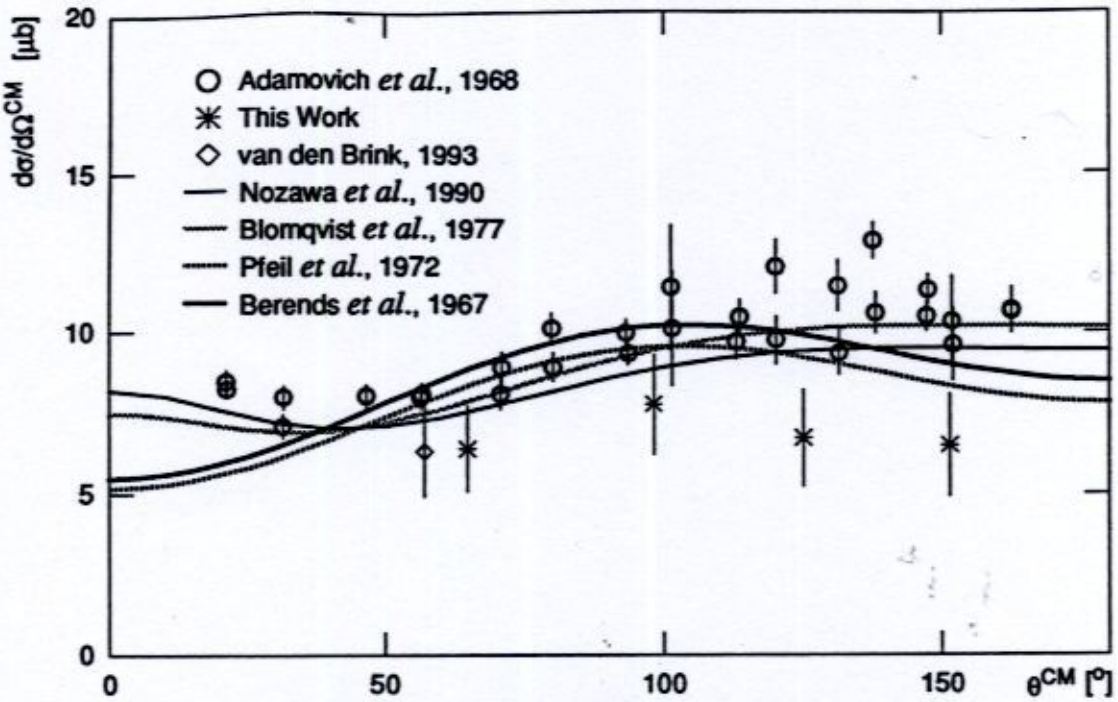

Figure 4.7: $p(\gamma,\pi^+)n$ for $E_\gamma = 194$ MeV

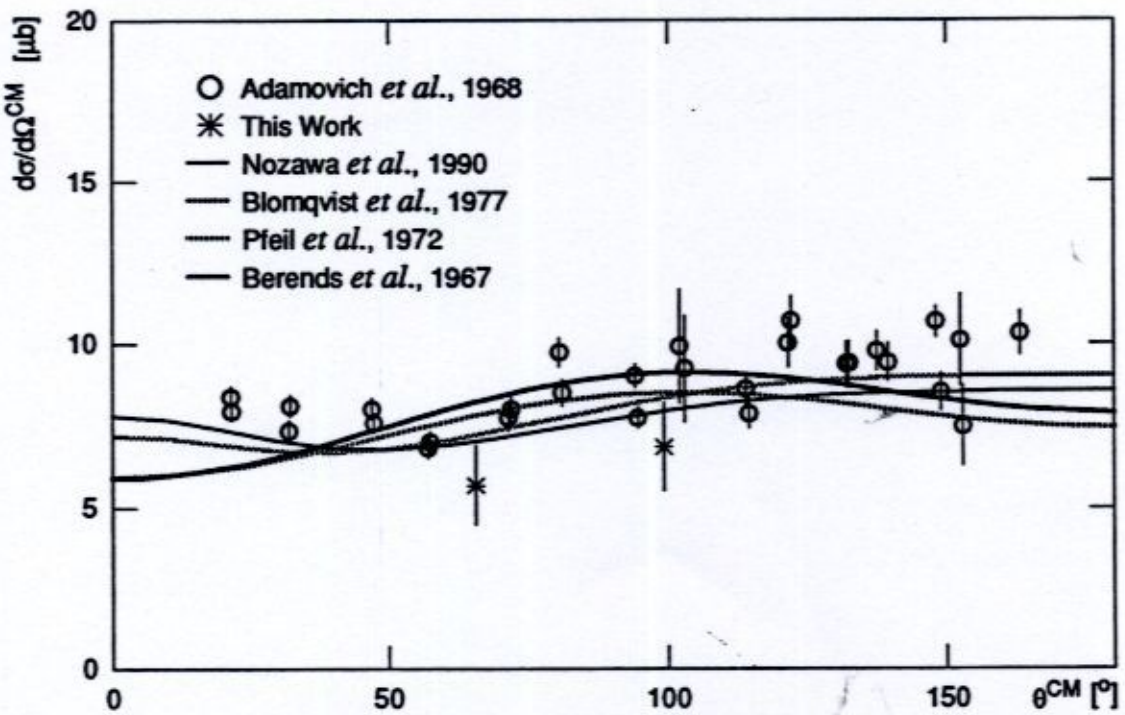

Figure 4.8: $p(\gamma,\pi^+)n$ for $E_\gamma = 184$ MeV

The data from this experiment tend to peak at about 100° in the CM frame, and seem to favor the results of the multipole analysis over the effective Lagrangian calculation of Blomqvist *et al.* and the dynamical calculation of Nozawa *et al.* The data from this work are lower than the bremsstrahlung data of Adamovich *et al.*, and agreement is poor. However, agreement with the one tagged photon data point of van den Brink is excellent.

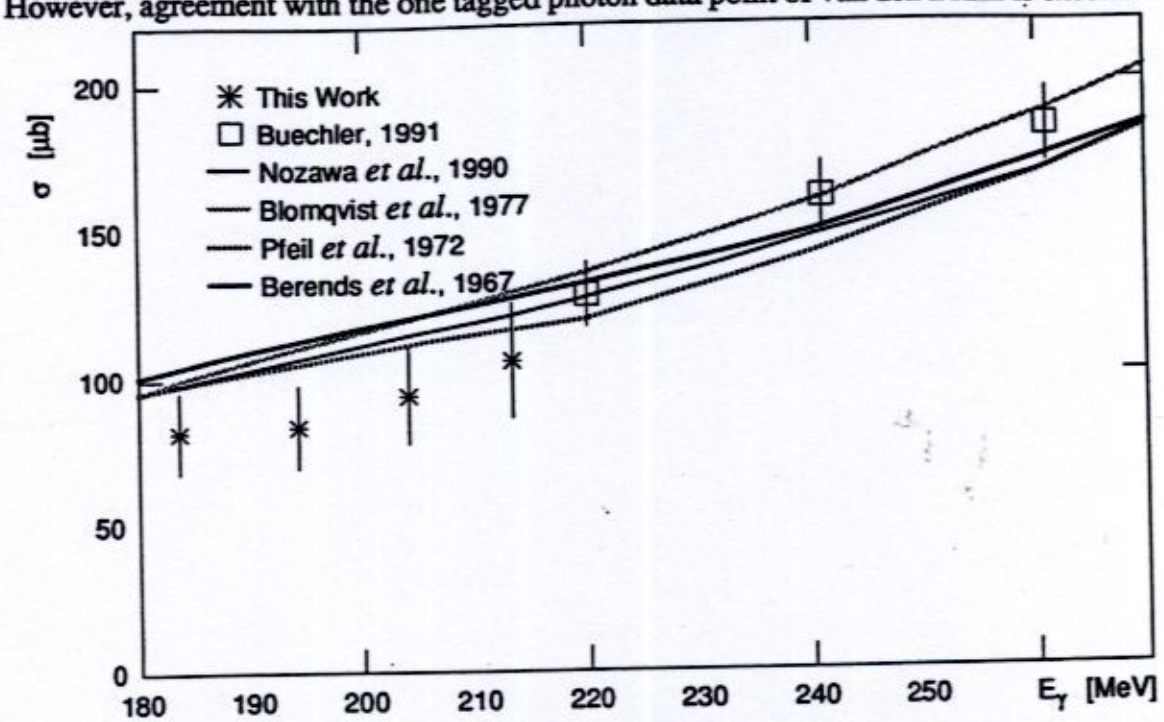

Figure 4.9: The Total Cross Section for $p(\gamma,\pi^+)n$

Figure 4.9 illustrates a comparison of the total cross sections obtained in this experiment via integration of the angular distributions with the integrated tagged photon data of Buechler and the theoretical predictions. Total errors are shown. Clearly, the two data sets are consistent, while the calculations tend to overestimate the total cross sections at the photon energies of this work.

Recall that the elementary cross section consists of a Born term (representing diagrams A, B, C, and D of Figure 1.2) and the Δ(1232) resonance (diagrams E and F). The magnitude of the contribution of the Born term to the elementary cross section is determined by the coupling constant $f_\pi^2/4\pi - 0.08$. In the past, the difference between experiment and theory was thought to be due to incorrectly calculating the effect of the Δ(1232) resonance. The magnitude of the Born term was thought to be well-known. However, very recently it has also been suggested that the value of the coupling constant

may be too high by as much as 5% (Stoks *et al.*, 1988; Workman *et al.*, 1992). The result of reducing the coupling constant is a reduction in the magnitude of the calculated total cross section presented in Figure 4.9. The exact effect is currently being investigated (Strakovsky, 1993), but was not available at the time of this work.

4.1.2 The Quasi-Free Reaction X(γ,π⁺)

Figures 4.10 and 4.11 illustrate comparisons between two double differential cross section sets obtained in this work, those extracted by Arends *et al.*, and those theoretically predicted by Carrasco *et al.* at ~ 215 MeV for laboratory angles of 50° and 110°. The π^+ energy bins are 10 MeV wide, and the values of the double differential cross sections are plotted at the center of the bins. Total error bars are shown.

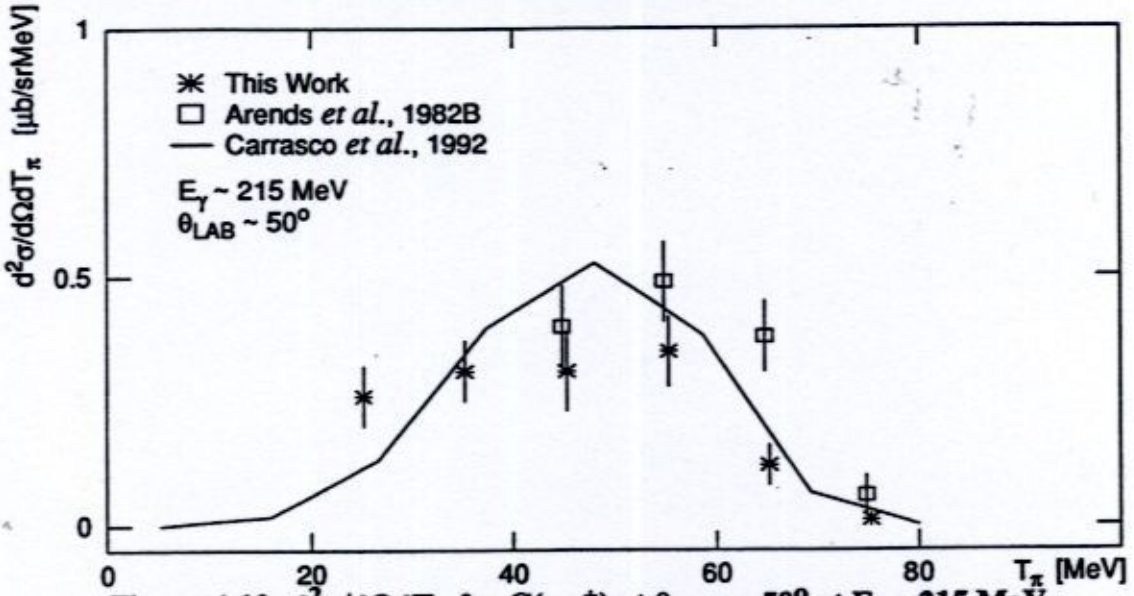

Figure 4.10: $d^2\sigma/d\Omega dT_\pi$ for $C(\gamma,\pi^+)$ at θ_{LAB} ~ 50° at E_γ ~ 215 MeV

The above figure represents the best agreement between the data of Arends *et al.* and the calculations of Carrasco *et al.* The data of this work is in general lower than that of Arends *et al.* in the region $T_\pi > 40$ MeV; however, overall agreement is good. Two new data points are presented at 25 MeV and 35 MeV. Clearly, the theory favors neither data set outright but does do a nice job of representing the entire distribution of data points.

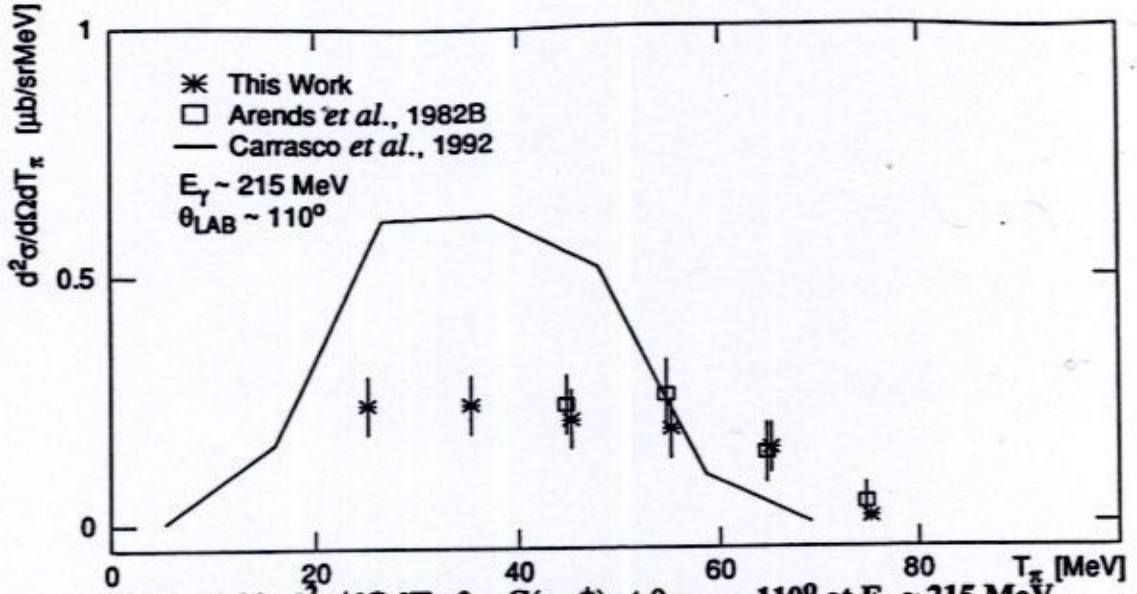

Figure 4.11: $d^2\sigma/d\Omega dT_\pi$ for $C(\gamma,\pi^+)$ at θ_{LAB} ~ 110° at E_γ ~ 215 MeV

Figure 4.11 represents poor agreement between the data of Arends *et al.* and the calculations of Carrasco *et al.* However, it is important to note the data of this work are in excellent agreement with that of Arends *et al.* in the region $T_\pi > 40$ MeV. Again, two new data points are presented at 25 MeV and 35 MeV. Clearly, the theory dramatically overestimates the magnitude of the double differential cross sections extracted from both experiments in the region $T_\pi < 50$ MeV. The excellent agreement between the two data sets indicates a problem with the theory rather than with the data.

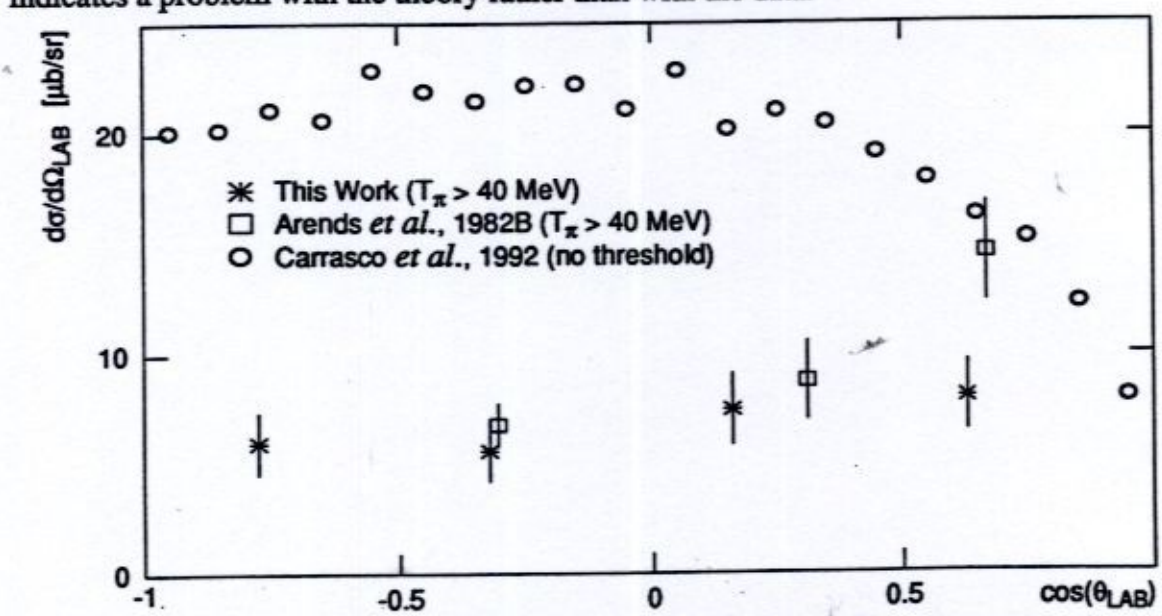

Figure 4.12: An Angular Distribution for $C(\gamma,\pi^+)$ at E_γ ~ 215 MeV

Figure 4.12 presents the angular distributions for C at $E_\gamma \sim 215$ MeV obtained from this experiment, by Arends *et al.*, and the predictions of Carrasco *et al.* The angular distribution attributed to Arends *et al.* was obtained by integrating published double differential cross sections. A software detector threshold of 40 MeV was applied to the present data to make the comparison between data sets possible. As previously mentioned, the calculations of Carrasco *et al.* represent the entire reaction yield. The data of this work is in excellent agreement with that of Arends *et al.* in the region $\theta_{LAB} > 65^o$ ($\cos(\theta_{LAB}) < 0.4$), but the agreement is poor at the forward angle. Note that the experiment is, in general, easier to perform at the backward angles due to the absence of background. Any background not properly discriminated against in the analysis will tend to increase the calculated differential cross section. The agreement of the two data sets at the back angles indicates a good knowledge of the absolute value of the differential cross sections in this region, which is not reproduced by the theory of Carrasco *et al.*, even in view of the inclusion of the entire range of π^+ energies in their calculation. This disagreement between the two data sets at the forward angle is believed to be associated with extraneous background being included in the yield determined by Arends *et al.*, since the π^+ identification in their measurement was less rigorous than that performed here.

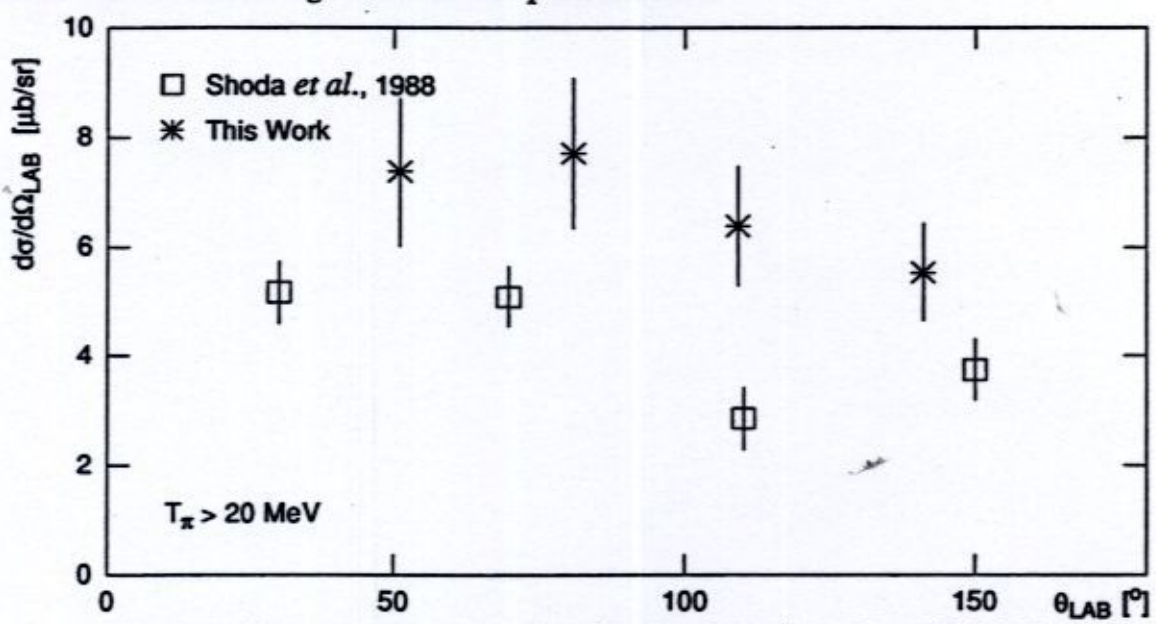

Figure 4.13: An Angular Distribution for $C(\gamma,\pi^+)$ at $E_\gamma \sim 200$ MeV

Figure 4.13 shows a comparison between the angular distribution for C at $E_\gamma \sim 200$ MeV obtained from this experiment, and that of Shoda *et al.* No mention of the first estimation to the QF π^+ photoproduction angular distribution is made since it was clear before

the experiment was even performed that the predictions were extremely poor with respect to the existing data. Total errors are shown for the data points of this work. The data points of Shoda *et al.* have statistical error bars only. A software detector threshold of 20 MeV was applied to the data of this work to make the comparison between data sets possible. The angular distributions from this work for $E_\gamma = 204$ MeV and $E_\gamma = 194$ MeV were simply averaged to estimate the angular distribution at $E_\gamma \sim 200$ MeV. Clearly, the agreement is poor. The results of this experiment are higher than those of Shoda *et al.* by as much as a factor of two. However, recall that Shoda *et al.*'s data were obtained using electroproduction of π^+ and the photon difference method. With this method, electron beams of two different energies are used to electroproduce π^+ using virtual photons, and the resulting spectra are normalized and subtracted, with the results being due to the difference in the two virtual photon distributions - "monoenergetic" virtual photons. Further, the measurement was made to several discrete final states which included both a π^+ and B or B^*, and the inclusive angular distribution was estimated by adding up these measurements. This constitutes an extremely difficult experiment - one that by design can only underestimate the inclusive process due to the inevitably missed reaction channels, however small. The difficulty of the experiment is reflected in the fact that no mention of systematic error is made. Thus, the disagreement between the angular distribution of Shoda *et al.* and that obtained from this experiment is not a large concern, particularly in view of the strong agreement between the more reliable tagged photon data of Arends *et al.* and that of this work at all angles save the most forward.

To compare the angular distributions of Carrasco *et al.* to those obtained in this measurement for all targets over the entire energy range of detected π^+, it was necessary to estimate the effect of the 17 MeV detector threshold on the experimentally determined differential cross sections and thus angular distributions. The effect was calculated by determining the ratio of the integral of the theoretically predicted double differential cross section from detector threshold to that from reaction threshold as given by

$$\text{lost} = 1 - \frac{\int_{\text{detector threshold}} \frac{d^2\sigma}{d\Omega dT_\pi} dT_\pi}{\int_{\text{reaction threshold}} \frac{d^2\sigma}{d\Omega dT_\pi} dT_\pi}. \qquad (4.36)$$

Table 4.2 summarizes this estimated loss in differential cross section. Because the double differential cross sections used for this purpose were calculations and not data, the estimates thus obtained should be viewed as zeroth order approximations only, since the calculations do not represent the data well anywhere but at the most forward angles.

Table 4.2: Estimated Detector Threshold Effects on $d\sigma/d\Omega$

Target	Angle [°]	lost [%]
C	51	0.68
	81	2.89
	109	5.00
	141	7.45
Ca	51	0.63
	81	3.10
	109	5.42
	141	7.78
Sn	51	0.63
	81	2.79
	109	5.12
	141	9.75
Pb	51	0.41
	81	2.05
	109	4.99
	141	8.03

Because of this, the differential cross sections comprising the angular distributions illustrated below have *not* been scaled by this factor. The calculations include the π^+ energy region from reaction threshold to 17 MeV, while the data do not.

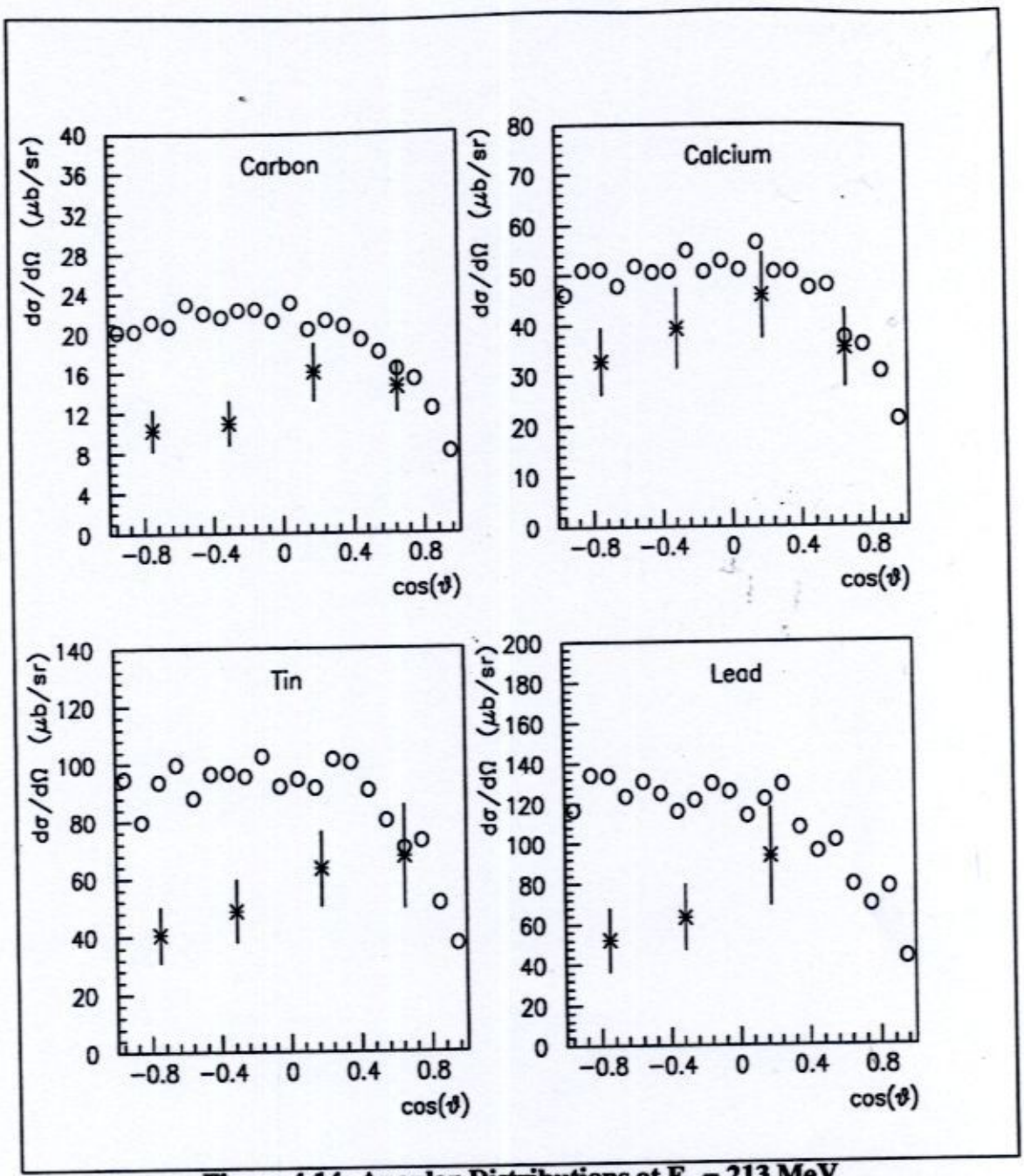

Figure 4.14: Angular Distributions at $E_\gamma = 213$ MeV

Figure 4.14 shows a comparison between the angular distributions obtained in this experiment for the four targets and those predicted by Carrasco *et al.* for $E_\gamma = 213$ MeV. Total errors are shown. Clearly, the agreement between the data point at the forward angle and the calculation is excellent. At the backward angles, as expected, the agreement is poorer.

Figure 4.15 presents the total cross sections for C obtained from this experiment, those of Arends *et al.*, and the calculations of Carrasco *et al.* obtained by integrating the angular distributions. Both data sets and the calculation have been modified to include the detector threshold of 40 MeV, and total errors are shown.

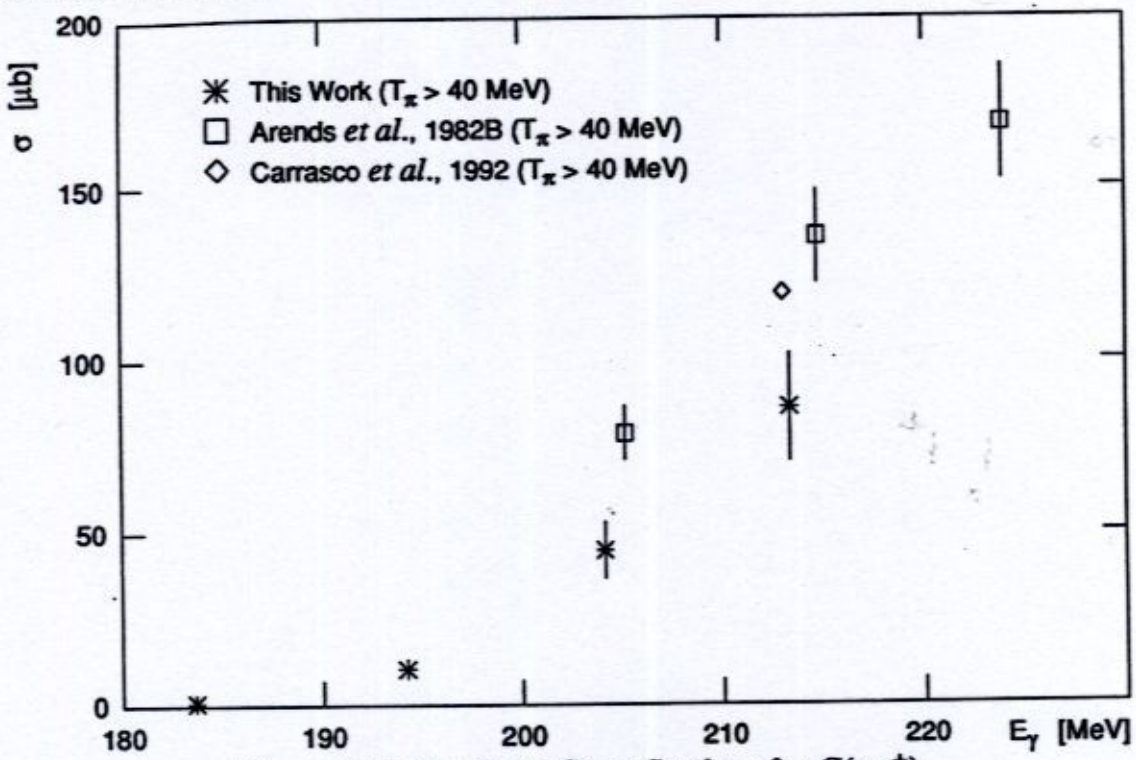

Figure 4.15: The Total Cross Sections for C(γ,π^+)

Again, no mention is made of the first approximation to the total QF π^+ photoproduction cross section because it was already shown to be a poor representation of the existing data. As expected from both the double differential cross sections and angular distributions previously discussed, the total cross section extracted in this work is less than that obtained by Arends *et al.* or predicted by Carrasco *et al.* In fact, with the detector threshold of 40 MeV applied in software to the data of this work, the reaction channel is basically closed at E_γ= 180 MeV, since the total cross section is consistent with zero.

Figure 4.16 illustrates the total QF π^+ photoproduction cross section per proton obtained for all five targets investigated in this experiment. A uniform detector threshold of 17 MeV is present in all the data, and total errors are shown. As expected, the value of the total QF π^+ photoproduction cross section per proton is less than that for the free process, and decreases as A increases.

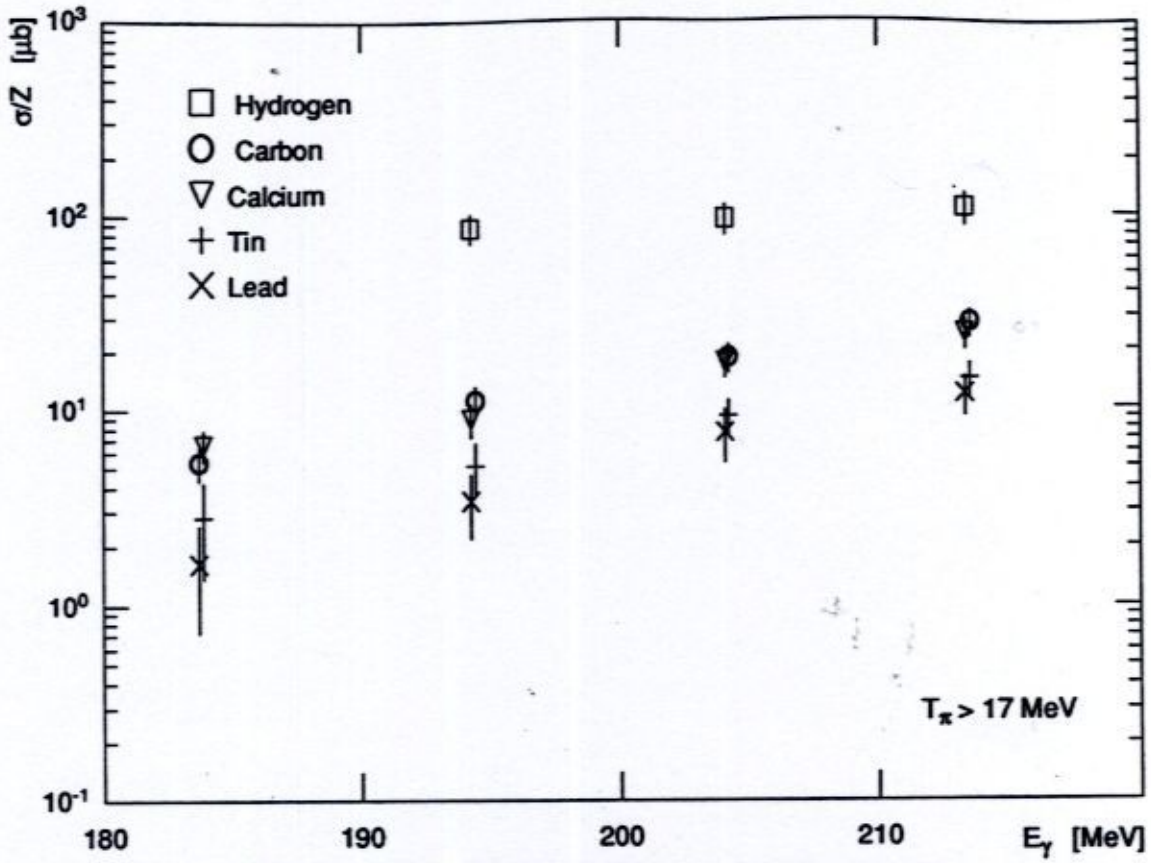

Figure 4.16: The Total QF Cross Section Per Proton

Figure 4.17 on the following page demonstrates the trend in the total cross section as a function of A for the four photon energy bins. Total errors are shown and again, a uniform detector threshold of 17 MeV is present in the data.

Recall that the total cross section was modelled as $\sigma(A) = kA^{n(A)}$, and that as the number of nucleons in the target nucleus increased, according to a very simple model the total cross section was to go smoothly from being proportional to A (a volume effect) to being proportional to $A^{2/3}$ (a surface effect). That is, the exponent n(A) was to reduce smoothly from a value of 1 to a value of 2/3. A second order polynomial was fit to the data as plotted in Figure 4.17.

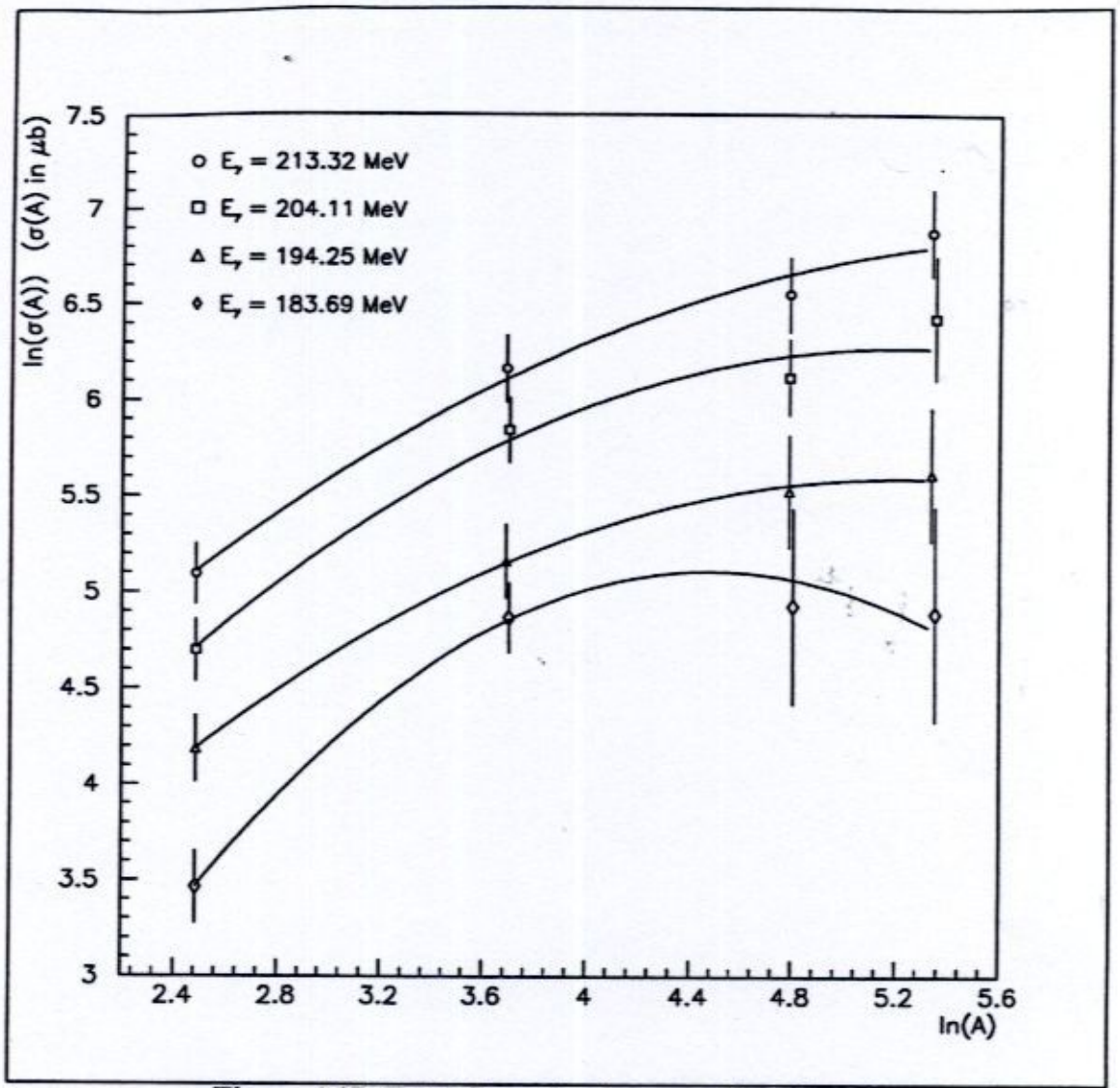

Figure 4.17: Total Cross Sections as a Function of A

Because

$$\ln(\sigma) = \ln(k) + [n(A)] \cdot \ln(A), \qquad (4.1)$$

and

$$\ln(\sigma) = A + B \cdot \ln(A) + C \cdot [\ln(A)]^2 = A + [B + C \cdot \ln(A)] \cdot \ln(A), \qquad (4.2)$$

by comparing equations 4.1 and 4.2,

$$n(A) = B + C \cdot \ln(A). \qquad (4.3)$$

Table 4.3 presents the values of the exponent n(A) calculated from the fit coefficients according to equation 4.3 for the various nuclei as a function of photon energy.

Table 4.3: A Summary of Total Cross Section Exponents

Target	E_γ = 213 MeV	E_γ = 204 MeV	E_γ = 194 MeV	E_γ = 184 MeV
C	1.39+/-0.47	1.67+/-0.51	1.50+/-0.62	2.67+/-0.74
Ca	1.21+/-0.52	1.42+/-0.57	1.27+/-0.69	2.18+/-0.83
Sn	1.04+/-0.58	1.19+/-0.63	1.07+/-0.76	1.72+/-0.92
Pb	0.96+/-0.60	1.07+/-0.66	0.96+/-0.79	1.50+/-0.96

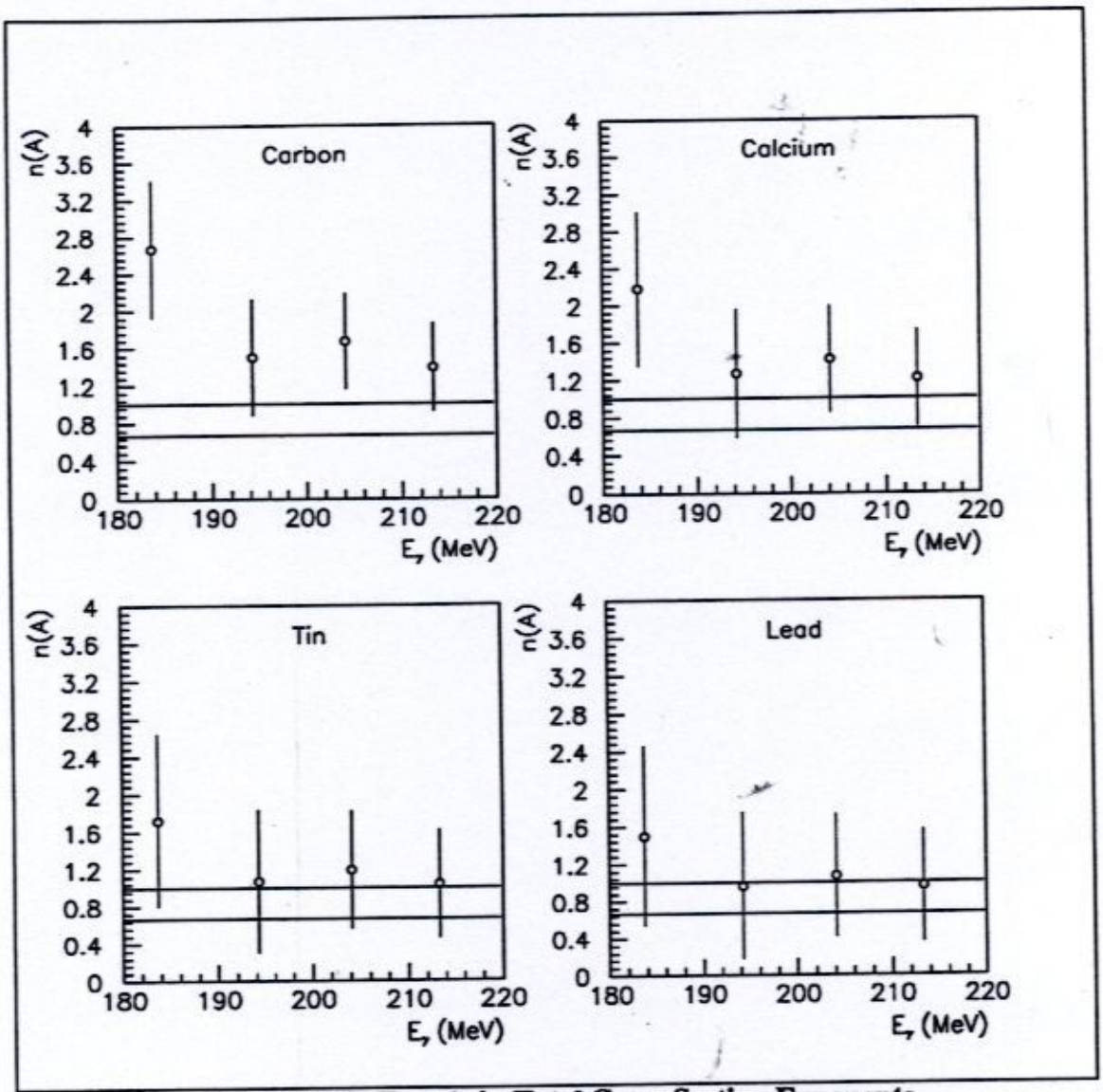

Figure 4.18: Trends in Total Cross Section Exponents

Figure 4.18 illustrates trends in the exponent n(A) of Table 4.3, together with lines representing the expected values of n(A) = 1 for "volume-type" nuclei and n(A) = 2/3 for "surface-type" nuclei. Clearly, the theory used to predict these values is far too simple. All data sets favor the n(A) = 1 prediction, while to within error, the Sn and Pb coefficients actually agree with both predictions. Further, at E_γ = 184 MeV, the value of the exponent is somewhat larger than the simple theory predicts, at least for C and Ca. The source distribution is obviously more complex than the volume or surface types predicted by the model. To investigate the trend in the fit exponent of the total cross section properly, smaller error bars on the total cross sections and a larger sampling of nuclei are required.

4.2 Conclusions

The purpose of this experiment was to investigate QF π^+ photoproduction from high Z nuclei using tagged photons from 175 to 215 MeV. Because some tagged photon data existed for photoproduction from both H and C over this energy range, these targets were selected to check the absolute normalization. H was also used to determine the energy resolution and calibration of the detectors. This experiment represented the first attempt at investigating π^+ from Ca, Sn and Pb using low-threshold ΔE-E type plastic scintillator telescopes.

While the elementary angular distributions do not, in general, reproduce the results of the calculations or the long standing data of Adamovich *et al.*, they are in good agreement with the tagged photon data point of van den Brink. Further, the total cross sections for the elementary reaction are consistent with the tagged photon data of Buechler. This agreement suggests some modifications of the calculations may be required. Agreement with the tagged photon double differential cross sections and angular distributions from C of Arends *et al.* was also good for all save the most forward angle. This suggests that the results obtained for the other Z targets, extracted in a consistent manner, should be good as well. The fact that serious disagreement exists with the angular distributions of Shoda *et al.* is not a great concern, since tagged photons were not used in his work.

The QF angular distributions from C, Ca, Sn, and Pb were compared to the recent theoretical calculations of Carrasco *et al.* Agreement was excellent at the forward angles for all targets where the π^+ are the most energetic, but poor at the backward angles, where

the π^+ are less energetic. Carrasco himself feels this is due to failings in their model for low energy π^+ which need to be addressed. This is why comparison is attempted only for a photon energy of 213 MeV, the highest in this measurement.

The absolute angular distributions were integrated to yield total cross sections. For nuclei, the total cross section per proton was less than that for the free proton, and decreased as A increased. Trends in the total cross section as a function of A were determined, but did not compare favorably with a simple model.

The next step in this work would be to repeat the experiment using the upgraded experimental facility at SAL. This upgrade includes both a 62 channel photon tagger and a complete revamping of the RF drive. The new tagger has demonstrated world record instantaneous focal plane rates of 240 MHz, while time-averaged duty factors over the course of experiments at SAL are now on the order of 60%. These two factors alone amount to approximately a factor of 10 in count rate. In a new experiment, backward laboratory angles would be concentrated on, since the agreement between theory and experiment was shown to be poor. If possible, double differential cross sections should be the focus, since the discrepancies between theory and experiment are best addressed at this level. Heavy targets other than Ca, Sn, and Pb should be chosen in order to map the total cross section as a function of A more completely, while H and C should be retained for the purposes of comparison to known results. Further, there are improvements which could be made to the detectors and electronics used in the experiment which would allow for further increases in count rate. These improvements are discussed in detail in Appendix G. The net result of all these improvements would be a better experiment which could investigate far more than this work did to a far better degree in a far shorter period of time.

REFERENCES and APPENDICES

REFERENCES

Aguilar-Benitez *et al.*, 1992 — M. Aguilar-Benitez *et al.*, Phys. Rev. **D45**, Part 2 (1992).

Adamovich *et al.*, 1968 — M. I. Adamovich, V. G. Larionova, S. P. Kharlamov, and F. R. Yagudina, Sov. J. Nucl. Phys. **7**, 360 (1968).

Amendt, 1991 — D. Amendt, *Differential Cross Sections for Compton Scattering off the Proton at 185 MeV*, M. Sc. thesis, Univ. of Sask., (1991) unpublished.

Amann *et al.*, 1981 — J. F. Amann *et al.*, Phys. Rev. **C23**, 1635 (1981).

Aniol *et al.*, 1986 — K. A. Aniol *et al.*, Phys. Rev. **C33**, 208 (1986).

Arends *et al.*, 1982A — J. Arends *et al.*, NIM **201**, 361 (1982).

Arends *et al.*, 1982B — J. Arends *et al.*, Z. Phys. **A305**, 205 (1982).

Ashery *et al.*, 1981 — D. Ashery *et al.*, Phys. Rev. **C23**, 2173 (1981).

Axen *et al.*, 1974 — D. Axen *et al.*, NIM **118**, 435 (1974).

Berends *et al.*, 1967 — F. A. Berends, A. Donnachie, and D. L. Weaver, Nucl. Phys. **B4**, 54 (1967).

Blecher *et al.*, 1979 — M. Blecher *et al.*, Phys. Rev. **C20**, 1884 (1979).

Blecher *et al.*, 1983 — M. Blecher *et al.*, Phys. Rev. **C28**, 2033 (1983).

Blomqvist *et al.*, 1977 — I. Blomqvist and J. M. Laget, Nucl. Phys. **A280**, 405 (1977).

Blomqvist, 1993 — I. Blomqvist, private communication.

Buechler, 1991 — K. Buechler, *Messung des differentiellen Wirkungsquerschnitts der Reaktion $\gamma p \rightarrow \pi^+ n$ am energiemarkierten Photonenstrahl des PHOENICS-Experiments*, Ph. D. thesis, Bonn University, (1991) unpublished.

Byfield *et al.*, 1952 — H. Byfield, J. Kessler, and L. M. Lederman, Phys. Rev. **17**, 17 (1952).

Carroll *et al.*, 1976 — A. S. Carroll *et al.*, Phys. Rev. **C14**, 635 (1976).

Carrasco *et al.*, 1992 — R. C. Carrasco *et al.*, Nucl. Phys. **A541**, 585 (1992).

Cence *et al.*, 1961 — R. J. Cence and B. J. Moyer, Phys. Rev. **122**, 1634 (1961).

Dallin, 1990 — L. O. Dallin, *High Duty Factor, Monochromatic Extraction from EROS*, Ph. D. thesis, Univ. of Sask., (1990) unpublished.

Doss *et al.*, 1988 — K. G. R. Doss *et al.*, *Inclusive Photopion Production from Nuclei*, SAL Proposal 013, (1988).

Florizone *et al.*, 1990 — R. E. J. Florizone and J. M. Vogt, *Users Manual Duty Factor Meter*, SAL Technical Memorandum, EROS/MAN/CONT/04 (1990).

Garrow, 1991 — K. R. Garrow, *High Energy Photoprotons From* ^{12}C, M. Sc. thesis, Univ. of Sask., (1991) unpublished.

Genzel *et al.*, 1973 — H. Genzel, P. Joos, and W. Pfeil, *Photoproduktion von Elementarteilchen*, (Springer-Verlag, Berlin Heidelberg, 1973).

Gill *et al.*, 1982 — D. R. Gill *et al.*, Phys. Rev. **C26**, 1306 (1982).

Gothe, 1993 — R. Gothe, private communication.

Igarashi, 1993 — R. Igarashi, *Coherent Photon Scattering on Nuclei in the Δ(1232) Resonance*, Ph. D. thesis, Univ. of Sask., (1993) unpublished.

Jackson, 1975 — J. D. Jackson, *Classical Electrodynamics 2nd Edition*, (John Wiley & Sons Inc., New York, 1975).

Kellie *et al.*, 1985 — J. D. Kellie *et al.*, NIM **A241**, 153 (1985).

Laxdal, 1980 — R. E. Laxdal, *Design of an Energy Compression System for the Saskatchewan Linear Accelerator*, M. Sc. thesis, Univ. of Sask., (1980) unpublished.

MacDonald *et al.*, 1979 — W. M. MacDonald, E. T. Dressler, and J. S. O'Connell, Phys. Rev. **C19**, 455 (1979).

Matthews *et al.*, 1971 — J. L. Matthews and R. O. Owens, NIM **91**, 37 (1971).

Meirav *et al.*, 1987 — O. Meirav *et al.*, Phys. Rev. **C36**,1066 (1987).

Moniz *et al.*, 1971 — E. J. Moniz *et al.*, Phys. Rev. Let. **26**, 445 (1971).

Moravcsik, 1956 — M. J. Moravcsik, Phys. Rev. **104**, 1451 (1956).

Nagl *et al.*, 1991 — A. Nagl, V. Devanathan, and H. Ueberall, *Nuclear Pion Photoproduction*, (Springer-Verlag, Berlin Heidelberg, 1991).

Nozawa *et al.*, 1990 — S. Nozawa, B. Blankleider, and T.-S. H. Lee, Nucl. Phys. **A513**, 459 (1989).

Obenshain *et al.*, 1983 — F. Obenshain *et al.*, Phys. Rev. **C27**, 2753 (1983).

O'Connell *et al.*, 1962 — J. S. O'Connell, P. A. Tippler, and P. Axel, Phys Rev **126**, 228 (1962).

O'Rielly, 1993 — G. V. O'Rielly, Ph. D. thesis, Univ. of Melbourne (1993), in progress.

Owens, 1990 — R. O. Owens, NIM **A288**, 574 (1990).

Pfeil *et al.*, 1972 — W. Pfeil and D. Schwela, Nucl. Phys. **B45**, 379 (1972).

Preedom *et al.*, 1981 — B. M. Preedom *et al.*, Phys. Rev. **C23**, 1134 (1981).

Pywell, 1987 — R. E. Pywell, *Tagger Information*, SAL Technical Memorandum, EROS/TM/PTS/03/R01 (1987).

Rosenzweig *et al.*, 1992 — D. P. Rosenzweig *et al.*, Phys. Rev. **C46**, 1968 (1992).

Rosenzweig, 1993 — D. P. Rosenzweig, *An Experimental Study of Inclusive Pion Inelastic Scattering and Pion Photoproduction at Pion Energies up to 100 MeV*, Ph. D. thesis, Univ. of Wash., (1993) unpublished.

SAL, 1989 — Saskatchewan Accelerator Laboratory, *Annual Report* (1989).

SAL, 1990A — Saskatchewan Accelerator Laboratory, *Annual Report* (1990).

SAL, 1990B — Saskatchewan Accelerator Laboratory, *LUCID Data Acquisition and Analysis System User's Guide*, Version 1.1 (1990).

Saltmarsh *et al.*, 1972 — M. J. Saltmarsh, B. M. Preedom, R. D. Edge, and C. W. Darden III, NIM **105**, 311 (1972).

Sarty, 1992 — A. J. Sarty, *A Measurement of the Three-Body Photodisintegration of Helium-3 and its Relation to Three-Body Forces*, Ph. D. thesis, Univ. of Sask., (1992) unpublished.

Schiff, 1951 — L. I. Schiff, Phys. Rev. **83**, 252 (1951).

Shoda *et al.*, 1988 — K. Shoda, T. Kobayashi, O. Sasaki, and S. Toyama, Nuc. Phys. **A486**, 526 (1988).

Stoks *et al.*, 1988 — V. G. J. Stoks, P. C. van Campen, T. A. Rijken, and J. J. de Swart, Phys. Rev. Lett. **61**, 1702 (1988).

Strakovsky, 1993 — I. Strakovsky, private communication.

Stricker *et al.*, 1979 — K. Stricker, H. McManus, and J. A. Carr, Phys. Rev. **C19**, 929 (1979).

Terasawa *et al.*, 1986 — T. Terasawa *et al.*, NIM **A248**, 429 (1986).

van den Brink, 1993 — H. B. van den Brink, Ph. D. thesis, Vrije Universiteit, (in progress).

Vogt, 1989 — J. M. Vogt, *The Tagger Electronics*, SAL Technical Memorandum, EROS/TM/PTS/12/R01 (1990).

Vogt *et al.*, 1993 — J. M. Vogt *et al.*, NIM **A324**, 198 (1993).

Weil *et al.*, 1953 — J. W. Weil and B. D. McDaniel, Phys. Rev. **92**, 391 (1953).

Wong, 1990 — S. S. M. Wong, *Introductory Nuclear Physics* (Prentice-Hall, Inc., New Jersey, 1990).

Workman *et al.*, 1992 — R. L. Workman, R. A. Arndt, and M. M. Pavan, Phys. Rev. Lett. **68**, 1653 (1992).

Appendix A. DECAY KINEMATICS

Figure A.1 shows the π^+ decay process.

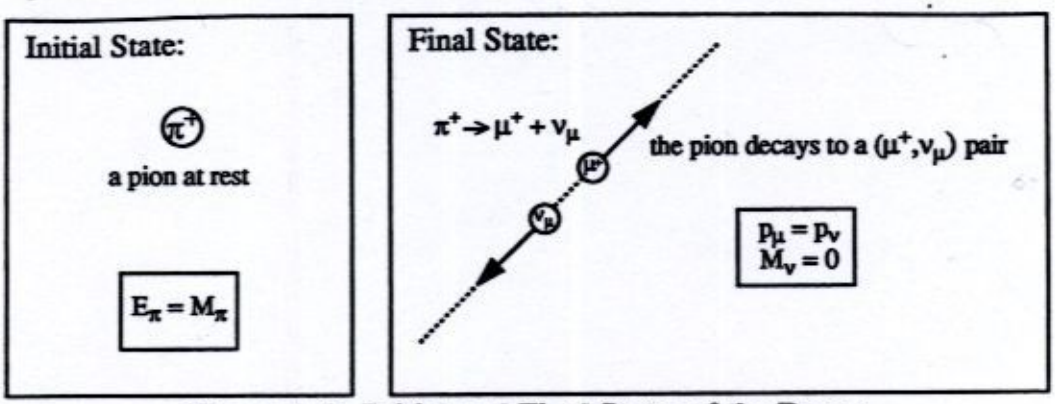

Figure A.1: Initial and Final States of the Decay

For the purposes of the following derivation, units of $h/2\pi = c = 1$ are assumed.

The relationship between the relativistic total energy of the decay μ^+ and its mass and momentum is

$$E_\mu^2 = p_\mu^2 + M_\mu^2. \tag{A.1}$$

Because the π^+ is at rest in the initial state, its momentum is zero. Further, the neutrino is taken to be massless. Applying the conservation of energy between initial and final states yields

$$M_\pi = E_\mu + p_\nu. \tag{A.2}$$

Further, conservation of momentum demands

$$\vec{p}_\mu + \vec{p}_\nu = 0. \tag{A.3}$$

The total energy of the μ^+ may also be expressed as the sum of its mass and kinetic energy

$$E_\mu = T_\mu + M_\mu. \tag{A.4}$$

Substituting equations A.3 and A.4 into equation A.2 produces

$$M_\pi = T_\mu + M_\mu + p_\mu. \tag{A.5}$$

Substituting equation A.4 into A.1 and solving for p_μ produces

$$p_\mu = \sqrt{T_\mu^2 + 2M_\mu T_\mu}. \tag{A.6}$$

Combining equations A.5 and A.6 yields

$$M_\pi = T_\mu + M_\mu + \sqrt{T_\mu^2 + 2M_\mu T_\mu}, \tag{A.7}$$

which, upon squaring and solving for T_μ results in the kinetic energy of the decay μ^+

$$T_\mu = \frac{1}{2}\left[M_\pi + M_\mu\left(\frac{M_\mu}{M_\pi}\right)\right] - M_\mu. \tag{A.8}$$

Since M_π = 139.6 MeV and M_μ = 105.7 MeV, the kinetic energy T_μ of the decay μ^+ is identically equal to 4.12 MeV.

Appendix B. LAB TO CENTER-OF-MOMENTUM TRANSFORMATIONS

Units of $h/2\pi = c = 1$ are assumed in this Appendix.

The CM values for photon energy (E_γ^{CM}), detector angle (θ^{CM}), and solid angle ($d\Omega^{CM}$) are related to their respective laboratory counterparts by

$$E_\gamma^{CM} = E_\gamma^{LAB}\sqrt{\frac{1-\beta_c}{1+\beta_c}}, \tag{B.1}$$

$$\theta^{CM} = \text{atan}\left(\frac{\sin(\theta^{LAB})\sqrt{1-\beta_c^2}}{\cos(\theta^{LAB})-\beta_c/\beta_p}\right), \tag{B.2}$$

$$\frac{d\Omega^{LAB}}{d\Omega^{CM}} = \frac{(\beta_p-\beta_c\cos(\theta^{LAB}))\sqrt{(1-\beta_p\beta_c\cos(\theta^{LAB}))^2-(1-\beta_p^2)(1-\beta_c^2)}}{\beta_p^2(1-\beta_c^2)}. \tag{B.3}$$

Equation B.3 is the Jacobian. The quantities β_c and β_p are given by

$$\beta_c = \frac{E_\gamma^{LAB}}{E_\gamma^{LAB}+m_p}, \tag{B.4}$$

$$\beta_p = \frac{\sqrt{2T_\pi^{LAB}m_\pi+(T_\pi^{LAB})^2}}{m_\pi+T_\pi} \tag{B.5}$$

where "m_p" is the rest mass of the proton (938.28 MeV), "T_π" is the kinetic energy of the π^+ in MeV, and "m_π" is the rest mass of the π^+ (139.6 MeV).

The CM value for the π^+ momentum "q" may be extracted from

$$W = \omega + E_f, \tag{B.6}$$

$$W = \sqrt{m_p(m_p+2E_\gamma^{LAB})}, \tag{B.7}$$

$$\omega = \sqrt{q^2 + m_\pi^2}, \tag{B.8}$$

$$E_f = \sqrt{q^2 + m_p^2}. \tag{B.9}$$

The Jacobians $d\Omega^{LAB}/d\Omega^{CM}$ were averaged over the angle subtended by the detector, the photon energy bin, and deposited π^+ energy (thus the two values for the Melbourne detector, which had two different collimators). Table B.1 summaries the conversion parameters.

Table B.1: Laboratory to Center-of-Momentum Conversion Parameters

LAB E_γ [MeV]	CM E_γ [MeV]	CM q [MeV]	LAB θ [°]	CM θ [°]	LAB T_π [MeV]	$d\Omega^{LAB}/d\Omega^{CM}$
213	177	122.1	51	65.6	57.90	0.735
			51	65.9	57.90	0.731
			81	98.6	45.12	0.969
			109	125.6	35.26	1.288
			141	151.7	28.21	1.649
204	170	112.1	51	65.8	49.92	0.732
			51	66.1	49.92	0.729
			81	99.5	38.61	0.968
			109	126.0	29.92	1.294
			141	152.0	23.74	1.674
194	163	100.6	51	66.5	41.28	0.723
			51	66.8	41.28	0.719
			81	100.3	31.52	0.967
			109	125.8	24.09	1.288
			141	151.9	18.87	1.667
184	156	87.0	51	67.0	31.88	0.716
			51	67.4	31.88	0.710
			81	100.1	23.80	0.966

Appendix C. KINEMATICS AND ENERGY LOSS

Details of the kinematics calculations and energy loss work performed to determine the relationship between π^+ energy at creation and at detection are presented. Units of $h/2\pi = c = 1$ are assumed.

C.1 Kinematics

Throughout this work, the word "kinematics" is a reference to the elastic photoproduction of a π^+. A two body final state is assumed and no energy brought into the reaction by the photon is carried off in the form of an excited recoil.

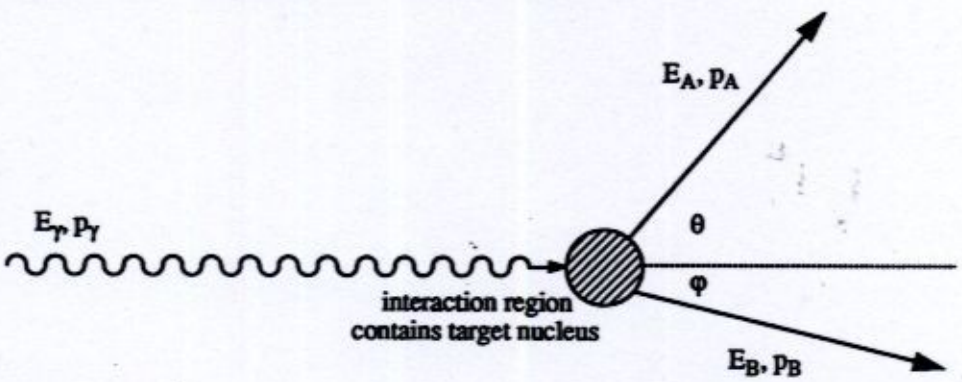

Figure C.1: A Two Body Photoproduction Reaction

Consider Figure C.1. Let "A" represent the detected particle (a π^+), let "B" represent the recoil particle, and let "T" be the target nucleus. The conservation of momentum implies

$$p_\gamma = p_A\cos\theta + p_B\cos\varphi, \tag{C.1}$$

$$0 = p_A\sin\theta - p_B\sin\varphi. \tag{C.2}$$

If equations C.1 and C.2 are solved for $\cos\varphi$ and $\sin\varphi$ respectively, and these expressions are then squared and added, application of the trigonometric identity $\sin^2\varphi + \cos^2\varphi = 1$ will yield

$$p_B^2 = p_A^2 + E_\gamma^2 - 2p_A E_\gamma\cos\theta. \tag{C.3}$$

The conservation of energy demands

$$E_\gamma + E_T = E_A + E_B. \tag{C.4}$$

If equation C.4 is solved for the total energy of the recoil particle, E_B, and this expression is squared, the result is

$$E_B^2 = E_\gamma^2 + E_T^2 + E_A^2 + 2E_\gamma E_t - 2E_\gamma E_A - 2E_T E_A. \qquad (C.5)$$

The total energy of the recoil particle is given by $E_B^2 = p_B^2 + m_B^2$. Substituting this into equation C.5 produces

$$p_B^2 = E_\gamma^2 + E_T^2 + E_A^2 + 2E_\gamma E_T - 2E_\gamma E_A - 2E_T E_A - m_B^2. \qquad (C.6)$$

A comparison of equations C.3 and C.6 using the fact that the target is at rest in the lab frame ($E_T = m_T$), results in

$$p_A^2 - 2p_A E_\gamma \cos\theta = m_T^2 + E_A^2 + 2E_\gamma m_T - 2E_\gamma E_A - 2E_A m_T - m_B^2. \qquad (C.7)$$

Finally, $p_A^2 = E_A^2 - m_A^2$, so that

$$E_A^2 - m_A^2 - 2\sqrt{E_A^2 - m_A^2}\,E_\gamma \cos\theta = m_T^2 + E_A^2 + 2E_\gamma m_T - 2E_\gamma E_A - 2E_A m_T - m_B^2. \qquad (C.8)$$

In order to solve equation C.8, define the quantities

$$M^2 = m_B^2 - m_A^2 - m_T^2, \qquad (C.9)$$

$$E_0 = E_\gamma + m_T. \qquad (C.10)$$

Squaring equation C.8 and rewriting in terms of the above quantities produces a quadratic equation in E_A

$$\{4[E_\gamma^2(\cos\theta)^2 - E_0^2]\}E_A^2$$

$$\{4E_0[2E_\gamma m_T - M^2]\}E_A$$

$$\{4E_\gamma[m_T(M^2 - E_\gamma m_T) - E_\gamma(\cos\theta)^2 m_A^2] - M^4\} = 0. \qquad (C.11)$$

By defining the following variables,

$$a = 4[E_\gamma^2(\cos\theta)^2 - E_0^2], \qquad (C.12)$$

$$b = 4E_0 [2E_\gamma m_T - M^2], \tag{C.13}$$

$$c = 4E_\gamma [m_T (M^2 - E_\gamma m_T) - E_\gamma (\cos\theta)^2 m_A^2] - M^4, \tag{C.14}$$

the solution to equation C.11 will be given by

$$E_A = \frac{1}{2a} [-b \pm \sqrt{b^2 - 4ac}]. \tag{C.15}$$

Only one of the two solutions to equation C.15 is physical. The kinetic energy of the detected particle is thus given by

$$T_A = E_A^{physical} - m_A. \tag{C.16}$$

Computer code was written to solve the quadratic equation, distinguish the physical solution, and then extract the kinetic energy using the formulas presented above. This code required knowledge of the energy of the incident photon, the mass of the target nucleus, the mass of the detected particle, the laboratory angle at which this particle was detected, and the mass of the recoil nucleus. The maximum possible π^+ kinetic energy at creation was thus known for any combination of photon energy, target nucleus, and detector angle.

C.2 Energy Loss

Because a π^+ had to traverse several layers of matter before it could be detected, a mapping algorithm was developed to relate π^+ energy at creation to that at detection via well-established energy loss routines. Section C.2.1 discusses the energy loss process in general, while section C.2.2 outlines energy loss calculations performed for the purposes of this work.

C.2.1 The Bethe-Bloch Energy Loss Formula

When incident upon matter, charged particles lose energy via collisions with the electrons of the medium. The relativistic Bethe-Bloch energy loss formula governs this process.

Consider a particle having charge "Z_1e" and velocity "$v=\beta c$". If this particle passes through a medium of atomic weight "A" and atomic number "Z", the kinetic energy loss "dT" over a path length "dz" is given by

$$-\left(\frac{dT}{dz}\right) = \frac{1}{(4\pi\varepsilon_0)^2}\left(\frac{2\pi N_A Z Z_1^2 e^4}{m_e v^2 A}\right)\left[\ln\left(\frac{2m_e v^2 W_{max}}{I^2(1-\beta^2)}\right) - 2\beta^2 - \delta - U\right] \qquad (C.17)$$

where "ε_0" is the dielectric permittivity of vacuum, "N_A" is Avogadro's number, and "m_e" is the mass of an electron. The mean excitation potential for the scintillator atoms is given by the experimentally determined relation $I = kZ$ (eV), where k=k(Z) for very light or very heavy atoms. For all other atoms, k is approximately 11. "W_{max}" is the maximum energy transfer from the incident particle to an atomic electron, and is given by the formula $W_{max} = 2m_e v^2/(1-\beta^2)$ for energies $<< M_1^2 c^2/2m_e$. "δ" is simply a correction for polarization of the medium, if any, and "U" takes into consideration that inner shell electrons may not behave as free electrons. This relation demonstrates that as the velocity of the particle incident upon the medium decreases, the energy lost per unit path length increases quadratically.

C.2.2 π^+ Energy Loss Calculations

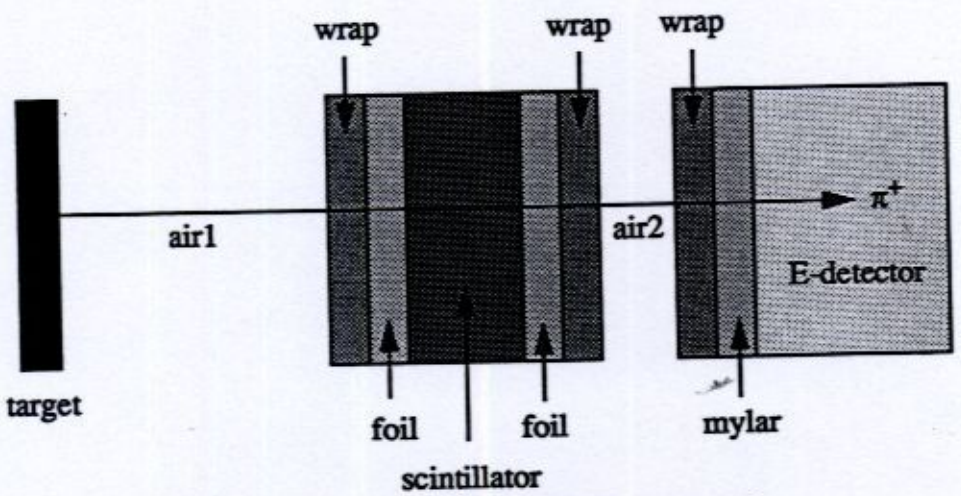

Figure C.2: Energy Loss Layers Schematic

Between photoproduction and detection, a π^+ had to escape the target and traverse nine subsequent layers of matter. In order to determine the relationship between the π^+ kinetic energy at creation and deposited π^+ energy, energy loss in the various layers of

matter had to be quantified. All energy loss work was performed using the SAL system program ELOSS. This program is a computer representation of the Bethe-Bloch energy loss formula detailed in section C.2.1.

Energy Loss In The Target

For approximate calculations, it may be assumed that the π^+ was produced on the midplane of a given target, and thus passed through half of the effective target thickness t' (see section 3.13.2) on its way to the detector. However, since energy loss through matter is very non-linear with respect to path length, it was decided to divide the target into 10 slices, each of thickness t'/10, produce the π^+ on the midplane of each layer, and then determine the resulting energy loss through each successive layer, with the mean energy loss being the average of the energy losses so determined (see equation C.18)

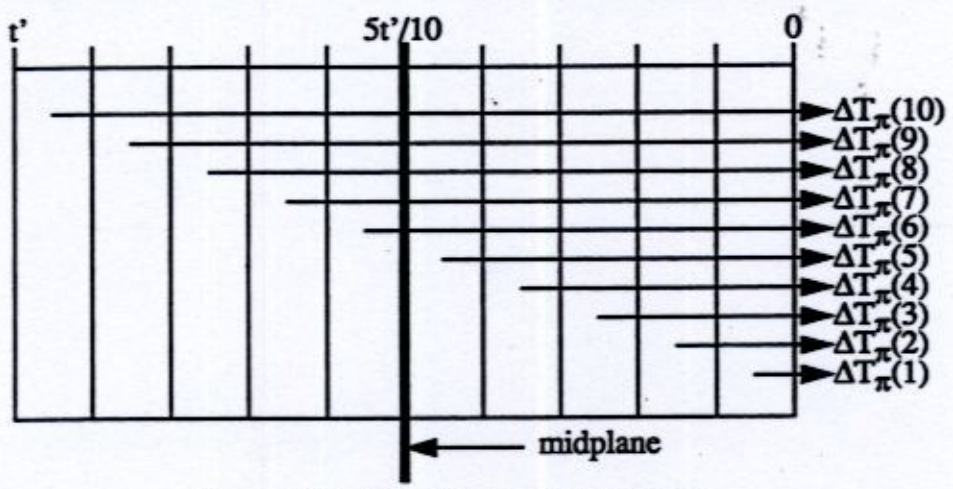

Figure C.3: The Slicing of the Target

$$\overline{\Delta T_\pi^{target}} = \frac{1}{10}\sum_{i=1}^{10} \Delta T_\pi(i)\,. \qquad \text{(C.18)}$$

This, in fact, yielded a correction of as much as 25% to the net energy loss for the π^+ in the target based on the midplane assumption.

Other Energy Loss

The calculation of the energy loss in the remaining layers was a straightforward procedure. ELOSS required the following parameters as input.

Table C.1: A Summary of Energy Loss Layers

Layer	Substance	ρt [mg/cm^2]	comments
air1	N_2	43	(oxygen ignored)
wrap	CH_2	47	(plastic)
foil	Al	3	(tinfoil)
scintillator	$C_{10}H_{11}$	655	(BC 400/NE 102A)
air2	N_2	3/5	Seattle/Australian
mylar	Al	<1	neglected

The relationship between π^+ kinetic energy at creation and deposited π^+ energy was

$$T_\pi^{deposited} = T_\pi^{created} - \overline{\Delta T_\pi^{target}} - \sum_{layers} \Delta T_\pi(layer)\,. \qquad (C.19)$$

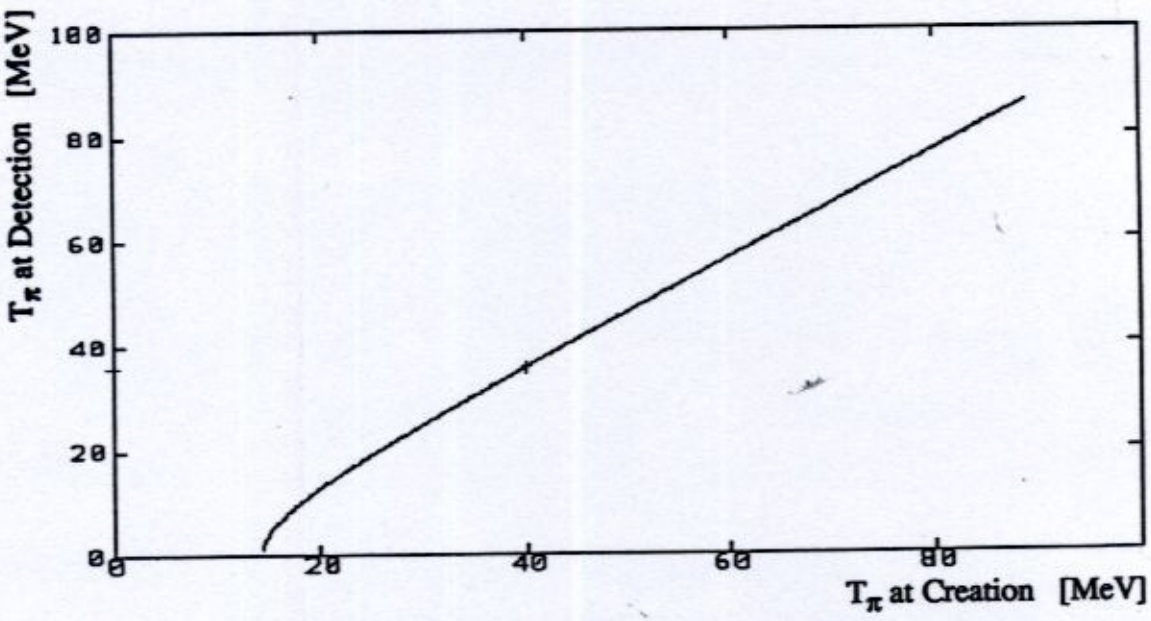

Figure C.4: T_π at Detection vs. T_π at Creation

Appendix D. DETECTOR RESOLUTION

Details of the calculations performed to determine the energy resolution of the E-detectors as a function of deposited π^+ energy are presented.

D.1 Theory

The number of photoelectrons "N_e" produced at the photocathode of a photomultiplier tube is proportional to the energy deposited by a charged particle in the E-detector to which it is attached. Thus,

$$T_\pi = kN_e. \tag{D.1}$$

The energy resolution of the detector is in turn determined by the statistical fluctuation in N_e. A Poisson distribution of photoelectrons is assumed, where $\sigma(N_e) = \sqrt{N_e}$. However, N_e is sufficiently large that a Gaussian distribution is a good approximation. The energy resolution may thus be expressed as

$$R(T_\pi) = \frac{\sigma T_\pi}{T_\pi} = \frac{\sigma(kN_e)}{T_\pi} = k\left(\frac{\sigma N_e}{T_\pi}\right) = \frac{k}{T_\pi}\sqrt{N_e} = \frac{k}{T_\pi}\sqrt{\frac{T_\pi}{k}} = \sqrt{\frac{k}{T_\pi}}. \tag{D.2}$$

The resolution $R(T_\pi)$ at any energy T_π is related to the known resolution $R''(T_\pi'')$ at another energy T_π'' by

$$R(T_\pi) = R''(T_\pi'')\sqrt{\frac{T_\pi''}{T_\pi}}. \tag{D.3}$$

Because of the monoenergetic nature of the π^+'s photoproduced from H, the CH_2 calibration data (large collimator only) were used to determine the point of known energy resolution according to

$$R''(T_\pi'') = \frac{\text{true FWHM}}{T_\pi''}, \tag{D.4}$$

where "true FWHM" was the FWHM of the calibration peak unfolded for angular acceptance of the detectors and π^+ energy loss in the target. The unfolding procedure is described in detail in section D.2.

Table D.1 presents the resolution data obtained from the CH_2 calibration peaks.

Table D.1: Detector Resolution

Detector	T_π" [MeV]	true FWHM [MeV]	R"
Melbourne	42.44+/-0.25	5.72+/-1.22	0.14+/-0.03
Sydney	30.90+/-0.19	4.89+/-0.89	0.16+/-0.13
Adelaide	20.96+/-0.13	5.05+/-1.03	0.24+/-0.05
Seattle	14.76+/-0.09	3.08+/-0.56	0.21+/-0.04

These data yielded the detector resolution as a function of deposited π^+energy as shown in Figure D.1.

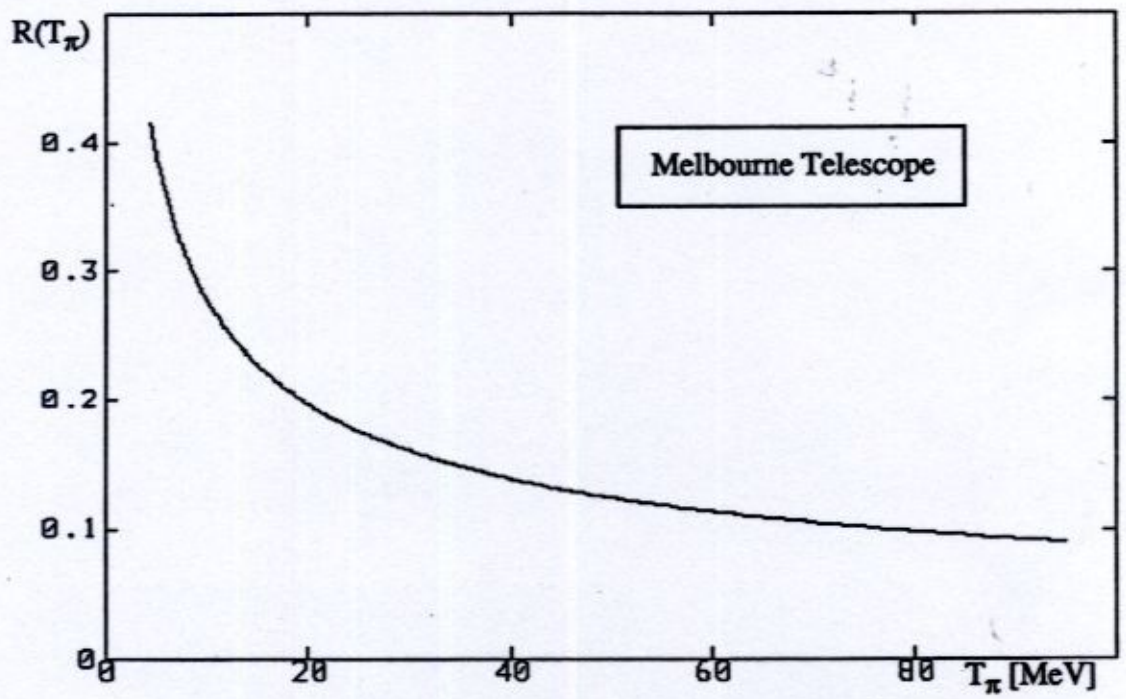

Figure D.1: Detector Resolution as a Function of T_π

D.2 The Unfolding Procedure

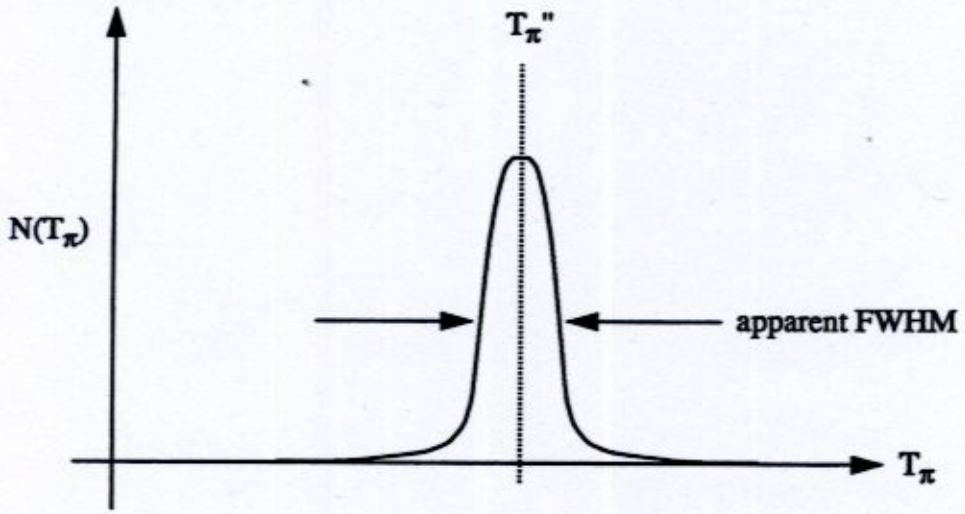

Figure D.2: Detector Resolution

Consider the peak observed in a typical energy calibration spectrum due to free π^+ photoproduction $p(\gamma,\pi^+)n$. The true (apparent) FWHM of the calibration peak was related to the true (apparent) standard deviation of the peak by

$$\text{FWHM} = 2.35 \cdot (\text{standard deviation}). \qquad \text{(D.5)}$$

Assuming Gaussian distributions, the actual "σ" and apparent "w" standard deviations were related by:

$$\sigma(T_\pi) = \sqrt{w^2(T_\pi) - d^2(T_\pi) - t^2(T_\pi)} \qquad \text{(D.6)}$$

where "d" was the contribution to apparent width of the angular acceptance of the detector, and "t" was that due to the energy spread within the target. The apparent standard deviation and mean of the peak were determined by fitting the energy calibration spectrum with a Gaussian.

The spread due to the angular acceptance of the collimator was determined by considering the first quadrant of the circular detector aperture, and assuming a point source of π^+'s at the target.

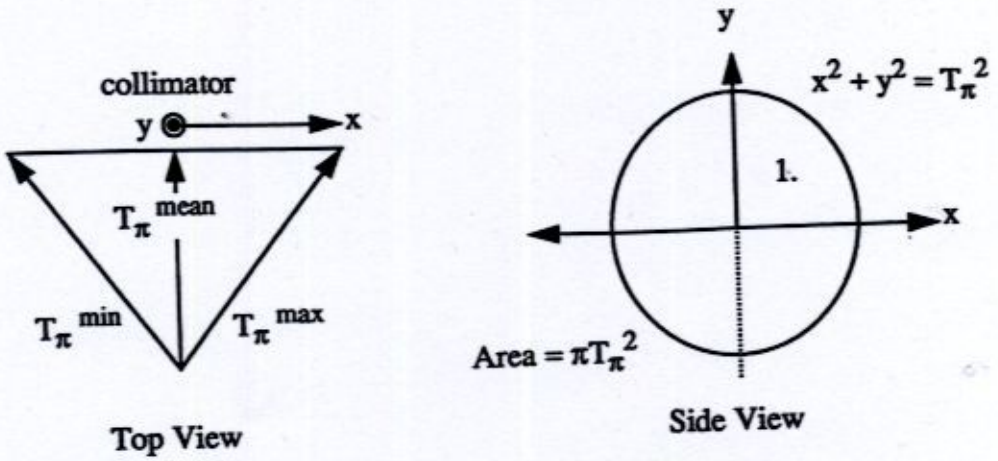

Figure D.3: Mapping the Collimator Aperture

The mean π^+ energy determined by the energy calibration work (see Appendix C) was taken to enter the telescope perpendicular to the plane of the collimator. Further, 68% of the off-mean π^+ energies were assumed to follow a trajectory from the point source to the detector face which resulted in them entering the collimator within one standard deviation of the path of normal incidence. A Gaussian was generated using these assumptions. According to Figure D.3, top view, the radius of the collimator in MeV was given by

$$T_\pi = \frac{1}{2}(T_\pi^{max} + T_\pi^{min}) - T_\pi^{mean}. \qquad (D.7)$$

According to Figure D.3, side view, the area of 1/4 of the circle so defined was then

$$\int_0^{T_\pi} dx \sqrt{T_\pi^2 - x^2} = \frac{1}{4}\pi T_\pi^2. \qquad (D.8)$$

The width of the energy distribution of detectable π^+ was estimated by finding the value of "d" for which

$$\int_0^{d} dx \sqrt{T_\pi^2 - x^2} = 0.68\,(\frac{1}{4}\pi T_\pi^2). \qquad (D.9)$$

This yields

$$\frac{1}{2}\left[d\sqrt{T_\pi^2 - d^2} + T_\pi^2 \arcsin\left(\frac{d}{T_\pi}\right)\right] = 0.68\left(\frac{1}{4}\pi T_\pi^2\right), \qquad \text{(D.10)}$$

which was solved numerically.

The contribution to the apparent width of the peak by energy spread in the target was determined by considering the mean energy loss of a π^+ in the target. For this purpose, the target was divided into 10 layers, and the π^+ was assumed to deposit energy $\Delta T_\pi(i)$ as it traversed the i^{th} layer (see Appendix C). It was thus a straightforward statistical procedure to determine the mean energy loss "μ" and deviation "t" in this energy loss according to the standard statistical formulas

$$\mu = \frac{1}{10}\sum_{i=1}^{10} \Delta T_\pi(i), \qquad \text{(D.11)}$$

and

$$t = \sqrt{\frac{1}{10}\sum_{i=1}^{10} [\Delta T_\pi(i) - \mu]^2}. \qquad \text{(D.12)}$$

Table D.2 summarizes the contributions of the various terms to the apparent width.

Table D.2: Contributions to the Detector Resolution

Detector	T_π" [MeV]	w [MeV]	d [MeV]	t [MeV]	σ [MeV]
Melbourne	42.44+/-0.25	2.84+/-0.44	1.42+/-0.01	0.39+/-0.01	2.43+/-0.52
Sydney	30.90+/-0.19	2.62+/-0.35	1.23+/-0.01	0.85+/-0.01	2.08+/-0.38
Adelaide	20.96+/-0.13	2.56+/-0.30	1.39+/-0.01	0.53+/-0.01	2.15+/-0.24
Seattle	14.76+/-0.09	1.64+/-0.18	0.68+/-0.01	0.72+/-0.01	1.31+/-0.24

Note that the straggling of the energy loss is not taken into account as the variable thickness of the target material produces the dominant effect.

Appendix E. THE MONTE CARLO SIMULATION

Crucial to this experiment was the efficiency for π^+ detection. Interactions between π^+ and the nuclei of the scintillator plastic, as well as π^+ decay in a detector before coming to rest significantly affected the efficiency at which the apparatus operated. A Monte Carlo simulation was produced to investigate the magnitude of these effects.

The following πA interactions were considered: multiple small angle Coulomb scattering, single large angle Coulomb and nuclear scattering, inelastic scattering, the charge-exchange reaction, and true absorption. Multiple small angle Coulomb scattering involved the π^+ undergoing a large number of scatterings from the scintillator atoms, while single large angle scattering was due to both Coulomb scattering from the nuclear charge and nuclear scattering from the nucleons. Elastic scattering did not change the energy deposited by the π^+, but may have caused it to scatter out of the scintillator volume. Inelastic scattering involved the π^+ being degraded in energy by exciting a scintillator nucleus and scattering through some angle. The charge exchange reaction involved the charge conversion of a π^+. The true absorption reaction resulted in the complete absorption of a π^+ on a complex nucleus. In both these cases, a decay μ^+ was no longer produced. Finally, in-flight π^+ decay took into consideration the fact that a π^+ may have decayed before it came to rest in the E-detector. Thus, it did not deposit the expected 4.12 MeV in the delay ADC gate, so it was misidentified.

For the purposes of this work, the scintillator plastic was taken to be $C_{10}H_{11}$. However, since the scattering and reaction mechanisms for π^+ from H are far suppressed with respect to those from C, only the C component of the plastic was considered.

Subsequent sections deal with the theory behind the Monte Carlo procedure, the input parameters needed to make the simulation work, the program itself, and the results.

E.1 Background

E.1.1 An Introduction to πA Interactions

The total πA cross section as a function of π^+ kinetic energy was decomposed into its constituent terms

$$\sigma_{TOTAL} = \sigma_{SCATTERING} + \sigma_{REACTION}, \quad \text{(E.1)}$$

where "$\sigma_{SCATTERING}$" was the total cross section for scattering of all types (including Coulomb effects), while "$\sigma_{REACTION}$" was the total cross section for all reaction mechanisms where the π^+ disappears. Further, the total scattering cross section was given by

$$\sigma_{SCATTERING} = \sigma_{ELASTIC} + \sigma_{INELASTIC}, \quad \text{(E.2)}$$

where "$\sigma_{ELASTIC}$" was the total cross section for elastic scattering of all types, and "$\sigma_{INELASTIC}$" was the total inelastic scattering cross section, including quasi-elastic contributions ($\pi,\pi N$). Lastly,

$$\sigma_{REACTION} = \sigma_{ABSORPTION} + \sigma_{SCX} + \sigma_{DCX}, \quad \text{(E.3)}$$

where "$\sigma_{ABSORPTION}$" was the total true absorption cross section, and "$\sigma_{S(D)CX}$" was the total cross section for single (double) charge exchange. The double charge exchange mechanism was assumed to be very small and was thus ignored. The remaining mechanisms were considered.

E.1.2 The Input Data Set

Table E.1 presents a list of available experimental data. These data were taken to be known to ±10 mb. Published angular distributions for elastic scattering were integrated (see page 173) to obtain the values indicated with an asterisk. Also note that the values quoted for the total, reaction, absorption, and single charge exchange cross sections are independent of Coulomb effects, while the scattering cross sections include them.

Table E.1: A Referenced Summary of the Input Data

T_π [MeV]	σ_{TOTAL} [mb]	σ_{SCAT} [mb]	σ_{ELAS} [mb]	σ_{INEL} [mb]	σ_{REAC} [mb]	σ_{ABS} [mb]	σ_{SCX} [mb]
14	150[1]		*100[11]				
20	165[1]		*100[10]				
30	195[1]		*85[7]		115[5]	100[5]	
35	215[1]		*75[12]				
40	230[1]		*65[9]				
50	275[1]		*70[7]		160[5]	125[5]	35[5]

Table E.1: A Referenced Summary of the Input Data

T_π [MeV]	σ_{TOTAL} [mb]	σ_{SCAT} [mb]	σ_{ELAS} [mb]	σ_{INEL} [mb]	σ_{REAC} [mb]	σ_{ABS} [mb]	σ_{SCX} [mb]
60	320[1]				255[5]	195[5]	
65	340[1]		*70[8]		200[6]	180[2]	
67	355[1]		*85[12]				
70	370[1]		70[4]	70[4]			30[3]
80	420[1]		*105[8]				
85	450[1]		180[3]	110[4]		110[3]	35[3]

Table E.2: References

[1]	Carroll *et al.*, 1976	[7]	Preedom *et al.*, 1981
[2]	Byfield *et al.*, 1952	[8]	Blecher *et al.*, 1983
[3]	Ashery *et al.*, 1981	[9]	Blecher *et al.*, 1979
[4]	Aniol *et al.*, 1986	[10]	Obenshain *et al.*, 1983
[5]	Stricker *et al.*, 1979	[11]	Gill *et al.*, 1982
[6]	Meirav *et al.*, 1987	[12]	Amann *et al.*, 1981

To fill in some of the numerous blanks in Table E.1, the data were rebinned. The rebinned data are displayed in Table E.3. If multiple data points fell in a single new energy bin, they were simply averaged. Points in bold were extracted from the rebinned data set using equations E.2 and E.3. No attempt was made to keep the energy bins uniform in width. Data points in columns 3, 4, and 5 of Table E.3 (the scattering data) include Coulomb effects.

Table E.3: A Summary of the Rebinned Input Data

T_π [MeV]	σ_{TOTAL} [mb]	σ_{SCAT} [mb]	σ_{ELAS} [mb]	σ_{INEL} [mb]	σ_{REAC} [mb]	σ_{ABS} [mb]	σ_{SCX} [mb]
30	195 ± 10		85 ± 10		115 ± 10	100 ± 10	**15 ± 20**
55	300 ± 10		70 ± 10		210 ± 10	160 ± 10	35 ± 10
65	340 ± 10		100 ± 10		200 ± 10	180 ± 10	**20 ± 20**
75	395 ± 10	**175 ± 20**	105 ± 10	70 ± 10			30 ± 10

Table E.3: A Summary of the Rebinned Input Data

T_π [MeV]	σ_{TOTAL} [mb]	σ_{SCAT} [mb]	σ_{ELAS} [mb]	σ_{INEL} [mb]	σ_{REAC} [mb]	σ_{ABS} [mb]	σ_{SCX} [mb]
85	450 ± 10	**290 ± 20**	180 ± 10	110 ± 10	**145 ± 20**	110 ± 10	35 ± 10

E.1.3 Decision Making

Consider a finite element of the π^+ trajectory "dr" small with respect to the total path length "r". The probability that a given reaction took place in the path element dr was given by

$$P(r) = 1 - e^{-\rho\sigma dr} \approx \rho\sigma dr, \tag{E.4}$$

where "ρ" was the density of scattering centers, and "σ" was the total cross section for the given mechanism. Thus, once the total cross section was known, it was a trivial procedure to decide whether or not a given process had occurred.

E.2 Total Cross Sections

E.2.1 The Scattering Cross Section

Recall the total scattering cross section

$$\sigma_{SCATTERING} = \sigma_{ELASTIC} + \sigma_{INELASTIC}. \tag{E.5}$$

Elastic Scattering

The total elastic scattering cross section was written as

$$\sigma_{ELASTIC} = \sigma_{COULOMB} + \sigma_{NUCLEAR}, \tag{E.6}$$

where

$$\sigma_{COULOMB} = \sigma_{COULOMB}(\text{protons}) + \sigma_{COULOMB}(\text{electrons}), \tag{E.7}$$

while

$$\sigma_{NUCLEAR} = \sigma_{NUCLEAR}(\text{protons}) + \sigma_{NUCLEAR}(\text{neutrons}). \tag{E.8}$$

Since Coulomb scattering from neutrons does not occur, collecting the terms as appropriate produces

$$\sigma_{ELASTIC} = \sigma_{COULOMB}\,(\text{electrons}) + \sigma_{COULOMB+NUCLEAR}\,(\text{nucleons})\,. \quad (E.9)$$

The direct Coulomb scattering of π^+ from electrons was neglected since the cross section was at least 1/Z times less than that for direct Coulomb scattering of π^+ from the nucleus, where "Z" was the atomic number of the target. Thus, equation E.9 reduced to

$$\sigma_{ELASTIC} \approx \sigma_{COULOMB+NUCLEAR}\,(\text{nucleons})\,. \quad (E.10)$$

Further, $\sigma_{ELASTIC}$ was divided into two angular regions: one of multiple, small angle Coulomb scattering, and one of single, larger angle nuclear and Coulomb scattering

$$\sigma_{ELASTIC} = \sigma_{SINGLE} + \sigma_{MULTIPLE}. \quad (E.11)$$

Multiple Small Angle Coulomb Scattering

The mechanics of Coulomb scattering by nuclei was first investigated by Rutherford, and is now considered to be well known (Jackson, 1975). The angular distribution for elastic Coulomb scattering which included electron screening of the nucleus is given by

$$\frac{d\sigma}{d\Omega} = \left(\frac{2zZ}{\gamma\beta}\right)^2 \left(\frac{\alpha}{m_\pi}\right)^2 \frac{1}{(\theta^2+\theta_{min}^2)^2}, \quad (E.12)$$

where $\theta_{min} = (\gamma m_\pi \beta a)^{-1}$, "$\gamma$" is the relativistic coefficient, "m_π" is the mass of the π^+ (139.6 MeV), "β" is the velocity of the π^+, $a = 1.4a_0Z^{-1/3}$, "a_0" is the hydrogenic Bohr radius, "z" is the atomic number of the π^+ (1), "α" is the fine structure constant (1/137), and "θ" is the angle scattered into. The cutoff angle "θ_{min}", typically 10^{-4} radians, is a direct result of including electron screening in the calculation. This eliminates the divergence of equation E.12 at small angles. The probability for scattering into a very small angle due to the Coulomb force dominated.

Integration of equation E.12 over solid angle yielded the total Coulomb elastic scattering cross section

$$\sigma_{COULOMB} = \pi a^2 \left(\frac{4\pi z Z e^2}{hv}\right)^2 = \pi a^2 \left(\frac{2zZ\alpha}{\beta}\right)^2. \qquad \text{(E.13)}$$

This cross section was huge (on the order of a Mb), which indicated the probability for a Coulomb elastic scatter into a very small angle was large. Since the scintillator element dr along the π^+ trajectory was large with respect to atomic dimensions, a π^+ underwent many of these small angle deflections within dr. The result of the deflections was an overall diversion from the original trajectory which was just the statistical summation of these deviations. This resulted in a Gaussian multiple scattering distribution

$$P_M(\theta')\,d\theta' = \frac{1}{\sqrt{\pi\langle\Theta^2\rangle}}\exp\left(-\frac{\theta'^2}{\langle\Theta^2\rangle}\right)d\theta' = \frac{1}{\sqrt{\pi}}e^{-x^2}dx, \qquad \text{(E.14)}$$

where $x = \theta'/\langle\Theta^2\rangle^{1/2}$. The mean square projected angle of scattering on any convenient plane with respect to the incident direction was given by $\langle\theta'^2\rangle = \frac{1}{2}\langle\theta^2\rangle$, and $\langle\Theta^2\rangle = 4\pi\rho\ln(204Z^{-1/3})\,(2zZ\alpha/\gamma m\beta^2)^2\,dr$ was the mean square angle. If a step-size dr = 0.05 was chosen and a single π^+ was allowed to travel its entire trajectory, the resulting distribution of small angle scatters had a FWHM of approximately 3^o. Equation E.14 was randomized (see page 190) at each step dr along the π^+ path to determine the total scattering angle and track displacement due to multiple small angle Coulomb scattering.

Single Large Angle Scattering

Large angle scattering of π^+ from the nucleus was due to the sum of the Coulomb and strong interactions. To simulate this mechanism, the elastic scattering cross sections found in the literature were fit to a consistent shape - this shape being a Gaussian superimposed on a flat background

$$\sigma(\theta) = (P_1)\,e^{-\frac{(\theta-P_2)^2}{2(P_3)^2}} + P_4 + (P_5)\,\theta. \qquad \text{(E.15)}$$

This shape was chosen because it best represented the results of published optical fits to the elastic data. The coefficients P_i are summarized in Table E.4.

Table E.4: Summary of Fit Parameters for the Elastic Scattering Data

T_π[MeV]	P_1	P_2	P_3	P_4	P_5
14	43.85	12.90	16.92	3.701	0.647E-02
20	55.99	14.36	13.61	0.760	0.401E-01
30	40.36	11.21	11.56	-1.102	0.671E-01
35	19.20	14.28	12.19	-0.924	0.663E-01
40	20.46	11.89	9.65	0.336	0.440E-01
50	20.77	14.89	13.40	2.224	0.193E-01
65	24.28	24.19	13.18	1.648	0.853E-02
67	38.16	14.83	15.72	4.383	-0.180E-01
80	65.14	14.68	17.18	2.591	-0.115E-01

The angular distributions had basically the same shape for all T_π. Thus, the parameters of the fit functions listed in Table E.4 were averaged over to yield a generic shape given by

$$P(\theta) = 1 + \left(\frac{\overline{P_1}}{\overline{P_4}}\right) e^{-\frac{(\theta - \overline{P_2})^2}{2(\overline{P_3})^2}} + \left(\frac{\overline{P_5}}{\overline{P_4}}\right)\theta. \qquad \text{(E.16)}$$

Table E.5: Large Angle Elastic Scattering Fit Coefficients

$(\overline{P_1/P_4})$	$\overline{P_2}$	$\overline{P_3}$	$(\overline{P_5/P_4})$
16.33	14.80	13.71	0.006448

The shape of the elastic scattering angular distribution determined the angle into which the π^+ scattered.

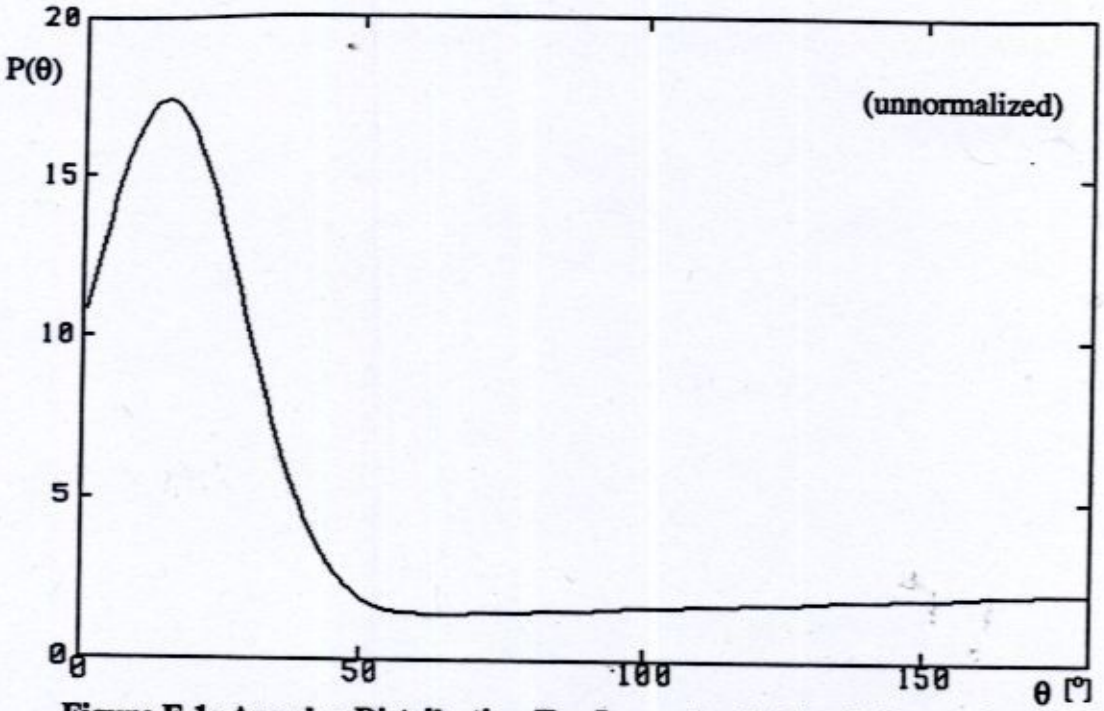

Figure E.1: Angular Distribution For Large Angle Elastic Scattering

The fit coefficients presented in Table E.4 were integrated over solid angle to obtain the total elastic scattering cross sections as a function of π^+ energy (see Table E.1). These total cross sections were then fit to a third order polynomial in T_π (see Figure E.2) to yield a parameterized version of the total elastic scattering cross section.

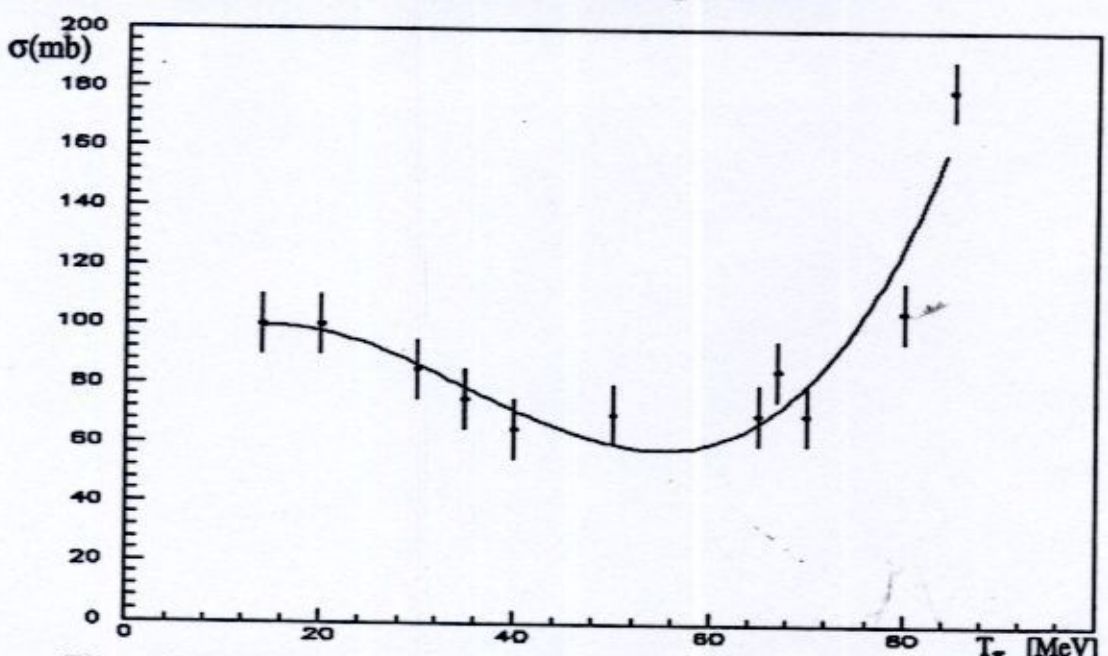

Figure E.2: The Total Cross Section For Large Angle Elastic Scattering

$$\sigma_{SINGLE}(T_\pi) = 75.70 + 3.351T_\pi - 0.1361T_\pi^2 + 0.001282T_\pi^3 \qquad \text{(E.17)}$$

The polynomial was extended to T_π=0 MeV, since no data existed over this energy range.

Knowledge of equation E.17 allowed decision making (see section E.1.3) as to whether a large angle elastic scatter occurred. It was then a relatively simple matter to randomize (see page 190) equation E.16, the generic angular distribution, and thus determine the angle through which the π^+ scattered.

Inelastic Scattering

Inelastic scattering of π^+ from C was perhaps the trickiest mechanism to deal with since the data set was the poorest. Both an angular distribution function and a relative probability to excite the individual states of C were needed.

Only two data points existed for the total inelastic cross section for this reaction. However, a third point, which tied the mechanism to zero at low π^+ energy was calculated. The first excited state of C is at 4.44 MeV, and since the incident π^+ had to overcome the Coulomb barrier of the C nucleus to inelastically scatter (3.15 MeV), the total cross section for inelastic scattering had to be zero at T_π = 7.59 MeV. Further, since the "continuum" of C excited states began at about 10 MeV, a large number of inelastic states opened up very quickly, and thus, the shape of the total inelastic cross section had to reflect this. It was decided to approximate the total inelastic cross section with a second order polynomial in π^+ energy.

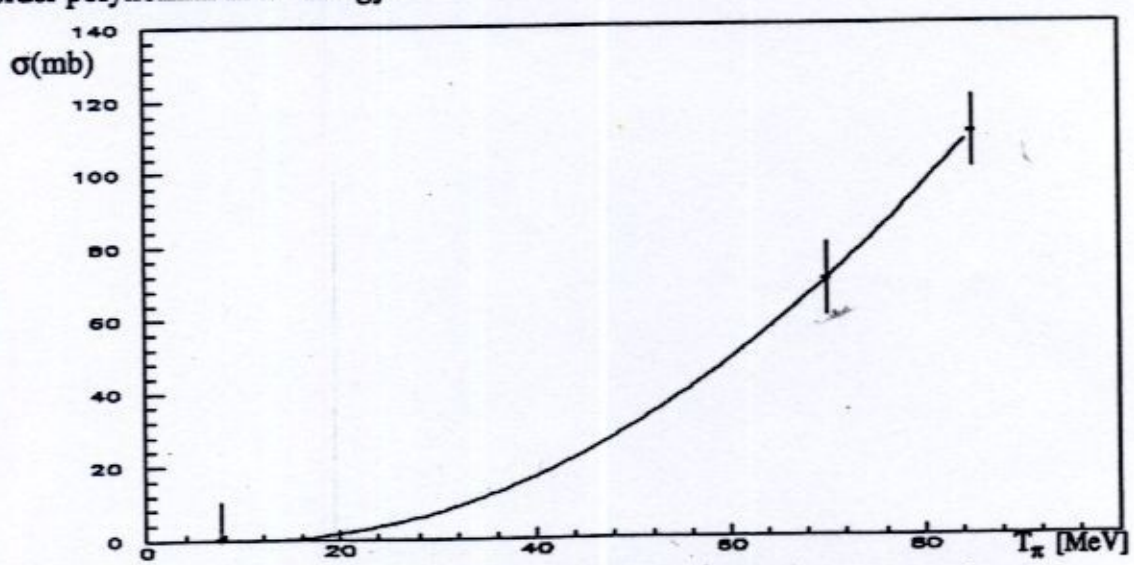

Figure E.3: The Total Cross Section For Inelastic Scattering

$$\sigma_{INELASTIC}(T_\pi) = 2.1505 - 0.42857T_\pi + 0.019969T_\pi^2 \qquad (E.18)$$

Values for the total inelastic cross section corresponding to π^+ energies in the extrapolation region were forced to zero. The shape of this "guesstimated" cross section is illustrated in Figure E.3. Once a π^+ had inelastically scattered, there was no information available as to which state was excited, or which angle was scattered into. In fact, the inelastic contribution to the detection efficiency was sufficiently small (see section E.4) that no further investigation into this mechanism was necessary.

E.2.2 The Reaction Cross Section

Recall the total reaction cross section

$$\sigma_{REACTION} \approx \sigma_{ABSORPTION} + \sigma_{SCX}. \qquad (E.19)$$

The reaction mechanism was well represented in the rebinned data set. Since an absorbed or charge-exchanged π^+ could not be detected using the μ^+ search method, as far as the hardware was concerned, any π^+ undergoing either of these reactions simply vanished from the active volume of the scintillator. The total reaction cross section as a function of T_π was obtained by fitting a second order polynomial in π^+ energy to the data set

$$\sigma_{REACTION}(T_\pi) = -160.5 + 12.24T_\pi - 0.1014T_\pi^2. \qquad (E.20)$$

Negative values occurring in the extrapolation region were forced to zero. Figure E.4 illustrates the shape of equation E.20 over the region in which data existed.

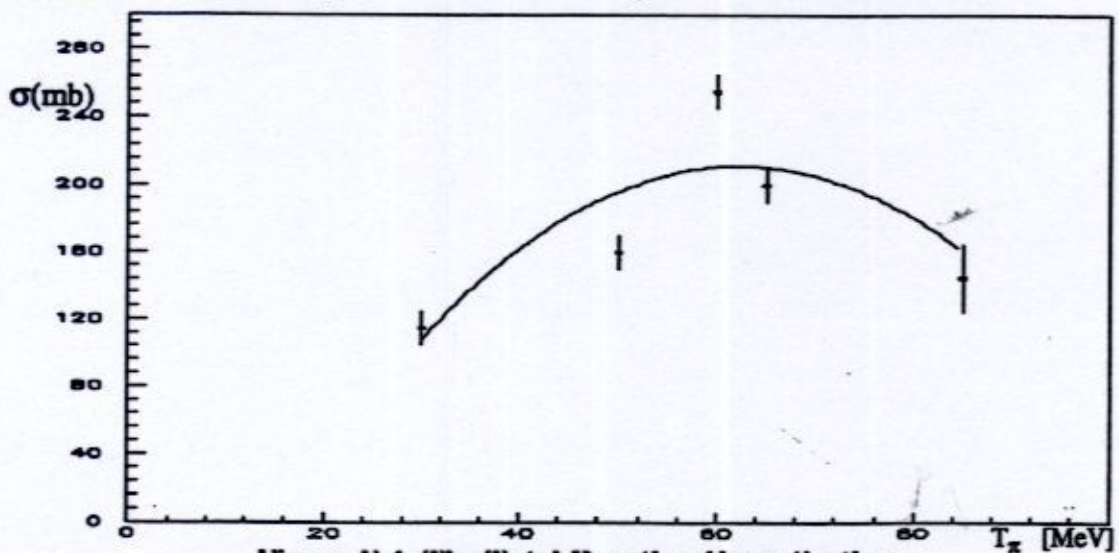

Figure E.4: The Total Reaction Cross Section

E.3 The Simulation

E.3.1 The Algorithm

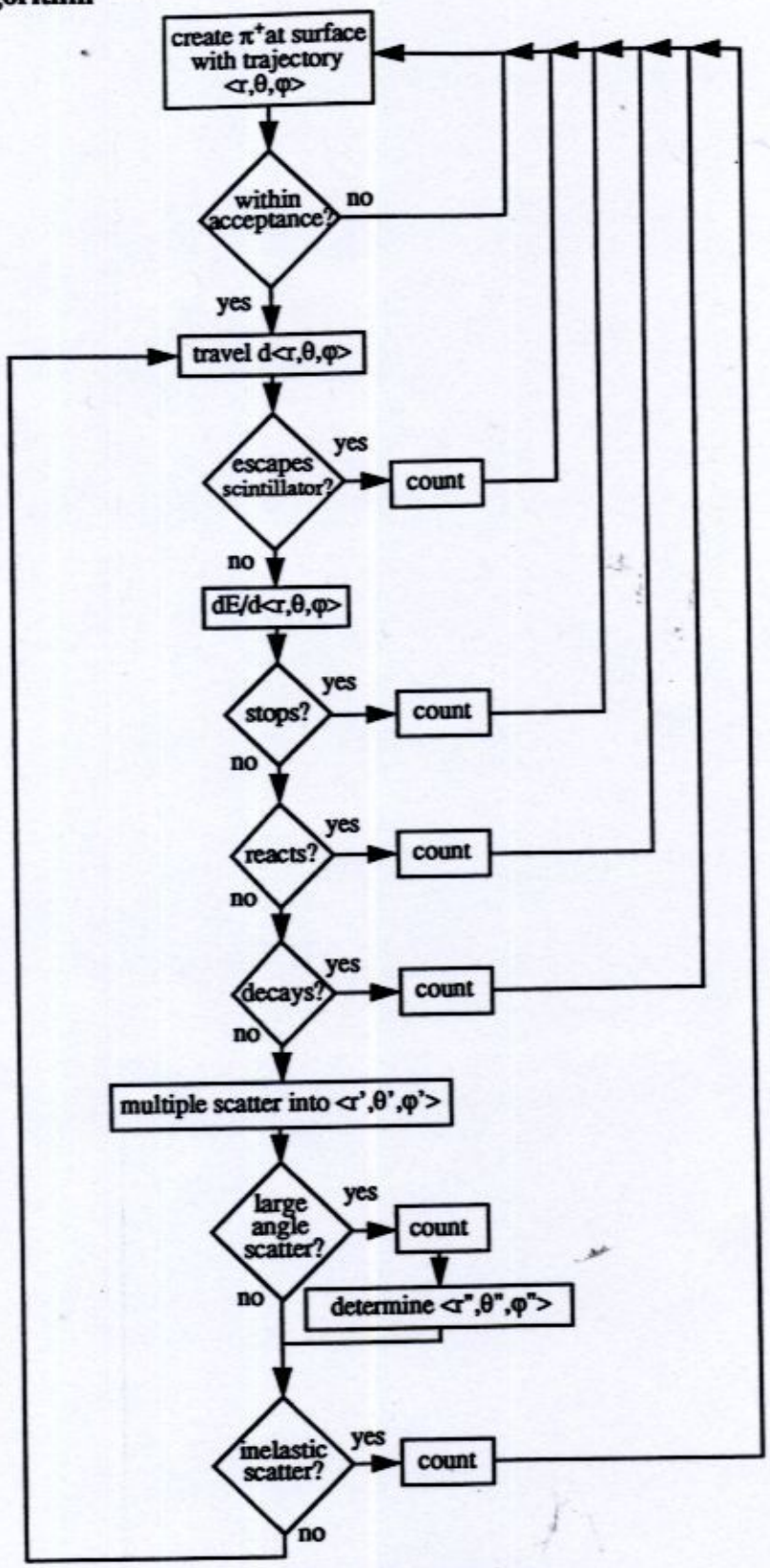

Figure E.5: The Algorithm

E.3.2 The Code

This section contains a listing of the Monte Carlo program. The code should work on any machine supporting FORTRAN. Selected subroutines and functions are discussed in more detail in section E.3.3.

```
c   program PIONPLASTIC.F

c   this program serves to monte carlo the loss of pion detection
c   efficiency in scintillator plastic due to the (piA) reaction mechanism
c   and outscattering from the active volume. the H component of the
c   plastic is ignored. RHO is the number/gram of scattering centers
c   and total cross sections sigma are measured in cm**2.

    implicit double precision (a-h,o-z)
    real EN
    real multarr (1000),elnuclarr (1000)
    logical react,elast,inelast,decay
    external smallangle,largeangle
    real smallangle,largeangle

    PI=3.1415927
    TWOPI=6.2831853

c   these variables count the number of pions which fall into the
c   various categories and should be self evident.

    idkay=0
    ipion=0
    ilost=0
    istop=0
    ireac=0
    icoll=0
    iscatlarge=0
    iinelas=0

c   EN prompts for the incident pion energy for which the simulation is
c   to be run.

    write(6,*) 'Enter the pion energy:'
    read(5,*) EN

c   PIMAX prompts for the number of pions to be successfully thrown at
c   the detector.

    write(6,*) 'Enter the number of collimated pions to be thrown:'
    read(5,*) PIMAX

c   the diameter is the collimator size projected onto the face of the
c   plastic assuming a point source in the target. the diameter was
c   10.98 cm for an australian counter with an 8.0 cm collimator,
c   6.92 cm for an australian counter with a 5.5 cm collimator, and 9.48 cm
```

```
c    for the seattle counter.

c    DIAMETER is the diameter of the effective collimated aperture
c    and is a function of detector. This line must be changed depending on
c    detector/collimator combination.

c    DIAMETER=10.98
c    DIAMETER=06.92
     DIAMETER=09.48

c    RSQR is the radius of the effective aperture squared and is a function
c    of detector.

     RSQR=(0.5*DIAMETER)**2

c    DR is the stepsize in g/cm**2

     DR=0.05

c    the origin of the coordinate system is taken to be the center of the
c    the effective diameter, with the z direction being along the scintillator
c    symmetry axis, while the x and y directions are in the plane of the
c    effective diameter. the active volume of an australian counter was
c    16.5 X 16.5 X 36.0 cm (rectangular), while the active volume of the
c    seattle counter was 15.24 X 30.48 cm (cylindrical).

c    these variables are a function of detector. This line must be changed
c    depending on detector/collimator combination.

c    XMAX=08.25
c    YMAX=08.25
c    ZMAX=36.00
     XMAX=07.62
     YMAX=07.62
     ZMAX=30.48

c    the random number generator seed.

     x=rand(987654321)

c    the random function generator is called. this is nothing more than
c    a subroutine which weights a machine generated random number
c    (which is uniform from 0 to 1) with a user defined function.

     call init_random_function (smallangle,multarr,1000,-3.0,+3.0)
     call init_random_function (largeangle,elnuclarr,1000,0.0,180.0)

c    a pion is 'produced' on the surface of the effective diameter (z=0)
c    with x and y coordinates selected at random. if the distance from
c    the origin of the coordinate system is greater than the effective
c    diameter of the detector, the event is rejected as having struck the
c    collimator.

100  tpi=EN
```

```
      x=(rand(0)-0.5)*DIAMETER
      y=(rand(0)-0.5)*DIAMETER
      z=0.00
      if (x**2+y**2.gt.RSQR) then
       icoll=icoll+1
       goto 100
      endif
      ipion=ipion+1
      if (ipion.gt.PIMAX) then
       write(6,*) EN,' MeV: ','lost->',ilost,' stop->',istop,'
     #react->',ireac,' decayed->',idkay
       write(6,*) EN,' MeV: ','coll->',icoll,' large->',iscatlarge
     #,' inelas->',iinelas
       stop
      endif

c     the cartesian direction of the pion is defined by the vector
c     <rx,ry,rz>. rz is the distance from the target to the effective
c     diameter along the z-axis. this line must be changed depending on
c     detector: 40.51 cm for an australian detector and 37.88 cm for the seattle
c     detector.

c     rz=40.51
      rz=37.88
      rx=x
      ry=y
      rxold=rx
      ryold=ry
      rzold=rz

c     the pion propagates through a layer dr of matter.

200   call TRAVEL (x,y,z,rx,ry,rz,DR)

c     if the following conditions are met, the pion has escaped the active
c     volume of the scintillator. this line must be changed depending on
c     detector: seattle requires cylindrical geometry.

      if (z.lt.0..or.z.gt.ZMAX.or.((x**2.0+y**2.0).gt.(XMAX**2.0))) then
c     if (z.lt.0..or.z.gt.ZMAX.or.abs(x).gt.XMAX.or.abs(y).gt.YMAX) then
       ilost=ilost+1
       goto 100
      endif

c     if the pion neither escapes or decays, degrade energy due to de/dr.

      call ELOSS (tpi,DR)
      if (tpi.le.0.00) then
       rold=sqrt(rxold**2+ryold**2+rzold**2)
       istop=istop+1
       goto 100
      endif

c     check to see if the pion undergoes a nuclear reaction in the plastic.
```

```
c    if it does, it is considered to have vanished from the scintillator,
c    and is thus not detected.

     if (REACT(tpi,DR)) then
      ireac=ireac+1
      goto 100
     endif

c    check to see if the pion decayed-in-flight in the scintillator.
c    if it does, it is considered to have vanished from the scintillator,
c    and is thus not detected.

     if (DECAY(tpi)) then
      idkay=idkay+1
      goto 100
     endif

c    autocall small angle (coulomb) elastic scattering, and determine
c    the scattering.

     call MULTIPLE (tpi,DR,theta,multarr)
     phi=TWOPI*rand(0)
     call SCATTER (rx,ry,rz,theta,phi)

c    check for large angle (nuclear&Coulomb) elastic scattering, and determine
c    the scattering if necessary.

     if (ELAST(tpi,DR,theta,elnuclarr)) then
      phi=TWOPI*rand(0)
      iscatlarge=iscatlarge+1
      call SCATTER (rx,ry,rz,theta,phi)
     endif

c    check for large angle nuclear inelastic scattering, and determine the
c    scattering if necessary.

     if (INELAST(tpi,DR,theta)) then
      phi=TWOPI*rand(0)
      iinelas=iinelas+1
      call SCATTER (rx,ry,rz,theta,phi)
     endif

     goto 200

     end

     logical function ELAST (tpi,DR,theta,elnuclarr)

c    this function uses the total nuclear and coulomb elastic scattering
c    cross section to determine whether a large angle scatter occurred.
c    the angle through which the pion can scatter is determined using a
c    randomized function corresponding to the generic form of the large
c    angle elastic scattering angular distribution.
```

```
      implicit double precision (a-h,o-z)
      real random_function
      real elnuclarr (1000)

      PI=3.1415927
      RHO=4.5977D22

c     fit parameters for the total elastic scattering cross section. negative
c     values in the extrapolation region are forced to zero.

      A0=+7.570D+01
      A1=+3.351D+00
      A2=-1.361D-01
      A3=+1.282D-03

      sigma=(A0+(A1*(tpi))+(A2*(tpi**2))+(A3*(tpi**3)))*1.0D-27
      prob=1.0-exp(-RHO*sigma*DR)
      ELAST=rand(0).le.prob
      if (elast.eq..true.) theta=random_function(elnuclarr,1000)
      theta=(PI/180.0)*theta
      return
      end

      logical function INELAST (tpi,DR)

c     this function uses the total inelastic scattering cross section to
c     determine whether an inelastic scatter occurred.
c     since the relative probabilities of scattering into the various states are
c     unknown, as are the angular distributions. the inelastically scattered
c     pions are simply counted.

      implicit double precision (a-h,o-z)

      RHO=4.5977D22

c     fit parameters for the total inelastic scattering cross section. negative
c     values in the extrapolation region are forced to zero.

      A0=+2.1505D+00
      A1=-4.2857D-01
      A2=+1.9969D-02

      sigma=(A0+A1*tpi+A2*(tpi**2))*1.0D-27
      if (tpi.le.13.5) sigma=0.0
      prob=1.0-exp(-RHO*sigma*DR)
      INELAST=rand(0).le.prob

      return
      end

      subroutine MULTIPLE (tpi,DR,theta,multarr)

c     this subroutine uses a randomized function previously to return
c     the multiple scattering angle. the variable 'th' is defined in eqn (13.111)
```

```
c     of jackson, while 'theta' is defined in eqn (13.108). 'x' is defined in
c     eqn (13.115).

      implicit double precision (a-h,o-z)
      real random_function
      real multarr (1000)

      ROOTTWO=1.4142136
      PI=3.1415927
      ZPI=1.0
      ZC12=6.0
      ALPHA=7.2992701D-03
      HBARC=197D-13
      MPIC2=139.6
      RHO=4.5977D22

      x=random_function (multarr,1000)

      beta=sqrt(1.0-(1.0/((tpi/MPIC2)+1.0)))
      gamma=1.0/sqrt(1.0-beta**2)

      term1=4.0*PI*RHO*DR*log(204*(ZC12**(-1.0/3.0)))
      term2=(2.0*ZPI*ZC12*ALPHA*HBARC)/(gamma*MPIC2*(beta**2))
      th=sqrt(term1*(term2**2))
      theta=ROOTTWO*th*x

      return
      end

      logical function REACT (tpi,DR)

c     this function uses the total reaction cross section to determine whether
c     a reaction occurred. reacted pions vanish from the plastic.

      implicit double precision (a-h,o-z)

      RHO=4.5977D22

c     fit parameters for the total reaction cross section. negative values
c     in the extrapolation region are forced to zero.

      A0=-1.605D+02
      A1=+1.224D+01
      A2=-1.014D-01

      cross=(A0+A1*tpi+A2*tpi**2)*1.0D-27
      prob=1.0-exp(-RHO*cross*DR)
      REACT=rand(0).le.prob
      return
      end

      logical function DECAY(tpi)

c     some pions make it into the detector but decay before coming to a
```

```
c    complete stop. these are counted.

     implicit double precision (a-h,o-z)

     MPI=139.6
     gamma=(tpi/MPI)+1.0
     beta=sqrt(1.0-(1.0/(gamma**2.0)))
     prob=1.0-exp(-6.2019477e-05/(beta*gamma))
     DECAY=rand(0).le.prob
     return
     end

     subroutine ELOSS (tpi,DR)

c    pion stopping power information for scintillator was determined using
c    the system program ELOSS and checked against that presented in VII-78
c    of the TRIUMF Kinematic Handbook. these values were fit to a chi-square
c    of less than 1.1, and the coefficients of the fit are used to determine the
c    stopping power (MeVcm**2/g).

     implicit double precision (a-h,o-z)

c    fit parameters for the pion stopping power.

     A0=+2.318D+00
     A1=+2.274D+01
     A2=+1.092D+01

     stop=A0+A1*exp(-tpi/A2)
     tpi=tpi-stop*DR
     return
     end

c    the following three subroutines were written by J. M. Vogt.

     subroutine TRAVEL (x,y,z,rx,ry,rz,DR)

c    this subroutine performs the necessary vector algebra to propagate
c    a pion through a layer dr of matter.

c    x,y,z: position before and after travelling
c    rx,ry,rz: direction in which to travel
c    dist: distance over which to travel

     implicit double precision (a-h,o-z)

c    calculate unit vector for direction

     r=sqrt(rx**2+ry**2+rz**2)
     xhat=rx/r
     yhat=ry/r
     zhat=rz/r

c    travel distance DR
```

```
      x=x+xhat*DR
      y=y+yhat*DR
      z=z+zhat*DR
      return
      end

      subroutine SCATTER (rx,ry,rz,theta,phi)

c     this subroutine performs the necessary vector algebra to correct the
c     pion trajectory for a scatter through an angle theta.

c     rx,ry,rz: direction of particle before and after scattering
c     theta: scattering angle
c     phi: defines plane in which scattering occurs

      implicit double precision (a-h,o-z)

c     vin is a unit vector in the direction of r

      r=sqrt(rx**2+ry**2+rz**2)
      vinx=rx/r
      viny=ry/r
      vinz=rz/r

c     calculate unit vector perpendicular to r in the xz-plane

      vec1=sqrt(rx**2+rz**2)
      vec1x=rz/vec1
      vec1y=0.d0
      vec1z=-rx/vec1

c     calculate vec2 so that vin,vec1,vec2 are right-handed

      call VECPRO (vec2x,vec2y,vec2z,vinx,viny,vinz,vec1x,vec1y,vec1z)

c     vec2 is a unit vector since vin and vec1 are perpendicular unit vectors
c     calculate unit vector perpendicular to vin in scattering plane

      co=cos(phi)
      si=sin(phi)
      vec3x=co*vec1x+si*vec2x
      vec3y=co*vec1y+si*vec2y
      vec3z=co*vec1z+si*vec2z

c     calculate route

      co=cos(theta)
      si=sin(theta)
      rx=co*vinx+si*vec3x
      ry=co*viny+si*vec3y
      rz=co*vinz+si*vec3z
      return
      end
```

```
      subroutine VECPRO (vx,vy,vz,v1x,v1y,v1z,v2x,v2y,v2z)

c     this subroutine calculates the vector product of two vectors.

      implicit double precision (a-z)

      vx=v1y*v2z-v1z*v2y
      vy=v1z*v2x-v1x*v2z
      vz=v1x*v2y-v1y*v2x
      return
      end

      double precision function rand (is)

c     details of the random function are taken care of.

      save iseed
      if (is.ne.0) iseed=is
      rand=ran(iseed)
      return
      end

      real function smallangle (x)

c     the weight function for the small angle random function generator is
c     defined here.

      smallangle=exp(-(x**2))
      return
      end

      real function largeangle (x)

c     the weight for the large angle random function generator is defined
c     here.

c     fit parameters to the generic angular distribution for large angle
c     elastic scattering.

      P1byP4bar=1.633D+01
      P2bar=1.480D+01
      P3bar=1.371D+01
      P5byP4bar=6.448D-03

      num=-1.0*((x-P2bar)**2)
      den=2.0*(P3bar**2)
      largeangle=(1.0+((P1byP4bar)*exp(num/den))+(P5byP4bar)*x)
      return
      end

c     the following subroutine and function were written by J. M. Vogt.
```

```
      SUBROUTINE INIT_RANDOM_FUNCTION (FUNC,ARRAY,N,WMIN,-
WMAX)

c     this subroutine integrates the array passed into it.

      external func
      DIMENSION ARRAY (N)
      STEP=(WMAX-WMIN)/(N-2)
      ARRAY(N)=STEP
      ARRAY(N-1)=WMIN
      DO 1 I=1,N-2
      Y=0.
      DO 2 J=0,9
      X=WMIN+(I-1+.1*J+.05)*STEP
    2  Y=Y+FUNC(X)
    1  ARRAY(I)=Y
      DO 3 I=2,N-2
    3  ARRAY(I)=ARRAY(I)+ARRAY(I-1)
      RETURN
      END

      FUNCTION RANDOM_FUNCTION (ARRAY,N)

c     this function randomizes the function passed into
c     INIT_RANDOM_FUNCTION

      double precision rand
      DIMENSION ARRAY (N)
      IF (ARRAY(N-2).EQ.0) THEN
      RANDOM_FUNCTION=ARRAY(N-1)
      RETURN
      ENDIF
   10   Y=RAND (0)
      IF (Y.EQ.0.AND.ARRAY(1).EQ.0) GOTO 10
      Y=Y*ARRAY(N-2)
      DO 1 I=1,N-2
      IF (ARRAY(I).GE.Y) THEN
      INDEX=I
      GOTO 2
      ENDIF
    1   CONTINUE
    2   IF (INDEX.EQ.1) THEN
      X=ARRAY(N-1)+Y/ARRAY(1)*ARRAY(N)
      ELSE
      X=ARRAY(N-1)+(INDEX-1)*ARRAY(N)+
       $       (Y-ARRAY(INDEX-1))/(ARRAY(INDEX)-ARRAY(INDEX-
1))*ARRAY(N)
      ENDIF
      RANDOM_FUNCTION=X
      RETURN
      END
```

E.3.3 Discussion of Selected Subroutines

Some of the most important subroutines in the code have little do to with the interactions being modelled by the Monte Carlo, yet deserved to be discussed. These include the TRAVEL subroutine, the SCATTER subroutine, and function randomization.

The TRAVEL Subroutine

This subroutine accepted from the main program values for the trajectory vector $\vec{r}$ projected on the Cartesian axes $\langle r_x, r_y, r_z \rangle$, the Cartesian coordinates of the π^+ event, and the trajectory stepsize dr. The Cartesian axes were centered at the face of a given detector, with the z-direction along the symmetry axis of the block, the y-direction being the lab vertical, and the x-direction chosen as necessary to complete a right-handed triad (see Figure E.6). Unit vectors corresponding to r_x, r_y, and r_z were calculated. These unit vectors were then multiplied by the stepsize dr to determine displacements along the x, y, and z axes. These displacements were then added to the original coordinates to produce the new Cartesian location of the π^+.

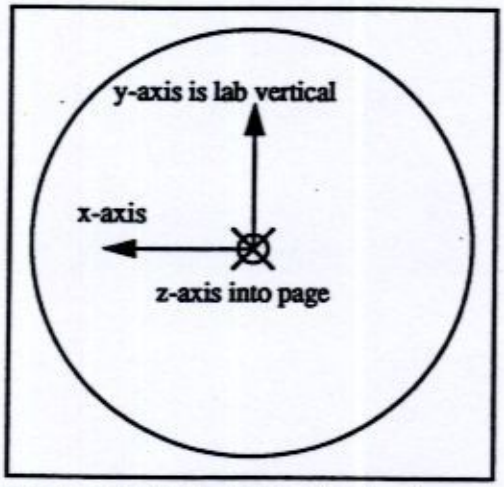

Figure E.6: The Coordinate Axes

The SCATTER Subroutine

This subroutine accepted from the main program values for the trajectory vector $\vec{r}$ projected on the Cartesian axes $\langle r_x, r_y, r_z \rangle$, and angles θ and φ through which the π^+ was to be scattered. The trajectory vector was converted to a unit vector $\hat{v}in = \langle vin_x, -vin_y, vin_z \rangle$. A new unit vector $\hat{v}1$ perpendicular to the trajectory vector and lying in the

xz plane was determined. This plane corresponded to the scattering angle φ=0. The vector product (subroutine VECPRO) of the unit vectors v̂in and v̂1 yielded the vector v̂2 and completed the new right handed coordinate triad.

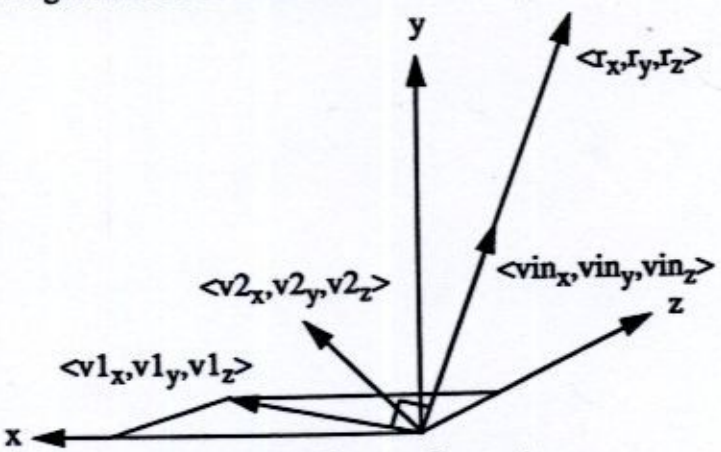

Figure E.7: Vector Geometry

The coordinate axes defined by vectors v̂1 and v̂2 were rotated by angle φ about the invariant axis v̂in such that the vector v̂1 was mapped into a new vector v̂3. The scattering plane was thus defined by vectors v̂in and v̂3. By rotating v̂in through angle θ in the scattering plane, v̂out, the post-scatter trajectory was obtained.

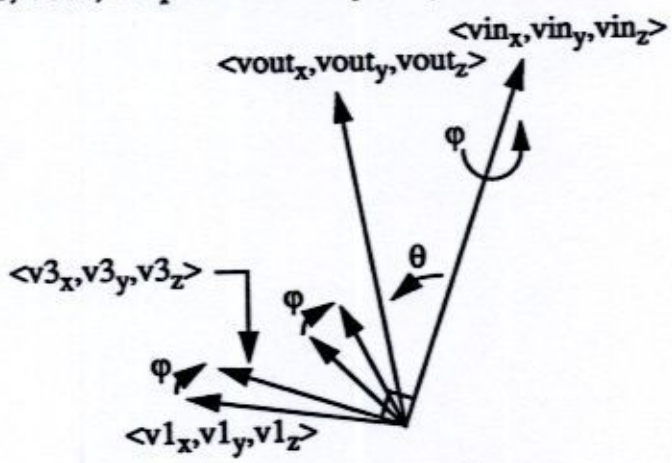

Figure E.8: More Vector Geometry

The Function Randomization Subroutine

This subroutine randomized a user-determined input function, which was passed to the subroutine in the form of an array. The function was integrated in steps 1/10 the original step size, and read into a new integrated function array. A random number was generated and multiplied by the integral of the input curve (the last element in the integrated

function array). The integrated function array was searched through for the weighted random number. Once it was located, the index was searched for in the input function array. The value of the input function array so indexed was the randomized functional value returned.

E.4 Results

Ten thousand π^+ events were Monte Carloed for each of three different situations: Australian detector with 55 mm diameter collimation, Australian detector with 80 mm diameter collimation, and Seattle detector with 80 mm diameter collimation. The results are summarized in Tables E.6, E.7, and E.8.

The table columns are as follows: "# stopped" was the number of π^+ which came to a stop within the plastic and were thus hardware visible, "# outscatter" was the number of π^+ which escaped the active volume of the scintillator due to all types of scattering, "# reacted" was the number of π^+ which underwent a reaction in the detector and thus could not be detected, "# decay" was the number of π^+ which decayed in the detector before coming to a stop, and were thus not detected, and "# inelastic" was the number of π^+ which underwent an inelastic scatter, and thus deposited an uncertain amount of energy. The error associated with each table entry was statistical ($\sqrt{N}$).

Table E.6: Australian Detector with 55 mm Diameter Collimation

T_π [MeV]	# stopped	# outscatter	# reacted	# decay	# inelastic
5	9968	3	0	29	0
10	9962	2	0	36	0
15	9949	2	0	49	0
20	9937	5	11	47	0
25	9852	13	40	95	0
30	9764	19	105	112	7
35	9647	21	203	129	16
40	9553	17	289	141	24
45	9268	28	385	319	38
50	9238	33	559	170	68
55	8954	36	792	218	89
60	8718	79	959	244	145
65	8498	109	1133	260	186
70	8257	185	1301	257	226
75	7958	333	1434	275	313

Table E.7: Australian Detector with 80 mm Diameter Collimation

T_π [MeV]	# stopped	# outscatter	# reacted	# decay	# inelastic
5	9968	3	0	29	0
10	9962	2	0	36	0
15	9949	2	0	49	0
20	9937	5	11	47	0
25	9849	13	38	100	0
30	9762	19	105	114	7
35	9650	18	203	129	14
40	9549	18	289	144	22
45	9267	41	382	310	34
50	9135	111	553	201	61
55	8785	249	742	224	90
60	8393	446	906	255	144
65	7896	713	1131	260	202
70	7517	922	1279	282	250
75	6944	1309	1458	289	299

Table E.8: Seattle Detector with 80 mm Diameter Collimation

T_π [MeV]	# stopped	# outscatter	# reacted	# decay	# inelastic
5	9968	3	0	29	0
10	9962	2	0	36	0
15	9949	2	0	49	0
20	9937	5	11	47	0
25	9852	13	40	95	0
30	9762	19	105	114	7
35	9651	18	203	128	14
40	9538	23	295	144	24
45	9231	57	391	321	35
50	9044	219	542	195	64
55	8603	418	742	237	92
60	8019	723	984	274	152
65	7475	1141	1142	242	202
70	6953	1498	1292	257	236
75	6337	1949	1424	290	291

Assuming the energy transfer in elastic scattering was very small, the uncertainty in detected π^+ energy due to the inelastic scattering term is presented in Table E.9.

Table E.9: π^+ Mislabelled in Energy due to Inelastic Scattering

T_π [MeV]	Aus.55mm [+/- 0.01]	Aus.80mm [+/- 0.01]	Sea.80mm [+/- 0.01]	Average [+/- 0.01]
5	0.00	0.00	0.00	0.00
10	0.00	0.00	0.00	0.00
15	0.00	0.00	0.00	0.00
20	0.00	0.00	0.00	0.00
25	0.00	0.00	0.00	0.00
30	0.00	0.00	0.00	0.00
35	0.00	0.00	0.00	0.00
40	0.00	0.00	0.00	0.00
45	0.00	0.00	0.00	0.00
50	0.01	0.01	0.01	0.01
55	0.01	0.01	0.01	0.01
60	0.01	0.01	0.01	0.01
65	0.02	0.02	0.02	0.02
70	0.03	0.02	0.02	0.02
75	0.03	0.03	0.03	0.03

At most, 3% of the data had incorrectly labelled energies due to inelastic scattering. The problem diminished with respect to the first excited state of C since 4.44 MeV was basically only 1/2 the width of an energy bin. Further, when these results were viewed in light of the fact that the detector resolution was about 15% (see Appendix D), the problem became negligible.

The contribution of the Monte Carloed term to the π^+ detection efficiency as a function of T_π was given by

$$\pi A\,(T_\pi) \;=\; 1 - \left(\frac{\text{lost} + \text{reacted} + \text{decayed}}{10000}\right) \;=\; \left(\frac{\text{stopped}}{10000}\right). \qquad \text{(E.21)}$$

This contribution is summarized in Table E.10, and shown in Figure E.9.

Table E.10: The Contribution of the Monte-Carloed Term

T_π [MeV]	Aus.55mm [+/- 0.01]	Aus.80mm [+/- 0.01]	Sea.80mm [+/- 0.01]
5	1.00	1.00	1.00
10	1.00	1.00	1.00
15	1.00	1.00	1.00
20	1.00	1.00	1.00
25	0.99	0.98	0.99
30	0.98	0.98	0.98
35	0.96	0.96	0.97
40	0.96	0.95	0.95
45	0.93	0.93	0.92
50	0.92	0.92	0.90
55	0.90	0.88	0.86
60	0.87	0.84	0.80
65	0.85	0.79	0.75
70	0.83	0.75	0.70
75	0.80	0.69	0.63

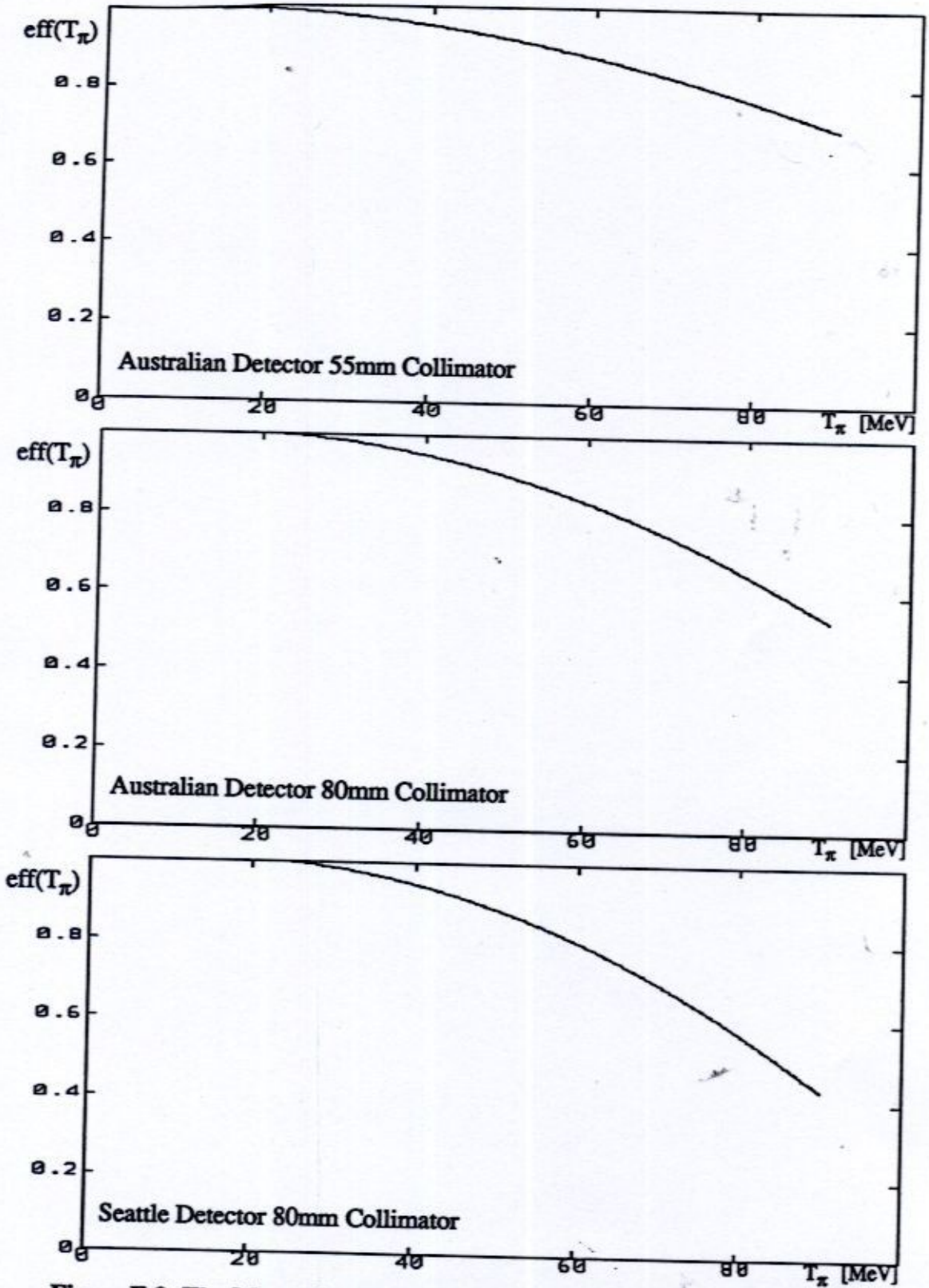

Figure E.9: The Monte Carlo Contribution to the Detection Efficiency

Appendix F. CROSS SECTIONS

Table F.1: $d^2\sigma/d\Omega dT_\pi$ for C at $\theta_{LAB} = 51^o$

E_γ [MeV]	T_π [MeV]	$d^2\sigma/d\Omega dT_\pi$ [μb/srMeV]	statistical error [μb/srMeV]	systematic error [%]	total error [μb/srMeV]
213	25	0.26	0.04	12.30	0.07
	35	0.31	0.02	12.42	0.06
	45	0.31	0.04	13.20	0.08
	55	0.35	0.03	14.33	0.08
	65	0.12	0.02	16.26	0.04
204	25	0.26	0.03	12.32	0.06
	35	0.25	0.04	12.50	0.07
	45	0.30	0.03	13.13	0.07
	55	0.10	0.02	13.90	0.03
194	25	0.28	0.04	12.30	0.07
	35	0.20	0.03	12.49	0.05
	45	0.07	0.02	12.91	0.03
184	25	0.23	0.01	12.33	0.04

Table F.2: $d^2\sigma/d\Omega dT_\pi$ for C at $\theta_{LAB} = 81^o$

E_γ [MeV]	T_π [MeV]	$d^2\sigma/d\Omega dT_\pi$ [μb/srMeV]	statistical error [μb/srMeV]	systematic error [%]	total error [μb/srMeV]
213	25	0.36	0.04	12.19	0.08
	35	0.38	0.04	12.30	0.09
	45	0.31	0.03	13.06	0.07
	55	0.29	0.03	14.58	0.07
	65	0.15	0.03	16.18	0.05
204	25	0.28	0.03	12.19	0.06
	35	0.27	0.03	12.32	0.06
	45	0.29	0.03	13.03	0.07
	55	0.04	0.02	14.38	0.03
194	25	0.20	0.03	12.20	0.05
	35	0.24	0.03	12.31	0.06
	45	0.08	0.02	12.95	0.03
184	25	0.21	0.03	12.21	0.06

Table F.3: $d^2\sigma/d\Omega dT_\pi$ for C at $\theta_{LAB} = 109^o$

E_γ [MeV]	T_π [MeV]	$d^2\sigma/d\Omega dT_\pi$ [μb/srMeV]	statistical error [μb/srMeV]	systematic error [%]	total error [μb/srMeV]
213	25	0.24	0.03	12.61	0.06
	35	0.24	0.03	12.73	0.06
	45	0.21	0.03	13.49	0.06
	55	0.19	0.03	14.94	0.06
	65	0.15	0.03	17.17	0.06
204	25	0.25	0.03	12.62	0.06
	35	0.16	0.03	12.74	0.05
	45	0.23	0.03	13.49	0.06
	55	0.08	0.02	14.76	0.03
194	25	0.15	0.02	12.62	0.04
	35	0.18	0.03	12.70	0.05
	45	0.08	0.02	13.23	0.03
184	25	0.15	0.02	12.62	0.04
	35	0.06	0.02	12.63	0.03

Table F.4: $d^2\sigma/d\Omega dT_\pi$ for C at $\theta_{LAB} = 141^o$

E_γ [MeV]	T_π [MeV]	$d^2\sigma/d\Omega dT_\pi$ [μb/srMeV]	statistical error [μb/srMeV]	systematic error [%]	total error [μb/srMeV]
213	25	0.20	0.03	11.75	0.05
	35	0.17	0.03	11.87	0.05
	45	0.13	0.02	12.89	0.04
	55	0.22	0.03	14.66	0.06
	65	0.24	0.03	17.45	0.07
204	25	0.18	0.03	11.73	0.05
	35	0.14	0.03	11.90	0.05
	45	0.21	0.03	12.87	0.06
	55	0.14	0.02	14.33	0.04
194	25	0.08	0.02	11.76	0.03
	35	0.12	0.02	11.88	0.03
	45	0.10	0.02	12.60	0.03
184	25	0.12	0.02	11.77	0.03

Table F.5: $d^2\sigma/d\Omega dT_\pi$ for Ca at $\theta_{LAB} = 81^o$

E_γ [MeV]	T_π [MeV]	$d^2\sigma/d\Omega dT_\pi$ [μb/srMeV]	statistical error [μb/srMeV]	systematic error [%]	total error [μb/srMeV]
213	25	0.80	0.09	12.18	0.19
	35	0.93	0.09	12.34	0.20
	45	0.94	0.09	13.11	0.21
	55	0.86	0.10	14.44	0.22
	65	0.55	0.09	16.93	0.18
	75	0.27	0.07	20.20	0.12
204	25	0.66	0.08	12.19	0.16
	35	0.82	0.08	12.31	0.18
	45	0.79	0.09	13.00	0.19
	55	0.57	0.08	14.26	0.16
	65	0.38	0.07	16.87	0.13
194	25	0.52	0.07	12.21	0.13
	35	0.56	0.07	12.32	0.14
	45	0.53	0.07	13.02	0.14
	55	0.26	0.06	14.18	0.10
184	25	0.54	0.07	12.20	0.14
	35	0.32	0.06	12.32	0.10
	45	0.10	0.06	12.81	0.07
	55	0.07	0.04	14.06	0.05

Table F.6: $d^2\sigma/d\Omega dT_\pi$ for Ca at $\theta_{LAB} = 109^o$

E_γ [MeV]	T_π [MeV]	$d^2\sigma/d\Omega dT_\pi$ [μb/srMeV]	statistical error [μb/srMeV]	systematic error [%]	total error [μb/srMeV]
213	25	0.56	0.07	12.62	0.14
	35	0.77	0.08	12.74	0.18
	45	0.68	0.08	13.54	0.17
	55	0.65	0.08	14.93	0.18
	65	0.60	0.08	17.29	0.18
	75	0.39	0.08	21.36	0.16
	85	0.14	0.06	25.93	0.10
204	25	0.53	0.07	12.59	0.14
	35	0.58	0.08	12.68	0.15
	45	0.49	0.07	13.61	0.14
	55	0.40	0.07	14.75	0.13
	65	0.30	0.06	17.31	0.11
	75	0.09	0.05	20.30	0.07
194	25	0.39	0.06	12.62	0.11
	35	0.46	0.06	12.71	0.12
	45	0.35	0.06	13.53	0.11
	55	0.30	0.06	15.03	0.11
184	25	0.41	0.06	12.62	0.11
	35	0.29	0.06	12.73	0.10
	45	0.25	0.06	13.52	0.09
	55	0.20	0.04	14.62	0.07

Table F.7: $d^2\sigma/d\Omega dT_\pi$ for Ca at $\theta_{LAB} = 141^o$

E_γ [MeV]	T_π [MeV]	$d^2\sigma/d\Omega dT_\pi$ [μb/srMeV]	statistical error [μb/srMeV]	systematic error [%]	total error [μb/srMeV]
213	25	0.60	0.08	11.72	0.15
	35	0.49	0.07	11.85	0.13
	45	0.57	0.07	12.69	0.14
	55	0.70	0.08	14.72	0.18
	65	0.36	0.07	17.64	0.13
	75	0.39	0.07	23.68	0.16
204	25	0.56	0.07	11.73	0.14
	35	0.51	0.07	11.87	0.13
	45	0.42	0.07	12.82	0.12
	55	0.36	0.07	14.75	0.12
	65	0.20	0.06	17.35	0.09
194	25	0.34	0.05	11.74	0.09
	35	0.21	0.05	11.94	0.08
	45	0.24	0.05	12.92	0.08
	55	0.11	0.04	14.45	0.06
184	25	0.28	0.06	11.75	0.09
	35	0.23	0.05	11.83	0.08
	45	0.09	0.05	12.91	0.06

Table F.8: $d^2\sigma/d\Omega dT_\pi$ for Sn at $\theta_{LAB} = 109^o$

E_γ [MeV]	T_π [MeV]	$d^2\sigma/d\Omega dT_\pi$ [μb/srMeV]	statistical error [μb/srMeV]	systematic error [%]	total error [μb/srMeV]
213	25	0.96	0.16	12.62	0.28
	35	0.99	0.16	12.71	0.29
	45	1.05	0.17	13.48	0.31
	55	0.90	0.17	14.92	0.30
	65	0.37	0.13	17.02	0.19
	75	0.40	0.12	20.83	0.20
204	25	0.60	0.14	12.63	0.21
	35	0.72	0.15	12.73	0.24
	45	0.45	0.13	13.52	0.20
	55	0.47	0.13	14.92	0.20
	65	0.13	0.08	16.18	0.10
194	25	0.64	0.12	12.62	0.20
	35	0.69	0.13	12.67	0.22
	45	0.43	0.11	13.37	0.17
	55	0.11	0.08	14.60	0.10
184	25	0.21	0.10	12.61	0.13
	35	0.31	0.11	12.75	0.15
	45	0.14	0.09	13.15	0.11

Table F.9: $d^2\sigma/d\Omega dT_\pi$ for Sn at $\theta_{LAB} = 141^o$

E_γ [MeV]	T_π [MeV]	$d^2\sigma/d\Omega dT_\pi$ [μb/srMeV]	statistical error [μb/srMeV]	systematic error [%]	total error [μb/srMeV]
213	25	0.59	0.16	11.73	0.23
	35	0.70	0.14	11.95	0.22
	45	0.64	0.14	12.75	0.22
	55	0.99	0.17	14.45	0.31
	65	0.63	0.16	17.94	0.27
	75	0.36	0.13	23.71	0.21
204	25	0.58	0.13	11.72	0.20
	35	0.79	0.15	11.94	0.24
	45	0.91	0.16	12.72	0.28
	55	0.80	0.15	14.70	0.27
	65	0.17	0.10	17.66	0.13
194	25	0.31	0.11	11.78	0.15
	35	0.36	0.11	11.93	0.15
	45	0.18	0.09	12.60	0.11
	55	0.14	0.09	15.84	0.11
184	25	0.31	0.12	11.76	0.16
	35	0.23	0.11	11.81	0.14
	45	0.19	0.09	12.63	0.11

Table F.10: $d^2\sigma/d\Omega dT_\pi$ for Pb at $\theta_{LAB} = 109^o$

E_γ [MeV]	T_π [MeV]	$d^2\sigma/d\Omega dT_\pi$ [μb/srMeV]	statistical error [μb/srMeV]	systematic error [%]	total error [μb/srMeV]
213	25	0.79	0.26	12.63	0.36
	35	1.12	0.26	12.74	0.40
	45	1.66	0.32	13.59	0.55
	55	1.06	0.30	14.83	0.46
	65	0.78	0.27	17.28	0.40
	75	0.42	0.21	20.50	0.30
204	25	1.01	0.24	12.64	0.37
	35	0.77	0.27	12.84	0.37
	45	1.64	0.29	13.53	0.51
	55	0.65	0.26	15.07	0.36
	65	0.25	0.17	16.80	0.21
194	25	0.94	0.21	12.63	0.33
	35	0.82	0.22	12.75	0.32
	45	0.58	0.20	13.58	0.28
184	25	0.63	0.22	12.65	0.30
	35	0.40	0.20	12.76	0.25

Table F.11: $d^2\sigma/d\Omega dT_\pi$ for Pb at $\theta_{LAB} = 141^o$

E_γ [MeV]	T_π [MeV]	$d^2\sigma/d\Omega dT_\pi$ [μb/srMeV]	statistical error [μb/srMeV]	systematic error [%]	total error [μb/srMeV]
213	25	0.66	0.33	11.76	0.41
	35	0.77	0.28	11.90	0.37
	45	0.71	0.24	13.04	0.33
	55	0.77	0.30	14.38	0.41
	65	1.06	0.33	17.60	0.52
	75	0.79	0.27	23.34	0.45
204	25	0.61	0.25	11.74	0.32
	35	1.04	0.30	11.98	0.42
	45	1.00	0.29	12.79	0.42
	55	1.12	0.30	14.77	0.47
	65	0.27	0.16	19.00	0.21
	75	0.47	0.17	22.68	0.28
194	25	0.51	0.23	11.77	0.29
	35	0.41	0.24	11.88	0.29
	45	0.54	0.21	12.61	0.28
184	25	0.33	0.26	11.77	0.30

Table F.12: Laboratory Angular Distributions for the H Target

E_γ [MeV]	θ_{LAB} [°]	$d\sigma/d\Omega$ [μb/sr]	statistical error [μb/sr]	systematic error [%]	total error [μb/sr]
213	51	10.16	0.89	16.18	2.53
	81	10.47	0.81	13.43	2.22
	109	7.02	0.67	12.88	1.57
	141	5.25	0.54	11.70	1.15
204	51	7.82	0.74	14.94	1.91
	81	10.15	0.73	12.66	2.01
	109	6.65	0.60	12.60	1.44
	141	5.06	0.48	11.72	1.07
194	51	8.82	0.68	13.05	1.83
	81	8.05	0.62	12.20	1.60
	109	5.16	0.49	12.66	1.14
	141	3.78	0.47	11.89	0.92
184	51	8.02	0.59	14.15	1.72
	81	7.11	0.52	12.24	1.39

Table F.13: Laboratory Angular Distributions for the C Target

E_γ [MeV]	θ_{LAB} [°]	$d\sigma/d\Omega$ [μb/sr]	statistical error [μb/sr]	systematic error [%]	total error [μb/sr]
213	51	14.44	0.75	12.29	2.52
	81	15.88	0.79	13.21	2.89
	109	10.87	0.68	13.90	2.19
	141	10.24	0.67	13.92	2.10
204	51	9.83	0.65	12.73	1.90
	81	9.13	0.63	12.57	1.78
	109	7.94	0.57	13.13	1.61
	141	7.65	0.55	12.63	1.52
194	51	6.08	0.49	13.71	1.32
	81	6.26	0.48	12.40	1.26
	109	4.81	0.41	12.84	1.03
	141	3.43	0.36	12.08	0.77
184	51	3.28	0.37	12.23	0.77
	81	2.62	0.33	12.27	0.65
	109	2.28	0.29	12.75	0.58
	141	1.72	0.28	11.81	0.48

Table F.14: Laboratory Angular Distributions for the Ca Target

E_γ [MeV]	θ_{LAB} [°]	$d\sigma/d\Omega$ [μb/sr]	statistical error [μb/sr]	systematic error [%]	total error [μb/sr]
213	51	35.14	2.69	14.32	7.72
	81	45.81	2.26	13.79	8.58
	109	39.23	2.07	15.25	8.05
	141	32.75	1.86	14.73	6.68
204	51	28.91	2.39	13.48	6.29
	81	33.82	1.92	13.29	6.41
	109	24.92	1.71	14.02	5.20
	141	22.14	1.58	13.13	4.49
194	51	9.49	2.46	12.72	3.67
	81	20.29	1.50	12.84	4.11
	109	17.05	1.33	13.44	3.62
	141	9.86	1.07	12.32	2.28
184	51	12.82	1.50	12.27	3.07
	81	9.92	1.10	12.43	2.33
	109	11.54	1.04	13.14	2.56
	141	6.35	0.91	12.08	1.68

Table F.15: Laboratory Angular Distributions for the Sn Target

E_γ [MeV]	θ_{LAB} [°]	$d\sigma/d\Omega$ [μb/sr]	statistical error [μb/sr]	systematic error [%]	total error [μb/sr]
213	51	67.53	9.00	13.52	18.13
	81	63.39	4.55	13.49	13.10
	109	48.73	3.85	14.41	10.87
	141	40.56	3.79	14.52	9.68
204	51	49.08	6.46	13.48	13.08
	81	33.24	4.49	12.93	8.79
	109	25.52	2.98	13.36	6.39
	141	33.99	3.21	13.18	7.69
194	51	27.55	6.86	13.11	10.47
	81	17.40	3.69	22.50	7.61
	109	21.71	2.40	12.92	5.20
	141	11.17	2.12	12.53	3.52
184	51	19.59	11.66	22.34	16.04
	81	7.49	3.08	12.45	4.01
	109	7.11	1.65	12.79	2.56
	141	7.27	1.78	11.97	2.65

Table F.16: Laboratory Angular Distributions for the Pb Target

E_γ [MeV]	θ_{LAB} [°]	$d\sigma/d\Omega$ [μb/sr]	statistical error [μb/sr]	systematic error [%]	total error [μb/sr]
213	81	93.45	11.30	13.89	24.28
	109	63.28	7.01	14.64	16.27
	141	52.10	7.52	14.64	15.14
204	81	51.95	9.57	23.11	21.58
	109	45.86	5.78	13.71	12.07
	141	46.54	6.30	14.28	12.95
194	81	16.68	9.11	12.86	11.26
	109	27.58	4.39	13.03	7.98
	141	16.16	4.58	12.33	6.57
184	81	12.12	6.87	22.37	9.58
	109	11.54	3.26	12.97	4.76
	141	5.81	3.74	11.96	4.43

Table F.17: CM Angular Distributions for the H Target

E_γ [MeV]	θ_{CM} [°]	$d\sigma/d\Omega$ [μb/sr]	statistical error [μb/sr]	systematic error [%]	total error [μb/sr]
213	66	7.45	0.65	16.18	1.86
	99	10.14	0.79	13.43	2.15
	126	8.99	0.86	12.88	2.02
	152	8.71	0.90	11.70	1.92
204	66	5.70	0.54	14.94	1.39
	100	9.82	0.71	12.66	1.95
	126	8.56	0.78	12.60	1.86
	152	8.48	0.81	11.72	1.80
194	67	6.38	0.49	13.05	1.32
	100	7.77	0.60	12.20	1.55
	126	6.70	0.64	12.66	1.49
	152	6.47	0.80	11.89	1.57
184	67	5.70	0.42	14.15	1.23
	100	6.86	0.50	12.24	1.34

Table F.18: Total Cross Sections for the H Target

E_γ [MeV]	σ [μb]	statistical error [μb]	systematic error [%]	total error [μb]
213	105.59	4.86	14.06	19.71
204	94.07	4.21	13.22	16.64
194	83.62	3.74	12.56	14.24
184	81.88	3.50	12.75	13.94

Table F.19: Total Cross Sections for the C Target

E_γ [MeV]	σ [μb]	statistical error [μb]	systematic error [%]	total error [μb]
213	163.51	4.62	13.16	26.14
204	109.76	3.86	12.76	17.87
194	65.77	2.84	12.90	11.32
184	31.92	2.08	12.22	5.98

Table F.20: Total Cross Sections for the Ca Target

E_γ [MeV]	σ [μb]	statistical error [μb]	systematic error [%]	total error [μb]
213	478.88	14.69	14.47	83.98
204	347.30	12.71	13.47	59.49
194	174.87	11.53	12.87	34.04
184	130.43	7.72	12.50	24.02

Table F.21: Total Cross Sections for the Sn Target

E_γ [MeV]	σ [μb]	statistical error [μb]	systematic error [%]	total error [μb]
213	705.21	40.12	13.85	137.79
204	457.73	30.80	13.28	91.59
194	252.51	29.91	14.92	67.58
184	138.61	46.02	17.77	70.65

Table F.22: Total Cross Sections for the Pb Target

E_γ [MeV]	σ [μb]	statistical error [μb]	systematic error [%]	total error [μb]
213	969.60	82.55	14.36	221.78
204	619.76	69.75	19.21	188.81
194	240.06	64.77	12.82	95.55
184	132.84	48.98	18.69	73.81

Appendix G. SUGGESTIONS FOR IMPROVING THE EXPERIMENT

Methods for minimizing the ringing in the photomultiplier signals from the E-detectors and a hardware modification to the μTDC event trigger are suggested.

G.1 Photomultiplier Signal Ringing

One of the most disappointing aspects of this experiment was the ringing of the photomultiplier signals from the E-detectors which appeared in the μTDC spectra and adversely affected the π^+ detection efficiency. This forced cuts to be placed on the data where there was no ringing, effectively rejecting a large portion of the otherwise valid events. By designing better photomultiplier tube bases that either eliminated or at least kept the ringing to a minimum, this could have been avoided, and a much more statistically significant statement could have been made.

The phenomenon of ringing has been observed by other experimental groups looking for π^+'s using the μTDC detection method. Several recommendations to reduce this problem have been made (Gothe, 1993). These recommendations include the following:

1. Active bases tend to introduce far more problems than they solve, so passive bases should be selected if at all possible (as they were in this measurement).

2. Vary the capacitance of the capacitors used to stabilize the voltages of the last several dynodes such that no two are the same.

3. Do not attempt to clip too strongly. The trade-off between a lesser level of clipping and baseline overshoots should be made in favor of a lesser level of clipping.

4. Any rough edges in the soldered bases lead to field emissions which can cause ringing. Care should be taken in assembling the bases, with wire leads kept as short as possible, and solder joints as smooth as possible.

If these relatively simple precautions are taken, the ringing of the anode signal of the photomultiplier tube will be minimized.

G.2 Circuit Modification to Reject Correlated Pairs

The other large problem in this experiment was the presence of correlated pairs in the π^+ energy spectra for high Z targets at forward angles in the lab. This undesired yield could only be estimated, since not enough hardware information was available to discern it from π^+. Assuming these pairs also pass through the ΔE detector, they can be discriminated against in the hardware by making a relatively simple modification to the μTDC event trigger. This upgrade is detailed in Figure G.1 below.

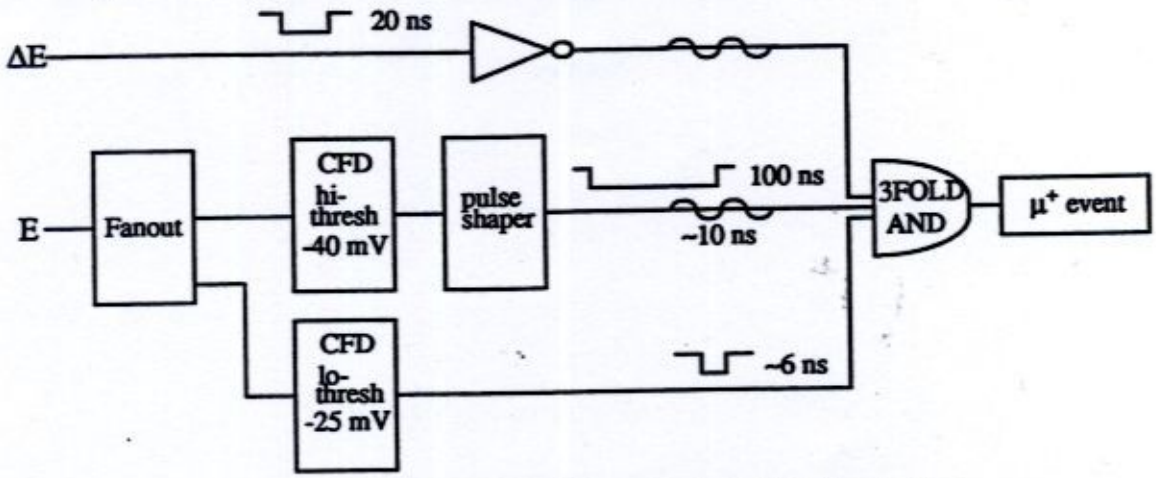

Figure G.1:Detail of the Upgraded μTDC Hardware

Consider the case of a correlated pair event. The prompt pair had the energy and timing characteristics of a π^+ event, and a random served to stop the μTDC, thereby thwarting all attempts to perform hardware rejection.

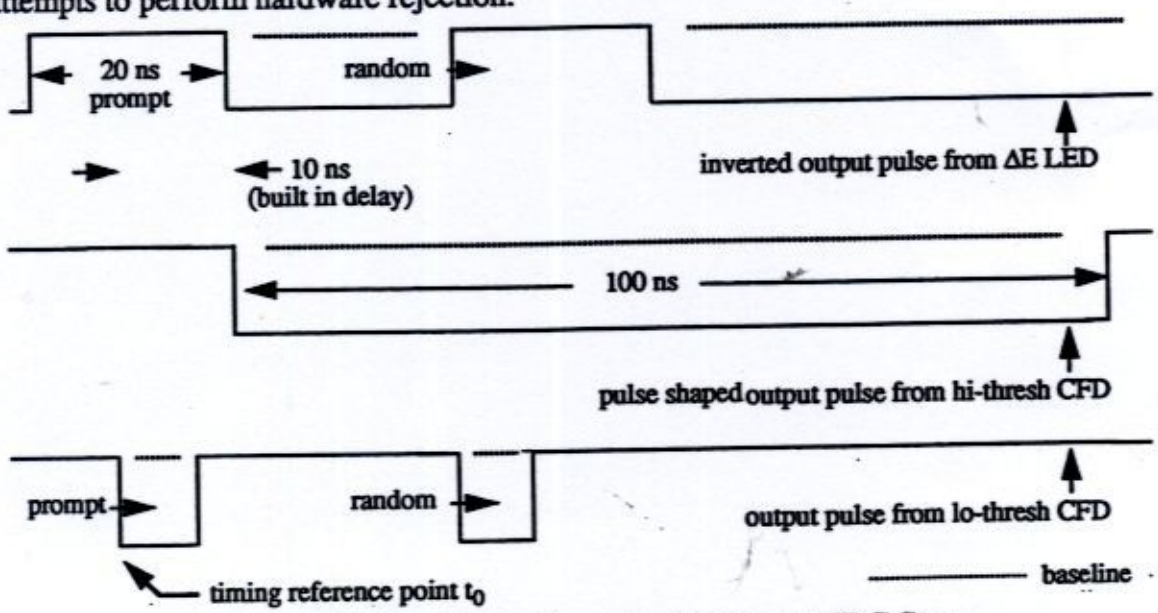

Figure G.2:The Prevention of a Random μTDC Stop

With the upgraded μTDC hardware definition, the situation presented in Figure G.1 would result. The three signals ($\overline{\Delta E}$, CFD^{hi}, CFD^{lo}) would be passed to a three fold coincidence unit which would be triggered only when all three were low. Random events defined by the ΔE detector would thus be prevented from triggering the μTDC, which would allow for effective hardware discrimination of pair events. Further, since it was these copious pair events which were the limiting factor on the singles rates for the high Z targets, eliminating them as triggers would allow the experiment to be run at a much higher rate.